Understanding the Behaviour of Aircraft Bearing Steels under Rolling Contact Loading

James Robert Nygaard
Peterhouse, Cambridge

Department of Materials Science and Metallurgy
University of Cambridge
27 Charles Babbage Road, Cambridge CB3 0FS, U.K.

August 2015

This dissertation is submitted for the degree of
Doctor of Philosophy

Preface

This thesis is submitted for the title of Doctor of Philosophy in Materials Science at the University of Cambridge. The work reported was carried out under the supervision of Professor H. K. D. H. Bhadeshia in the Department of Materials Science and Metallurgy between April 2011 to April 2015.

Some of the work contained in Chapters 3 - 5 of this thesis has been published previously and can be found in:
Nygaard et al., *Mat. Sci. & Tech.* **30** (2014), pp. 1911-1918 [1];
Nygaard et al., *ASTM STP.* **1580** (2015), pp. 525-537 [2].

This dissertation is the result of my own work and includes nothing which is the outcome of work done in collaboration except as declared in the preface and specified in the text. It is not substantially the same as any that I have submitted, or, is being concurrently submitted for a degree or diploma or other qualification at the University of Cambridge or any other university or similar institution except as declared in the preface and specified in the text. I further state that no substantial part of my dissertation has already been submitted, or, is being concurrently submitted for any such degree, diploma or other qualification at the University of Cambridge or any other university of similar institution except as declared in the preface and specified in the text. The length of this dissertation is less than 60,000 words and therefore does not exceed the prescribed word limit for the Degree Committee for the Faculty of Physics and Chemistry.

James Nygaard

August 2015

For my brother, Edward

An engineer of sound

Acknowledgments

I must first thank my academic supervisor Professor Sir Harry Bhadeshia for his enthusiasm in steel metallurgy. As head of the Phase Transformations and Complex Properties research group in Cambridge he oversaw much of the work detailed in this thesis together with that of my fellow group members whom I must also pay thanks: Dr Steve Ooi provided his assistance and endless patience throughout my time in Cambridge, as has Dr Mathew Peet who proof read this work along with Dr Pedro Rivera. Other close colleagues who deserve my thanks include Dr Wilberth Solano, Peter Walker, Gael Guetard, Olivier Messe and Chris Hulme-Smith. Ex-members of the Phase Transformations group who have now moved on also deserve special mention, particularly Dr Ed Pickering, Dr Lin Sun, Dr Yan Pei and Dr Lucy Fielding.

This work would not have been possible without the sponsorship and funding of the engineering and physical sciences research council (EPSRC) in partnership with Rolls-Royce plc. The industrial guidance offered by my supervisors at Rolls-Royce was invaluable, and so special thanks must go to Martin Rawson, Pete Danson and Tim Moreton for sharing their technical expertise. Additional guidance and the provision of metallographic samples was provided by SKF group and so my gratitude also goes to Erik Vegter of the SKF engineering and research centre, The Netherlands, for his kindness and direction, and also to Hans Verschoor and Gary Harrison for sharing their knowledge of X-ray diffraction. Finally, I would like to thank David Nicol and Simon Griggs for providing training in electron microscopy techniques.

Abstract

The purpose of the work presented in this thesis is to comprehensively characterise two steels currently used for rolling bearings in the aircraft gas-turbine engine. The physical metallurgy of these high-strength steel components is examined with a focus on the material behaviour under the rolling contact loads of service. The unique operating conditions posed by the aircraft gas-turbine engine environment are summarised, followed by a review of the myriad damage mechanisms traditionally encountered during rolling contact fatigue. The experimental work focuses on extensive examination of actual components from civil aircraft engines. Steel bearings from operation are compared with control samples and laboratory test pieces to gain understanding into their behaviour under rolling contact loading.

The results show evidence of sliding at the component surfaces that occurs during operation and causes severe plastic flow in the direction of tangential shear stress. This damage progresses with continued service, culminating in the creation of a nanocrystalline surface layer of equiaxed ferrite. Component tribology is worsened by the presence of hard residual carbide precipitates that intersect the contact surface. Chemical segregation during steel solidification is responsible for the coarsening of these surface carbides on bearing balls that cause extensive damage to the grooved raceways.

The onset of mechanical instability in the stressed volume beneath the contact surface is evidenced by changes in material properties. Work-hardening occurs after a large number of fatigue cycles, providing evidence of gradual strain accumulation. Evolution of a compressive residual stress field in carburised raceways has also been identified, and the subtle development of a preferred crystallographic texture further confirms that fatigue damage accumulates over prolonged periods of rolling contact. New evidence is presented showing localised plasticity in the form of mechanical twinning at inhomogeneities in the microstructure. This unique deformation mechanism is seen at interfaces between primary carbides and the matrix, and in widespread twin networks that nucleate along prior austenite grain boundaries. An entirely new theory of mechanical twin localisation is presented and suggestions are made to improve the future performance of aircraft bearing steels.

Contents

Nomenclature

a = lattice parameter
α = ferrite
α' = martensite
b = semi-major axis of a contact ellipse
d_{hkl} = interplanar lattice spacing
E = elastic modulus
E' = reduced elastic modulus
ϵ_{hkl} = interplanar strain
F = force (load)
g = acceleration due to gravity
γ = austenite
h = height
h_{min} = lubrication film thickness
K = stress intensity factor
K_{IC} = fracture toughness
L_{10} = fatigue life of 10% from a population
λ = lubrication film parameter
M_S = martensite start temperature
M_F = martensite finish temperature
μ_{th} = thermal efficiency
N = number of cycles
N_f = number of cycles to failure
P_L = mean lineal intercept
P = pressure
R = radius
R' = combined radius
R_a = surface roughness (mean centreline average)
R_q = surface roughness (root mean squared)
R_t = peak surface roughness
σ_y = yield stress
σ_z = Hertzian contact stress
σ_{UTS} = ultimate tensile stress
σ_{VM} = Von Mises stress
T_C = ambient air temperature
T_H = maximum combustion temperature
τ_{45} = Hertzian shear stress

τ_{zy} = orthogonal shear stress

$\Delta\tau_{zy}$ = orthogonal shear stress range

τ_{max} = maximum shear stress

ν = Poisson's ratio

z = depth

z_0 = depth of maximum shear stress

AFM = Atomic Force Microscope

ASTM = American Society for Testing and Materials

BCC = Body Centred Cubic

BF = Bright Field

BIB = Broad Ion Beam

DER = Dark Etching Regions

DF = Dark Field

EBSD = Electron Backscatter Diffraction

EDX = Energy Dispersive X-ray

FCC = Face Centred Cubic

FIB = Focused Ion Beam

FWHM = Full Width Half Maximum

HAADF = High Angle Annular Dark Field

HCP = Hexagonal Close Packed

HIP = Hot Isostatic Pressing

HP = High-Pressure turbine stage

HRC = Rockwell C Hardness

HV = Vickers Hardness

IP = Intermediate Pressure turbine stage

LP = Low Pressure turbine stage

ND = Normal Direction

ODF = Orientation Distribution Function

PM = Powder Metallurgy

RCF = Rolling Contact Fatigue

RD = Rolling Direction

SAD = Selected Area Diffraction

SEM = Scanning Electron Microscope

SFE = Stacking Fault Energy

STEM = Scanning Transmission Electron Microscope

TD = Transverse Direction

TEM = Transmission Electron Microscope

VIM-VAR = Vacuum Induction Melting with Vacuum Arc Remelting

XRD = X-ray Diffraction

Chapter 1

Introduction

Martensitic tool steels can be strong and durable making them ideal for engineering applications. With appropriate heat treatment these alloys retain hardness at high temperatures and show good dimensional stability essential for precision components [6]. Therefore, aside from cutting tools, martensitic steels are also used to manufacture rolling element bearings, which are traditionally comprised of either balls or cylinders constrained between two grooved rolling tracks called raceways. Rolling bearings are designed to support significant loads while offering low-friction, rotational movement, and require strict tolerances to be maintained over millions of stress cycles without failure. Two particular martensitic steels have dominated the aircraft bearings industry for decades; M50 and M50NiL are secondary hardened steels suitable for the elevated temperatures of the aircraft gas-turbine engine. These steels gain strength and thermal stability through the precipitation of alloy carbides rich in molybdenum, chromium and vanadium during heat treatment at elevated temperatures of 550° [7]. Table 1.1 lists the different compositions of these two bearing steels, together with the most widely used martensitic steel for use in standard rolling bearings, 52100.

The impressive stability and long service lives of the M50 and M50NiL aircraft bearing alloys derives from high cleanliness during steel production [8],

Table 1.1: Bearing steel compositions by element (in wt%).

Steel	C	Mo	Cr	V	Ni	Ref
M50	0.80-0.85	4.0-4.50	4.0-4.25	0.90-1.10	$\leq$ 0.15	[3]
M50NiL	0.10-0.15	4.0-4.50	4.0-4.25	1.13-1.33	3.20-3.60	[4]
52100	0.94	0.03	1.47	<0.01	0.19	[5]

and careful heat-treatment to tailor their mechanical properties for optimal performance. The lower-alloyed 52100 bearing steel does not benefit from secondary hardening during heat-treatment so it is inappropriate for the high-temperature conditions of the aircraft gas-turbine engine [9, 10]. However, there has been a wealth of metallurgical research into the rolling contact fatigue behaviour of this carbon-rich, chromium containing alloy. Unlike the 52100 bearing steel used in ambient temperatures, there have been no characterisation studies on the microstructural behaviour and damage mechanisms which occur in aircraft bearing steels.

Material fatigue describes the mechanism of damage accumulation through the cyclic application of stress, often characterised by steady crack propagation before fracture [11]. Rolling Contact Fatigue (RCF) is a unique variant experienced by components in loaded contact. The fatigue damage arises from recurring compression and deloading cycles exerted by the rolling elements as they pass over one another. This combination of contact pressure and movement creates a multiaxial stress field in the material which has a maximum shear component at a shallow depth beneath the surface [12]. Historically, it is in this stressed volume beneath the point of contact that fatigue damage and microstructural alterations have occurred in 52100 and other bearing steels. Localised plastic deformation takes place in the region of maximum shear stress, resulting in a softening of the microstructure [9] and decay of the martensitic matrix [13]. The stress induced transformation of retained austenite can occur [14], resulting in work-hardening [15], and residual stress development [16]. Carbides in the stressed volume may dissolve [17], and re-precipitation behaviours are seen [18], leading to strongly orientated bands [19], and the development of crystallographic texture [20].

Fatigue responses of this kind typically develop gradually in the subsurface of bearings - accumulating over tens of millions of stress cycles - but premature failures are also encountered [21]. Fatigue cracks can initiate at inhomogeneities in bearing steels, particularly when they are found at critical depths beneath the contact surface where the shear stress is a maximum [22]. Defects such as voids [12], non-metallic inclusions [23] and even carbides [24] can act as local stress raisers under RCF conditions. Plastic deformation occurs in the vicinity of defects where the yield strength is locally exceeded and cracking initiates [19, 25]. Continued rolling cycles provide conditions for incipient crack propagation; often travelling in the direction parallel to the contact surfaces encouraged by tensile stresses which develop in the bearing raceways [20], or combining into larger crack networks before eventually breaching the surface causing failure [26].

A second and competing fatigue mechanism involves the initiation of failures at defects on the contact surface itself, caused by raised asperities [24, 27], excessive roughness [28] or debris indentation from contaminated lubricant [29, 30]. Surface tribology effects, such as these, are the primary source of fatigue failure in aircraft engine bearings [31, 32], and dominate when lubrication conditions are poor [33], culminating in material flaking away from the contact surface in the characteristic failure mode of RCF called spalling [34].

RCF is limited not only to the rolling-element bearings found in jet engines and wind turbines. Any mechanical system, where cyclical loads are transmitted between components in direct contact, may encounter RCF [34]. Mechanical gear teeth, rotating cams and even railway tracks experience similar RCF mechanisms [35, 36, 37], but the specific operating conditions are an important consideration when selecting materials with appropriate fatigue resistance. The frequency of an aircraft bearing fatigue cycle is extremely fast compared with that experienced by a rail track for instance, where instead much softer pearlitic or bainitic steels can be used [38], and the engine temperatures above 200° require superior thermal stability. Advances made in high performance bearing steels over the last century stem from meeting the specific demands of the aircraft gas-turbine engine [39]. In continuing the drive for increased engine speeds and improved fuel-burn efficiency [40], the aerospace industry requires the continual development of rolling bearing steels [41, 42, 43]. Modern improvements in lubrication and steel cleanliness - such as vacuum processing to reduce the propensity of non-metallic inclusions in M50 and M50NiL [8, 33] - have proved an effective way to increase the service lifetime of aircraft bearings [31, 44]. Yet there is still a lack of knowledge regarding the microstructural behaviour of these steels during prolonged periods of rolling contact.

1.1 Aircraft Gas-Turbine Engine Bearings

The main focus of the work presented in this thesis is the examination and characterisation of bearing steels taken directly from civil aircraft gas-turbine engines after a variety of operating periods. These "ex-service" bearings are valuable given that they have experienced actual working conditions whilst in aircraft engines. The assumption is made that ex-service bearings have been used only as intended within their design specifications and no additional damage has been incurred since their removal from the aircraft engine. It follows that the study of this material constitutes an examination of the effects of representative stresses and the typical working conditions experienced during normal aircraft gas-turbine engine operation. Additional characterisation of control samples, or "virgin" bearing material that is unused, constitutes an examination of the default steel microstructures before the application of external engineering stresses.

Engine manufacturers Rolls-Royce, who co-sponsored this work, have donated a number of ex-service bearings from their Trent^{TM} series of civil turbofan engines. Each of these components was produced from the same steel grades but were supplied in different batches by two competing rolling-bearing manufacturers, SKF and FAG. Since both of these suppliers must meet the same material specifications outlined by Rolls-Royce another assumption is made that the bearing components were of near-identical material quality when first produced and fitted for service. This allows for a comparison between each of the ex-service bearings based upon key operating variables, such as the different amounts of time spent in service and the working stresses.

The bearing ball components and the grooved raceways are each examined separately and confined to their own respective chapters. This distinction is made because the components are formed from two different steels with their own unique compositions and would therefore be expected to exhibit different mechanical behaviours under rolling contact loading.

1.1.1 Engine Operating Conditions

Air is taken in at the mouth of the gas-turbine engine where it is compressed by fan blades and then ignited with fuel in the combustion chamber before expanding rearwards providing thrust and driving the turbine blades [Figure 1.1]. This process is an example of an open Brayton Cycle where the difference in heat exchanged with the air as it travels through the engine determines the thermal efficiency, according to Equation 1.1:

$$\mu_{th} \leq 1 - \frac{T_C}{T_H} \tag{1.1}$$

where μ_{th} is the thermal efficiency, T_C is the ambient air temperature and T_H is the maximum temperature reached during combustion. Following this thermodynamic principle, aircraft gas-turbine engines seek to operate at higher temperatures and greater pressures for improved efficiency [45].

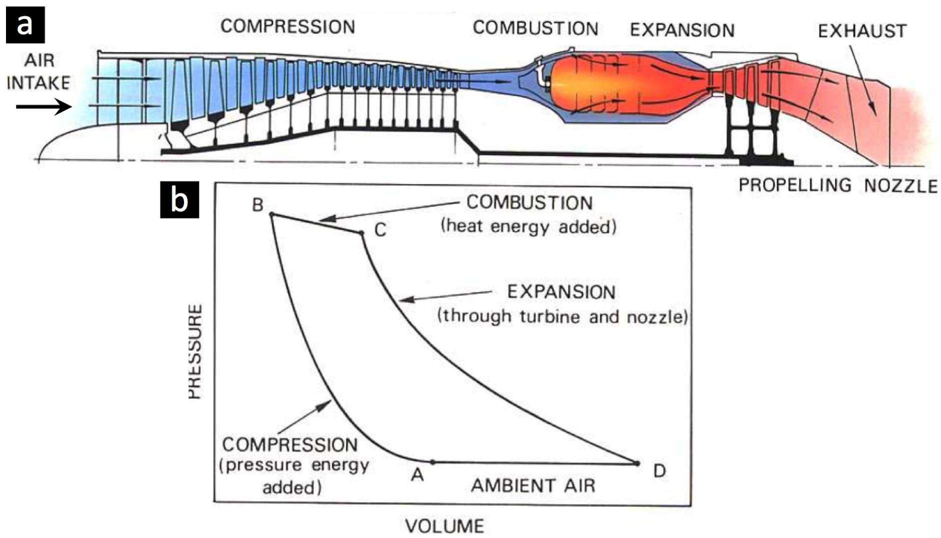

Figure 1.1: (a) Cross-sectional diagram of the aircraft gas-turbine engine. (b) Thermodynamic description of the Brayton Cycle showing the pressure and volume of a gas (air) as it passes through the engine. After [45].

The Rolls-Royce Trent™ series of civil turbofan engines burn fuel at pressures exceeding 850 kPa and temperatures reaching 1,300°C in the combustion chamber. Thermal barrier coatings and cooling air channels are essential for the nickel superalloy turbine blades used in this hottest part of the engine where temperatures exceed the melting point of these alloys. The rolling-bearings operate in a cooler part of the engine where temperatures are lower, peaking at around 200°C when supplied with sufficient cooling lubricant. A large quantity of air from the fan blades is designed to bypass the turbine core and pass straight through to the rear exhaust. This actually improves propulsive efficiency of the engine by increasing the mass of air ejected, and simultaneously reduces engine noise.

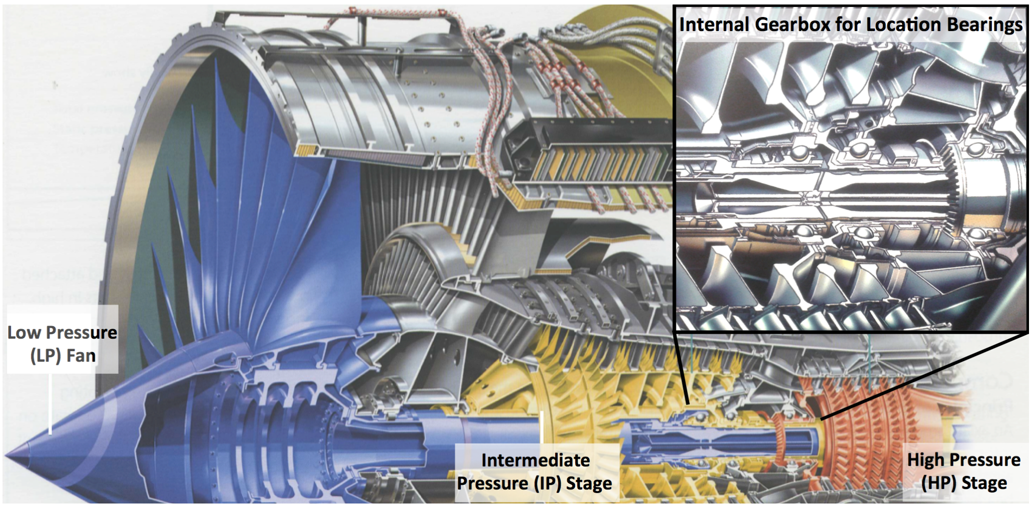

Figure 1.2: Front section of the Rolls-Royce Trent^{TM} 900 engine, after [45]. The three location bearings are visible between the intermediate and high-pressure stages (inset).

The Trent^{TM} engine has a multi-shaft transmission assembly supported by three dedicated rolling-bearings that allow the low-pressure, intermediate-pressure and high-pressure stages of the engine to independently rotate at different speeds [Figure 1.2]. The high-pressure stage (HP) at the interior of the engine rotates fastest, reaching upwards of 12,500 rev min $^{-1}$, followed by the intermediate-pressure stage (IP) and slower low-pressure outer fan stage (LP). Figure 1.2 displays a cross-section of the Trent 900 engine with the three stages identified in false-colour and the three bearings visible within the internal gearbox. The rolling elements in these bearings are spherical balls rolling upon deep-grooved raceways, and each bearing contains around 20 or more balls whose individual separation is maintained by the bearing cage. When rotating at high speeds a considerable number of stress cycles are accrued rapidly; all 20 rolling elements will pass over any given section of the raceway track with each revolution, transmitting a contact stress under high-cycle fatigue conditions. This loading frequency contributes significantly to the service life of a bearing which may see up to 30,000 h of cumulative flight-time before a maintenance overhaul. Centrifugal loads are also a factor at high rotation speeds since the rotational inertia of large diameter bearings with high mass will create a tensile hoop-stress around the raceway circumference [46]. Hoop stress is also produced by tight fitting of the inner raceways onto the engine shaft.

When rotating at 12,500 rev min $^{-1}$ a bearing containing 20 rolling elements will see over 10^{10} stress cycles before an inspection is due. Such gigacycle fatigue conditions should test the stability of bearing steel microstructures [47]. The examination of ex-service bearings in this work aims to identify signs of instability in material, both in its early stages and by observing the fatigue damage which can result.

1.1.2 Location Bearing Design

The contact geometry between spherical rolling-elements and grooved raceway provides stability under combined loads in both the radial and axial directions. Gas flow through the engine causes large pressure gradients along the axis of the shaft and corresponding thrust loads which must be supported by bearing design, with the balls positioning themselves further up the raceway groove during motion. Figure 1.3 a describes this ball movement during thrust loading as illustrated by the contact angle of the bisecting lines away from the central position. Because of their role in maintaining this lateral positioning of the shaft, these components are known as "location bearings". It is expected that the loads and contact angles will vary throughout different stages of the flight cycle, such as take-off and high-altitude cruising, during which time the location bearings respond to variations in pressure and aircraft speed. Figure 1.3 b shows the variation in contact stress over an average aircraft flight cycle. This plays an important role in the fatigue stress conditions experienced by the location bearings as each flight cycle is effectively superimposed onto the more general high-cycle fatigue conditions of bearing revolution.

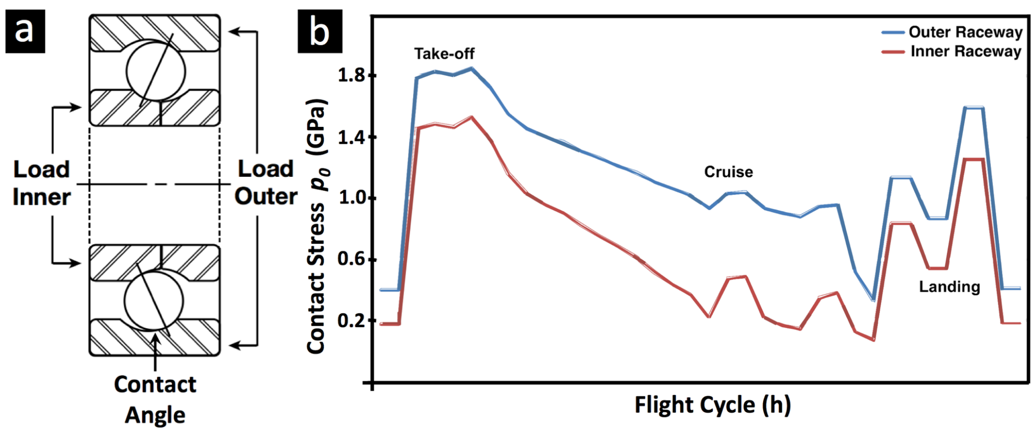

Figure 1.3: (a) Schematic cross-section of a location bearing with split inner raceway, adapted from [48]. (b) Variation in contact stress for the inner (red) and outer (blue) raceways during an average flight cycle for civil aircraft. The contact angle between ball and raceway may change during these different stages of flight.

Other geometrical factors important in location bearing design are the clearance and conformity between the ball and raceway curvature. Dimensions are carefully chosen so that the structural loads between the meeting components are spread over a finite contact area that takes the form of an ellipse. The contact stress is directly related to the pressure acting over this ellipse and can be calculated using simple geometry if fully elastic loading conditions are assumed. Chapter 2 discusses the important contact mechanics in more detail. For a typical bearing steel with high elastic modulus the contact ellipse may be between 1 - 2 mm^2, but many other factors besides geometry influence this value, including lubrication conditions, speed of rotation and surface roughness. An excessively large contact ellipse encourages ball sliding at the surface and lubricant drag inefficiencies. Tribological factors such as these are discussed in Section 2.2.

Figure 1.4 contains all of the ex-service location bearings central to this work. Each component was taken from a different Rolls-Royce Trent$^{\mathrm{TM}}$ engine with individual service lives listed in Table 1.2. The key discerning variable between each of the ex-service bearings is the number of fatigue cycles experienced, which roughly corresponds to the length of time spent in service, given in hours. There are, however, variations in speed expected between Trent 800 and Trent 900 engines, and between each of the LP, IP and HP stages. Two of the longest running location bearings reached almost 30,000 h in service before suffering single ball failures that led to the entire bearing being discontinued and removed from their respective engines. Figure 1.5 shows these failed rolling-elements from the ex-service bearings which display a characteristic fatigue spall typical of rolling contact fatigue damage. Chapters 3 - 5 detail the investigation of these failed samples and the other location bearings at length. The remaining ex-service bearings did not suffer ball failures but were instead discontinued after different lengths of time for unknown reasons not thought to be relevant to this study [Table 1.2]. One of the location bearings is brand new (denoted 0 h) and never entered service, nor was it ever constructed and fitted into an engine [Figure 1.4 a]. This un-stressed bearing will act as the control sample material straight from manufacture and its “virgin” microstructure will play an important role in comparison studies.

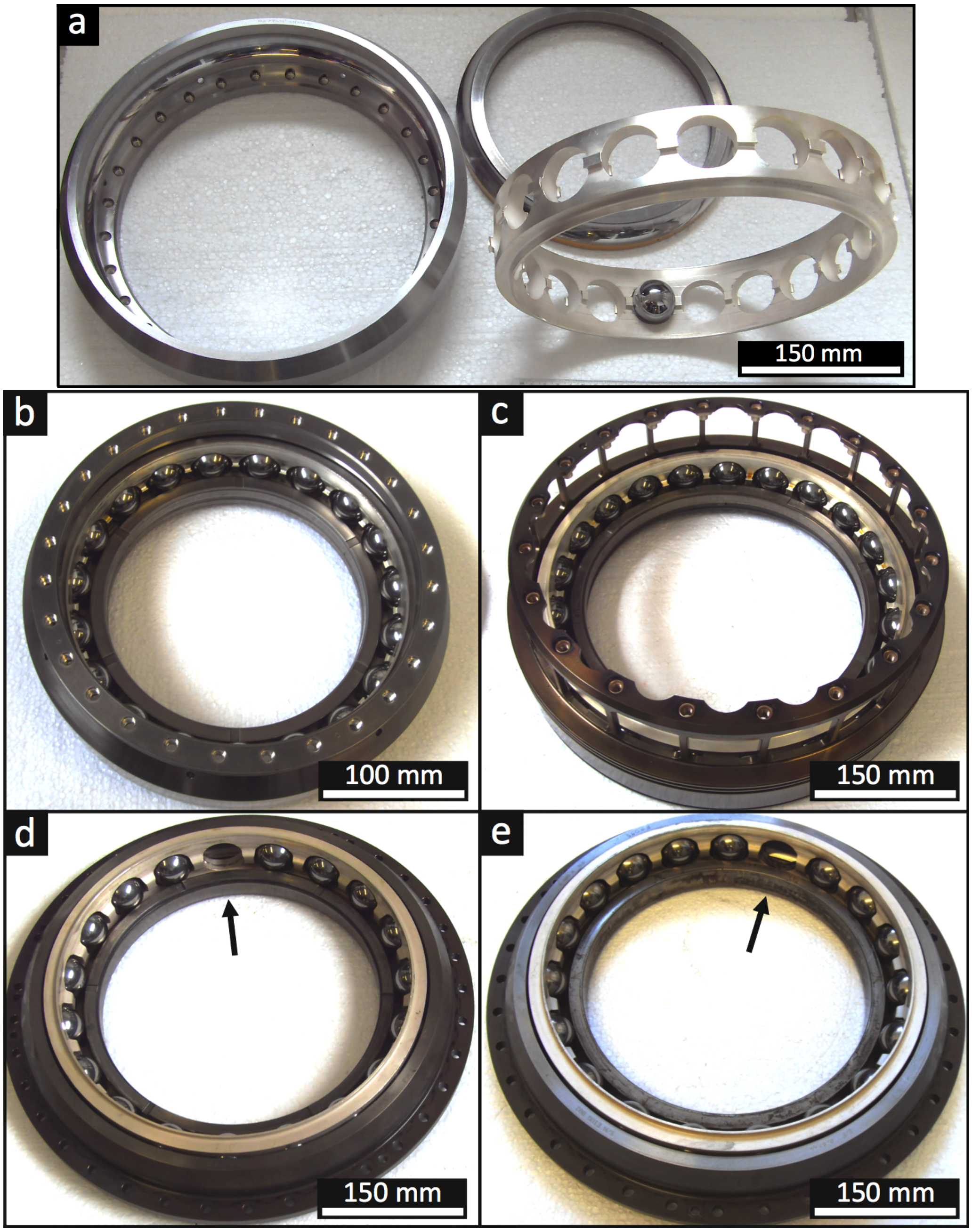

Figure 1.4: Rolls-Royce Trent engine location bearings. (a) The new and unused 900 LP bearing with 0 h service, deconstructed into its component parts. (b) 900 LP bearing after 120 h service with inner raceway removed to show rolling elements. (c) 900 HP bearing after 6,515 h service has an integrated squirrel cage outer raceway. (d) 800 IP bearing after 29,118 h service with failed ball removed (indicated). (e) 800 IP bearing after 29,900 h service with failed ball removed (indicated).

Table 1.2: Ex-service location bearing samples from Rolls-Royce civil aircraft gas-turbine engines with their respective service lives.

Life	Engine stage	Average flight	Supplier
0 h	900 LP	-	SKF
120 h	900 LP	4.4 h	FAG
6,515 h	900 HP	-	FAG
29,118 h	800 IP	-	SKF
29,900 h	800 IP	4.5 h	SKF

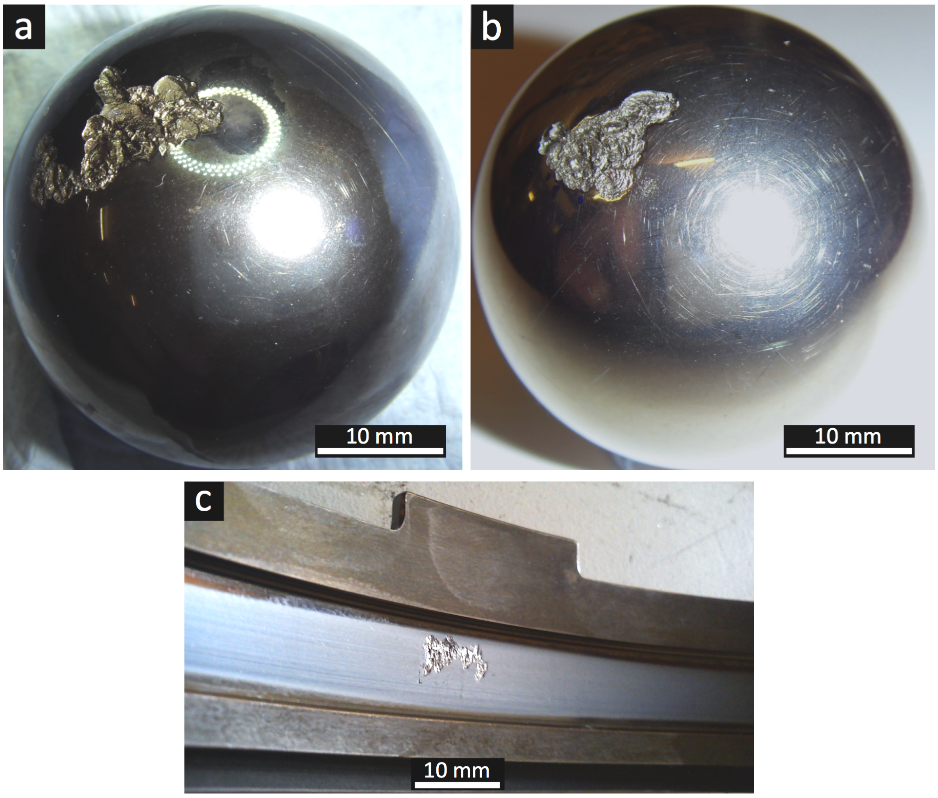

Figure 1.5: (a) Failed M50 bearing ball with fatigue spall after 29,118 h service in the 800 IP location. (b) Failed M50 ball after 29,900 h service in a different 800 IP location. (c) M50 roller raceway with surface fatigue spall after 18,000 h. Note, this component is not a location bearing but is provided for supplementary investigation.

Additional samples studied in this work include a failed cylindrical-roller bearing from the Trent 900 LP stage [Figure 1.5 c]. This component is not a location bearing and is instead fitted near the mouth of the engine to support rotation of the large turbofan. Only radial loads are encountered here so ball-elements are not necessary and cylindrical rolling-elements are suitable instead. The roller bearing is made entirely of through-hardened

M50 steel and in this sample a fatigue spall failure has occurred at the contact surface of the outer raceway which led to its discontinuation after 18,000 h service [Figure 1.5]. Chapter 6 contains supplementary investigations of laboratory-made test pieces of M50 and M50NiL under accelerated RCF rig testing.

Table 1.3 contains compositional data for a number of popular bearing steel grades, including the aircraft-grade alloys M50 and M50NiL in the first two rows. The rolling-elements in location bearings are manufactured from through-hardened M50 steel, but the inner and outer raceways are both made from carburised M50NiL [Table 1.3]. These two alloys differ considerably in their core mechanical properties, primarily due to differences in carbon concentration, as will be detailed in the following Section 1.2. The bearing cage that holds the rolling elements is typically made from 4340 grade steel (AMS 6414) and coated with magnesium sulphide or silver plated to address landing wear [49]. Cages and their coatings can sometimes cause issues in bearings [50, 51] but they do not play a role in the RCF behaviour of the components in this study. Location bearings are mounted onto the mainshaft using a two-part, split inner raceway through which lubrication is fed, and the outer raceways have integrated flanges [Figure 1.4]. Some additional bearing alloys are also presented in Table 1.3 for later comparison: 52100 is the most popular multi-purpose bearing steel with high strength but insufficient hot hardness for aircraft applications. 440-C is a corrosion resistant bearing steel with high chromium content. Cronidur-30 is another corrosion resistant grade with high chromium and additional nitrogen content of 0.4 wt%. The British-made T1 (18-4-1) is a high-speed tool steel variant suitable for aircraft bearing applications, containing large quantites of tungsten. RBD is also an aircraft-grade steel containing tungsten but has low-carbon and is fully carburisable.

Table 1.3: High-strength bearing steel compositions by element (in wt%).

Steel	C	Mo	Cr	V	Ni	Mn	Si	P	S	W	Ref
M50	0.80-0.85	4.0-4.50	4.0-4.25	0.90-1.10	$\leq$ 0.15	0.15-0.35	$<$ 0.25	$<$0.015	$<$0.008	$<$0.008	[3]
M50NiL	0.10-0.15	4.0-4.50	4.0-4.25	1.13-1.33	3.20-3.60	0.15-0.35	0.10-0.25	$<$0.015	$<$0.008	-	[3]
52100	0.94	0.03	1.47	$<$0.01	0.19	0.34	0.22	0.009	0.012	-	[5]
Cronidur-30	0.33	0.93	15.70	0.02	0.25	0.41	0.80	0.017	0.002	-	[5]
440-C	1.10	0.75	17.00	-	-	1.00	1.00	-	-	-	[52]
T1 (18-4-1)	0.76	0.07	4.34	1.11	0.06	0.28	0.28	0.007	0.006	18.2	[7]
RBD	0.16-0.21	-	2.75-3.25	0.35-0.50	0.59-0.90	0.20-0.40	$<$0.35	0.009	0.005	9.50-10.50	[7]

1.2 Material Selection

Martensitic tool steels are ferrous alloys containing carbon and essential refractory metals added for increased strength at high temperatures. To resist plastic yielding the impedance of dislocation movement can be achieved with solid-solution strengthening of interstitial carbon, and the formation of carbon-rich precipitates during tempering [53]. Introducing carbon to iron is a relatively cheap strengthening addition compared with adding tungsten or molybdenum, but the additional presence of these substitutional solutes helps to strengthen tool steel at elevated temperatures by precipitating stable alloy carbides [Section 1.2.2].

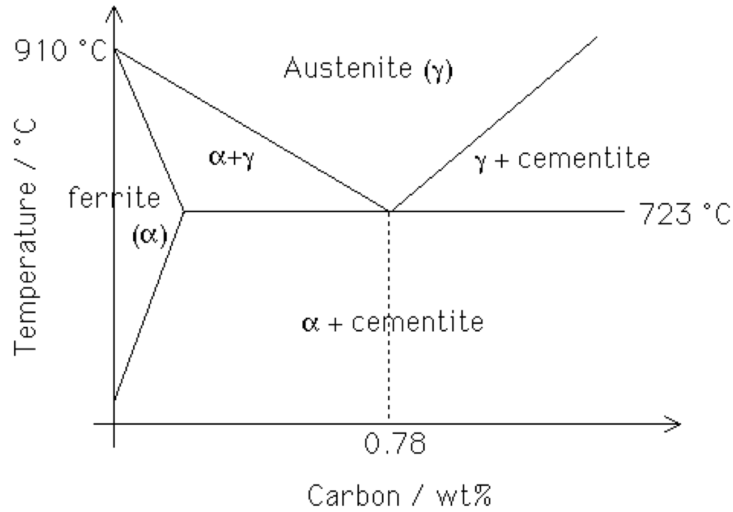

Figure 1.6: The reduced iron-carbon phase diagram, focussing on the ferrite (α) to austenite (γ) transition. After [54].

A portion of the iron-carbon equilibrium phase diagram is shown in Figure 1.6. Iron is allotropic and under normal atmospheric conditions body centred cubic (BCC) ferrite is the stable phase, but there are more desirable metastable phases for the design of high-strength bearing steels. When heated above 910°C, ferrite (α-iron) begins transformation into austenite (γ-iron), accompanied by a change in crystal structure to face centred cubic (FCC). The resulting austenite lattice has larger interstitial sites which solutes such as carbon and nitrogen can occupy. Bearing steels are heat-treated to capitalise on this high carbon solubility of austenite relative to ferrite [6]. M50 has a carbon content of 0.8 wt% but typically tool steels may contain anywhere between 0.6 - 1.2 wt% carbon [52].

As the steel cools from the austenite phase the reverse $\gamma \rightarrow \alpha$ transformation will prompt rejection of carbon from the austenite and cementite will form. Controlling the growth of this iron-rich carbide and other precipitates is particularly important for the fatigue strength of steel, as their presence can be beneficial or detrimental depending on size, morphology and distribution [Section 1.2.2]. Rejection of carbon during transformation can be prevented by the rapid-cooling (quenching) of austenite, allowing insufficient time for the diffusion of carbon atoms. If quenched sufficiently fast the carbon in solid-solution is retained as the austenite lattice undergoes a displacive shear transformation into martensite, α', with a slight volume expansion [55]. Diffusion does not occur during this athermal transformation that takes place when steel is undercooled below the martensite-start temperature, M_S [6]. The fraction of α' obtained is purely a function of the undercooling temperature, so some γ will be retained unless the steel is quenched to below the martensite finish temperature, M_F [56]. Retained austenite is thought to be undesirable for fatigue resistance, so bearing steels can be quenched to below room temperature to produce a fully martensitic microstructure, meaning all the austenite has transformed completely to martensite [Section 1.2.1].

The aircraft gas-turbine engine bearing steels M50 and M50NiL are both martensitic but have different carbon contents. M50 steel is used for the bearing balls; heat-transfer through these smaller components allows them to be quenched sufficiently fast so as to produce a martensitic structure throughout. Through-hardened steels with a high interstitial carbon content like M50 are very hard but characteristically brittle [6]. Martensite cracks can even occur in high carbon steels if they are quenched too rapidly [57], so it is preferable to moderate the cooling rate from austenite in steps whilst still ensuring eventual undercooling for the martensitic transformation [Section 1.2.1]. Large steel components take longer to cool during quenching and require more time to reach a uniform thermal equilibrium throughout their thickness. The large raceways of location bearings are not through-hardened, but are instead made from a reduced carbon steel with far less than 0.8 wt% carbon [52]. M50NiL is a low-carbon variant of M50 that is selectively hardened at its contact surfaces by the diffusion of carbon. The carburisation process saturates the raceway surfaces with carbon - between 0.65 - 1.10 wt% C - so that when quenched the M50NiL becomes case-hardened. Beneath this fully martensitic case, the bulk material with

Table 1.4: Bearing steel mechanical properties, including yield strength (σ_y), ultimate tensile strength (σ_{UTS}), elastic modulus (E), rockwell hardness (HRC), and fracture toughness (K_{IC}). The values for M50NiL are the bulk, not carburised properties. Data from [7, 52, 58, 47].

Steel	σ_y (MPa)	σ_{UTS} (MPa)	E (GPa)	HRC	K_{IC} (MPa$\sqrt{m}$)
M50	2110	2660	190	60-64	21
M50NiL	1175	1387	-	47	56
52100	1158	2316	210	60-64	21

its lower carbon content of only 0.15 wt% C may retain some ferrite with corresponding ductility. The inhomogeneous carbon content affects the M_S temperature of M50NiL and the resulting volume expansion of martensitic transformation leaves the high-carbon case under compressive residual stress relative to the bulk [Section 1.2.3].

Some important refractory metal additions are also present in aircraft bearing alloys. M50 is derived from high speed tool-steels and has been utilised in aerospace applications since its experimental introduction in 1954 [59]. Fearing shortages of tungsten for alloying purposes, American manufacturers devised the molybdenum-rich M50 steel composition with additional chromium and vanadium. These are strong carbide forming elements which bond with carbon to produce strengthening precipitates that are particularly well suited for high temperature conditions [60, 53]. Section 1.2.2 discusses these carbides and their behaviour in more detail. Case-hardened M50NiL was not developed until the early 1980's at a time when it reportedly doubled the fatigue life of through-hardened M50 [61, 62]. With lower carbon and some added nickel, the M50NiL alloy displayed a higher fracture toughness in the bulk material [63, 64]. Fracture toughness K_{IC}, defines the critical stress intensity required at a crack tip to enable rapid fracture [Section 1.3], and is inversely proportional to the carbon content in bearing steels [63]. Table 1.4 contains mechanical property data for some of the high-strength bearing steels after heat treatment. The ductile core material of M50NiL is more resistant to crack propagation [65], and in the case-carburised condition the alloy surfaces display hardness values similar to that of M50 [66].

1.2.1 Heat Treatment

It is often necessary to temper high-carbon, martensitic steels to correct for their brittle nature and poor toughness [Table 1.4]. Tempering is a heat treatment carried out on finished parts after manufacture and involves holding the steel at elevated temperature for extended periods. When tempered anywhere between 150°C - 700°C the outward diffusion of carbon from the saturated martensite acts to soften the microstructure, bringing about an increase in ductility and improved machinability of the steel [6]. The excess carbon, no longer in solid-solution within the martensitic matrix, will migrate to form carbides during sufficient tempering. Their precipitation can provide a beneficial strengthening mechanism [60] but excessive carbide growth can also prove detrimental, bringing increased inhomogeneity [24] and lowering the local fracture toughness at brittle carbides [65, 67]. The compromise between strength and toughness is tailored with careful control over tempering, together with informed selection of alloying elements.

Molybdenum, chromium and vanadium are strong carbide forming elements which display a secondary hardening effect in steels tempered between 500°C - 600°C [6]. After the initial softening effect of carbon rejection from the martensite, the long-range diffusion of Mo, Cr and V solutes forms alloy carbides, increasing the hardness of the steel once again. These secondary carbides are stable at high temperatures, unlike cementite, and are fundamental in M50 and M50NiL bearing steels. Figure 1.7 shows the secondary hardening effect in M50 steel heat treated at a range of different temperatures [68]. The aircraft gas-turbine engine bearings operate at temperatures around 200°C but deterioration of lubricant or excessive sliding at the contact zone may raise the working temperature 20°C - 30°C higher still [69]. Performing at temperatures nearing 230°C requires a bearing steel which can retain its hot hardness under these conditions, avoiding in-situ tempering and softening of the microstructure during service. Secondary hardened M50 is capable of maintained performance up to 315°C [61, 70, 71], achievable thanks to the thermal stability of alloy carbides. Carburised parts, such as M50NiL, are also suitable up to temperatures around 300°C [60, 72]. Stability in the lower alloyed 52100 bearing steel however can only be maintained below a maximum temperature of 177°C, thus it is unsuitable for gas-turbine engines. Figure 1.8 shows the hot hardness behaviour for a number of bearing steels [7].

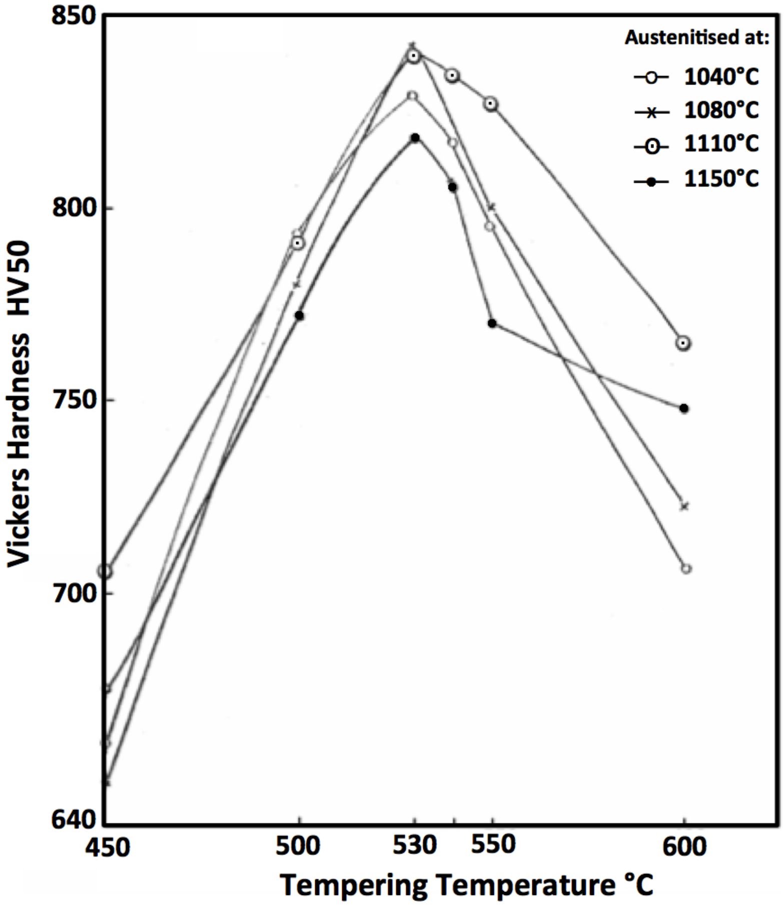

Figure 1.7: Vickers hardness of M50 as a function of tempering temperature. Four different austenitisation temperatures are shown and three repeat tempers were performed in each case. Adapted from [68].

Aside from hot hardness, another advantage of secondary hardening is that the overall carbon concentration can be reduced without sacrificing strength. For example, M50 contains 0.8 wt% C whilst still maintaining a hardness matching that of 52100 which contains 1 wt% C [Table 1.4]. A reduction in carbon allows greater machinability of the steel necessary for forming and shaping the rolling elements, limits the likelihood of quench cracking [7], and leads to fewer residual carbides [Section 1.2.2]. Alloying additions have an effect on the transformation behaviour of steel. For highly-alloyed bearing steels the M_F temperature is often suppressed to below room temperature, meaning there will be some austenite retained in the microstructure after transformation at room temperature and above [60]. A sub-zero heat treatment can be employed to quench the steel closer to M_F and further reduce the amount of retained austenite [3, 73].

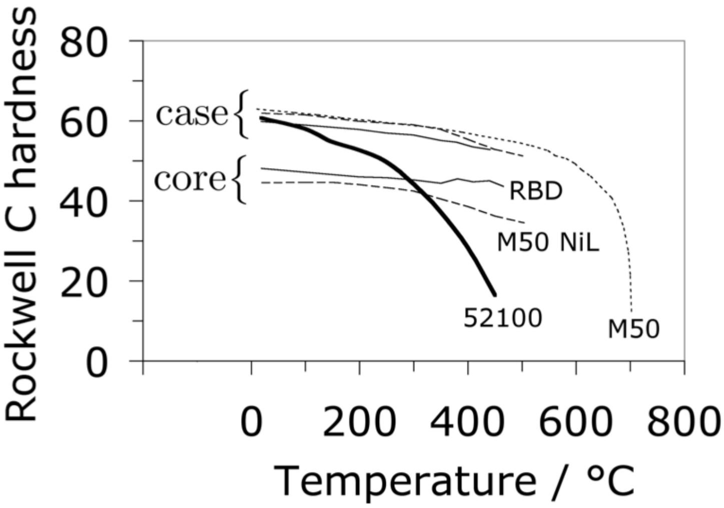

Figure 1.8: Hot hardness as a function of temperature for a range of bearing steels. After [7].

It is generally considered that retained austenite is bad for the fatigue performance of bearing steels [74], due to the inherent instability of the austenite phase at high temperatures and operational stresses [61]. A subsequent benefit of tempering bearing steels at higher temperatures is the transformation of retained austenite to martensite [68], but multiple temper cycles are often required to account for the formation of fresh martensite from this transformed austenite [68]. A reduction in γ following quenching and temper cycles improves dimensional stability of the bearing steel by preventing the stress induced $\gamma \rightarrow \alpha'$ transformation during service. Figure 1.9 shows the effect of tempering temperature on the retained austenite content in M50 steel. The minimum amount of austenite is achieved at tempering temperatures slightly higher than the peak hardness value obtained during secondary hardening [59]. A tempering temperature of above 530°C is optimal in aircraft bearings for Rolls-Royce to limit the retained γ to a maximum of 2-3% in the final heat treated M50 [3], and a similar level is used by other manufacturers [75].

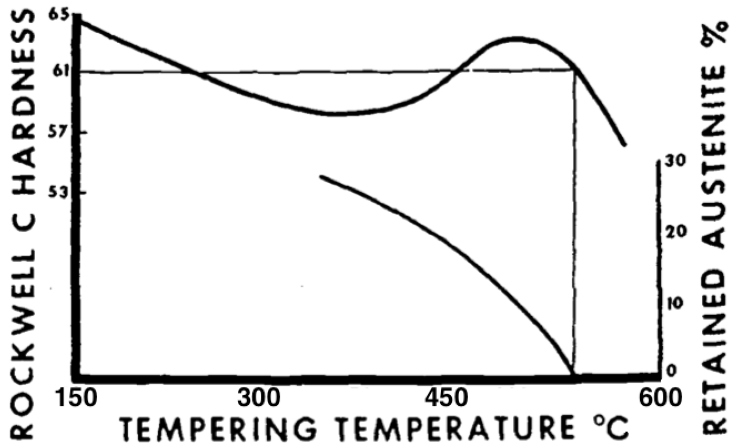

Figure 1.9: The level of retained austenite in M50 during tempering reaches a minimum value at temperatures just above the secondary hardening peak. Adapted from [59].

Figures 1.10 and 1.11 show the full heat treatment procedure for M50 and M50NiL respectively. The precise temperatures and hold times may deviate slightly between each manufacturer, but the critical stages involve initial austenitisation, martensitic quenching and repeated tempering cycles with a sub-zero treatment [52, 60, 75]. The location bearings are first machined close to their correct dimensions in the soft annealed state before heat treatment. In either a neutral salt bath, or a low vacuum (3×10^{-3} torr), the austenitisation stage begins with stepwise heating from 500°C to 900°C after 20 min to 1,100°C for more than 6 min. This is followed by a two stage quench in either a salt bath or pressurised nitrogen/argon atmosphere to room temperature. The first temper follows here for M50, held at between 530 - 555°C for 2 h, then a quench to room temperature, and below to - 70°C for 30 min. Two further temper cycles complete the secondary hardening heat treatment and the steel is now ready for a final grind and surface finishing before service.

The M50NiL treatment differs in that it begins with a lengthy carburisation process at temperatures close to austenitisation. The component surfaces are carburised at around 1,000°C for approximately 60 h, before being air-cooled and beginning the heat treatment [58]. M50NiL also has a - 70°C heat treatment after quenching to room temperature following austenitisation, and the subsequent temper cycles last slightly longer than 2 h, reflecting the greater likelihood of retained austenite due to the added nickel.

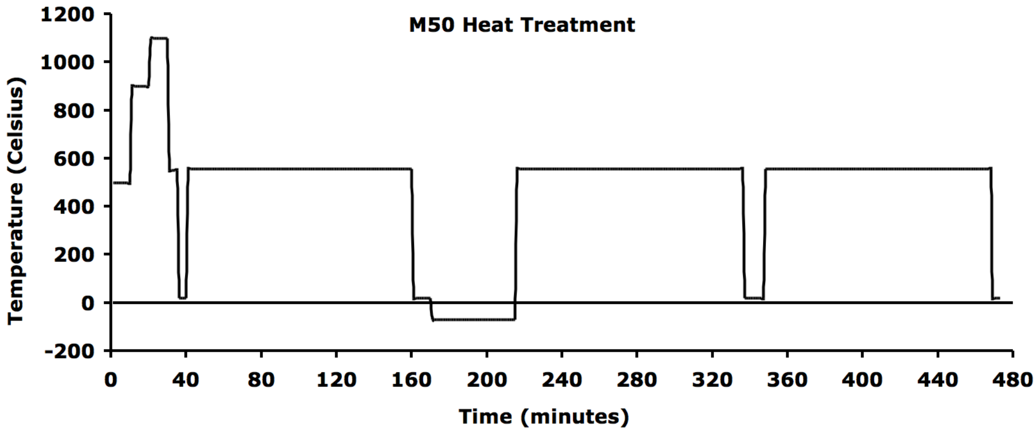

Figure 1.10: M50 heat treatment cycle [3].

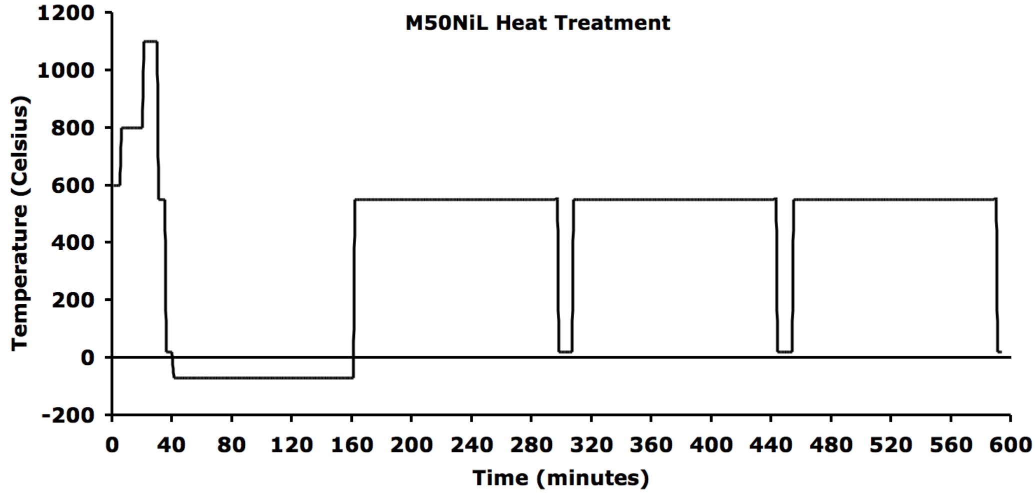

Figure 1.11: M50NiL heat treatment cycle [3].

It is likely that the 60 h long carburisation heat treatment will lead to significant differences in the microstructure of M50NiL compared with through-hardened M50. In polycrystalline steels, grain growth is carefully controlled during heat treatment because grain refinement provides a viable strengthening mechanism relating increased yield strength, σ_y, to a reduction in grain size, d through the Hall-Petch relationship [Equation 1.2].

$$\sigma_y = \sigma_o + \frac{k_y}{\sqrt{d}} \tag{1.2}$$

where σ_o and k_y are material constants. Austenitisation temperature and hold time will determine the austenite grain size and influence the M_S temperature [56]. The parent austenite grain size also limits the length of martensite plates, since the α' - transformation involves a disciplined movement of atoms that cannot be sustained across grain boundaries. Hence, creation of a fine martensitic microstructure that is beneficial to strength can be obtained through refinement of an optimal austenite grain size during heat treatment [76]. Chapter 4 contains evidence of grain size variation in M50NiL raceways.

Vacuum Processing

Steels for modern-day aerospace bearings are formed using a dual Vacuum Induction Melting plus Vacuum Arc Re-melting (VIM-VAR) process [66]. The benefits of vacuum processing include the careful control of the system variables, such as the pressure and temperature, contamination is preventable and degassing of entrapped oxygen, nitrogen and hydrogen gas traces is achievable [52]. Selected scrap of appropriate composition together with necessary alloying additions are fed into an induction furnace in the vacuum chamber. Deoxidation of the melt is achieved with carbon under high vacuum and the desorbed CO pumped away [8], eliminating the usual practice of adding aluminium or silicon deoxidisers [7]. The ultra-high purity ingots that result are then used as consumable electrodes in the following VAR process. Under high vacuum an electric arc is struck between the VIM ingot and a base plate, melting the ingot steadily, which drips into the water-cooled copper mould controlling solidification [77]. The homogeneity of the resulting clean ingot is improved and porosity reduced [52], together with further separation of any remaining oxides and sulphides [7].

Non-metallic inclusions have traditionally served as the main cause of RCF failures in bearings that do not share the clean VIM-VAR production route of aircraft-grade bearing steels [12, 23, 78]. Chapter 2 details the historical link between non-metallic inclusions and their reduction on fatigue life which instigated progress away from traditional air-melting methods and towards cleaner processing. Double vacuum melted VIM-VAR M50 can attain an oxygen content as low as 6 ppm (parts per million) [8]. Since it is at unwanted Al and Si oxide inclusions where fatigue cracking often initiates, steel cleanliness continues to provide a direct route to improved fatigue life [79, 80]. Both M50 and M50NiL are VIM-VAR processed as standard so in the interests of brevity the VIM-VAR prefix will be omitted.

1.2.2 Carbide Phases

The high-temperature strength and thermal stability of aircraft gas-turbine engine bearing steels would not be possible without the presence of carbide precipitates which form during solidification and secondary hardening [9]. These carbides exhibit values of hardness and elastic moduli greater than those of the surrounding matrix [81], helping to resist plastic deformation and improve wear resistance [24]. In the following notation for carbide phases, M, denotes the number of metal atoms which is often a mixture of different elements and, C, denotes the carbon atoms. For example, M_3C cementite, is an iron-rich carbide where M represents metal atoms (e.g. Fe, Cr). Despite its growth being kinetically favourable, M_3C is less stable than the secondary carbides, particularly at higher temperatures [82]. Cr atoms can replace Fe in M_3C and this change in composition is seen in heat treated 52100 bearing steel [73]. Mo and V have limited solubility in cementite so will form new carbide phases instead, such as the M_2C carbide rich in molybdenum and the MC carbide rich in vanadium. Table 1.5 lists some of the most prominent carbide phases in M50 and M50NiL bearing steels.

Table 1.5: Average chemical composition of some common bearing steel carbides in atomic fraction.

	Fe	Cr	Mo	V	C	Structure	Space Group	Ref
MC	0.02	0.04	0.14	0.32	0.48	FCC	$Fm\bar{3}m$	[24, 83]
M_2C	0.06	0.12	0.36	0.15	0.31	HCP	$P6_3/mmC$	[24, 83]
M_6C	0.35	0.07	0.56	0.02	-	FCC	$Fd\bar{3}m$	[83]
M_7C_3	0.41	0.46	0.07	0.06	-	HCP	$P3_1C$	[83]
$M_{23}C_6$	0.54	0.28	0.15	0.03	-	FCC	$Fm\bar{3}m$	[83]

A review of the literature reveals a number of different carbide species are present in aircraft bearing steels containing Mo, Cr and V solutes. Bridge et al. (1971) investigated the carbides in M50 steel by X-ray diffraction, extraction and micro-chemical analysis after tempering at a range of different temperatures [84]. The first carbide to form upon tempering was the Cr-rich $M_{23}C_6$ phase at temperatures above 315°C, followed by both V-rich MC and Mo-rich M_2C at approximately 550°C, marking the onset of secondary hardening. Pickering (1978) examined the precipitation of secondary carbides during tempering, finding the Cr-rich M_7C_3 carbide to nucleate above 500°C [53]. Although not reported by Bridge et al. the presence of the M_7C_3 phase has been confirmed in more recent studies of M50 bearing steel by Decaudin et al. (1995) [83]. This non-equilibrium M_7C_3 carbide is known to exhibit secondary hardening effects but is less stable than the other Cr-rich phase, $M_{23}C_6$, which dominates [85]. One final carbide reported in M50 bearing steel is the Mo-rich M_6C phase which precipitates at high temperatures in regions locally enriched with molybdenum [84]. M_6C remains stable at temperatures of up to 1,100°C, representative of austenitisation or carburisation treatments. Other carbides insoluble at high temperatures are MC and M_2C, which remain stable up to 1,200°C in M50 and can prove problematic when attempting to homogenise bearing steel microstructures [86].

Residual carbides may leach solute atoms and carbon from solid-solution causing inhomogeneity and local gradients in steel composition. The high solvus temperatures of M_2C and MC residual carbides means they will precipitate soon during solidification from the liquid melt and may grow excessively coarse as the steel cools [87]. This is an example of chemical segregation; an undesirable process which can occur during steel production. As the liquid cools fastest from the outer edges of the containing vessel dendrites of frozen steel grow inwards, partitioning at their solid/liquid interface regions of different chemical composition [52]. Figure 1.12 shows how the inter-dendrite regions can become solute-enriched, resulting in steel with an inhomogeneous banded microstructure and segregation of residual carbides which cannot be dissolved during austenisation [65, 88].

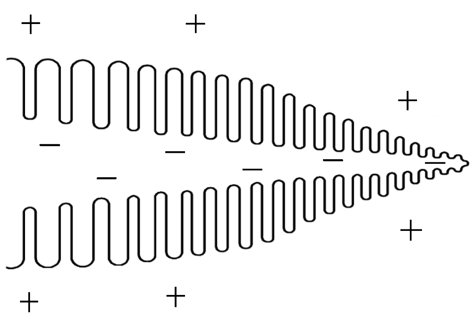

Figure 1.12: Diagram describing the solute partitioning of dendritic growth that occurs during solidification. Negative signs denote solute depleted solid regions and positive signs denote solute enriched regions. After [89].

Despite the beneficial wear resistance provided by M50 carbides [24], a poor distribution of excessively large carbides is detrimental to fracture toughness [65, 67] and rolling contact fatigue in bearing steels [23, 90]. Chapter 2 contains a review of the damage mechanisms associated with having such stress raising inhomogeneities in the microstructure. Methods for reducing carbide segregation include soaking the steel at very high temperatures over long periods of time to promote diffusion and homogenise the composition [8, 91]. Alternatively, metallurgists can hot-work the steel in an attempt to physically break up the segregated regions. This work can be done during the solidification stage in a process called continuous casting, or performed after solidification during an ausforming heat treatment. Continuous casting involves reducing and forming the molten steel immediately as it flows from a vessel [Figure 1.13], producing smaller residual carbides due to mechanical reduction and a faster cooling rate thanks to a reduced cross-section [92, 93].

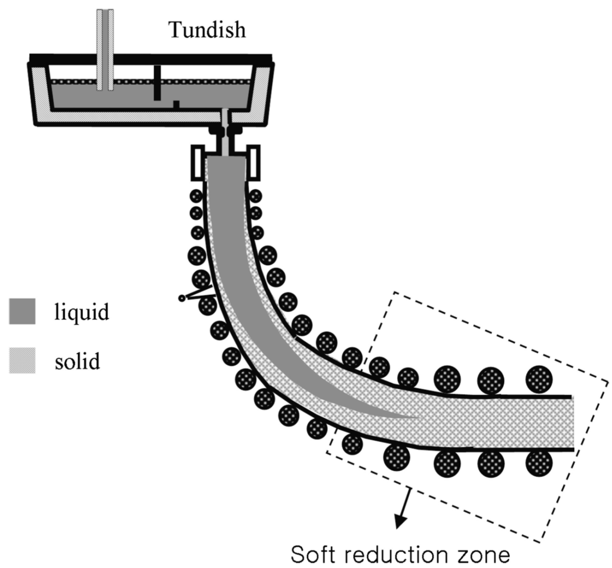

Figure 1.13: Continuous casting solidification process. After [87].

The continuous casting process is shown in Figure 1.13. The liquid portion at centre of the casting is last to freeze and can become enriched with solutes, resulting in a core microstructure full of impurities and carbides along the centreline [94, 95]. Although the continuous hot-reduction breaks up the coarse carbides somewhat there still remains a non-uniform distribution of segregated carbides along the central axis [87]. This inhomogeneity may be passed on to components formed from the continuously cast steel [96, 97]. Chapter 3 contains evidence of centreline carbide segregation in M50 bearing balls. Okamoto et al (1967) found that the larger the amount of hot reduction undergone during solidification the smaller the carbides in 52100 bearing steel became, compared with traditional ingot casting [98]. This reduction also had a positive effect on the experimental fatigue life of bearing balls, reflected by 1.5 - 2 times the improvement in life of continuously cast bearing steel over ingot cast [99]. However, Butterfield and McNelley (1986) found that hot-rolling does not refine the insoluble carbides in M50 bearing steel and in fact leads to porosity at the carbide-matrix interface which is also detrimental to fatigue performance [86].

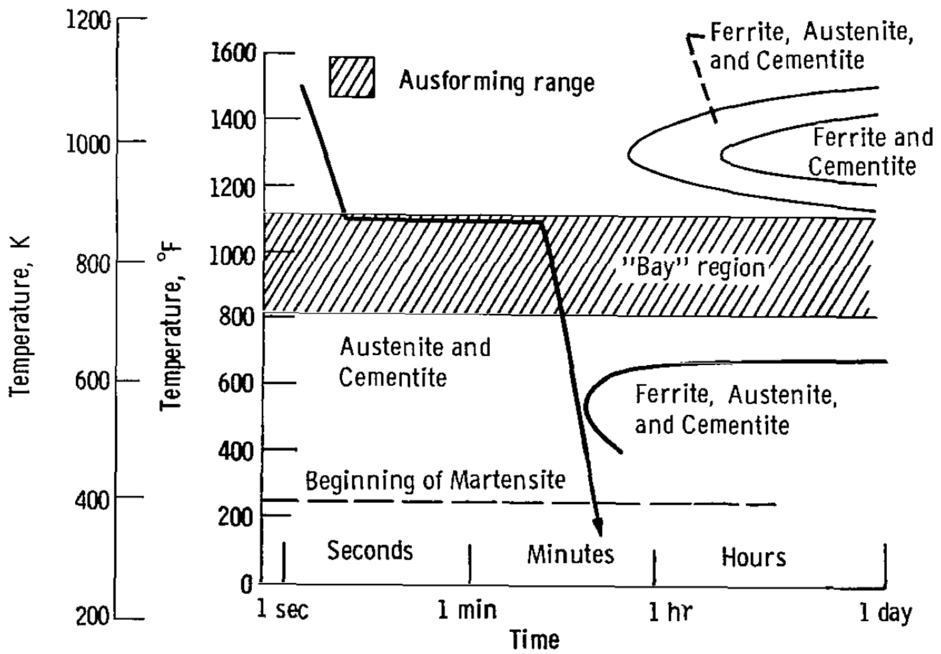

Figure 1.14: M50 stepped-cooling diagram indicating the approximate nucleation of phases and the ausforming range. After [100].

Ausforming is another thermo-mechanical process (TMP) designed to reduce segregation that takes place at high temperatures while the steel cools from the austenite phase [39]. The time window for ausforming is small due to the undercooling rate requirements of the martensite transformation, and avoidance of the pearlite and bainite phase fields. Figure 1.14 describes the ausforming range for M50 where hot-working can be performed. The process can prove costly for large workpieces but the ausforming of M50 bearing balls can reportedly increase their fatigue life three-fold [100]. Ooki et al. (2004) also reported beneficial grain refinement in ausformed 52100 bearing steel that corresponded to an extension in fatigue life [76]. A promising future route towards a more uniform steel microstructure free of coarse residual carbides is offered by powder metallurgy: the hot isostatic pressing (HIP) of gas atomised M50 powders can significantly reduce the size of residual carbides [101].

Computational thermodynamic models can be used to predict the relative proportions of stable carbide phases present in a steel as a function of temperature and composition [82]. Figure 1.15 shows some of the stable carbides expected in M50 steel at thermodynamic equilibrium, as calculated using MTData software. The high-temperature precipitation of MC and M_6C in Figure 1.15 at 1,200°C and 1,100°C respectively supports the literature on residual carbide species in M50 [84]. At these high temperatures the other Mo-rich carbide, M_2C, is less stable than M_6C and so is not predicted until lower temperatures in the region of tempering, where $M_{23}C_6$ and M_2C precipitate during secondary hardening [82]. $M_{23}C_6$ appears to be the most stable Cr-rich phase, occupying a significant volume fraction at equilibrium, and the meta-stable M_7C_3 carbide is not predicted at all by the calculations, in line with the literature [85].

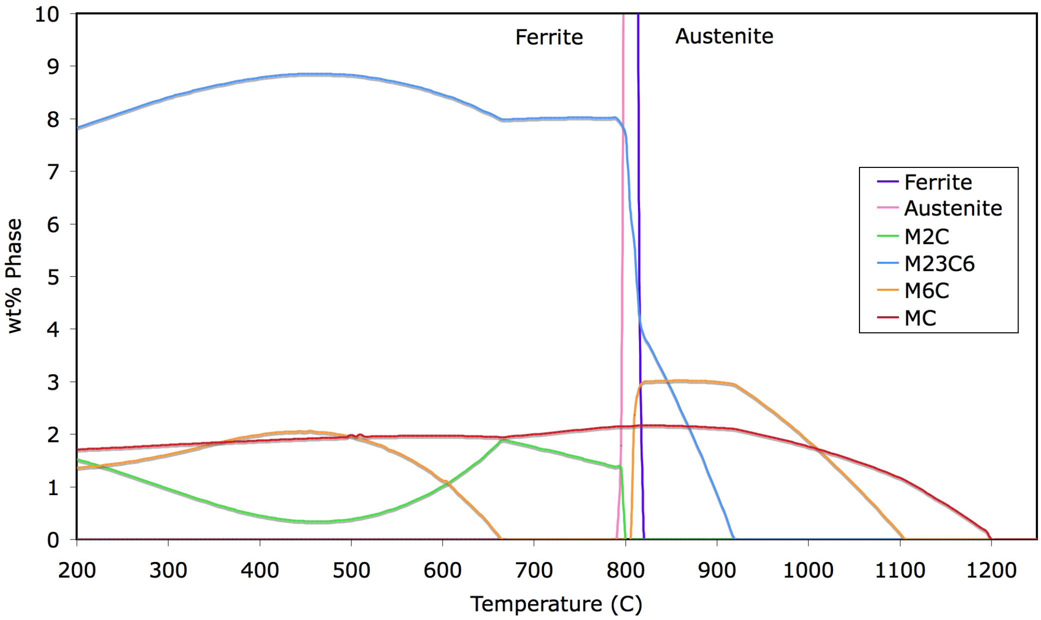

Figure 1.15: Calculated equilibrium M50 phase composition using MTDATA software V. 4.73 and the TCFE database. The allowed phases include all of those present and M_3C cementite (which is not observed).

The inherent assumption of thermodynamic equilibrium does not favour the meta-stable phases, nor allow for the local effects of chemical segregation, known to occur in M50 [83], so can lead to some discrepancies between calculations and observations. Chapter 3 contains detailed characterisation of the carbides present in M50 bearing balls where the presence of M_3C cementite is confirmed.

M50NiL has a much lower carbon concentration than M50, at 0.15 wt% throughout its bulk, so residual carbide segregation is not an issue [102]. Nickel alloying additions in M50NiL do not contribute to carbide formation, but instead remain in solid solution and help to suppress the formation of cementite. The carburisation process produces many small, spherical carbides in the material that are well distributed [81], and have a population density that directly correlates with an increase in hardness [Figure 1.16]. These carbides in the carburised case were found to be predominantly the V-rich MC phase, with some additional M_2C [73]. Carburising M50NiL also has the additional benefit of introducing a compressive residual stress in the case-hardened region after transformation [Section 1.2.3]. Song et al (2002) reported the secondary hardening precipitates that form during tempering of M50NiL bearing steel at 525°C were also the M_2C carbides [103].

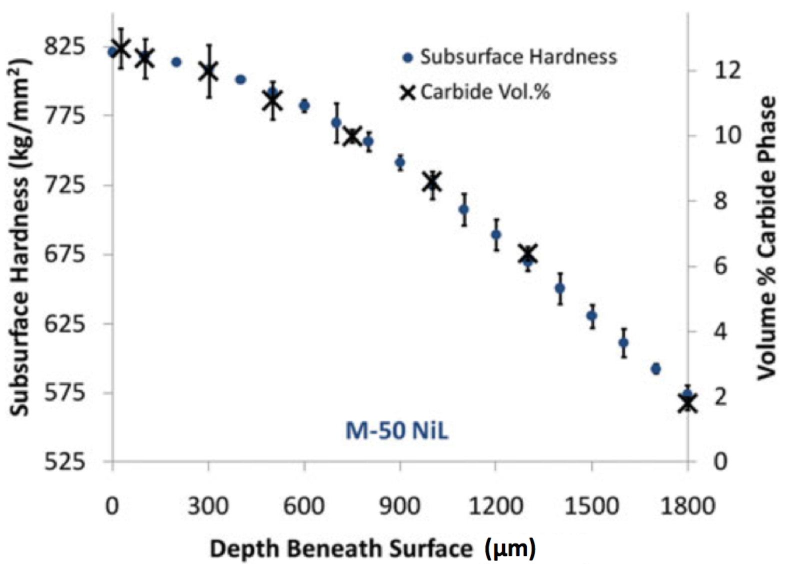

Figure 1.16: M50NiL hardness profile and MC carbide volume fraction as a function of carburised-case depth. After [81].

1.2.3 Residual Stress

The performance of bearing steels may be affected by finishing procedures carried out after heat treatment, such as the final grinding of the components and their fitting into the aircraft engine itself. Machining and surface treatments can leave behind residual stresses within the components that remain in bearing steels after manufacture, and these local stress fields combine with the applied stress during service. Residual stresses can develop over many length scales, and typically arise from two main sources; microstructural features inherent to the material, and mechanically-induced external factors.

The carburisation of M50NiL is a surface treatment which produces compressive residual stresses in the case-hardened region of bearing steel raceways [104]. The source of these residual stress fields are material-based; lattice strains are caused by interstitial carbon atoms and intragranular strains accompany the displacive martensite transformation [105]. The carbon saturated surface experiences a volume expansion upon transforming to martensite, leaving the case-carburised region under a state of compression relative to the lower carbon core material [106]. It is well understood that compressive stress at a free surface is beneficial for fatigue resistance, as it inhibits crack propagation by encouraging crack closure, and combines with the applied stress resulting in a net reduction in stress magnitude [11, 107]. In this way compressive residual stress lends strength to bearing steels [108, 109] and is reported to extend the fatigue life of carburised M50NiL over M50 [64, 110, 111].

Heat treatments can often reduce the effects of local residual stress by enabling diffusion and dislocation mobility [82]. Tempering high-carbon martensite can relieve the residual stresses that remain after quenching, reducing strain in the microstructure and softening the steel. The compressive residual stress profile of carburised M50NiL remains after tempering thanks to the large carbon gradient in the microstructure. Figure 1.17 shows some typical residual stress profiles beneath the surface for hardened bearing steels [110]. The negative stress values in MPa correspond to a compressive stress which extends to a depth of more than 750 μm in M50NiL [Figure 1.17]. The maximum shear stress of rolling contact fatigue occurs at similar depths beneath the contact surface [Section 2.1.1], so bearing designers must ensure the compressive residual stress extends to a necessary depth if it is to be

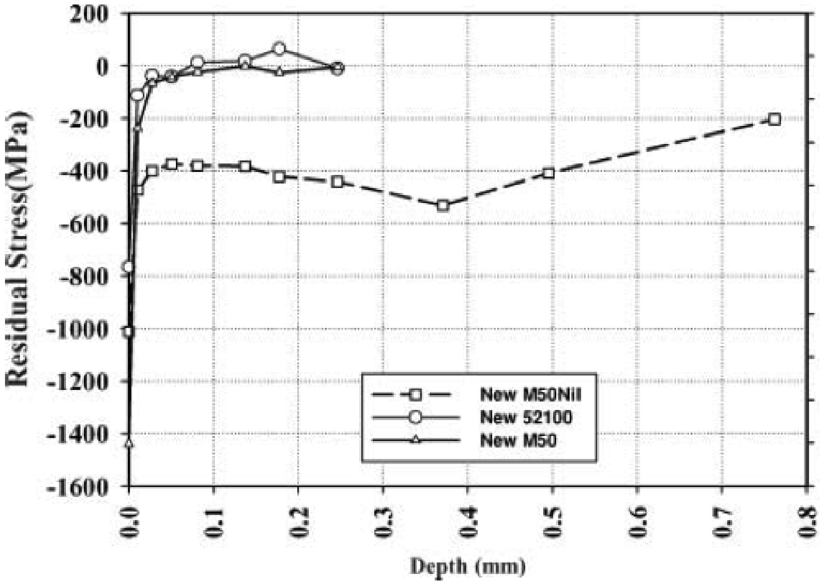

Figure 1.17: Residual stress profiles as a function of depth below the surface for hardened bearing steels in the unused condition. A compressive residual stress is seen in the carburised M50NiL material. After [110].

of benefit [46, 64]. The long-range residual stresses in the component will always balance out to equal zero, so the presence of a compressive stress at the surface is eventually accompanied by a balancing tensile stress at greater depths [112].

All the steels in Figure 1.17 show a sharp compressive stress in a shallow region at the surface due to finishing. Mechanically working the component surfaces provides another way to produce residual stresses in bearing steels through plastic deformation. Mechanical treatments such as shot-peening or hard-turning can be beneficial for rolling contact fatigue resistance [113, 114], and have proven to extend the life of M50 bearing steel [115]. The accumulation of plastic strain caused by dislocation pile-up at grain boundaries acts to work-harden the surface material, and these mechanisms can even take place during bearing service [15, 74]. The repeated application of stress in rolling contact fatigue can work-harden bearing steel and develop residual stresses [109, 116]. Chapter 2 introduces these fatigue mechanisms and the implications they can have on bearing steel behaviour.

A final grind of the bearing components after heat treatment is essential to obtain a smooth surface finish but this machining process may introduce unwanted residual stresses [117, 118]. Excessive grinding can cause plastic deformation and localised heating that will leave behind a transformed and brittle surface layer with tensile residual stress [119, 120]. Cracks can propagate easily through these deformed regions as tensile stresses acting perpendicular to the crack tip pull them apart, accelerating fracture [64, 107]. A tensile opening stress can increase the net effect of the maximum shear stress in RCF [121], however it is an unavoidable feature of bearing raceways fitted within the aircraft gas-turbine engine [106]. It is industry practice to press-fit the inner raceways of location bearings onto the main-shaft of the aircraft engine so that they fit tightly. This assembly produces a tensile residual stress component around the raceway circumference known as hoop-stress [46, 122]. A fatigue crack can rapidly propagate in the presence of hoop-stress, leading to catastrophic through-fracture of bearing raceways [123, 124], so the introduction of low-carbon M50NiL with its ductile core and high fracture toughness was designed to combat this problem [63, 31]. The centrifugal loads experienced during high-speed bearing operation also encourage hoop stress [108], and the effect of rotating mass imparts the most severe contact stress on outer raceway compared with the inner raceway.

We can measure the residual stresses present in a component using a number of different analytical techniques [105]. X-ray Diffraction (XRD) is probably the most widespread method and uses scattered photons to measure the interplanar spacings in polycrystalline materials to evaluate local lattice strains [125, 126]. Other techniques rely on the interactions of electromagnetic fields with a conductive sample material, such as Eddy current testing [127], and the magnetic Barkhausen noise technique [128]. Many of these approaches are non-destructive, meaning the bearing components can be safely examined for residual stress prior to entering service or even during operational maintenance checks. The ability to assess the local stress field in this way is crucial in understanding the behaviour of bearing steels under an applied stress. Chapter 5 contains XRD evidence of residual stress evolution in ex-service bearing raceways.

Chapter 2

Literature Review: Damage Mechanisms in Bearing Steels

Spalling damage is a characteristic outcome of rolling contact fatigue (RCF) in all bearing steels. Material flakes away from the contact surface leaving behind a fractured void which causes further damage. Once initiated, spalls propagate rapidly with continued stress cycling so their presence effectively marks the end of a component's safe operation. Preventing spall initiation from fatigue cracks is a priority in bearing steel design so this chapter introduces the wide variety of damage mechanisms and unique stresses that may lead to such failures under RCF. Not all of these effects would be expected in the aircraft bearing steels due to their unique secondary hardened microstructures so efforts are made to highlight these differences when necessary.

Regions of stress concentration in structural components will amplify the applied loads making local plastic yield more likely, hence there is good reason to ensure the homogeneity of bearing steel microstructures and an absence of stress-raising defects. A review of RCF failures from the literature often points towards impurity particles which act to concentrate stress, initiating fatigue cracks and eventually spalling [Section 2.1]. Traditionally these stress-raising inclusions have been non-metallic oxides and sulphides in steels, but the modern VIM-VAR processed aircraft-grades like M50 and M50NiL possess few of these. As steel cleanliness improves the occurrence of surface initiated fatigue failure becomes the more dominant life-limiting mechanism. Poor lubrication and excessive surface roughness will accelerate failure at the bearing surfaces, particularly under the high-speeds and elevated temperatures of the aircraft gas-turbine engine [Section 2.2]. There is also an increased emphasis on microstructural durability as modern bearings experience millions more stress cycles during their lifetime. Changes in the stressed material beneath the contact zone are known to occur in many bearing steels, gradually reducing their fatigue resistance over time. Microstructural evolution can be a slow and complex phenomenon, so accelerated laboratory testing has become commonplace to shorten the time scales involved [Section 2.3]. The applied loads during accelerated testing are usually far higher than those expected during normal bearing operation so they may not encourage a representative material response, however, they help provide statistical failure data which can be useful in the estimation of fatigue life.

The ultimate location of bearing failure will be at points of weakness in the component design - whether they are asperities on a poorly machined surface, or defects in a poorly homogenised microstructure. The dominating failure mode will be whichever one of these competing mechanisms is the least resistant to RCF stress cycling.

2.1 Rolling Contact Fatigue

The critical difference between uniaxial fatigue testing and that of rolling contact fatigue (RCF) is the more complicated nature of the cyclic stress field which may lead to crack initiation, propagation and spalling failure [34]. In location bearings, the rolling elements transmit heavy loads across a finite contact area, but the inherent movement of each passing rolling element produces a multiaxial stress distribution in the material beneath the surface which changes direction during each stress cycle.

The onset of fatigue damage begins with highly localised plastic deformation in the material [11]. Plasticity and the movement of dislocations occurs under shear stress so it is this shear component that has proven most critical in RCF. The maximum shear stress is found beneath the contact surface at a depth that often correlates with the most pronounced signs of fatigue damage in the material [25]. To calculate the depth of maximum shear stress bearing designers must consider the contact geometry between ball and raceway, together with the loading conditions and the material modulus and Poisson's ratio. A number of assumptions are often made to simplify the calculations, such as assuming fully elastic loading of uniform solids in a suitably well-lubricated system with no sliding at the contact surface. This approach first dates back to 1882 with the work of Hertz [129]. His analysis of the stress field between static elastic bodies in loaded contact can still today provide an adequate description of RCF stresses [35], despite the many assumptions. This is particularly the case for well-lubricated aeroengine bearings in normal operation.

2.1.1 Hertzian Contact Stress

When a load is applied between two solid objects with curvature, they will deform elastically to share a conformal contact ellipse of precise area proportional to the normal force [130], according to:

$$b = \left(\frac{3FR'}{4E'}\right)^{\frac{1}{3}} \tag{2.1}$$

where b is the semi-major axis of the contact ellipse as a function of the normal force F, the combined radius of curvature of the meeting objects R' [Equation 2.2], and the reduced elastic moduli E' of the two solids [Equation 2.3]:

$$\frac{1}{R'} = \frac{1}{R_1} + \frac{1}{R_2} \tag{2.2}$$

$$\frac{1}{E'} = \frac{(1-\nu_1^2)}{E_1} + \frac{(1-\nu_2^2)}{E_2} \tag{2.3}$$

For typical bearing steels the Elastic Modulus, $E = 200\,\mathrm{GPa}$ (30×10^6 psi), and Poisson's Ratio, $\nu = 0.30$, but the carbide phases will display different properties. Figure 2.1 a describes the contact ellipse formed between

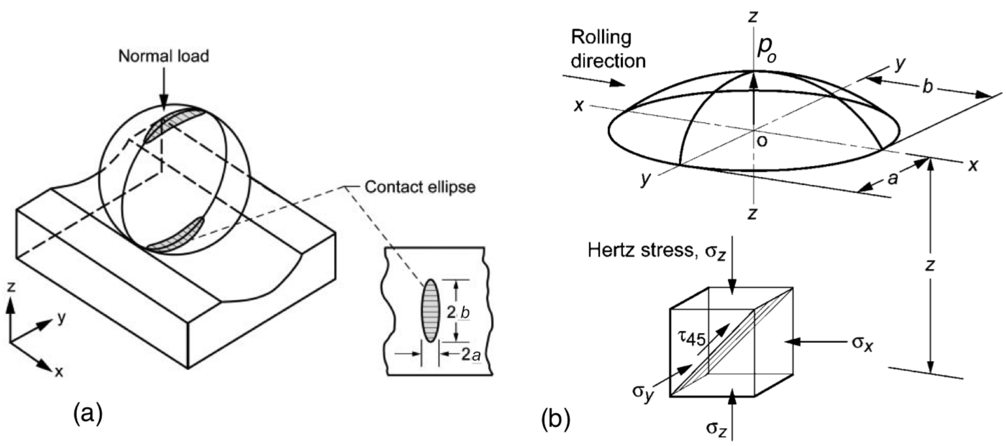

Figure 2.1: (a) The shaded contact ellipse has a semi-minor axis of length a and semi-major axis of length b. (b) The pressure across this contact ellipse is hemispherical in magnitude with maximum p_0 at the central position. The Hertzian stress, σ_z, is shown at a depth z beneath the contact ellipse together with the other principal stresses and the 45° shear stress, τ_{45}. After [66].

ball and raceway in aircraft location bearings. The pressure exerted across this contact surface has a maximum value p_0 at the centre of the ellipse [Figure 2.1 b]. Under Hertzian point contact the elastic strain is concentrated in an ellipsoidal volume of stressed material directly beneath the contact ellipse. This stressed volume is small compared to the size of the components and the three principal stresses, $\sigma_x\,\sigma_y\,\sigma_z$, are proportional to the contact pressure. The convention is to define the normal force along the z axis, so that the Hertzian stress, σ_z, is perpendicular to the contact ellipse. The resulting shear stress, τ_{45}, occurs at some depth, z, beneath the contact ellipse and is oriented at 45° to the x-y plane [Figure 2.1 b].

Figure 2.2 plots the values of the three principal stresses as a function of depth, z, beneath the centre of the contact ellipse. In the absence of tan-

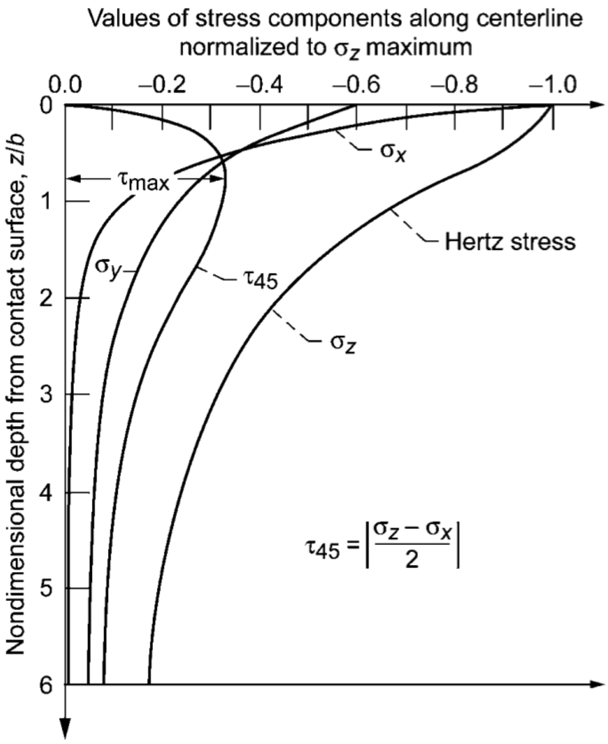

Figure 2.2: The Hertzian contact stress distribution as a function of depth z beneath the contact ellipse, showing the three principal stresses and the resultant maximum shear stress. After [66].

gential forces at the contact surface, the shear stress has a maximum value, τ_{max}, at a depth, z_0, proportional to the size of the contact ellipse [66]:

$$z_0 = 0.78b \tag{2.4}$$

where b is the semi-major axis of the contact ellipse. In this way the maximum shear stress depth, z_0, is only dependent on the contact geometry and material moduli under Hertzian contact loads.

Early examinations of failures in low-alloy bearing steels found that z_0 correlates remarkably well with regions of localised RCF damage in rolling-bearings [52]. Fatigue cracks were found to initiate at depths corresponding with the maximum shear stress and the direction of crack propagation often travelled at 45° to the contact surface, parallel to the τ_{45} shear stress [16, 96]. Figure 2.3 shows some examples of subsurface fatigue cracks in non-aircraft bearing steels that have initiated at non-metallic inclusions in the stressed volume beneath the contact zone. Local plastic yielding at these stress concentrating features leads to the nucleation of voids and fatigue cracks which then propagate under the action of the maximum shear stress [16, 131, 132]. Countless other deformation mechanisms are also seen to occur in bearing steels at the depth of maximum shear stress and many of these too show strong orientation [Section 2.1.2].

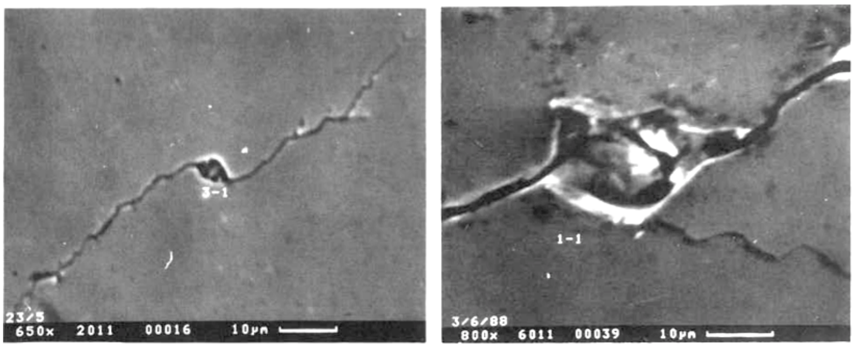

Figure 2.3: Fatigue cracks initiated at non-metallic inclusions in 52100 bearing steel and are orientated at approximately 45° to the contact surface (the rolling direction is left to right). After [133].

Lundberg and Palmgren (1947) applied Hertzian contact theory to consider the movement of rolling bodies and identified an alternating shear stress component acting parallel to the contact surface [12]. Through experimental observations of fatigue cracks lying in the subsurface plane parallel to the bearing raceway surface they reasoned that this alternating, orthogonal shear stress was a driving force for initiating failures under RCF. The Lundberg-Palmgren model for bearing fatigue life was constructed based upon the probability of crack initiation in this stressed volume [Section 2.3]. The alternating shear stress is dynamic, undergoing a complete 180 degree reversal along the rolling direction $\pm\tau_z$ with each rolling cycle [Figure 2.4 b].

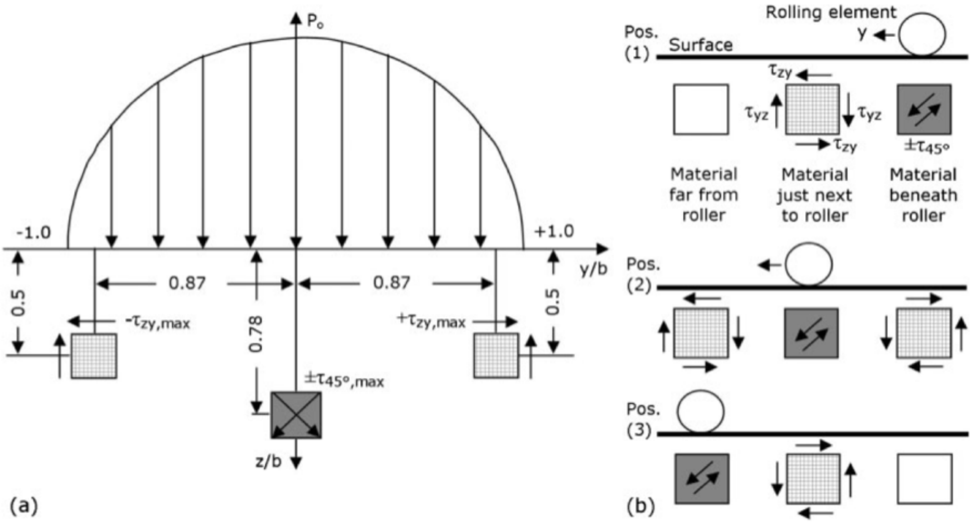

Figure 2.4: (a) Under rolling contact the orthogonal shear stress τ_{zy} is a maximum beneath the edges of the contact ellipse. (b) The passing rolling element leads to an alternating orthogonal shear stress direction in the x-y plane. After [38].

Figure 2.4 a shows the peak orthogonal stresses, $\pm\tau_{zy,max}$, are located nearer the edges of the contact ellipse at $y = \pm 0.87\,b$, and at shallower depths of $z = 0.50\,b$, closer to the contact surface compared with the maximum shear stress τ_{45} at $z = 0.78\,b$. Littman (1970) reviewed the literature on fatigue crack initiation as a function of depth in bearing steels [134]. RCF failures were also seen to occur at the shallower depths corresponding to the orthogonal shear stress [14, 133]. Fatigue cracks were also found orientated parallel to the contact surface, consistent with propagation in the plane of alternating shear stress [135]. Figure 2.5 plots a comparison between these two pernicious shear stresses as a function of the contact stress and position under the contact ellipse. It can be seen in Figure 2.5 that by considering the stress range $\Delta\tau_{zy}$ of the alternating shear stress cycle, its effective magnitude is then greater than the maximum shear stress, according to:

$$\Delta\tau_{zy} = 2\,|\pm\tau_{zy,max}| \tag{2.5}$$

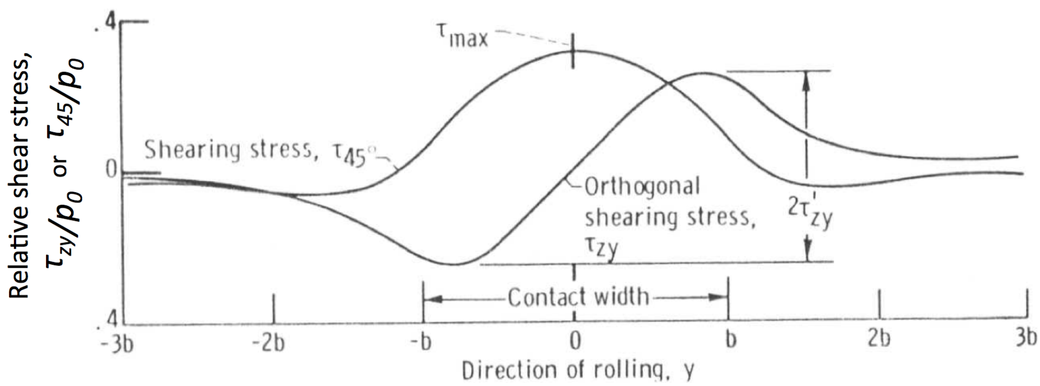

Figure 2.5: Relative shear stress magnitude as a function of the contact stress, p_0, with displacement along the contact ellipse of semi-major axis b, for the maximum shear stress τ_{45} and the orthogonal shear stress τ_{zy}. After [134].

The depths at which cracks are observed in RCF provides circumstantial evidence for failures initiating at a critical shear stress, but this can also lead to ambiguity. It is unsatisfactory to rely on the growth orientation of fatigue cracks, since these may be affected by local grain orientation and crystallographic texture. Disagreement between authors on the subject of which shear stress is most critical highlights the dangers of focusing too deeply on stress calculations made under idealised Hertzian conditions [74, 134]. A proper fatigue failure analysis should take into account all aspects of bearing steel operation. During aircraft takeoff the contact stress between ball and raceway will reach 1.8 GPa in location bearings, assuming Hertzian contact, producing a maximum shear stress of $\tau_{max} = 560$ MPa at depths of 0.2 mm beneath the point of contact. These values apply only for perfectly elastic bodies in a lubricated system, so the real stress situation is strongly governed by surface tribology [Section 2.2]. Bodies are not perfectly smooth, nor frictionless and homogeneous in composition. The initiation of fatigue failures at stress raising defects is evidence for the presence of these inherent flaws in real materials. Surfaces exhibit defects too, and in reality there is occasional metal to metal contact at raised asperities causing friction and tangential stresses at the surface [136].

Modifying the Hertzian contact stress calculations to include a tangential stress component as well as a normal force leads to some interesting effects. The stress profile becomes asymmetric, with the maximum contact pressure no longer central in the contact ellipse but instead strongly skewed in the direction of surface shear [137]. Crucially, the depth of the maximum shear stress, z_0, moves closer toward the contact surface [38, 134, 138]. Thus, the occurrence of surface initiated failures becomes more likely when tangential stresses are present in the contact ellipse [139]. Chapter 4 contains evidence of surface shear in ex-service aircraft bearing steels.

In assuming elastic behaviour, Hertzian contact theory overlooks some of the well-established principles of fracture mechanics, such as localised plasticity at a fatigue crack tip [Section 2.3]. Plasticity may be encountered in the stressed volume under RCF even if the contact loads remain well below the elastic limit of these high yield strength bearing steels. Evidence for localised plasticity at stress raisers is conclusive [38], as is the steady accumulation of plastic strain in the subsurface over many rolling cycles [19, 20]. Bearing designers seeking a combined elastic-plastic approach to RCF stress modelling may consider evaluating the von-Mises equivalent stress [52, 140]. This 3-dimensional yield criterion describes the onset of plasticity in the subsurface region beneath the contact ellipse, according to:

$$\sigma_{VM} = \frac{1}{\sqrt{2}}[(\sigma_x - \sigma_y)^2 + (\sigma_y - \sigma_z)^2 + (\sigma_z - \sigma_x)^2]^{1/2} \tag{2.6}$$

where $\sigma_x, \sigma_y, \sigma_z$ are the three principal stresses in the material. The von-Mises stress also has a maximum within the subsurface region beneath the contact ellipse [141, 142]. In deterministic RCF models, plastic behaviour can be used as a quantifier for the progression of fatigue damage in bearing steels. Voskamp (1985) describes the chronological stages of RCF, beginning with some plastic yielding of the stressed volume, up until a saturation point where the material then resists further deformation and behaves elastically [143, 144]. This effect pertains to the work hardening of the bearing material during initial loading [145], but is only one of the many material responses encountered under RCF. Despite the inability to fully incorporate plasticity into Hertzian contact stress solutions, the approach remains synonymous with RCF behaviour in bearings [35].

2.1.2 Microstructural Changes

Prior to the development of vacuum melted aircraft-grade steels it was common to see rolling bearings fail because of damage initiated at non-metallic inclusions in the stressed volume. When bearings were examined in cross-section there were consistent reports of altered microstructures in this stressed volume too, suggestive of damage accumulation. The material beneath the contact surface appeared different to the surrounding matrix and was particularly susceptible to chemical etchants. Affected material would often etch darkly, indicating localised changes in the steel microstructures below the rolling track after RCF stress cycling.

Jones (1947) was one of the first authors to note material changes beneath the contact surface of early bearing steels: locally transformed martensite converted into a combination of ferrite and cementite, accompanied by softening in the affected regions [130]. Similar findings were made by Barwell (1953), who identified strong etching characteristics in regions of the subsurface where the shear stress was greatest, and these increased in severity with bearing operation time [146]. Early examinations of M1 tool steels under RCF by Carter (1960) also observed these dark etching phenomena: he concluded that the transformed regions consisted of tempered martensite resulting from subsurface stressing and heating effects [96]. This thermomechanical tempering mechanism took place in-situ under RCF, and was accelerated by a rise in temperature and an increased number of cycles [97]. Bush et al. (1961) observed this phenomenon in the low-alloy 52100 bearing steel: although the etched microstructure appeared similar to tempered martensite, it was plastically deformed and found at depths in the region of orthogonal shear stress [116]. Sugino et al. (1970) provided evidence of localised deformation of the martensite plates making up the dark etching constituent in 52100 steel, describing a non-uniform and patchy appearance inconsistent with normal tempering but softened [17]. Figure 2.6 shows characteristic Dark Etching Regions (DER) in metallographic cross-sections of Cronidur 30 bearing steel raceways. When chemically etched, the stressed volume beneath the rolling tracks etches deeply in a crescent shape with symmetry reminiscent of the contact pressure hemisphere [Figure 2.1 b]. The DER does not extend fully to the contact surface but instead remains isolated beneath it, concordant with the maximum shear stress distribution [Figure 2.6].

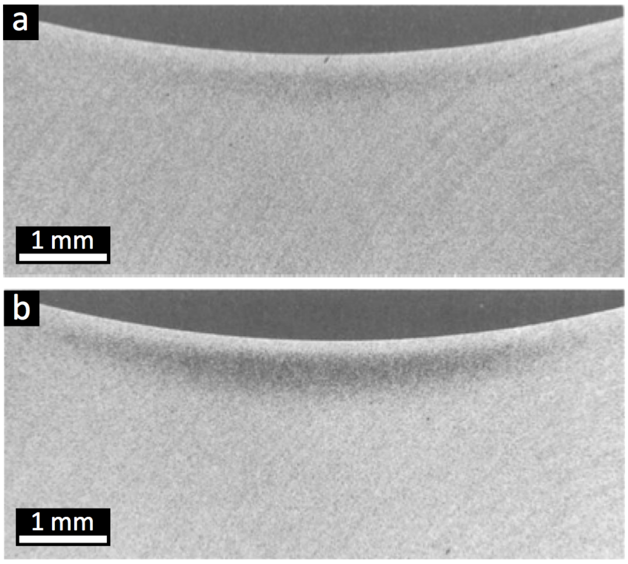

Figure 2.6: Cross-sections of martensitic Cronidur 30 steel raceways displaying crescent-shaped dark etching regions (DER) in the stressed subsurface. (a) Operating at 80°C produces only a subtle RCF response. (b) At 210°C the DER is more severe. After [5].

RCF testing of secondary hardened bearing steels by Bohmer et al. (1998) showed no evidence of the dark etching response: at temperatures of 210°C and stresses of 3 GPa the M50 and M50NiL alloys showed no signs of DER after $N = 5 \times 10^6$ cycles [5]. The authors attributed this absence of DER to the insufficient number of loading cycles undergone, in line with fatigue limit predictions put forth in work by others [16]. However, it is more satisfactory to base the absence of DER in M50 and M50NiL on the fact that the steels are already severely tempered before entering service, resulting in improved thermodynamic stability of their secondary hardened microstructures. Braza et al. (1993) performed RCF tests on the aircraft-grade bearing steels at higher contact stresses of 3.6 GPa for $N > 10^8$ cycles: The M50 and M50NiL steels displayed no material softening or DER in the stressed subsurface, yet the lower-alloyed 52100 steel showed both of these phenomena [9]. The secondary-hardened microstructures of aircraft engine bearing steels apparently offer an increased resistance to the effects of thermomechanical tempering [110].

Swahn et al. (1976) investigated the dark etching microstructures of RCF in 52100 bearing steel: The softened DER was attributed to the stress-induced decay of the martensitic matrix, resulting in a ferritic phase with an inhomogeneous carbon distribution. Bearing testing was carried out at ambient temperatures so thermal tempering of the microstructure was ruled out. Instead, the cumulative effect of $N > 10^7$ cycles at contact stresses between 3.3 - 3.7 GPa led to transformation [13]. Figure 2.7 shows the progression of microstructural decay in 52100 steel with increasing number of fatigue cycles.

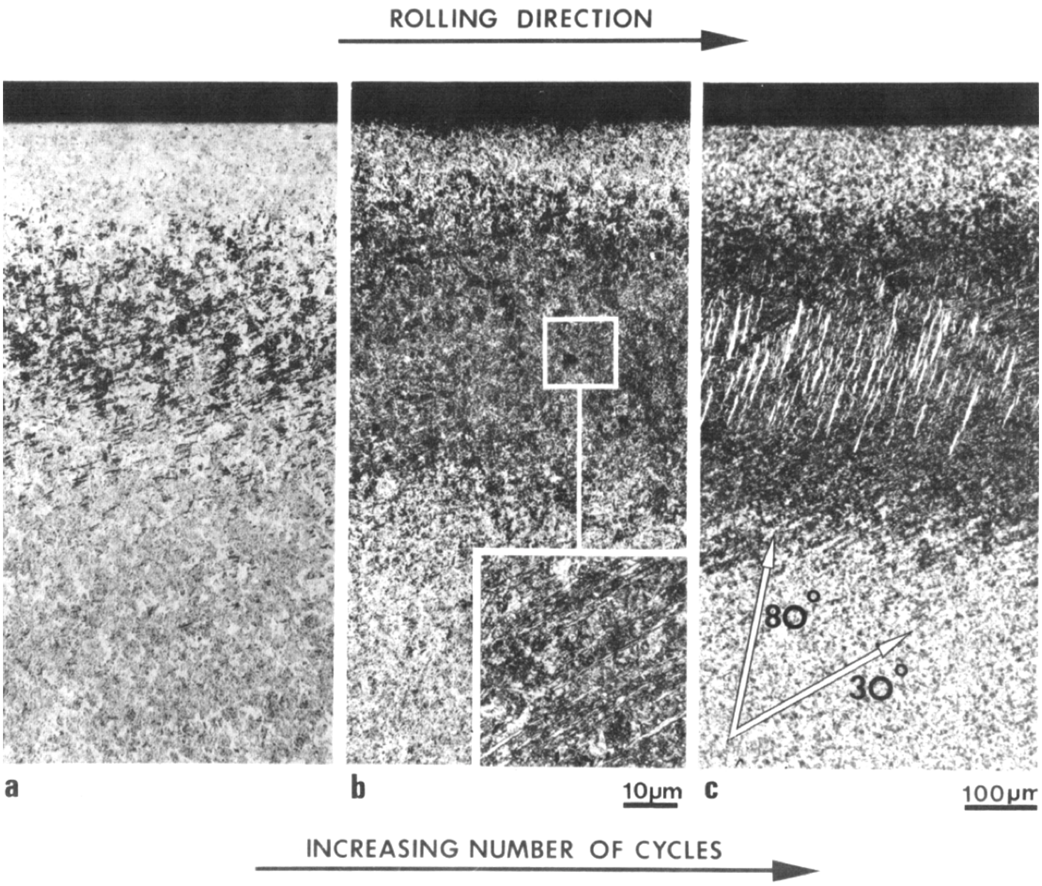

Figure 2.7: Cross-sections of martensitic 52100 bearing steel raceways showing progressive DER development, followed by white etching bands with strong orientation. After [13].

At very high numbers of cycles ($N > 10^8$) the appearance of white etching bands is sometimes encountered within the stressed volume [Figure 2.7 c]. These strongly directional features were thought to be a progression from DER [13, 16], however white etching bands have been observed in M50 and M50NiL steels in the absence of preceding dark etching material [9, 110, 147], implying different mechanisms behind their formation. Figure 2.8 shows examples of white etching bands in M50 bearing steel after RCF testing: The deformation features were located near a fatigue spall that occurred after 10^6 fatigue cycles at 3.1 GPa [110]. Hardness values measured in these affected regions were lower than those measured elsewhere, consistent with the softening of martensite decay. However, Braza et al. (1993) reported no softening accompanying the presence of similar white etching bands in M50 and M50NiL [9].

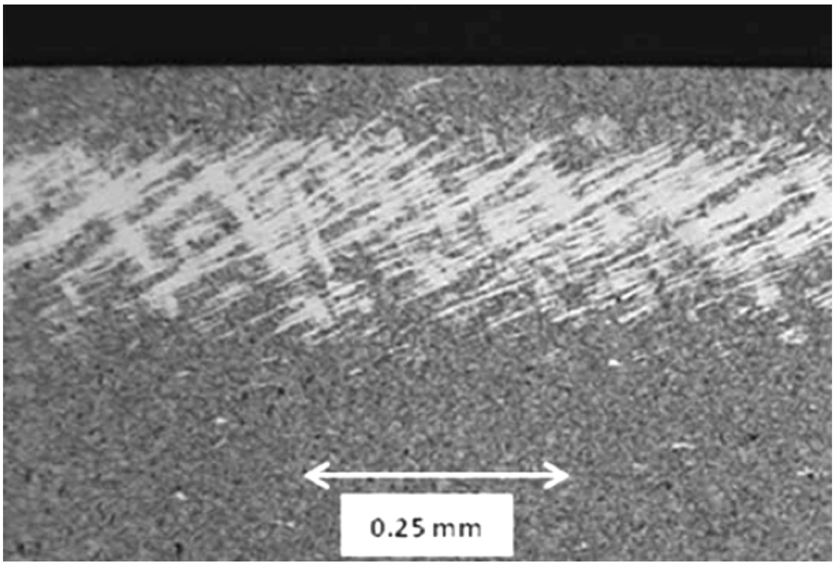

Figure 2.8: White etching bands without prior DER found in a circumferential cross-section of M50 bearing steel, run at 3.1 GPa Hertzian contact stress for $N > 16 \times 10^6$ cycles. After [110].

Martin et al. (1966) presented mechanisms for the formation of white etching region based upon localised plastic shear in 52100 steel: transformed ferrite bands in these highly stressed regions are supersaturated with carbon and large elongated carbides grow under the action of interfacial energy [18]. A similar idea was put forth by Osterlund and Vingsbo who spoke of aligned carbide disks sandwiched between a ferrite phase [148]. The orientation of the white etching bands appears to be influenced by the macroscopic rolling direction of the bearing assembly and is independent of local grain orientation [13]. The shear stresses of RCF are thought to play a role in producing such orientation but the specific angles observed in the literature tend to vary between systems.

Cracks are sometimes seen in combination with white etching regions. Martin and Eberhardt (1967) noted that cracks would propagate along the easy paths created by the white deformation bands [22]. Schlicht at al. (1988) observed white etching bands running parallel to the contact surface, containing fatigue cracks along their length: it was claimed that rubbing between crack faces under loaded contact acted as a source for localised heating, plasticity and transformation of the material, which subsequently resists etching [16]. This is now a popular theory behind the formation of white etching material, particularly when it surrounds cracks or neighbours defects [38]. Conclusive evidence is provided by the observation of white etching material at artificial cracks introduced in bearing steel microstructures prior to fatigue testing [149]. The deformed material adjacent to cracks consists of nano-grained ferrite in which carbides are dissolved resulting in high local hardness [21], apparently different from the softer angled bands which steadily accumulate only after a high number of fatigue cycles [13].

The RCF testing of M50 bearing steel has been shown to create small cracks in the stressed volume with localised white etching material at the crack faces [9]. The appearance of these features has been likened to butterflies, due to the pair of white etching 'wings' of transformed ferrite spreading out either side of cracks or other stress-raising defects [150]. Figure 2.9 shows a typical 'butterfly' feature at a carbide in M50 steel, together with a another butterfly example at a non-metallic inclusion in 52100 steel.

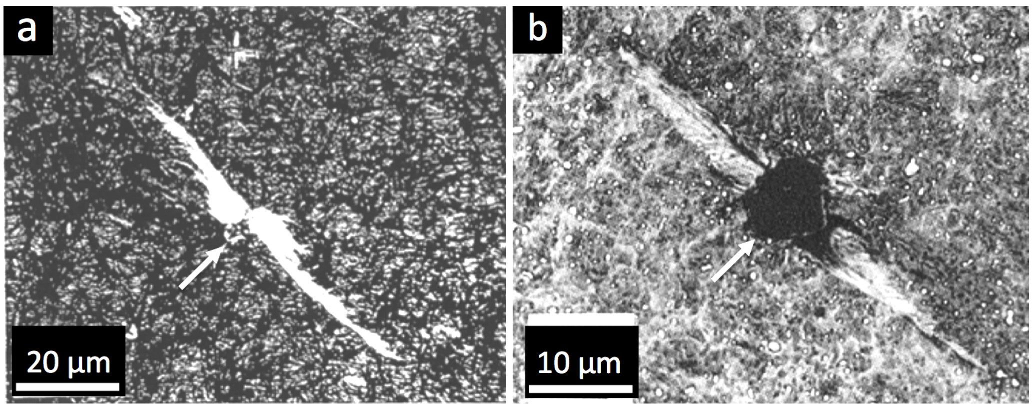

Figure 2.9: (a) Butterfly formed at a carbide in M50 bearing steel after 3×10^8 cycles at 3.62 GPa [9]. (b) An aluminium oxide inclusion initiated butterfly in 52100 bearing steel [17]. Note the approximate 45° angles of the white etching wing features relative to the horizontal rolling direction.

Butterflies are isolated, non-propagating cracks which initiate at defects in the stressed volume beneath the contact surface, at depths corresponding to the maximum subsurface shear stresses [134]. Osterlund et al. (1982) presented a mechanism for the formation of white etching wings at the interface between non-metallic inclusions and the matrix: high strain at the inclusion-matrix interface encourages a dynamic phase transformation and recrystallisation of the nano-grained ferritic phase [150]. The resulting ferrite resists chemical etching and possesses high hardness through the Hall-Petch relationship [Equation 1.2]. The presence of this new hardened phase surrounded by relatively softer matrix then provides a source of further strain and cracking [150]. Other theorists have since refined and expanded on this mechanism, claiming heat generation at the rubbing crack surfaces is sufficient to reach austenitising temperatures, leading to local rehardening zones and carbide dissolution [16].

Grabulov et al. (2009) performed detailed transmission electron microscopy of butterfly wing microstructures, paying close attention to the non-metallic inclusion/matrix boundary. The recrystallisation previously suggested [150], was deemed inappropriate due to insufficient heating during the process and instead a low temperature recrystallisation mechanism was put forth for the white etching structure [131]. High resolution microscopy also revealed that crack formation began with debonding at the inclusion-matrix interface, an effect previously suggested by others [151]. Vincent et al. (1998) recognised that the elastic-plastic strain mismatch at carbide-matrix interfaces leads to high local stress fields, eventually accommodated by plastic flow [132]. Void creation and decohesion of the matrix bordering coarse carbides has been witnessed in M50 [24, 23], and has deep implications for the RCF behaviour of these aircraft grade steels. Chapter 3 contains observations of carbide decohesion in M50 bearing balls.

Fatigue crack initiation at defects is influenced by their specific thermal expansion coefficients and elastic moduli, together with shape factors, such as size, aspect ratio and their orientation with respect to the stress field [78, 133]. Those in the subsurface which lie with an acute apex in the plane of maximum shear stress are apparently more likely to nucleate butterfly cracks [21, 150]. Butterfly wings are often found at approximately 45° to the contact surface [Figure 2.9], concordant with crack growth along the maximum unidirectional shear stress direction [16, 150, 151].

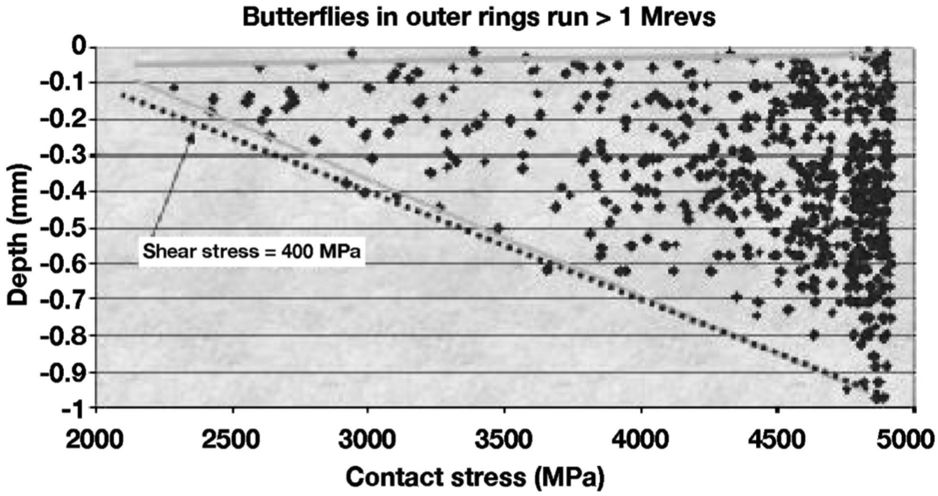

Figure 2.10: Butterfly locations as a function of depth beneath the contact surface in 52100 steel tested for over 10^6 cycles. After [21]. Note, the appearance of butterflies takes place at contact stresses over 2 GPa.

Lund (2010) examined location data on the depths of butterfly cracks as a function of contact stress [Figure 2.10], finding strong correlation between the maximum shear stress and the threshold for fatigue crack initiation at defects [21]. In this way, butterfly cracks apparently differ from the progressive development of DER and white etching bands within the stressed regions beneath the bearing surface, which instead accumulate over time with increased cyclic strain and slow material decay [152]. Forster et al. (2010), discovered extensive white etching bands in M50 and M50NiL steels after large numbers of cycles, but only butterflies and no banding whatsoever in these steels at fewer cycles [110].

Voskamp (1985) proposed a deterministic model for RCF progression in bearing steels that tracked the development of microstructural alterations throughout different stages of operation. Figure 2.11 describes the degree of retained austenite decomposition in 52100 steel after RCF stress cycling [74]. Three distinct stages are presented in this RCF timeline: Stage 1 begins with 'shakedown', stage 2 is a 'steady-state' period of operation, and stage 3 heralds 'instability' [Figure 2.11]. During the first few thousand stress cycles microplastic deformation occurs in an initial period of 'shakedown', conditioning the material through transformation of retained austenite and work-hardening up until a saturation point (Stage 2). Residual stresses that accompany the inherent shape change of α' transformation are also developed during this initial running-in stage [20].

Stage 2 is a steady-state incubation period where bearing steels supposedly

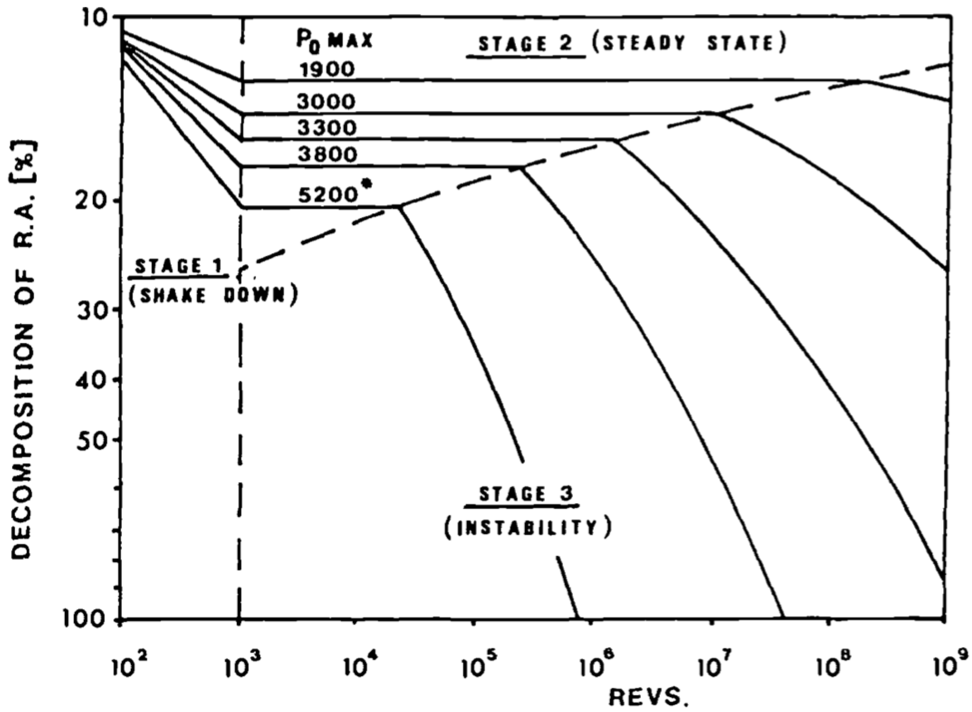

Figure 2.11: Decomposition of retained austenite (R.A.) in the stressed volume of a 52100 bearing steel given the number of revolutions for a series of Hertzian contact pressures, ($p_{0\,MAX}$ in MPa). After [153].

exhibit elastic behaviour [25]. The work hardened material resists further plasticity, providing the yield stress is not exceeded by the applied loads or excessive temperatures, and the majority of bearing life is spent operating at this stage. Stage 3 brings instability through localised plasticity, together with martensite decay and material softening (DER), discussed earlier in this section. Further changes in residual stress are encountered here too, with the development of subsurface tensile stress perpendicular to the contact surface, and compressive stresses in the tangential and axial directions [16, 74].

Figure 2.12 shows residual stress measurements in the tangential direction for a series of M50 bearings after RCF testing, indicating changes in the subsurface compressive stress profile with stress cycling [9]. According to Voskamp, residual stress profiles in bearings are altered during both the early and latter stages of RCF, (Stages 1 and 3 in Figure 2.12). The residual stress evolution significantly reduces bearing life by amplifying the applied stress

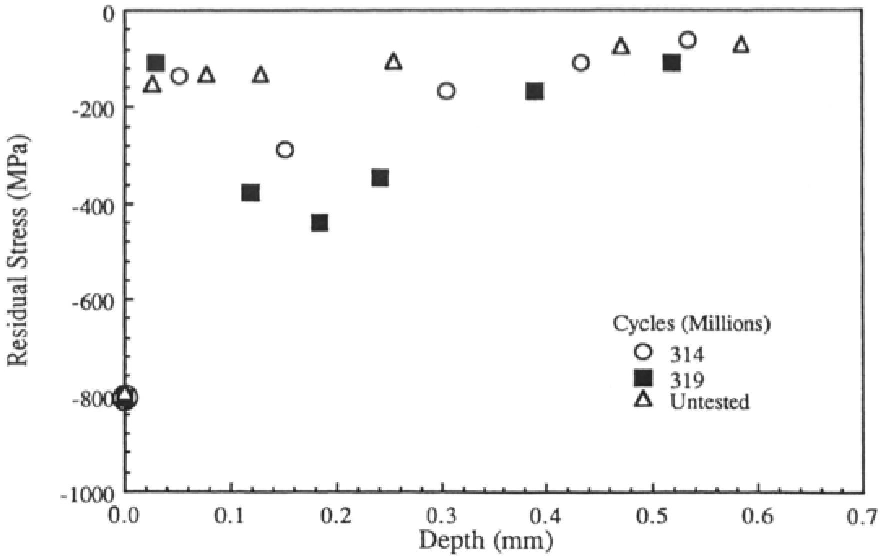

Figure 2.12: Residual stress profiles as a function of depth below the surface of M50 bearing steels inner raceways after 3×10^8 cycles. After [9].

and lowering the threshold for yielding, accelerating fatigue failure. In this way, the Voskamp RCF model better appreciates the rolling history of bearing materials and the evolving effects of damage accumulation over time. Muro and Tsushima (1970) observed beneficial compressive residual stress development almost immediately during the shakedown stage in bearing fatigue testing, together with work hardening [15]. These effects are not too dissimilar to those of certain manufacturing techniques designed to pre-stress bearing materials before service [Section 1.2.3]. Figure 2.12 demonstrates that the change in residual stress profile with fatigue cycling can provide a quantitative marker of damage progression during RCF. Retained austenite decomposition proved revealing in 52100 steel [Figure 2.11], but would be of limited scope in the aircraft-grade bearing steels since austenite levels are already very low. Forster even suggests that the minimal retained austenite content in M50 and M50NiL explains the lack of DER they show [110]. Chapter 5 contains evidence of both work-hardening and residual stress evolution in M50NiL bearing steel.

Microstructural changes may remain an exclusively long-life phenomenon, seldom seen in aircraft bearing service because when failures do occasionally occur they are instead caused by surface defects. The competing fatigue failure modes that initiate at the contact surface may override the subtle evolution of the microstructure. Whilst it is true that M50 and M50NiL are not immune to damage accumulation, as seen for example in Figure 2.8, these alterations in the stressed volume are usually encountered under laboratory conditions using very high loads that are not necessarily representative of aircraft gas-turbine engine operating conditions [Section 2.3.2]. Chapter 6 assesses the suitability of laboratory-based RCF rig testing for examining M50 and M50NiL bearing steels.

2.2 Tribology

Hertzian contact stress is calculated under the assumption of 'elastohydrodynamic' (EHD) lubrication conditions, in which a thin film of lubricant fully separates the elastic bodies of ball and raceway [139]. The contact stress is transmitted through this frictionless, non-compressive medium of oil so the components ideally never actually touch one another. The lubrication conditions are therefore of vital importance for maintaining bearing performance. Proper consideration must be given to surface effects which may prevent ideal conditions. Inadequate lubrication and microplasticity of asperities are common effects in real bearing components, whose separation is not always guaranteed [154].

Tribology is the field of science concerned with issues of friction, wear and lubrication between surfaces in contact [155]. In rolling-bearings, excessive roughness of the component surfaces [136] or starved lubrication conditions [156] will lead to asperity contact and metal-on-metal traction. Under these circumstances, gross sliding can occur within the contact ellipse producing tangential stresses at the surface that, when combined with the normal loads, completely alter the Hertzian stress distribution. Sliding between components causes the maximum shear stress of RCF to move closer towards the contact surface [137], bringing with it new damage mechanisms and fatigue initiating phenomena [157]. Failures will initiate at stress concentrating defects on the contact surface itself so a high quality surface finish is vital [Section 2.2.1]. Polyester-based synthetic lubricants are used to maintain component separation and prevent asperities breaking through the lubricant film causing friction, but they also fulfil a number of other important roles including cooling of the location bearings during service and flushing away any foreign particulates [Section 2.2.2]. Constant oil circulation is required, during which debris contaminants are actively filtered out to avoid indentation of the component surfaces, which could create further stress concentrations to initiate fatigue failures [29, 30].

Some degree of sliding within the contact ellipse is inevitable, regardless of whether bearing lubrication fails or metal-on-metal traction is present. After geometrical considerations, pure rolling cannot occur over the entire area of the contact ellipse because different velocities are experienced as a function of position. Figure 2.13 shows this phenomenon exhibited between a spherical ball element rolling upon a grooved raceway. The condition for pure rolling is only satisfied in two locations of the contact ellipse where the relative velocity vectors of the ball and plane are equal [Figure 2.13]. Inherent sliding occurs at all other regions where the velocity vectors are not equal; an action known as Heathcote slip [155]. It is important to note that the sliding direction is not always identical to the rolling direction [28]. Adequate lubrication limits the shear stresses at the contact surface caused by Heathcote slip.

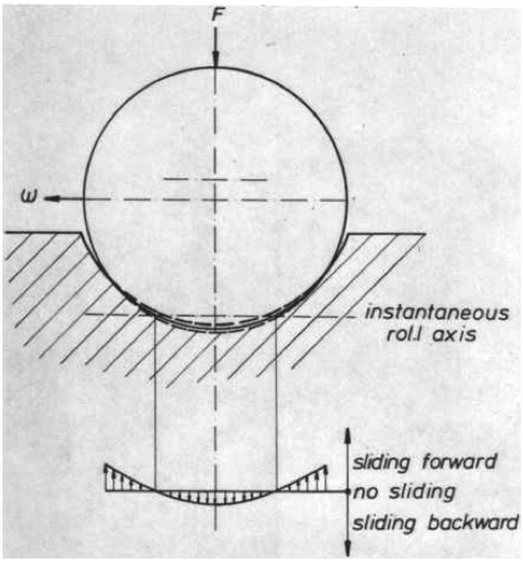

Figure 2.13: Sliding in the contact ellipse of ball bearings due to Heathcote slip under a normal load F rotating with angular frequency ω. After [158].

Under thrust loads, the ball elements will spin and precess causing the slip velocities to become even more complex [139]. Direct evidence for slip in ball bearings is sometimes seen in the literature through specific damage features called kinematic marks. Pearson and Dickinson (1988) found scratches in a swirling pattern at the contact surface of raceways which indicated the sliding behaviour of bearing balls [24]. Gloeckner (2010) also found kinematic marks at the contact surface of aircraft engine bearing raceways, indicating the slip velocity vectors of the rolling elements during service [159]. Chapter 4 contains evidence of kinematic marks in aircraft engine location bearings. These features are not caused by the Hertzian contact stress distribution traditionally cited in RCF failures, but instead they result from sliding damage at the contact surface. Some of the other unique modes of surface damage associated with bearing tribology are listed below:

- wear involves the removal of material by plastic deformation and is often expressed quantitatively through the volume of material lost [28];
- scuffing or smearing damage describes the process of material transfer between one component to another by adhesion [136];
- corrosion and oxidation of the component surfaces may occur with lubricant breakdown or contamination [160];
- tribofilms are sometimes created by lubricant or contaminant species altering the surface chemistry [161];
- heating in the absence of lubrication may rapidly elevate the surface temperature and lead to transformations or hot-corrosion [134];
- fretting is a damage mechanism caused by vibrations in misaligned components where clearances are imprecise [162];
- brinelling occurs when static loads in stationary bearings create plastic impressions on the surface and dimensional distortion [163];
- pitting of the surface appears as small, superficial imperfections but these can worsen and progress towards spalling [27].

The damage modes listed above may occur independently or simultaneously with the subsurface effects of the maximum shear stress [Section 2.1.2]. Many can be prevented by ensuring adequate bearing design to eliminate misalignment or lubrication failure. In most cases the material properties have been carefully chosen to limit these detrimental effects of surface tribology. Suitable hardness at the contact surface prevents wear and smearing damage, which is exacerbated by having dissimilar materials in contact with vastly different moduli or solubility. The surface chemistry is tailored during heat treatment and special coatings may be applied to prevent corrosion or excessive friction and heat generation.

M50 bearing steel is highly susceptible to corrosion [164]. Mohn et al. (1984) reported that corrosion was the most significant cause of bearing rejection in aircraft gas-turbine engines that failed to reach their fatigue capabilities [49]. Environmental contamination of the bearing assembly from dust, sand or salt-water will greatly reduce steel performance so maintaining appropriate bearing seals to prevent the intrusion of foreign particles and chemicals is essential. Lubrication is continually filtered to clean and remove the largest contaminants. In the harshest environments, where improved corrosion resistance is desired, metallurgists may turn to high-chromium concentration stainless steels such as 440-C [61] or Cronidur-30 [52]. It is also possible to modify existing M50 bearing steel through ion implantation of charged Cr^+ and Ta^+ ions to improve its resistance to salt-water corrosion [165, 166].

Hager et al. (2011) performed non-lubricated rolling contact testing of M50 steel, reporting adhesive wear and the formation of an FeO oxidation layer at the surface [160]. Characterising the wear performance of bearing steels is arguably just as important as fatigue testing [167], particularly given the high-speed conditions of aircraft engine operation. Wang et al. (2012) examined the tribological performance of M50 steel at different slide-roll ratios, finding adhesive wear, material transfer, severe oxidation and eventual spalling failure with increased sliding shear. There was also a transformed white etching layer formed under heating of the damaged surfaces and a shallow region of grain refinement [168]. Chapter 4 contains evidence of a deformed surface layer created by sliding damage during aircraft bearing service.

2.2.1 Surface Condition

Manufacturing smooth bearing components with a high degree of surface finish is crucial in preventing stress concentrations and metal-on-metal contact between asperities. Minimising roughness at the surfaces of M50 bearing steel components leads to improvements in the operational life of this alloy under RCF [169]. Controlling surface topography is therefore an important consideration during bearing design and should include both the general height profile and any localised features displayed. Grinding defects or scratches represent isolated examples of surface inhomogeneity, and whilst large bumps or depressions at the component surfaces can be avoided through careful machining techniques, there will always be some degree of disorder at a free surface [170].

It is important to be able to characterise the topography of a surface quantitatively and there are a number of parameters used for this description. Surface roughness is typically defined using a summation expression for the average height deviation over a discretized line across a surface. The most common definitions used in the bearings industry are the mean centreline average R_a roughness, and the root mean squared R_q roughness:

$$R_a = \frac{1}{N}\sum_{i=1}^{N}|Z_i| \tag{2.7}$$

$$R_q = \sqrt{\frac{1}{N}\sum_{i=1}^{N}Z_i^2} \tag{2.8}$$

Where N is the total number of measurements made along a test line of desired length, and Z is the height at each position along that line relative to the mean height. The real surface is continuous so by measuring discrete heights along a line of fixed length we may lose detail. The resolution is limited by both the accuracy of the measuring technique adopted and also the number of discrete measurements taken along the line. By taking the statistical average height deviation certain information about the nature of the surface may be lost. Figure 2.14 shows two topographical profiles which may give the same R_a value despite being quite different in character. Additional parameters are sometimes used in conjunction with surface roughness to describe the long range waviness R_w, skewness R_{sk}, and maximum peak heights R_t, which are equally important [171, 117]. The length of the test line should ideally be long, and multiple different regions should be measured to give statistically reliable height averages over the entire surface profile.

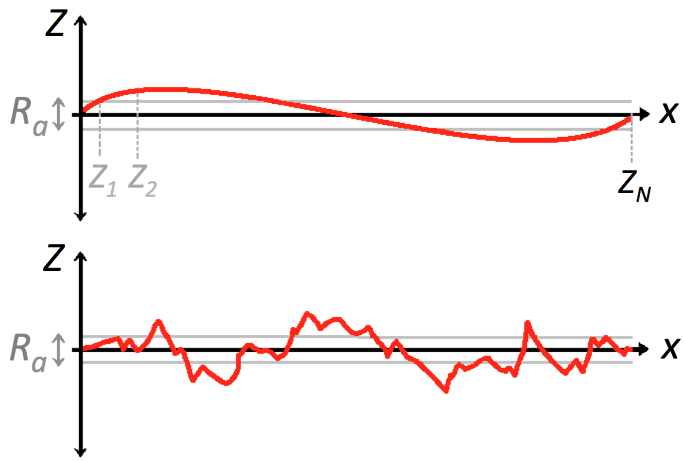

Figure 2.14: Line scan profiles for two surfaces, both having the same R_a roughness value despite apparent height differences.

The two parameters defined in Eq. 2.7 and 2.8 differ in their response to extreme values and outliers. The R_a roughness averages out the random asperities and anomalous data points, muting their effect, whereas the R_q roughness squares these values, amplifying their effect. It is therefore common for the R_q value of a surface to be larger than R_a for that same surface; approximately $R_q = 1.25\, R_a$ is quoted [139]. Figure 2.15 gives an example of this discrepancy for an M50 raceway surface [115]. Given that the R_q value is more sensitive to surface asperities it is perhaps more relevant to RCF [117], and is used as an input parameter for describing the lubrication conditions in bearings [Section 2.2.2]. Chapter 6 contains an investigation into the effects of surface roughness on aircraft-grade bearing steels under RCF laboratory testing.

Manufacturers may seek to define a maximum defect size on the surface of new components using the various parameters such as maximum peak height value R_t. Rolls-Royce require that new bearing balls and raceways entering aircraft engine service should not exceed $R_a = 0.05\ \mu\text{m}$, and similar values are quoted elsewhere [139]. Techniques for measuring the roughness of a finished sample include tracing a physical stylus across the surface whilst attached to a piezoelectric cantilever [119], and non-contact optical methods which exploit the reflection and interference of light [172]. In general,

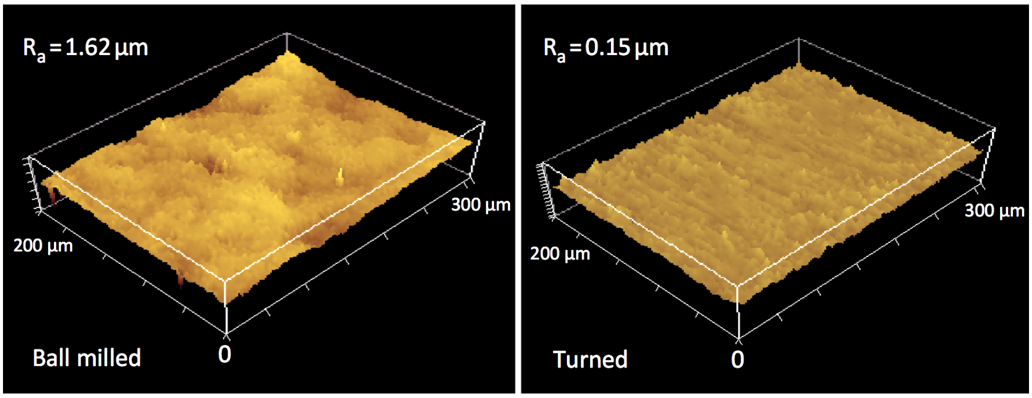

Figure 2.15: Surface topography maps of M50 steel sample rods prepared using ball-milling and turning, as measured using optical interferometry. These data are discussed in Chapter 6.

optical interferometry techniques are faster and examine statistically larger areas [Figure 2.15], but stylus profilometry techniques are better suited for examining localised features. The interferometric techniques have also been successfully applied to lubrication film monitoring as well as surface roughness examination [173]. Obtaining a high degree of surface finish with low R_a will require careful grinding processes after heat treatment such as honing the surfaces. Some procedures will leave residual stresses in the surface that may reduce performance [118, 120], so the integrity of finished surfaces may also need to be controlled [115].

Alanou et al. (2004) found that case-carburised steels superfinished to below $R_a = 0.1$ µm showed significant reductions in friction and heat generation during wear testing [174]. Nelias et al. (1998) performed RCF testing on 52100 and M50 bearing steels at two surface roughness values of $R_a = 0.1$ µm and $R_a = 0.5$ µm. The latter led to more significant surface damage including micro-spalling, with the initiation of spalls occurring at locations of surface defects [154]. Martin et al. (1967) showed multiple examples of fatigue spalls initiated by surface defects such as grinding scratches and indents. Figure 2.16 shows the characteristic V-shaped apex of these surface initiated spalls which allows failure analysts to trace the damage back to the source [22]. Chapter 3 contains evidence of a surface initiated fatigue spall at a dent on an M50 roller race.

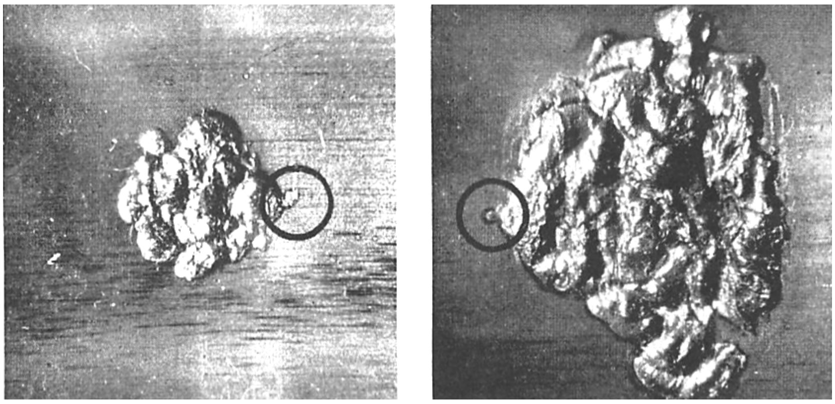

Figure 2.16: Surface spalls initiated at dents on the contact surface show a clear apex (circled) and subsequent damage spreading outward from this location in a V-shape. At ×30 magnification, after [22].

A number of authors have sought to investigate surface fatigue behaviour in bearing steels by creating artificial indents in the contact region and observing their effects under RCF [29]. Cheng et al. (1994) reported the most detrimental surface indents for encouraging failure were those that were sharply angled, deep with high edges, and ran transversely to the rolling-sliding direction [175]. Figure 2.17 shows examples of surface damage initiating at artificial indentations. Mota et al. (2008) combined modelling of indents with experimental testing to show that the edges of indents are the most highly stressed regions where cracks will initiate [176]. Similar observations by Arakere et al. (2010) on spall propagation in M50 and M50NiL steel raceways found the most significant stresses were located at the spall edges where ball impacts spread damage in the rolling direction [177].

Defects at the contact surface can also cause detrimental effects on the lubrication conditions. Indents provide reservoirs for the lubricant to pool within causing localised starvation in the surrounding contact area. Jackson et al. (1974), found that artificially roughened surfaces with asperities reduced the overall thickness of the lubricant film and caused local depletion of lubrication and traction at the edges of defects [173]. Excessive surface roughness therefore necessitates additional lubricant in order to maintain adequate separation between meeting components, so ideal elastohydrodynamic lubrication conditions will be harder to maintain without smooth bearing components. Chapter 6 contains an investigation of surface roughness, including the profiling of new M50 bearing balls displaying machining scratches.

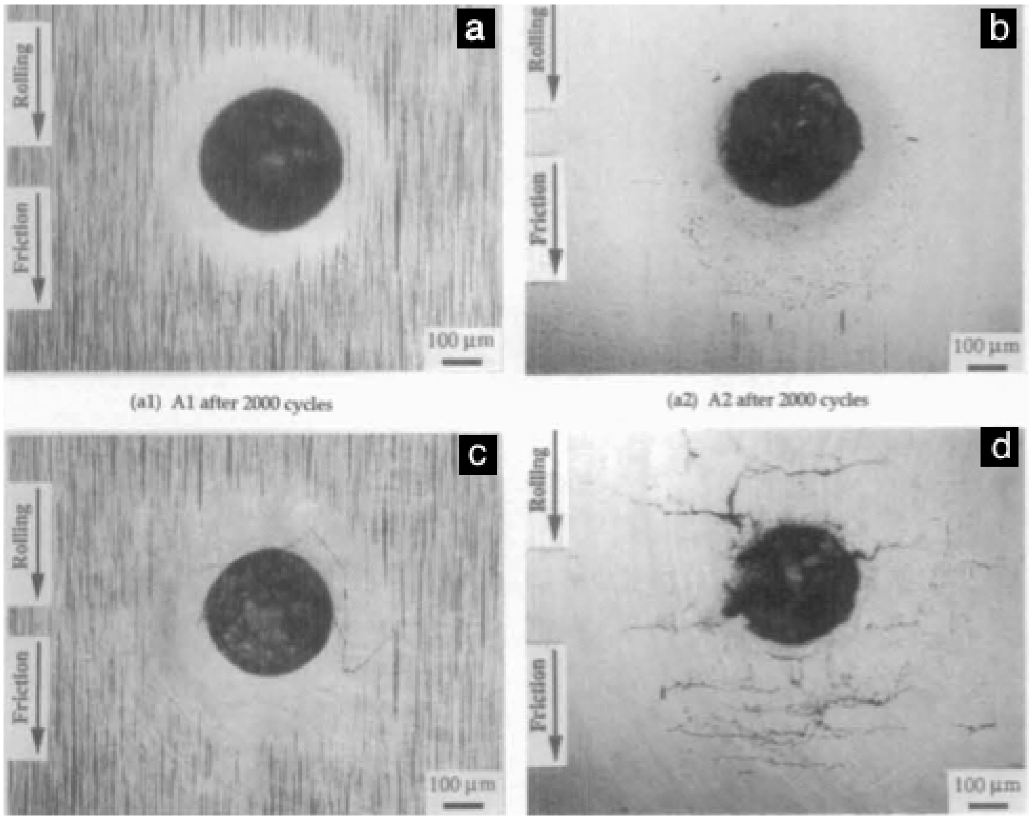

Figure 2.17: Artificial indentations on 52100 steel raceways tested under RCF loading at 2.44 GPa. Surface damage has initiated at the edges of these defects after (a-b) 2,000 cycles, and (c-d) 15,000 cycles. After [178].

2.2.2 Lubrication

The properties of lubricants chosen for aircraft gas-turbine engine bearings must be appropriate for operation at elevated temperatures up to 260°C [179]. It is essential that the flashpoint of oil-based fluids is well above the normal operating temperature to ensure thermal stability and prevent their accidental combustion within the bearing system which would be highly damaging. The viscosity of a fluid describes its resistance to shear stresses provided by the internal frictional forces between molecules passing one another. The viscosity at operating temperatures and the quantity of lubricant available will determine its ability to provide EHD lubrication and improve rolling contact performance. Other parameters important in the choice of lubricants include the pour point at low temperatures, chemical inertness and oxidation prevention capabilities [72].

Ester-based lubricants are a popular choice for aircraft bearings: military-grade, aviation oils, such as MIL-L-23699, are often used to separate M50 bearing steels [162, 179]. This lubricant has a typical viscosity of 4.93 cSt at 100°C [180]. Other engine oils appropriate for aeroengines include Castrol 580 [181], MIL-L-87100 [182] and the tricresyl-phosphate-based EXXON Turbo 2380, which contains anti-wear additives [161]. These lubricants are directly fed into the location bearings through small oil ducts made between the split inner raceway [Figure 1.4]. The oil flow rate into the bearing assembly may be adjusted depending on bearing rotation speed to control the flow of lubricant during the variable stages of the aircraft flight cycle. Maintaining a constant lubricant film between the steel components is essential for ideal EHD conditions, so the volume of lubricant available and thickness of the resulting oil film must be considered [183]. Figure 2.18 shows examples of an optical interferometry technique used to calculate the lubricant film thickness between a ball bearing and a flat glass plate. The degree of lubricant starvation can be deduced based upon the interference fringes [173].

Hamrock and Dowson (1976) formulated a quantitative expression to define the lubricant film thickness h_{min} between loaded components in elliptical rolling contact, according to:

$$h_{min} = 3.63U^{0.68}G^{0.49}W^{-0.073}(1 - e^{-0.68k}) \tag{2.9}$$

where U, G and W are dimensionless speed, material and loading parameters respectively [184]. k is the ratio of the semi-major axis b to the semi-minor axis a in the contact ellipse under Hertzian conditions. Calculation of the lubricant film thickness using Equation 2.9 has proved applicable to a wide range of engineering systems [185].

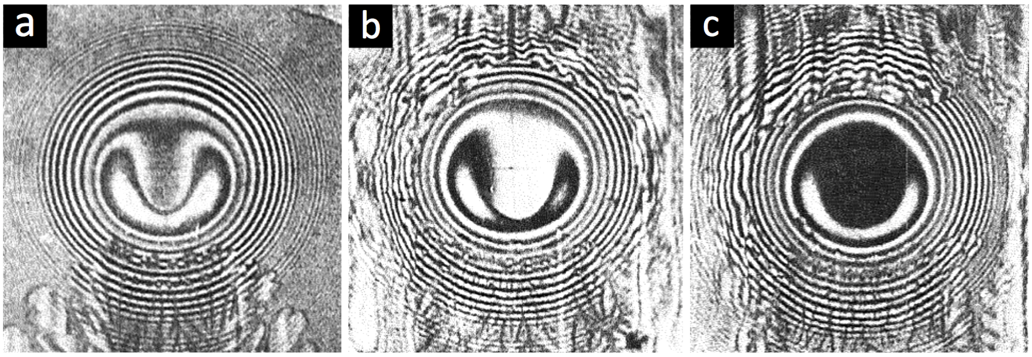

Figure 2.18: Oil film thickness between a ball bearing and a glass plate showing progressive depletion of lubricant (starvation) from (a-c). After [183].

Oil-based lubricants are non-compressive meaning the contact loads are transmitted directly through the lubricant film with no damping. These EHD conditions are only provided when surfaces are fully separated, avoiding tangential shear stresses. This is not always the case in real bearing systems, particularly for low levels of lubrication and in the presence of surface defects or excessive roughness [Figure 2.18]. The severity of sliding and frictional forces in the contact ellipse will depend upon the composite effect of both surface roughness and lubricant film thickness. Bearing designers often combine these two properties together in defining an empirical lubricant film parameter, λ, according to:

$$\lambda = \frac{h_{min}}{\sqrt{(R_{q1})^2 + (R_{q2})^2}} \tag{2.10}$$

where λ is a dimensionless parameter combining the lubricant film thickness, h_{min}, and the composite roughness, R_q, for the two surfaces in contact [139]. The use of λ values in bearing tribology is industry-wide and helps in defining the different friction regimes of bearing operation. At low values of λ, the lubrication conditions are poor and surface roughness may be significant, but for high λ values the fully-lubricated bearing behaves as an ideal EHD system [156].

The Stribeck curve describes the relationship between λ and the frictional forces experienced within the contact zone [186]. Figure 2.19 shows the Stribeck curve over a range of lambda values and their resulting friction regimes, where the friction coefficient is the ratio of kinetic friction to the normal force.

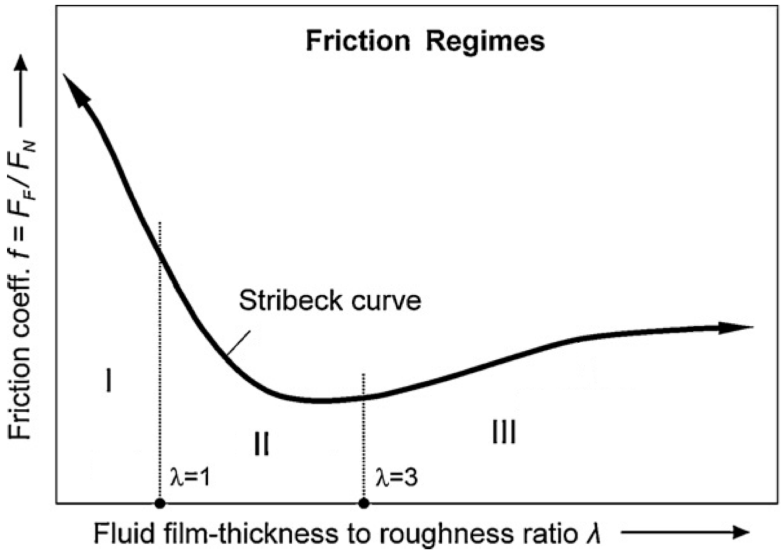

Figure 2.19: The relationship between the lubricant film parameter λ and the coefficient of friction, given as the ratio of kinetic friction F_F, to the normal force F_N. After [186].

The three friction regimes, as identified in the Stribeck curve in Figure 2.19 can be categorised as follows [134]:

- $\lambda < 1$
  Boundary lubrication conditions with an inadequately thin film of lubricant where surfaces make direct contact due to excessive roughness and penetration of lubricant film, producing large frictional forces.

- $1 > \lambda < 3$
  Mixed lubrication regime with only occasional metal-on-metal contact due to large asperities, but full-film separation conditions are typically met and surface friction is minimised.

- $\lambda > 3$
  Fully flooded lubrication conditions such that no metal-on-metal con-

tact occurs. Here the frictional drag of lubricant viscosity may begin to affect operational speed and efficiency.

At low lambda values where $\lambda < 1$, there is inadequate lubricant film thickness h_{min} to prevent asperity contact, causing high levels of tangential shear at the surface [Figure 2.19]. Trivedi et al. (1995) found the RCF life of M50 bearing steel was systematically reduced by testing in this lowest lubrication regime, despite trying a range of different lubricants [180]. Under starved lubrication conditions, plastic deformation and smearing of bearing steel surfaces occurs, although M50 has been shown to suffer less than 52100 [187]. Most aircraft gas-turbine engine bearings are designed to operate in the mixed lubrication regime, for example where $\lambda = 1.4$. Under these conditions the EHL assumption is appropriate and Hertzian contact stress calculations make for a good approximation of RCF. Figure 2.19 shows that frictional forces reach an absolute minimum when $\lambda = 2$, but then increase once again as $\lambda > 3$, due to the inefficiency of excessive lubricant causing viscous drag. Therefore, there appears to be an ideal region of the Stribeck curve to design for which offers the most desirable surface tribology for bearing performance.

The negative effects of low λ bearing operation go beyond the increase in friction at the contact surface. Insufficient lubricant reduces the ability to flush away debris contaminants and also limits the cooling effect on components necessary for temperature regulation. Flourous et al. (2006) examined the heat generated in lubricated Rolls-Royce aircraft engine bearings. The authors showed that the position of oil inlets at the inner raceway and the oil feed direction relative to the rolling direction had a significant influence on limiting temperature increases during operation [72]. Bohmer et al. (1999) tested the thermal stability of M50 and M50NiL steels using pre-heated lubricant, observing a steady decrease in their fatigue properties with increasing oil temperatures approaching 200°C [5].

Contamination of the lubricant from environmental debris may lead to surface damage by abrasive wear or indentation of foreign particles [152]. Contaminated lubricants are a major cause of aeroengine bearing failures and can directly reduce the fatigue life of aircraft bearing steels [33]. Modern bearing systems in aircraft gas-turbine engines constantly recycle and filter the lubricant to quickly remove debris, but an insufficient film of oil will reduce the ability to flush away debris from between the component surfaces.

Magnetic plates pick up ferromagnetic debris during oil recirculation to detect spalling damage and the lubricant is passed through a filter screen which catches other particulates greater than 200 μm in size [179]. During recirculation the oil may also be passed through an intercooler to remove excess heat.

Hager at al. (2011) found that a greater quantity of lubrication was needed for M50 bearings operating with a higher slide-to-roll ratio: An increase in sliding from 5% to 45% led to accelerated oil depletion [160]. Some authors have investigated novel ways to reduce the effect of lubricant starvation during engine operation by introducing artificial textures at the contact surfaces. Krupka et al. (2007) showed that a shallow array of indents at the raceway surface can actually serve as beneficial reservoirs for lubricant, providing a local increase in lubricant film thickness and reducing asperity interactions, so long as the indents remain spherical and below 4 μm [188]. The direction of these artificial surface topographies with respect to the rolling-sliding direction is also an important factor in determining their influence on RCF, as has been reported by others [178, 175]. Nelias et al. (1998) reported that the friction direction during sliding is the dominant driving force for surface fatigue failures, not the rolling direction, when investigating the tribological behaviour of M50 bearing steel under RCF. When $\lambda < 1$, the occurrence of surface damage is dependent on sliding and seemingly less affected by the contact pressure, producing similar damage at 1.5 GPa and 3.5 GPa respectively [154].

In the presence of defects or pre-existing cracks at the contact surface the lubricant will penetrate into these cavities under hydrostatic pressure. This effect can accelerate damage by forcing open cracks and encouraging their propagation [176]. Littman (1970) discusses this propagation of spalls under hydraulic pressure, claiming that low lubricant viscosity or low revolution speeds promote this behaviour [134]. Lubricants may also transport chemical species deep into the crack, and in this way encourage oxidation or hydrogen embrittlement. Chapter 3 contains evidence of lubricant penetration within a fatigue crack found on an M50 bearing ball.

2.3 Fatigue Life Methods

Bearing failures due to spalling are undesirable and difficult to accurately predict using traditional fracture mechanics. The behaviour of engineering components containing local stress concentrations is a well established research area in materials science, however there are problems with extending traditional fatigue testing to the description of bearings under rolling contact fatigue. The multi-axial stress distribution unique to RCF is complex and not well-replicated by the uniaxial stress conditions used in standardised fatigue tests [34]. The maximum shear stress in the bearing subsurface encourages microstructural evolution and these phenomena are not accounted for in static fatigue models. Despite these inadequacies, resistance to crack growth is a vital property in bearing steels for which traditional fatigue tests prove insightful.

The myriad damage mechanisms in bearing steels under RCF compete to cause unexpected fatigue failures that are highly scattered. The fatigue lives of individual samples are not reproducible and do not lead to a well-defined fatigue life for a population [52]. Instead, bearing lives seem to follow a Weibull distribution that is probabilistic in nature and engineers make use of reliability factors for the safe design of bearing steels. Life estimates require extensive laboratory testing in bespoke RCF test rigs, followed by statistical analysis of the failure data for large populations of identical bearings. Chapter 6 contains rolling contact test rig experiments on aircraft bearing steel test pieces.

2.3.1 Fracture Mechanics

Uniaxial fatigue testing is a foundation of fracture mechanics that is regularly used to reliably estimate the life of a component under an oscillating stress [189]. The early work of Griffith (1921) on the rupture of solids containing pre-existing defects [190], and later work by Paris and Erdogan (1962) on fatigue crack growth [191], continue to provide engineers with a reliable framework for designing against failure.

The fracture toughness and fatigue crack propagation rates in M50 and M50NiL bearing steels were investigated by Averbach et al. (1985). Using compact tension specimens, the stress concentration at a man-made notch cut perpendicular to the uniaxial tensile stress axis encourages fatigue crack growth under so-called mode I opening stress conditions. As the applied stress is increased, the stress intensity K at the crack tip reaches a critical value K_{IC} at which fracture of the specimen occurs, according to:

$$K_{IC} = \sigma_F \sqrt{\pi\, a_{crit}} \tag{2.11}$$

where σ_F is the stress at fracture for a critical crack length a_{crit}. (Note, in compact tension experiments Equation 2.11 will have additional parameters to account for the dimensions of the specimens). For M50, the fracture toughness $K_{IC} = 23\,\mathrm{MPa\,m^{1/2}}$, but for the low carbon M50NiL $K_{IC} = 51\,\mathrm{MPa\,m^{1/2}}$ [63]. The non-carburised M50NiL material showed a toughness value double that of M50, meaning that a crack would have to grow to a larger length before fracture. Table 1.4 contains the fracture toughness data for these aircraft bearing steels as well as some of their other mechanical properties, such as yield strength. Given these parameters, Equation 2.11 can now be rearranged to find the critical size of a crack which causes plastic yielding and failure in our steels, according to:

$$a_{crit} = \frac{K_{IC}^2}{\pi \sigma_y^2} \tag{2.12}$$

Substituting values for the yield strength, σ_y, and fracture toughness, K_{IC}, into Equation 2.12 gives estimates for the critical crack size in M50NiL core material of 590 µm but in M50 only 37 µm. This approach shows the increased tolerance of M50NiL to sizeable defects compared with M50, and is one way in which fracture mechanics can be applied to bearing design [192]. Failures in bearing steels can still occur at applied stresses that are below the yield stress, however, through the process of fatigue. Paris and Erdogan (1962) formulated a powerful fatigue law under the assumption that pre-existing flaws are always present in a material but are only fatal upon growing to a critical size a_{crit} [191]. The growth of fatigue cracks in aircraft bearing steels under the action of cyclic stress have been examined by many authors [63, 64, 65]. An oscillating stress range, $\Delta\sigma = \sigma_{max} - \sigma_{min}$, is fundamental in fatigue mechanisms. This alternating stress may be concentrated at a crack tip producing a stress intensity range, $\Delta\, K$, which encourages fatigue crack growth in small increments of length, da, per stress cycle, dN, according to:

$$\frac{da}{dN} = A\Delta K^m \tag{2.13}$$

Where the crack growth rate is proportional to the applied stress through $\Delta\, K$ from Equation 2.11. The material exponents A and m can be evaluated by measuring the crack growth and plotting these data against the stress intensity on a logarithmic scale. Figure 2.20 shows fatigue crack propagation curves for M50 and M50NiL bearing steels. Averbach et al. (1985)

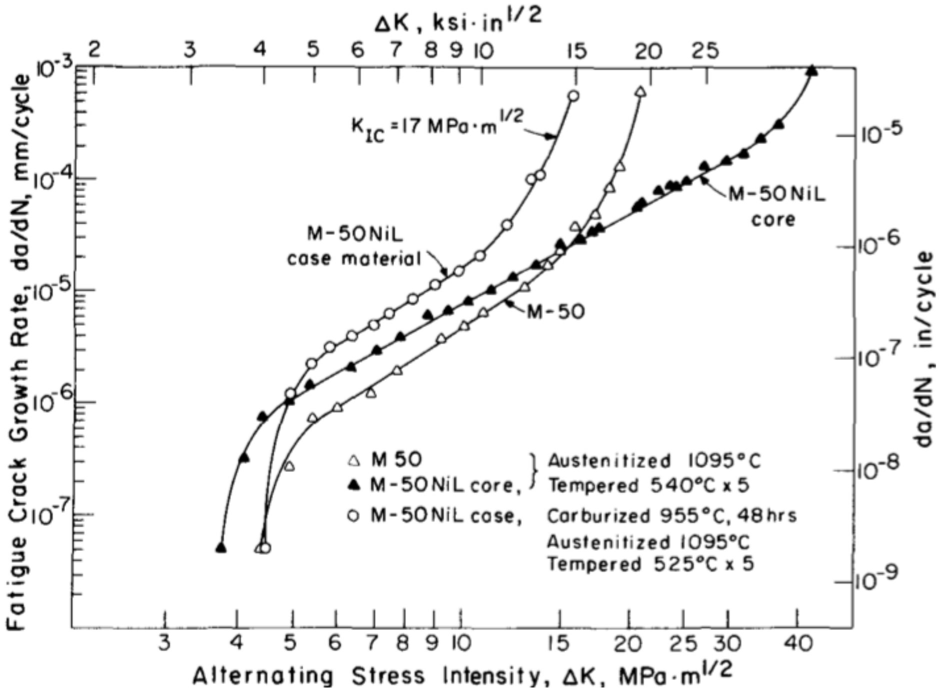

Figure 2.20: Fatigue crack growth rates in aircraft bearing steels under an alternating stress cycling at 50 Hz with stress ratio $\sigma_{min}/\sigma_{max} = 0.1$. After [63].

found the rate of fatigue crack growth in M50NiL core material was slower than for through-hardened M50, as indicated by the shallower gradient m

of the fatigue curve [Figure 2.20]. Thanks to the increased carbon content, the case-carburised M50NiL test pieces showed more rapid crack propagation than the core material. Averbach and Lou (1984) investigated fatigue crack propagation behaviour as a function of case depth in carburised M50NiL. Figure 2.21 shows the rate of crack growth is significantly inhibited by the compressive residual stresses present in the case [107]. The stress intensity factor at the crack tip is actively reduced due to crack closure effects and an effective reduction in the applied stress local to the crack tip [64].

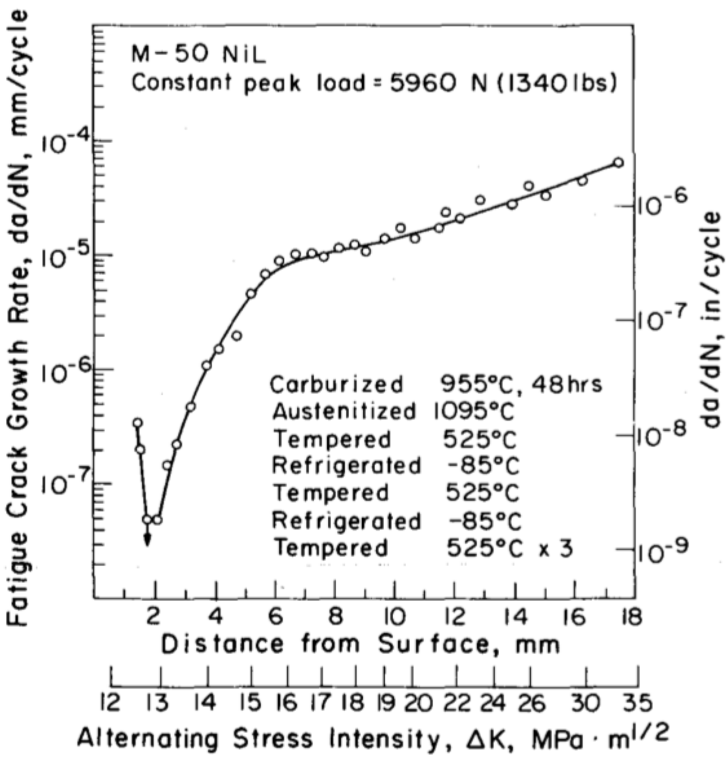

Figure 2.21: Fatigue crack growth rates as a function of depth in case-carburised M50NiL bearing steel under alternating stress cycling. After [63].

Whilst the fracture toughness and defect tolerance of carburised M50NiL has been celebrated, some properties of through-hardened M50 are less desirable. Iqbal and King (1990) examined the fatigue crack propagation behaviour of a number of high-speed bearing steels, finding the highest crack growth rates in M50 samples. The steepest propagation gradient m of all the steels investigated was shown in M50 and crack growth was often intergranular [65]. This sensitivity to stress raising defects in M50 highlights the risk posed by non-metallic inclusions and hence underlines why clean steel production routes have led to improved fatigue life [8]. Prevention of fatigue crack growth in damage tolerant design requires limiting the applied stress range ΔK to below the threshold for propagation $\Delta\, K_{th}$, left of the growth curves [Figure 2.20]. This will be easier to achieve with beneficial compressive stresses, but the crack growth curves are also highly sensitive to the specific loading conditions. The waveform of the oscillating stress can be varied in amplitude, frequency and the ratio of maximum to minimum tensile stress, R, according to:

$$R = \frac{\sigma_{min}}{\sigma_{max}} \tag{2.14}$$

The stress ratio R can take different values between -1 and 1 where $\sigma_{min/max}$ are positive for a tensile stress and negative in compression. For example, $R > 0$ represents a fully tensile stress cycle and $R < 0$ represents an alternating compressive-tensile stress. In general, -R reduces the fatigue performance of steels, as an alternating stress lowers ΔK_{th}, shifting the crack propagation curves to the left [64]. It was the alternating character of the orthogonal shear stress cited by Lundberg and Palmgren (1943) as the most critical factor in developing RCF damage [12] [Section 2.1.1]. Unfortunately the mode I opening stress usually assumed during fracture mechanics does not apply to shear stress (mode II or III), and the multiaxial stress distribution of RCF is not well-replicated by uniaxial stress cycling.

Some authors have made attempts to adapt the Paris laws of fatigue to bearing steels under rolling contact [25]. Eryu et al. (1988) measured crack growth during RCF testing on a specially adapted test rig: the experiments showed three distinct stages of fatigue, with the majority of cycles taking place in the second stage of steady crack propagation [193], (analogous to the three-stage Voskamp model [74]). The authors also comment on the appearance of multiple crack fronts which combine into crack networks under the mode II shear stress of RCF, rather than the single linear crack of mode I tensile tests [193]. A fracture mechanics approach has also been applied to the growth of fatigue spalls after initiation. Rosado et al. (2009) measured the amount of material lost per stress cycle during spall propagation for aircraft bearing steels. Figure 2.22 shows that M50NiL displayed the longest spall propagation lives under RCF stress at 2.41 GPa [10].

Integrating Equation 2.13 with respect to crack length a allows predic-

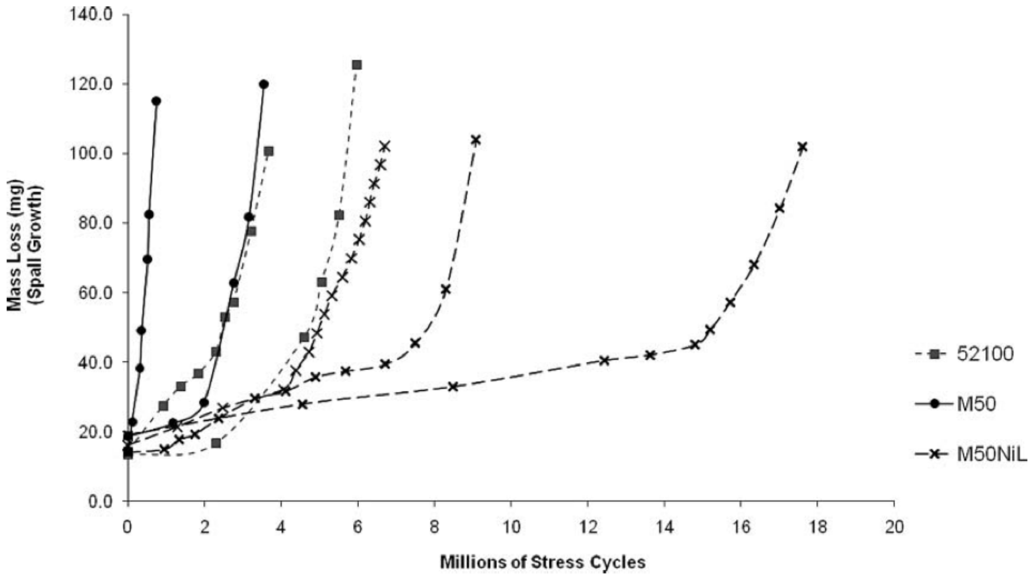

Figure 2.22: Spall propagation data during ball bearing testing at a contact stress of 2.41 GPa. After [10].

tion of the number of propagation cycles, N, before failure and hence offers an approximate estimate for the fatigue life. If bearing failures were only caused by fatigue crack propagation from critical defects then this approach using standard fracture mechanics might be acceptable [11]. However, there are many competing damage mechanisms in the stressed volume beneath the contact surface of bearings which make deterministic approaches unsuitable. Probabilistic approaches to bearing fatigue are more popular. These make use of empirical equations based upon statistical analysis of failure data rather than design rules based on fracture mechanics.

2.3.2 Endurance Testing

In the interests of safety, engineers may look for ways to predict the fatigue life of structural components like rolling bearings. Sustained fatigue testing of steel samples until their eventual failure allows the construction of total life curves which plot the number of cycles to failure N_f at a given stress range. Endurance testing of materials to obtain these so-called S-N curves is often time consuming and may require a very large number of cycles before failure occurs. Figure 2.23 shows a model S-N curve for a mild steel constructed using a small number of data points.

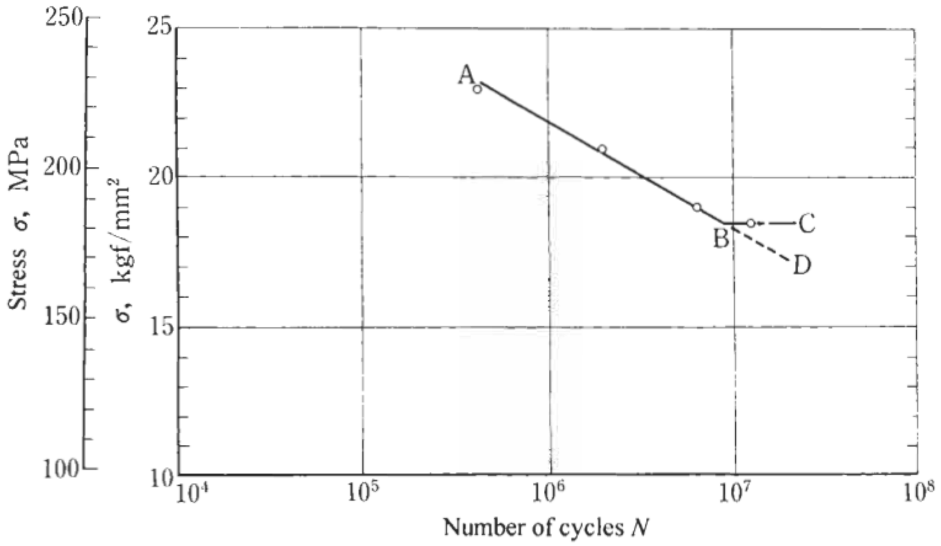

Figure 2.23: S-N curves for a mild steel under uniaxial tension, showing failure data for a given stress σ. Point A indicates early failure at high stress, Point B later failure at a lower stress, Point C is unfailed at the fatigue limit, and Point D shows no fatigue limiting stress. After [11].

Operation beneath the total life curves provides a safe design stress for materials to operate at over an estimated number of cycles. Engineers typically make use of S-N curves like the one in Figure 2.23 by implementing a design offset curve, parallel to and beneath the failure curve, which allows for the presence of defects and other local stress intensity factors. A common criterion for the design offset is 2/3 lower than the failure curve, but this can often be overly conservative.

In some cases the test material will not fail at low stress values where the

S-N curves level out, reaching a hypothetically infinite number of fatigue cycles. This fatigue limit is the threshold stress below which the material remains stable and could operate indefinitely without ever reaching failure. In Figure 2.23 the data point labelled C has an arrow indicating the sample did not fail but was only discontinued after a high number of cycles upon reaching the fatigue limit at B. Label D on the curve indicates the behaviour of a material that does not show a fatigue limiting stress.

Since classical fatigue tests do not suitably replicate the shear stresses experienced in bearings, special rolling contact test rigs have been designed over the years to better recreate RCF effects [194]. Blau (1992) catalogues a number of laboratory-based RCF test rigs and summarises their various approaches [195]. The general theme of all the different rigs is that a cyclical contact stress is developed between rolling components under load and the test conditions can be carefully controlled to limit the large number of variables that operate during RCF. The temperature of operation, rotational speed, lubrication conditions and rolling to sliding ratio may all be controlled as necessary, and their individual effects on fatigue life can then be extrapolated. Figure 2.24 shows cross-sectional diagrams of a particular RCF test rig designed with a three ball-on-rod configuration. The cylindrical rod in

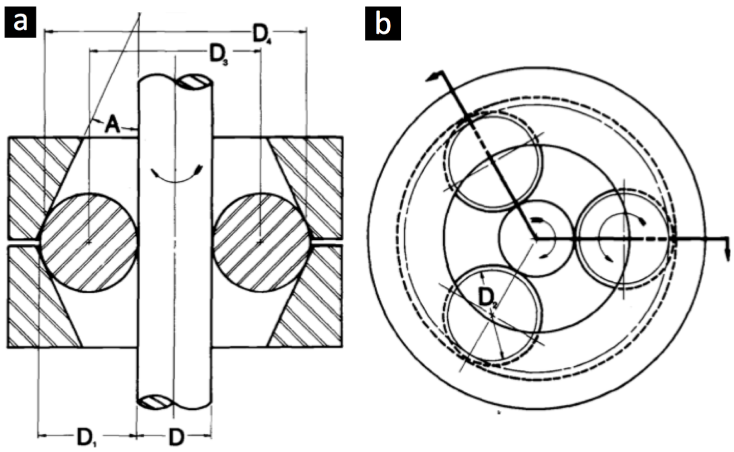

Figure 2.24: Schematic cross-sections of a three ball-on-rod RCF test rig, from the side (a) and from above (b). The diameters, D, and contact angles, A, of the components are labelled. After [196].

the centre of Figure 2.24 a is the test material which is rotated by an electrical motor gripping it from one end [196]. The three surrounding balls are compressed against the rod by the outer raceway cups which are loaded using three coiled springs. Tightening the springs adjusts the loading conditions and hence the contact stress experienced by balls on the rotating test rod. Chapter 6 contains fatigue experiments using this particular RCF test rig configuration.

The careful measurement of fatigue crack propagation rates is less achievable in RCF test rigs due to more complicated geometries so they are principally used for endurance testing. Test pieces are rotated for millions of stress cycles until failure occurs and total life curves can be compiled similar to Figure 2.23. Unfortunately, RCF failures behave unpredictably and total life data is highly scattered for rolling bearings, showing poor repeatability [141]. The resulting S-N curves lack clarity and extrapolation of a safe life or fatigue limit from them is unsuitable [197]. Instead a probabilistic approach to bearing fatigue life has been favoured in industry, beginning with the early work by Lundberg and Palmgren (1947): Using empirical data on rolling bearing failures the authors defined a relationship relating the probability of component failure L to the alternating shear stress τ_{zy} in a volume [12]. Equation 2.15 shows the probability of bearing survival under rolling contact fatigue:

$$\ln\frac{1}{L} = A\frac{\tau_{zy}^{c}N^{e}}{z^{h}}V \tag{2.15}$$

where L is the probability of survival given the alternating shear stress τ_{zy} acting at depth z in a volume of material V after a number of fatigue cycles N. The empirical constants A, e, h and c can all be obtained after endurance testing and plotting the failure data on probability paper with a logarithmic scale [198]. Figure 2.25 shows Weibull plots for three different bearing steels after full-scale bearing testing at 3.1 GPa contact stress. Each data point indicates an individual sample failure from a population of identical bearings.

The data in Figure 2.25 shows the probability of fatigue failure in standard 52100 bearing steel is sooner than in the aircraft grade steels. (Note, the relatively low M50NiL life in comparison to M50 was due to non-representative damage affecting the experimental data [10]). It is also clear from the Weibull exponents e displayed by the gradients in Figure 2.25 that bearing failures occur over a range of fatigue lives, despite identical test conditions. Engineers can only estimate the percentage of failures likely after a given number

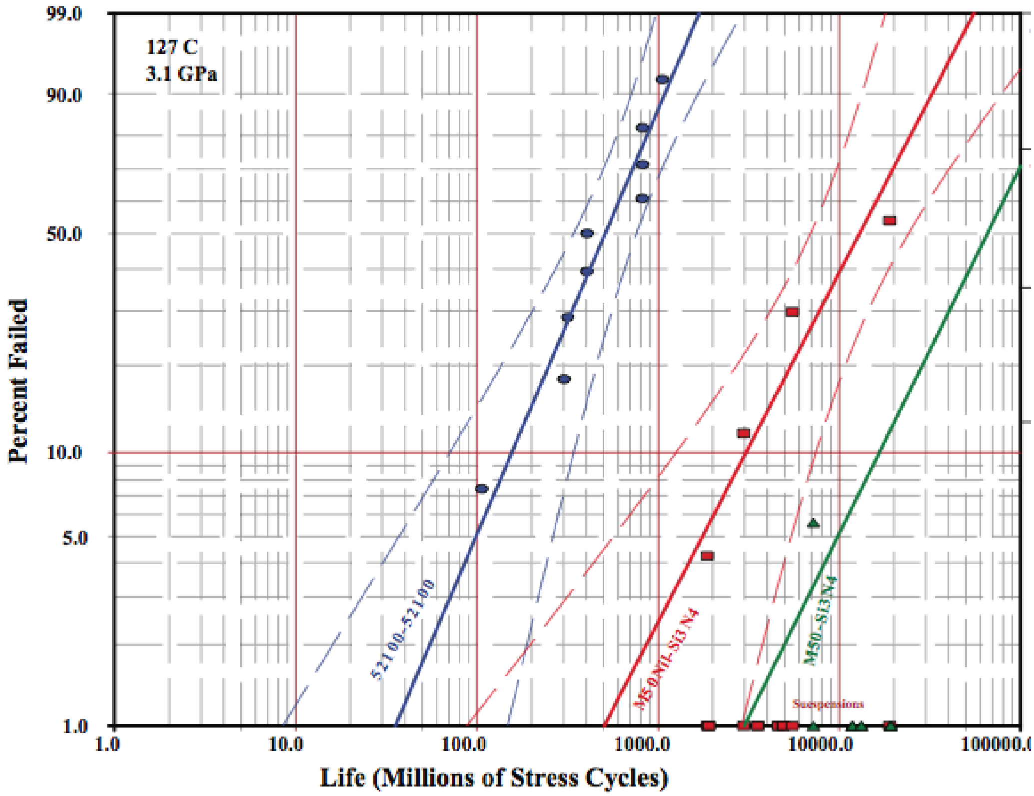

Figure 2.25: The probability of bearing failure through RCF under a contact stress of 3.1 GPa for a number of different bearing steels. Many of the M50 (triangles) and M50NiL (squares) samples survived the testing. After [10].

of fatigue cycles through intersection with the data. The intersect made at 10% failed gives most common life parameter used in the bearings industry, called the L_{10} life, which corresponds to a survival rating of 90% [66]. Equation 2.16 gives the modified L_{10} fatigue life equation, which is a simplified version of the Lundberg-Palmgren equation in Equation 2.15 and has found widespread use in the bearings industry [197]:

$$L_{10} = \frac{C^p}{P} \tag{2.16}$$

where C is the dynamic capacity of the bearing based upon size and geometry, P is the applied load and p is an exponent which equals 3 for ball bearings and 3.3 for roller bearings.

Table 2.1 contains the L_{10} lives of aircraft bearing steels as calculated by Harris (1992). The L_{10} life of M50NiL is found to be more than triple that of M50 [62]. Many authors have built upon the fatigue life theory, incorpo-

Table 2.1: L_{10} fatigue life for two aircraft bearing steels. After [62].

Contact Stress (MPa)	M50 (L_{10} $\times 10^6$ cycles)	M50NiL
1,400	21.5	65.4
2,000	213	789

rating additional modifiers for lubrication and material factors [197, 33], but in essence Equation 2.16 remains the industry standard for estimating the life of a bearing based on experimental data.

Gathering enough failure data to perform statistically reliable fatigue analysis can be time consuming over a large number of cycles. In order to accelerate the process and produce fatigue failures in a shortened timeframe RCF testing is often performed at excessively high contact loads. Accelerated testing is so-called because the high stresses greatly reduce the duration of the test, inducing early fatigue failures for more rapid statistical analysis [194]. Contact stress values in excess of 5 GPa are not uncommon in laboratory testing [196], yet during aircraft service the contact stresses in location bearings would not be expected to exceed 2 GPa [124]. It is conceivable that the failure modes accompanying accelerated testing may not be representative of the more gradual RCF mechanisms encountered under the lower stresses of actual bearing operation. The main purpose of this text is to assess the behaviours of aircraft bearing steels under the representative stresses of gas-turbine engine operation.

There are strict safety guidelines that must be adhered to regarding aircraft engine integrity and that of any critical component whose failure would have wider implications on the remaining engine. Airworthiness directives like those overseen by the European Aviation Standards Authority (EASA) are in place to ensure the safety of engine parts are properly considered, and often this includes demonstration of a minimum life or fatigue limit [199]. Certain standards have also been constructed to target the specific fatigue mechanisms in bearing assemblies and their constituent materials [200, 163]. In industry, the aircraft operators rely upon early detection. Modern bearing housings are fitted with vibration sensing accelerometers and magnetic chip detectors used to notify of spalling and register bearing failure, but only after adequate damage is brought about [110].

Chapter 3

M50 Ball Characterisation

This chapter contains a detailed examination of the rolling element balls from aircraft location bearings. The spherical components are examined at their surfaces for signs of wear and beneath the surface to investigate the general microstructure. Some important carbide behaviours are identified at the contact surface and the fatigue spalls of failed bearing balls are characterised with fractography. Intergranular failure is seen and supported by the supplementary investigation of a spalled M50 roller raceway. The M50NiL raceway material is examined in the following Chapter 4.

Experimental Methods

Rolling elements from Rolls-Royce Trent engine location bearings have been cross-sectioned and examined in the unused condition (0 h), and after various running times approaching 30,000 h [Table 1.2]. The two longest running bearings (29,118 h, and 29,900 h) had both suffered single ball failures. The failed M50 balls were cut free from their bearing cages and their spalls examined using fractography [Section 3.3]. Bearing balls without fatigue spalls were also removed for comparison studies and deeper microstructural investigation. Balls were cross-sectioned using electrode discharge machining (EDM), then ground and polished using progressively finer silicon carbide grinding papers followed by polishing with a 1 μm diamond paste. Marbles reagent was used as an etchant to reveal the residual carbides; a solution comprising 5% copper sulphate to equal parts hydrochloric acid and water. Carbide populations were quantified using optical microscopy and image analysis software. Micro-chemical analyses of residual carbides were performed using energy dispersive X-ray (EDX) spectroscopy on the JEOL 5800LV scanning electron microscope (SEM).

Thin foils were produced from EDM slices of M50 balls by mechanical grinding to a thickness of $< 50\,\mu m$ followed by electropolishing using the twin-jet Struers Tenupol machine. The electrolyte consisted of 5% perchloric acid, 20% glycerol and 75% ethanol held at a temperature of 10°C. Optimal electropolishing settings were achieved at a potential of 24 V with a current of 34 mA, maintained for approximately 100 s per foil. High-resolution imaging was achieved using the JEOL 200CX transmission electron microscope with selected-area diffraction pattern analysis. EDX microanalysis of temper carbides was performed on the FEI Tecnai microscope in scanning transmission electron microscopy (STEM) mode.

X-ray diffraction has been used to identify the phases present in M50 bearing balls, using the Bruker B3 Gen-9 goniometer with a Lynx-Eye position sensitive detector. The Cu Kα source results in an incident photon energy of 8.1 keV. 2θ scans were made between 30° - 96° with a step size of 0.05° and dwell time of 38 s per step. Highscore Plus software was used for data analysis and the spectra intensities were fitted using a Rietveld refinement after appropriate background and defocussing corrections.

3.1 Surface Condition

The surfaces of M50 steel bearing balls after service in aircraft engines display discolouration and scratches visible to the naked eye. Figure 3.1 shows examples of this surface damage, the severity of which appears to correlate with the length of time spent in service. The scratches are mostly randomised, crossing the surface in all directions, but some of the balls show more systematic patterns of damage. Circular scratches are seen which suggest repeated spinning about a preferred axis of rotation [Figure 3.1 a]. Ball spinning is expected under thrust loads but this behaviour should be chaotic, spreading damage evenly across the entire ball surface. Concentrated damage may indicate that rolling elements are not perfectly uniform and instead possess asymmetry, which is known to create these sorts of circular wear patterns [43]. The initiation of a microspall at a surface scratch was observed, displaying a characteristic V-shaped apex which usually indicates the growth direction [Figure 3.1 d].

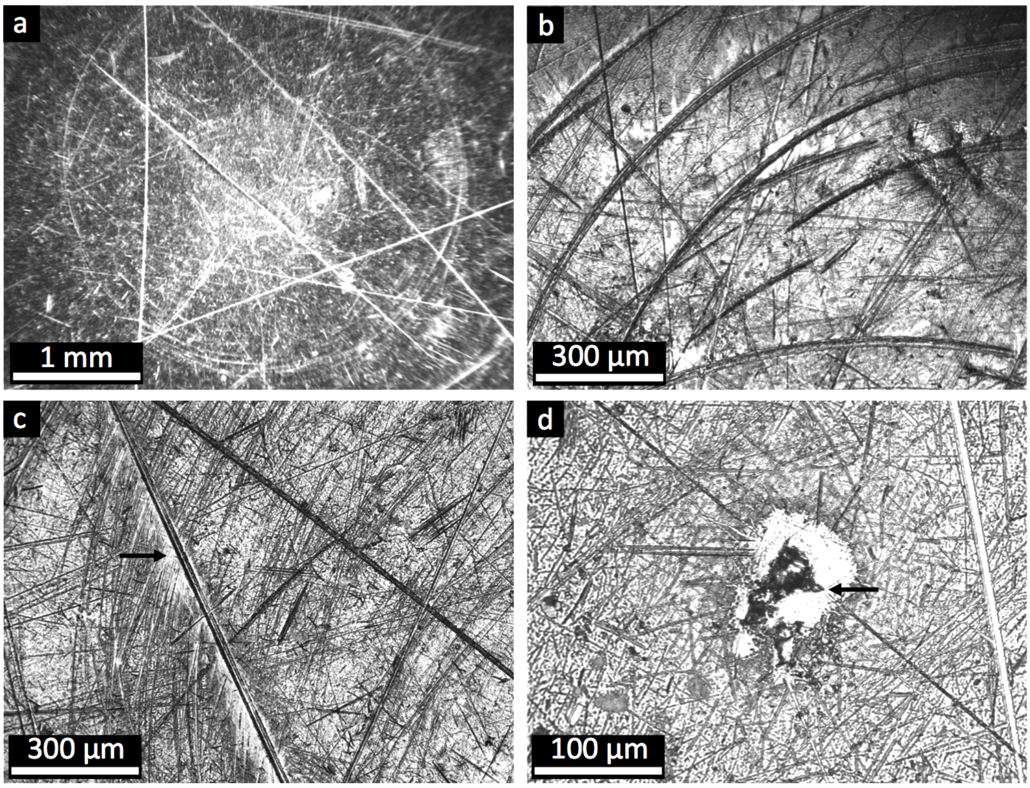

Figure 3.1: a) Circular scratches on bearing balls after 30,000 h service. b) Deep scratches and dents cover the surface. c) Plastic deformation occurs at the edges of deep scratches (indicated). (d) Microspall with deformed edges initiated at a scratch (indicated).

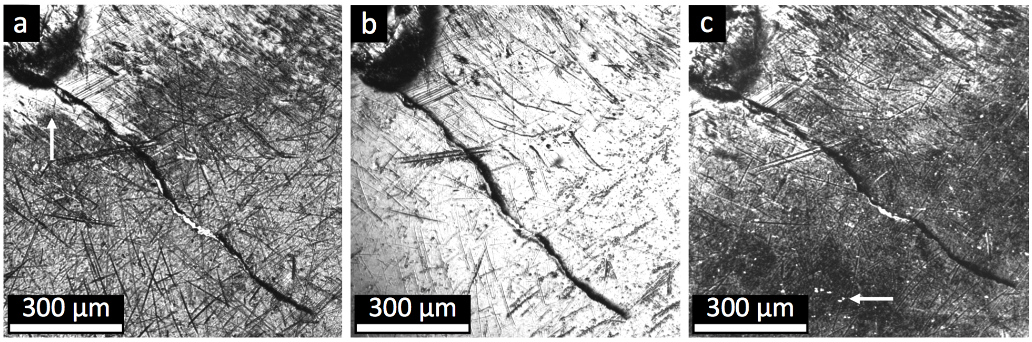

Figure 3.2: a) Deformed material appears polished in contrast to the general discolouration (indicated). (b) Etching with nital completely removes the discoloured layer. (c) Etching with marbles reagent darkens the matrix revealing residual carbides (indicated).

Plastic deformation is seen at the edges of microspalls and deep scratches [Figure 3.1 d]. The polished appearance of deformed regions differs from the general discolouration of the ball surfaces. Cleaning the ex-service balls with ethanol has no effect on the discoloured appearance but use of a nital etchant completely removes the discolouration, suggestive of an oxidised layer [160], or tribofilm [161]. Figure 3.2 shows the effects of chemical etchants on M50 steel surfaces. Etching with marbles reagent is extremely effective at darkening the matrix and revealing bright residual carbides in contrast, even on the worn surfaces ex-service balls [Figure 3.2 c]. The large carbides are inhomogeneously distributed and appear to align themselves in common directions. Figure 3.3 shows aligned residual carbides at the surfaces of an unused bearing ball (0 h) and an ex-service component (30,000 h).

The strong contrast offered between the bright residual carbides and darker matrix after chemical etching allows for quantitative image analysis. The average carbide diameter and cumulative population data can be measured after appropriate image processing. This involved normalising the brightness levels for a number of optical micrographs taken at the same magnification. A total of six images were taken per ball, amounting to a comparable surface area of $1280 \times 1530\,\mu m$ for each component. The greyscale contrast is discretised to selectively count the number of pixels covering carbides [Figure 3.3 d]. To filter out noise from the counting statistics a threshold minimum carbide area of $5\,\mu m^2$ was chosen, as has been used by others [98].

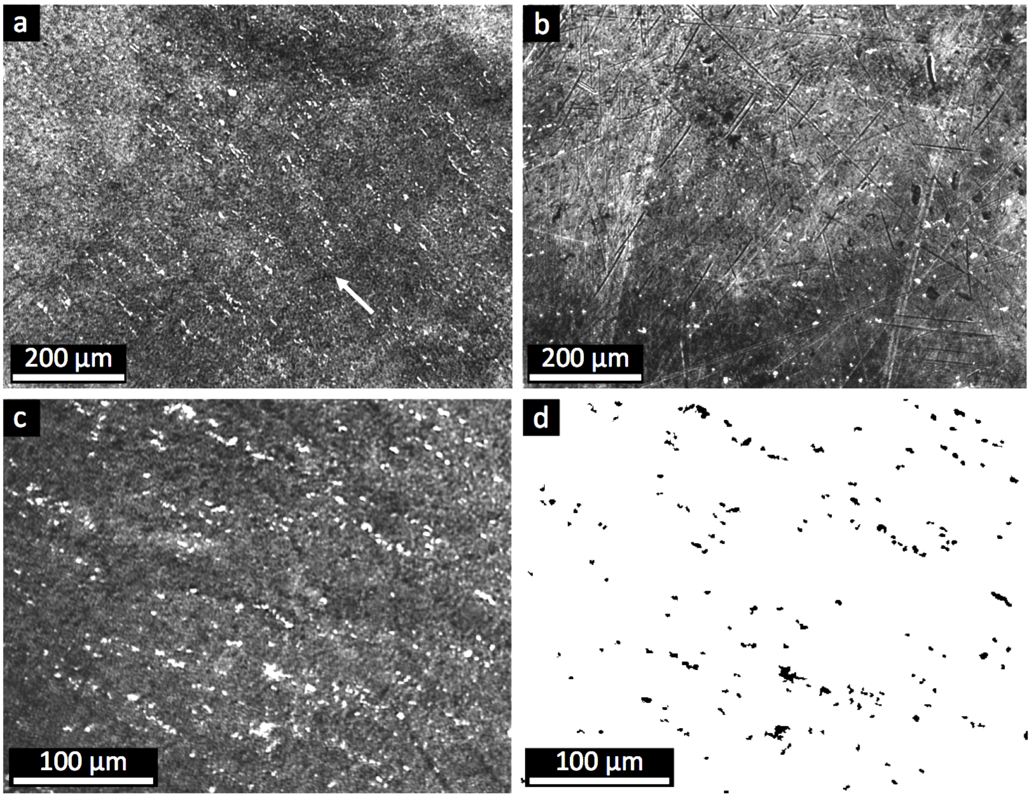

Figure 3.3: (a) Residual carbides on new M50 ball surfaces show a common orientation. (b) Ex-service bearing balls show residual carbides in amongst general surface damage. (c-d) Identical regions of an etched ball surface with its subsequent image analysis map quantifying the carbides in this region.

Table 3.1 provides cumulative data comparing the total residual carbide populations for an unused M50 bearing ball (0 h) with that of an ex-service bearing ball after approximately 30,000 h. The results show fewer carbides are present after service, although the average diameter of the carbides remains relatively constant. These data have been plotted in terms of their frequency distributions and cumulative frequencies in Figure 3.4. The graphs show a skewed distribution for both balls, signifying a median average carbide diameter that is smaller than the mean diameter. There is also a slight reduction in the median diameter following engine operation, together with a 30% decrease in total carbide population after 30,000 h service when compared with the unused 0 h bearing ball [Figure 3.4 b].

The post-service reduction in carbides is thought to be evidence of precipitate removal under the action of surface shear during rolling contact. The

Table 3.1: Surface carbide statistics for M50 bearing balls before and after 30,000 h service. The number of carbides, their average feret diameters and the standard deviations are given.

Ball	No. Carbides	Mean Size	Median Size	Std. Dev.
Unused	1521	6.3 µm	4.5 µm	2.5 µm
Used	1060	6.1 µm	4.0 µm	2.8 µm

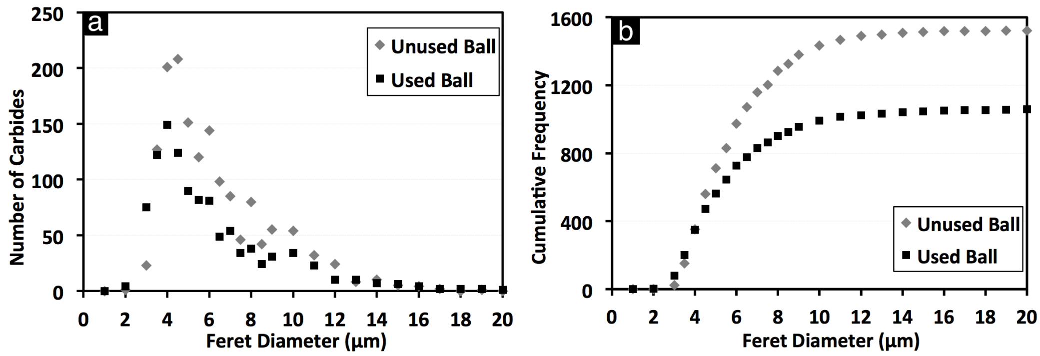

Figure 3.4: (a) Frequency distribution of residual carbide sizes on M50 bearing ball surfaces. (b) Cumulative frequency plots comparing total number of surface carbides before and after service.

interface between residual carbides and the matrix is known to be prone to decohesion in M50 [23, 201]. Pearson and Dickinson presented evidence of cracked carbides breaking up under surface shear in M50 test bearings [24]. The carbide asperities in their work were also found to cause peeling damage at raceway surfaces under low lubrication conditions. Evidence of surface damage caused by residual carbides is contained in Chapter 4, and Chapter 6 looks at the surface topographies of M50 balls for evidence of carbide protrusions.

The loss of surface carbides during bearing operation seems reasonable, given the high-speed and high-stress conditions of the aircraft engine. These observations may be purely statistical, however, since the comparison of bearing balls from different batches is likely to see variation from one component to the next. The central assumptions of this thesis, as outlined in Chapter 1, are that the ex-service bearings are all manufactured to the same specifications and can therefore be directly compared with one-another. Any variation between the ex-service bearings is assumed to be due to the different operating lives they have experienced during service. Another cause for uncertainty is that scratches and damage on the used ball surface may act to obscure the carbides during mapping. This is unlikely however, since scratches tend to show stronger contrast than the matrix and are more likely to be miscounted as a false positive, thereby increasing the relative frequency rather than decreasing it.

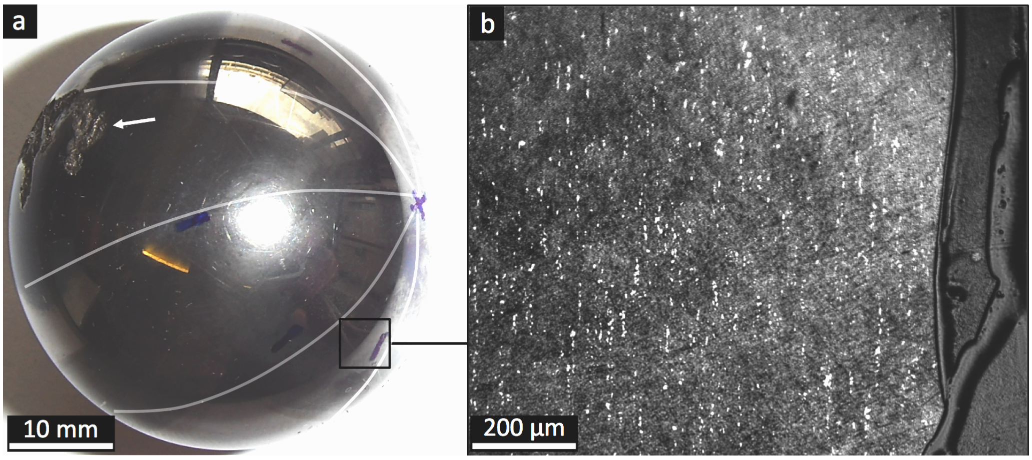

Figure 3.5: (a) Etched surface of spalled bearing ball marked with carbide directionality (b). The fatigue spall did not occur at the poles (indicated).

The highly directional nature of the surface carbides on bearing balls warrants further investigation. A systematic etching procedure was conducted across the surface at a number of different positions, revealing that residual carbides trace lines of longitude about the spherical components, leading towards two poles at opposite ends of the ball. Figure 3.5 shows how the carbide directions were marked on the surface of the spalled M50 ball bearings in permanent ink: with sufficient markings, the polar regions could be inferred and compared against the fatigue spall locations. It was found that the positions of the two M50 fatigue spall failures did not occur near the polar regions, contrary to reports in the literature which suggest failures are more likely at these locations [19, 96, 97, 194, 202].

3.2 Metallography and Microstructures

M50 rolling elements have been cross-sectioned using EDM and the heat affected zone removed with subsequent grinding. Figure 3.6 shows macro-segregation in the polished microstructures of M50 bearing balls. Large-scale anisotropy is seen in the residual carbide distribution which follows lines of chemical segregation akin to the layers of an onion [Figure 3.6 a]. Solute-rich and solute-depleted zones respond differently to chemical etching, revealing segregation bands spaced between 50 - 100 µm. The origin of such anisotropy in through-hardened bearing steels comes from solidification: during cooling the solute-rich carbides are distributed parallel to the central axis of the steel bar used as the raw material for ball manufacture [Section 1.2.2]. The

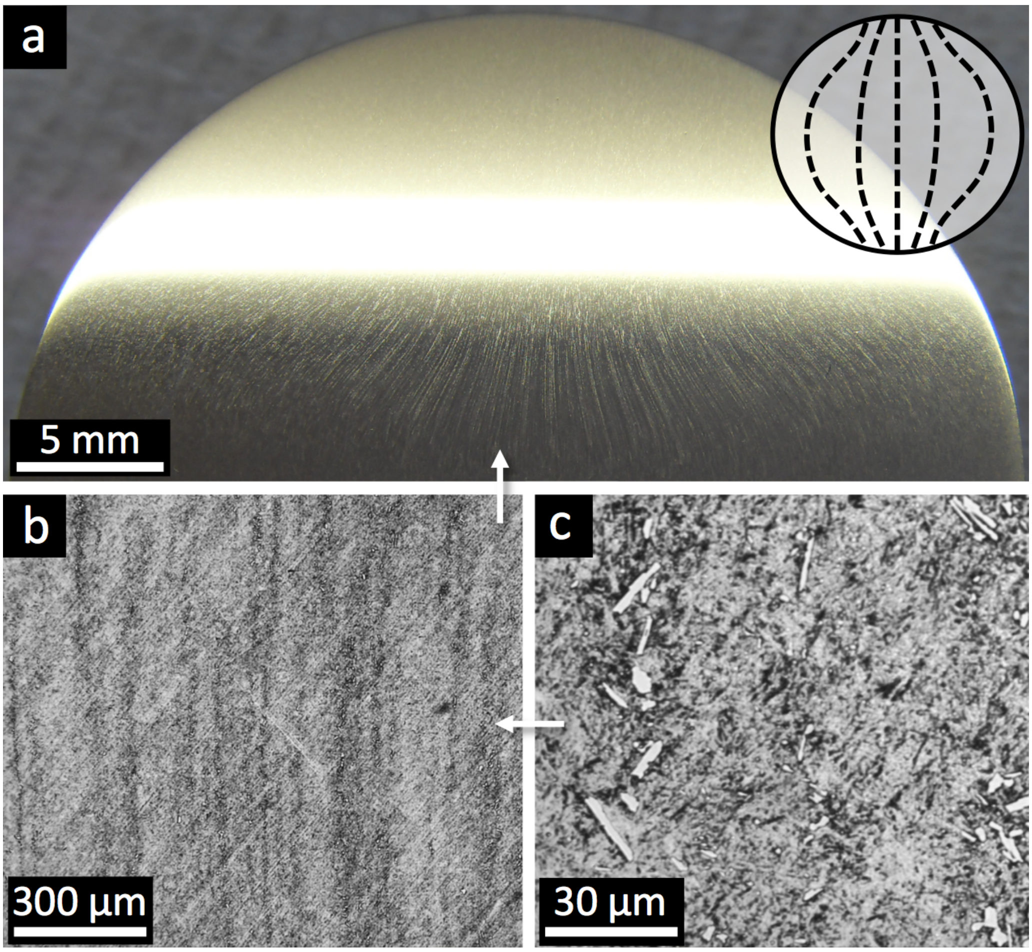

Figure 3.6: (a) M50 bearing balls display inhomogeneous microstructures with visible macro-segregation after polishing akin to the layers of an onion (inset). (b) Bands of chemical segregation are seen after etching with nital. (c) Residual carbides cluster along the segregated bands.

spherical components inherit a polar symmetry after forging, with two well-defined poles where the carbides intersect the contact surface at angles close to 90°. Figure 3.7 displays how the segregated residual carbide orientation is dependent on position. At the poles, carbides intersect the contact surface at right angles but at the equatorial positions the carbides lie parallel to the contact surface [Figure 3.7]. It is suggested that such anisotropy could lead to differences in mechanical properties as a function of position and dynamic imbalance in M50 bearing balls.

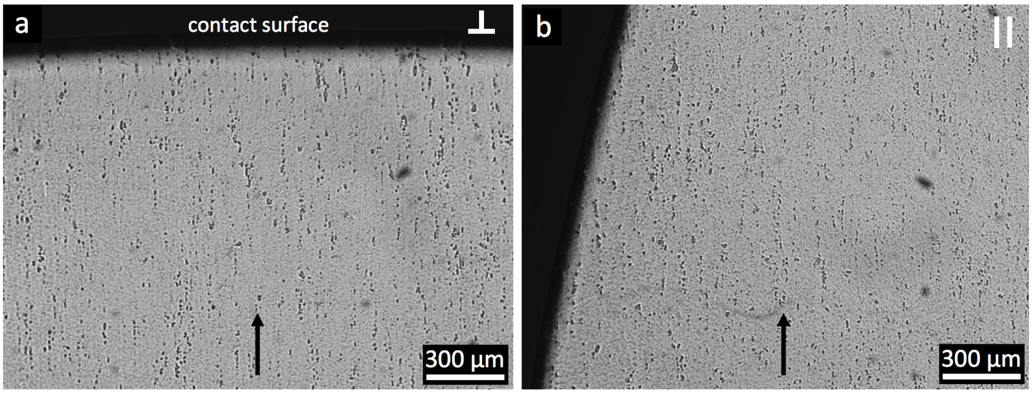

Figure 3.7: Cross-sectioned M50 balls show internal bands of segregated carbides that intersect the contact surface in the normal direction at to the polar regions (a), and parallel to the surface at the equatorial positions (b).

Characterisation of the M50 carbide phases using SEM with EDX micro-analysis identified the presence of small, well-distributed precipitates surrounding the larger residual carbides. Figure 3.8 shows this second precipitate morphology in the M50 microstructure, thought to be the primary carbides formed during annealing heat treatments. The larger residual carbides formed during solidification show strong atomic weight contrast under backscattered-electron imaging [Figure 3.8 b]. Local enrichment of molybdenum, vanadium and chromium alloying elements in these carbides leads to a variation in greyscale which can help distinguish the different phases against the iron-rich matrix. The strongest signal intensity indicates heavier elements and a high molybdenum content, consistent with the M_2C residual carbide [84]. The darker vanadium-rich species is consistent with the MC phase, and these smaller spherical carbides are more evenly distributed amongst the residual carbides [Figure 3.8 a].

Table 3.2: Normalised EDX compositions for M50 carbides in wt % (neglecting carbon signal).

	Fe	Mo	Cr	V
Matrix	91.4 ± 0.4	3.7 ± 0.2	4.4 ± 0.3	0.6 ± 0.1
M_2C	6.6 ± 0.7	69.0 ± 2.3	10.7 ± 0.9	13.8 ± 1.3
MC	9.4 ± 5.0	42.2 ± 4.2	6.1 ± 0.3	42.8 ± 5.2

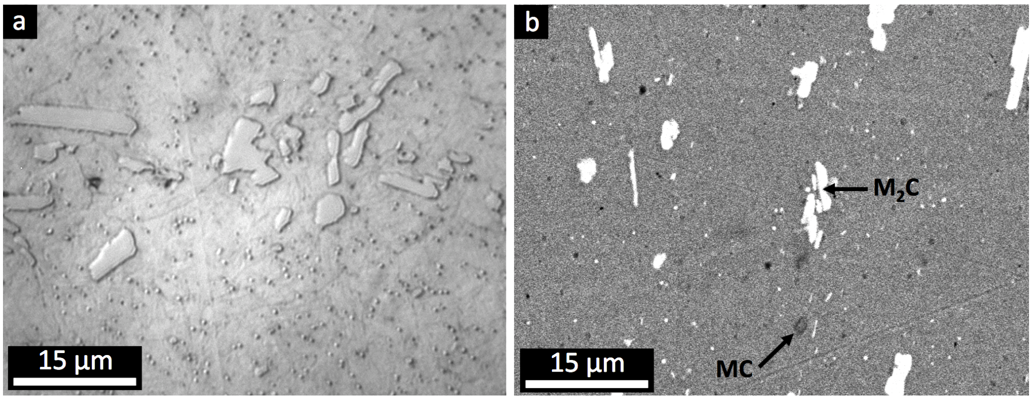

Figure 3.8: (a) Small and spherical primary carbides are well-distributed in the M50 matrix compared to the large residual carbides. (b) SEM backscattered-electron image showing atomic contrast between the bright Mo-rich carbides (M_2C) and darker V-rich phase (MC).

Table 3.2 contains EDX micro-analysis data for the different carbide phases in weight percent (wt %). These data have been normalised to focus on the main alloying elements (Mo, Cr, V) so do not show carbon or other trace elements that may be present in the actual composition. The carbon signal is generally unreliable in SEM-EDX because of contamination from organic matter such as oil from the vacuum pumps. The low atomic mass of carbon also gives a correspondingly low backscatter yield, making phase comparisons difficult. Instead, the average proportion of molybdenum or vanadium relative to iron gives a suitable estimate for the stoichiometry of the phase. With reference to the literature on M50 primary carbides after heat treatment [Section 1.2.2], the data in Table 3.2 identify the M_2C composition of $(Fe_{0.07},Mo_{0.69},Cr_{0.11},V_{0.14})_2C$ [84], and the MC composition of $(Fe_{0.09},Mo_{0.42},Cr_{0.06},V_{0.43})C$ [83]. The matrix composition reflects slight reductions in Mo and V compared with the bulk composition for M50 [Table 1.3]. A more accurate measure of the carbide phases is performed later using XRD.

The penetration depth of an incident electron with energy of 15 kV in iron is approximately 1 μm, according to Kanaya-Okayama range [203]. Adjacent phases may contribute to the EDX signal detected at small carbides, therefore a larger degree of error surrounds the MC composition [Table 3.2]. Analysis of the smallest primary carbides cannot be reliably performed using SEM-EDX alone so transmission electron diffraction pattern analysis and phase fraction analysis using x-ray diffraction are employed later in the text. To investigate the effects of macro-segregation on M50 steel chemistry, an EDX line scan was taken perpendicular to the segregated bands. Figure 3.9 plots the composition variation along a 100 μm test line taken through the regions indicated. Apart from the variations associated with M_2C residual carbides, the composition appears to remain constant throughout the matrix, as might be expected after tempering for 6 h.

Metallographic comparisons between the ex-service bearing balls show no ob-

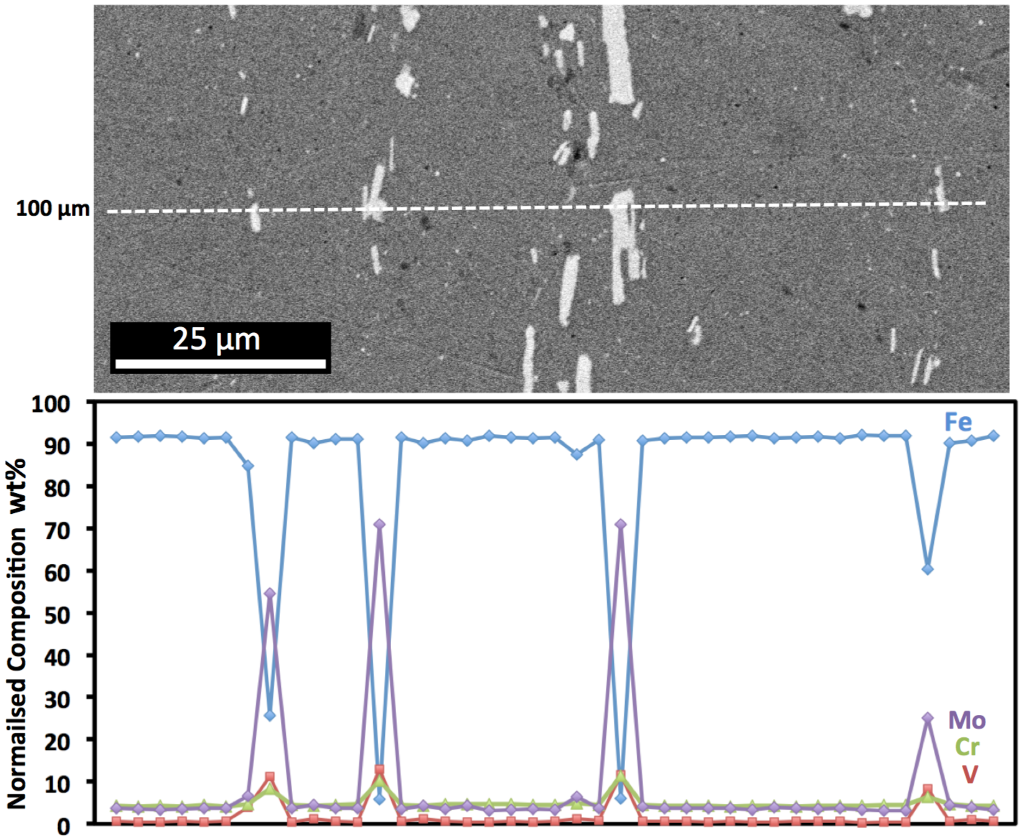

Figure 3.9: EDX compositional line scan across 100 μm of M50. Apart from the residual carbides there is little chemical segregation in the matrix after tempering, correct to ±1%.

vious differences in their general microstructure, despite operating for large numbers of stress cycles. The condition of M50 material directly beneath the contact surface showed no immediate signs of damage or structural alteration, even for the longest running bearing (30,000 h). These observations highlight the stability of the microstructure during operation and suggests the service stresses remain below that necessary for contact fatigue and micro-yielding in this steel. Very few examples of non-metallic inclusions were found within the steel samples examined, and none displayed localised damage features such as butterfly wings or etching features [Section 2.1.2].

Temper Carbides in M50

Transmission electron microscopy (TEM) offers increased resolution that is essential for characterising the smallest M50 carbides that precipitate during tempering. Preparation of 3 mm diameter foils starts with a thin slice of EDM sectioned bearing ball. After thinning to 50 μm and subsequent electropolishing using the settings described earlier the thin foils were imaged in bright field TEM mode. Figure 3.10 reveals the M50 matrix is that of fine martensite plates with a high density of dislocations, deduced from the complex contrast variation. The spherical primary carbides are the vanadium-rich MC phase and range from 1 μm to less than 500 nm in diameter [Fig 3.10 a]. Smaller precipitates are also observed with a plate-like morphology and average thickness of around 50 nm, but can be much longer in length [Fig 3.9 b]. These TEM foils were taken from a random region of the M50 ball so they may have come from segregated regions, however this is not thought to be an issue since the composition of the tempered microstructure was shown earlier to be relatively uniform [Figure 3.9].

TEM imaging in high angle annular dark field mode (HAADF) offers greater contrast between different phases which scatter electrons as a function of the average atomic number of the constituent atoms. Figure 3.11 shows a HAADF image of the M50 microstructure, showing clearer evidence of the plate-like precipitates in large numbers. The likelihood is that these features are the temper carbides which form in secondary hardened steels during heat treatment at 550°C. Characterisation of the nano-scale temper carbides was performed using a combination of STEM-EDX micro-analysis, XRD phase

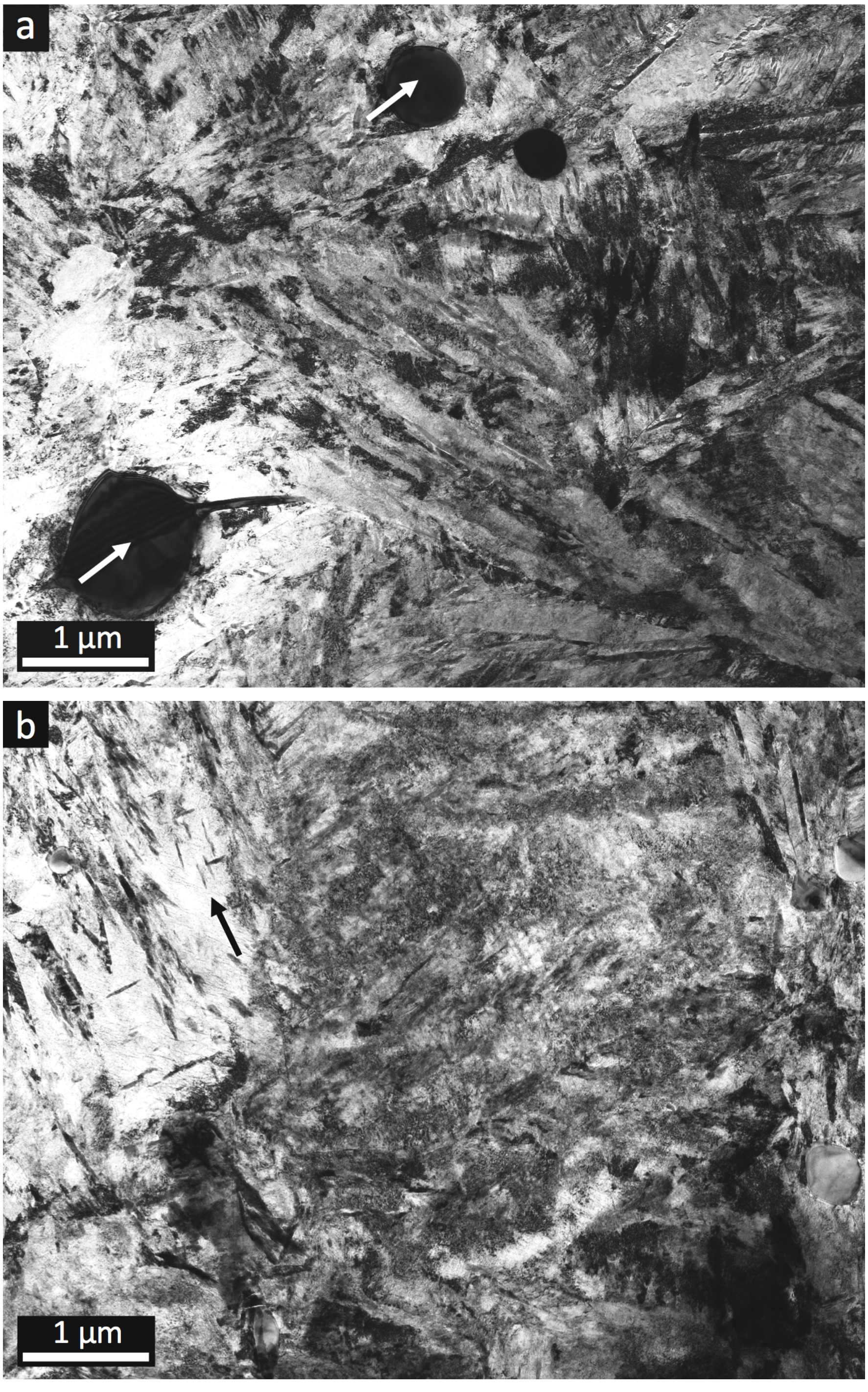

Figure 3.10: (a) Bright field TEM micrograph of M50 showing fine plate martensite with high dislocation density and spherical primary carbides (indicated). (b) TEM micrograph showing nano-scale precipitates with a plate morphology (indicated).

quantification and TEM with selected-area diffraction (SAD) pattern analysis. Figure 3.12 shows a HAADF image of the temper carbides at high magnification, together with elemental maps of the same region found using STEM-EDX.

Figure 3.11: High angle annular dark field (HAADF) TEM micrograph of M50 shows channeling contrast and mass-thickness contrast to reveal the plate-like secondary carbides.

There is an increase in signal intensity at the precipitates that appears to suggest enrichment in Fe and Cr in particular [Figure 3.12]. This may be a misinterpretation of the data, since the relative thickness of the TEM foil will also contribute to the signal. Electropolishing during TEM sample preparation leads to an inhomogeneous foil thickness because different phases etch with varying severity. An increase in the Fe signal at the precipitates suggests the sample is thicker in this region, since iron content is likely to be higher in the matrix not in the carbide. The EDX maps cannot be used to quantify the temper carbide compositions but they can still provide qualitative information. For example, comparison between the four elemental maps shows a spherical precipitate is present and enriched in all but Mo [Figure 3.12].

X-ray diffraction was employed to help identify the temper carbide species in M50 bearing balls. Figure 3.13 shows the experimental setup for this XRD investigation. Phase identification was performed on a polished cross-section

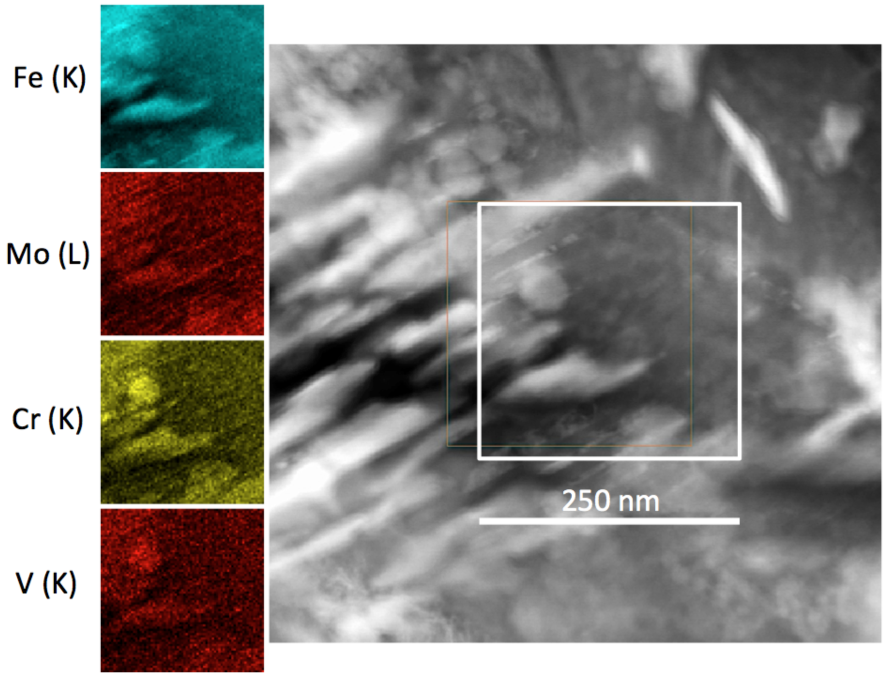

Figure 3.12: HAADF TEM micrograph of a region containing temper carbides and STEM-EDX elemental maps of this region. The x-ray lines K and L are chosen to avoid overlapping signal. Note the spherical carbide is not present in the Mo map.

of bearing ball that was rotated throughout the process to minimise the influence of macro-segregation [Figure 3.13 a]. A 10 mm diameter area at the centre of the sample is irradiated by the primary photon beam which passes through a Ni filter to remove the Cu Kβ line. The large sampling volume

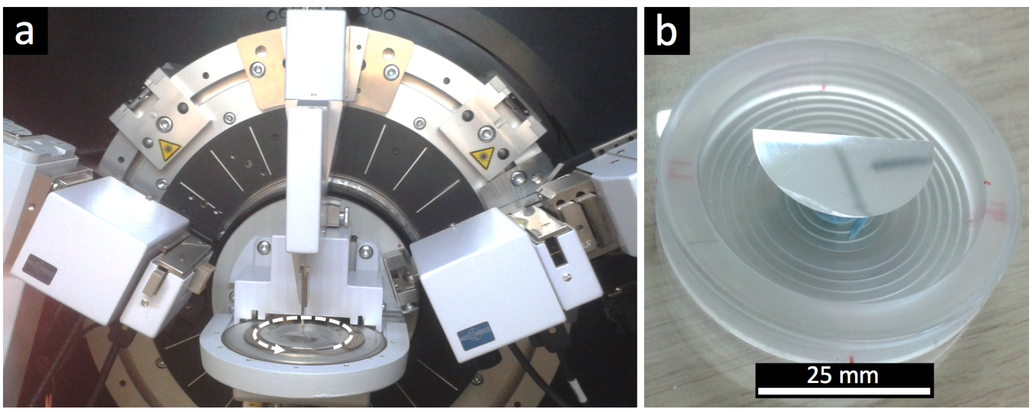

Figure 3.13: (a) X-ray goniometer loaded with rotating M50 ball sample at the centre of the image. (b) The cross-sectioned M50 bearing ball is polished with a 1 µm diamond paste.

combined with a long dwell time of 38 s were chosen to improve the signal intensity and help reveal the smallest temper carbide peaks.

Table 3.3: XRD data for the phases present in an M50 bearing ball. The crystal structures and calculated lattice parameters are given for each phase, as ranked in order of approximate volume percent after calculation with reference to known crystallographic data [204, 205, 206, 207].

Phase	Structure	a (Å)	b (Å)	c (Å)	Ref.
α'	BCT	2.87	-	2.89	-
MC	FCC	4.18	-	-	[204]
M_2C	HCP	2.95	-	4.64	[205]
M_3C	Orthorhombic	5.07	6.73	4.51	[206]
M_6C	FCC	11.05	-	-	[207]
γ	FCC	3.61	-	-	-

Figure 3.14 presents the x-ray spectrum for M50 together with peak fitting at the lower 2θ angles using Rietveld refinement. The phases identified from these XRD data and their calculated lattice parameters are presented in Table 3.3. Evidence for a number of new phases is contained in the XRD spectra: M_3C cementite and the molybdenum-rich M_6C carbide accompany

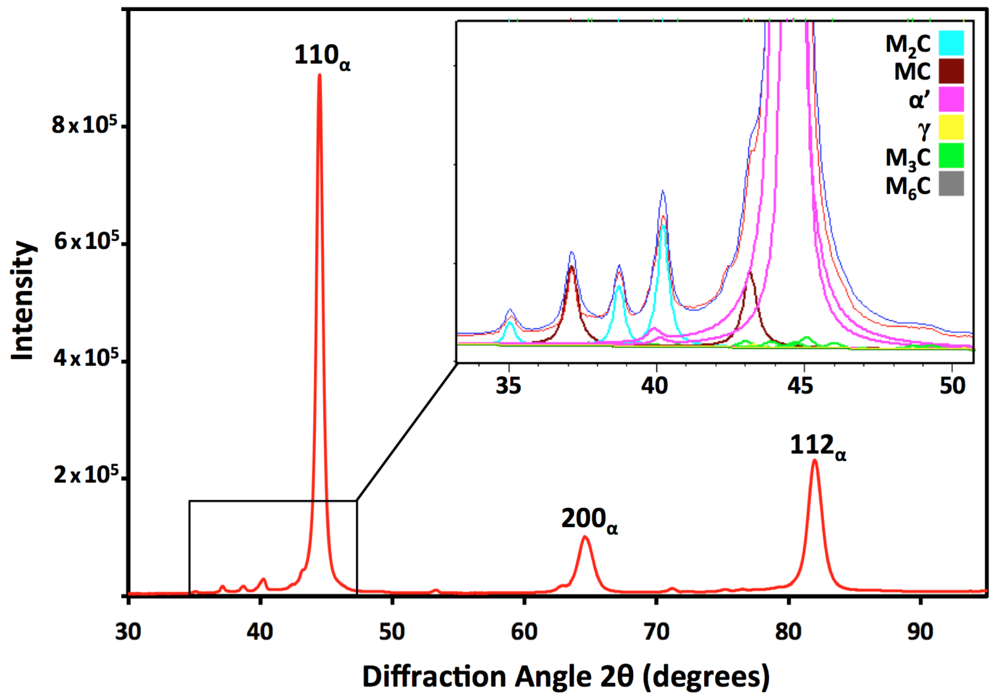

Figure 3.14: Experimental XRD data for an M50 bearing ball, shown in red. The $(110)_\alpha$ peak is most intense but residual carbide peaks are clearly seen at low angles indicate (inset). The calculated spectrum is shown in dark blue.

the two residual carbide phases MC and M_2C already identified. A very low level of retained austenite (γ) is also present in this quenched and tempered bearing steel. A comparison of the relative peak intensities can estimate the approximate volume fraction for each phase, however the precise carbide compositions will vary from those referenced in the powder diffraction data [204, 205, 206, 207], so these volume estimates are unreliable and have not been included.

Low signal intensity from the two new carbide phases make their peaks difficult to observe in the full x-ray spectrum. Figure 3.15 focuses more closely on particular 2θ angles where M_3C and M_6C are present in the data. The subtle peaks have low intensity but after Rietveld refinement their positions fit well with reference to known crystallographic data for these phases [Figure 3.15]. The presence of M_6C in the heat-treated M50 has been reported by other authors [84, 83], but the identification of M_3C cementite is a new discovery that was not expected [Section 1.2.2]. No $M_{23}C_6$ peaks were observed in the XRD data for M50 bearing steel.

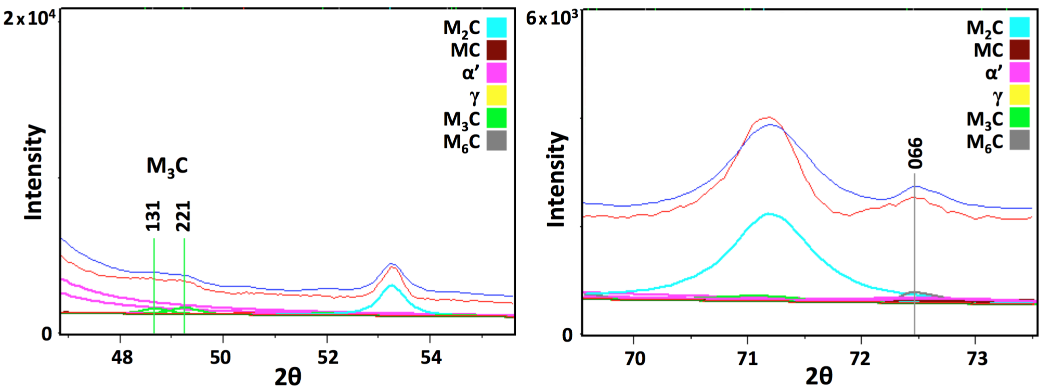

Figure 3.15: Magnified portions of the XRD dataset for M50 shown in red with the calculated spectrum in dark blue. (a) There are two M_3C peaks close to 49°. (b) The M_6C molybdenum-rich carbide has a peak near 72.4°.

The lattice parameters identified using XRD in Table 3.3 can aid further identification of the temper carbides through analysis of their electron diffraction patterns. Figure 3.16 shows regions of M50 bearing balls containing twins and temper carbides. The associated SAD patterns from these regions confirms both twinned martensite and M_3C cementite [Figure 3.16 c]. The close proximity of cementite near twins often makes it difficult to distinguish between the two features, as their plate-like morphologies appear similar when viewed under bright field imaging in the TEM [Figure 3.16 a]. Figure 3.17 shows high resolution examples of cementite precipitates adjacent to martensitic twin boundaries in M50 TEM foils. The cementite growth direction shares a common orientation along the twinning direction, suggestive of nucleation on the twin boundaries or possibly a favoured orientation relationship [Figure 3.17 b]. Evidence for this growth relationship is seen in diffraction pattern analysis where there is strong overlap between the $(112)_{\alpha'}$ twin plane [Figure 3.16 b], and $(006)_{M_3C}$ lattice planes [Figure 3.16 c]. An overlapping diffraction pattern will occur when the parallel interplanar lattice spacings of both phases are close to equal.

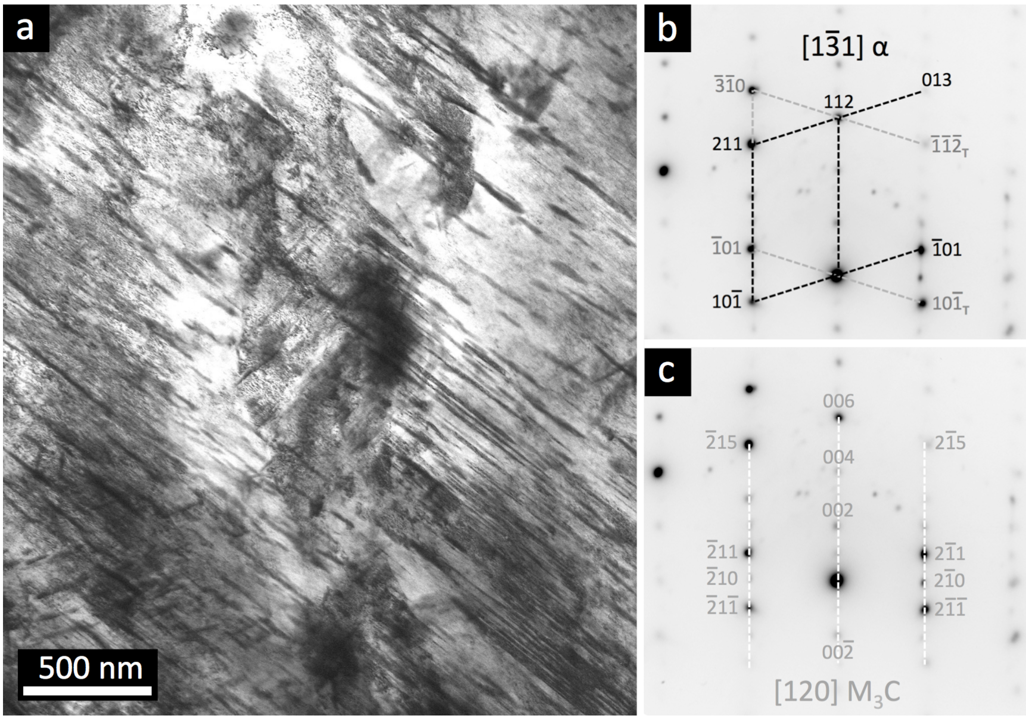

Figure 3.16: (a) Bright field TEM micrograph of M50 containing temper carbides and twins. (b) The indexed SAD pattern from this region showing twinned martensite. (c) The same pattern also shows M_3C cementite.

The data in Table 3.3 have been used to calculate some of the overlapping interplanar lattice spacings of α' and M_3C, according to:

Tetragonal (α'):

$$d_{hkl}^2 = \frac{1}{(h^2+k^2)a^{*2} + l^2c^{*2}} \tag{3.1}$$

Orthorhombic (M_3C):

$$d_{hkl}^2 = \frac{1}{h^2a^{*2} + k^2b^{*2} + l^2c^{*2}} \tag{3.2}$$

where h, k, l are the Miller indices and a^*, b^*, c^* are the reciprocal lattice parameters [208]. For example, the lattice mismatch $\Delta\, d_{hkl}$ calculated between $(\bar{1}01)_{\alpha'}$ and $(2\bar{1}1)_{M_3C}$ is approximately 3% using Equations 3.1 & 3.2. This is well within the margin of error associated with measurement of the reciprocal lattice vectors from diffraction patterns, at approximately $\pm 0.2\,\text{Å}^{-1}$. Therefore, this calculated lattice mismatch supports the observation of an overlap in the $(\bar{1}01)_{\alpha'}$ and $(2\bar{1}1)_{M_3C}$ patterns and thus an ordered relationship between the cementite and the twinned martensite lattices.

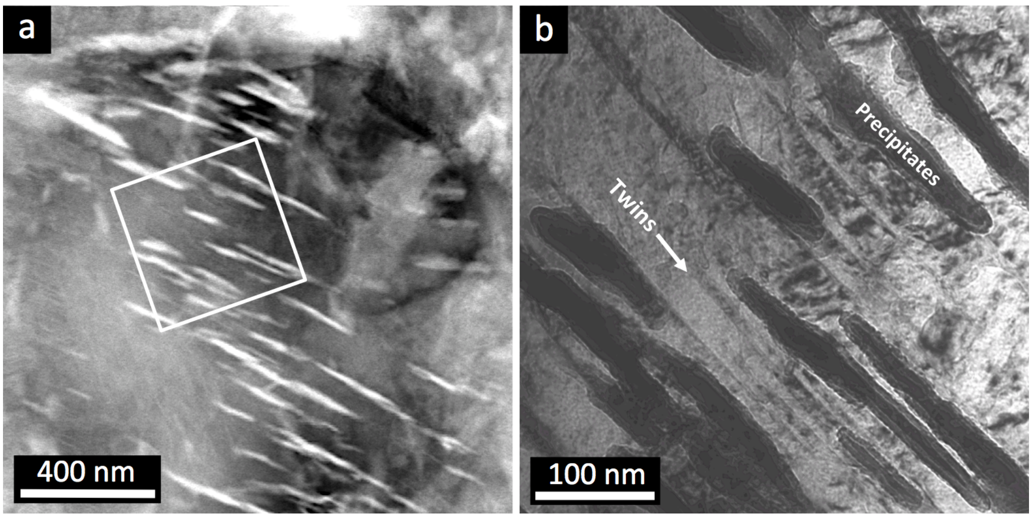

Figure 3.17: (a) HAADF image of cementite in M50. (b) Bright field image showing their precipitation along twin boundaries.

3.3 Fatigue Spall Fractography

Two ex-service M50 bearing ball elements displaying fatigue spalls have been removed from location bearings. Both ball failures occurred after extended periods of operation, at 29,118 h and 29,900 h service respectively. Figure 3.18 shows the characteristic material flaking from the ball contact surfaces typical of fatigue spalling.

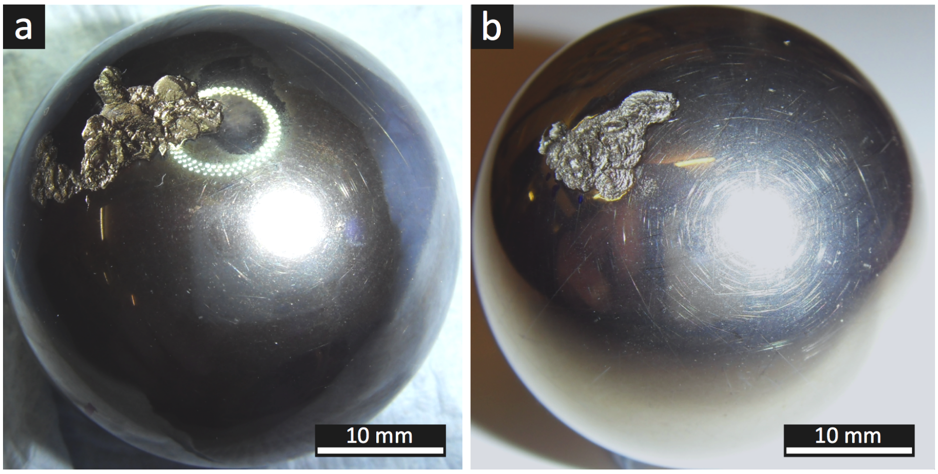

Figure 3.18: Failed M50 bearing balls with fatigue spalls after (a) 29,118 h service, and (b) 29,900 h service. In each case the complete location bearing was discontinued as a result.

Optical microscopy of the fractured regions shows significant damage to the spall interior and plastic deformation about the edges resulting in a polished appearance. The edges appear rounded and flattened, with superficial cracks radiating outward from the spall centre. More severe cracks were also identified running through the spall interior; a feature present on both spalled M50 balls. Figure 3.19 shows these isolated cracks with evidence of damage branching outward from them in all directions. These radiating damage features are sometimes called "beach marks" due to their appearance similar to that of a receding shoreline. Their presence strongly suggests that the interior crack came prior to the subsequent spalling damage which followed.

The linear nature of the spall crack in Figure 3.19 b allowed attempts to forcibly open the crack along its length, in an effort to observe the depth of crack penetration beneath the surface. The spalled section was cut away from the ex-service ball using EDM. A three-point-bend mechanical test rig was then used to apply a load along the crack plane and force it open, fracturing the sample in two. Figure 3.20 shows the resulting fracture surfaces, revealing a semi-circular zone of fatigue crack propagation (dark grey) prior to the artificial overload and brittle fracture of the remainder (lighter grey). The dark contrast of the fatigue zone may also result from oxidation, which

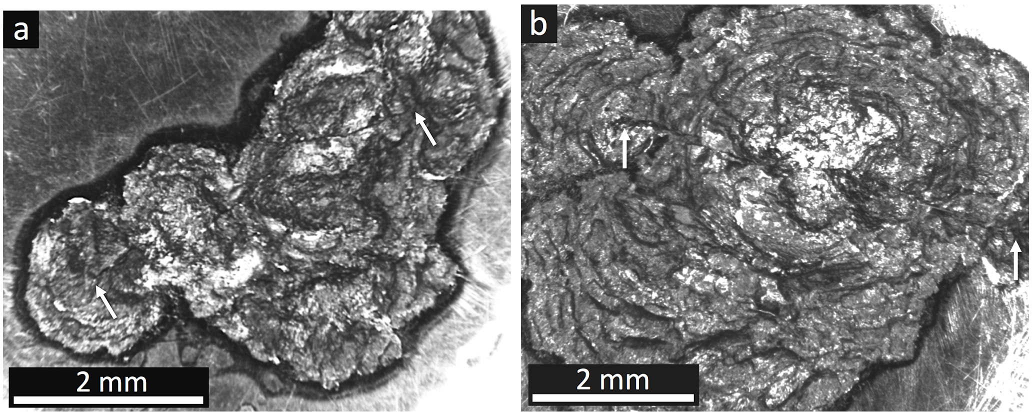

Figure 3.19: Fatigue spalls show internal cracks from which damage radiates. (a) The crack leads diagonally from the bottom left hand corner of the figure (indicated). (b) The crack remains roughly horizontal (indicated).

would occur once the crack breached the surface, allowing lubricant penetration. The depth of the fatigue zone extends to over 1 mm, which is deeper than the maximum subsurface shear stress depth (under ideal Hertzian conditions this is approximately 300 μm). It is possible that fatigue crack initiation occurred at a shallower depth and subsequent crack networks radiated outwards, penetrating deeper beneath the surface. Crack branching in this way has been reported in lower-alloyed bearing steels [133, 14, 209].

The opened fracture surfaces were examined in more detail using SEM with EDX micro-analysis. Figure 3.21 shows the M50 ball fracture surface at the border of the fatigue zone. There is a faceted appearance to the fatigue zone (B) compared with the overloaded fracture region (A). Table 3.4 contains EDX data taken from these two regions of the fracture surface. An increased level of oxygen and phosphorus was detected in the fatigue zone B [Table 3.4]. Phosphates are common additives present in aircraft engine lubricants, and the increased oxygen signal implies exposure to air and oxidation. It is suggested that these data provide evidence for lubricant penetration into the fatigue crack occurred after it had breached the contact surface.

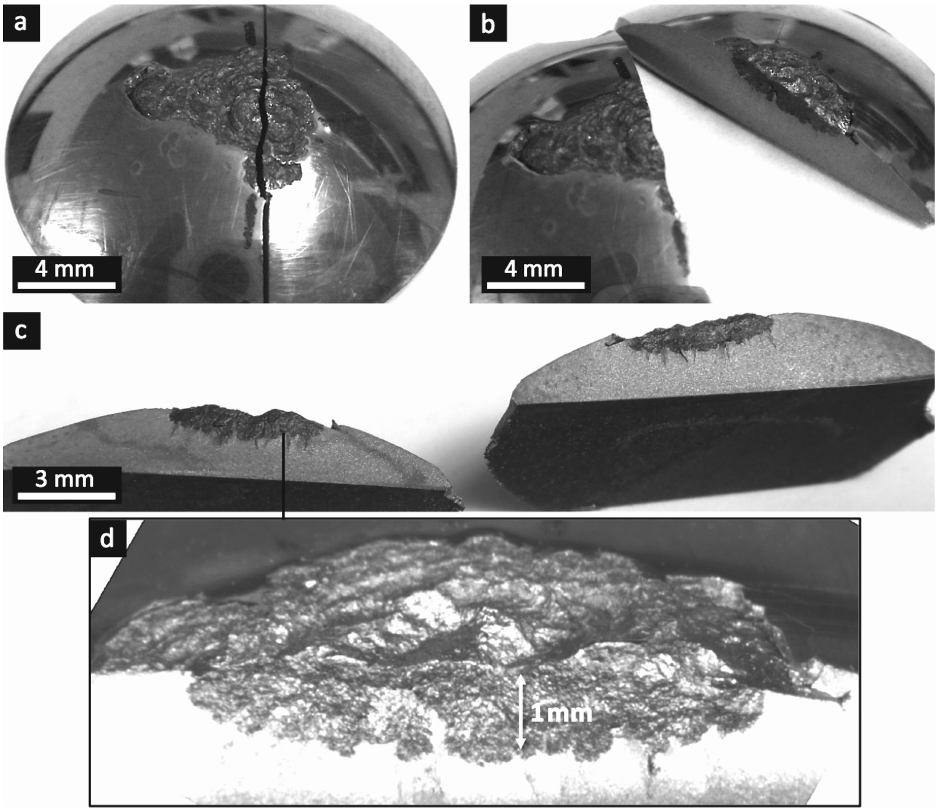

Figure 3.20: (a-b) The spall crack is forced open producing two fracture surfaces, showing (c) a darkened region of fatigue crack propagation. (d) The subsurface fatigue zone extends to a depth of 1mm. Note, at the bottom right of the figure a crack has propagated parallel to the contact surface.

Striation features are observed within the fatigue zone that provide evidence for the propagation of a crack front with stress cycling. Figure 3.22 shows that the striations are somewhat chaotic and do not always propagate in a well-unified direction. The multi-axial stress distribution during RCF coupled with randomised ball spinning would presumably alter the direction of crack propagation in this way. The faceted appearance of the fatigue zone is strongly suggestive of intergranular crack propagation in M50 [Figure 3.22 c]. Also found among the striations are cracked residual carbides and non-metallic inclusions [Figure 3.22 d]. A number of these oxide inclusions were identified in the fatigue zone, ranging from between 10 - 40 μm in diameter. Table 3.5 contains EDX data for some of these oxide inclusions in M50 bearing balls. Their compositions appear consistent with the alumina

Table 3.4: Normalised EDX compositions for the two regions of the fracture surface in Figure 3.21, in wt % (neglecting carbon signal).

Region	Fe	Mo	Cr	V	O	P
A	90.0 ±0.3	3.9 ±0.2	4.4 ±0.1	1.0 ±0.1	0.6 ±0.1	0.1 ±0.1
B	86.9 ±0.3	3.6 ±0.2	4.4 ±0.1	0.8 ±0.1	3.6 ±0.2	0.8 ±0.1

(Al_2O_3), silica (SiO_2) and calcium aluminate (CaO_y Al_2O_3) species reported in the literature [23]. Potassium, sodium and chlorine traces were also found [Table 3.5].

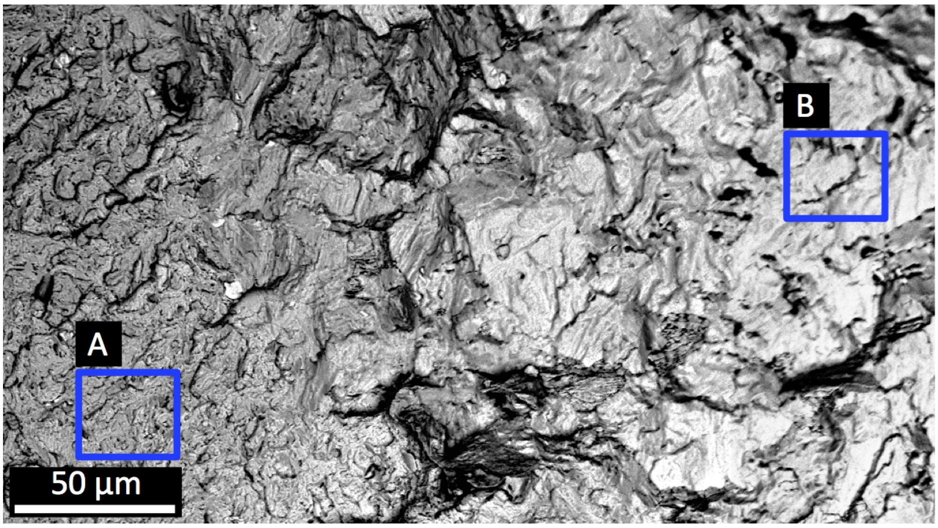

Figure 3.21: SEM image of the boundary between the brittle fracture zone (A) and fatigue crack propagation zone (B). The EDX data from these regions is presented in Table 3.4.

Despite the identification of fatigue striations and many stress-raising non-metallic inclusions, it was not possible to identify the specific location of crack initiation within the fatigue zone. The intergranular crack propagation behaviour appears to be chaotic in direction, inhibiting the possibility of tracing damage back to the source. As spalling damage progresses the branching of crack networks, rubbing at the crack interfaces, lubricant penetration and oxidation effects all combine to obscure the initiation site.

Table 3.5: Normalised EDX compositions for a number of oxide inclusions found in the fatigue zone, in wt %.

O	Na	Al	Si	Cl	K	Ca
56.8 ±0.5	10.2 ±0.2	0.2 ±0.1	0.6 ±0.1	6.6 ±0.2	17.5 ±0.3	8.3 ±0.2
72.5 ±0.4	3.3 ±0.2	4.1 ±0.2	1.0 ±0.1	6.3 ±0.2	1.4 ±0.2	11.3 ±0.2
49.9 ±0.6	2.2 ±0.2	3.1 ±0.2	20.0 ±0.3	3.8 ±0.2	2.2 ±0.2	18.7 ±0.4

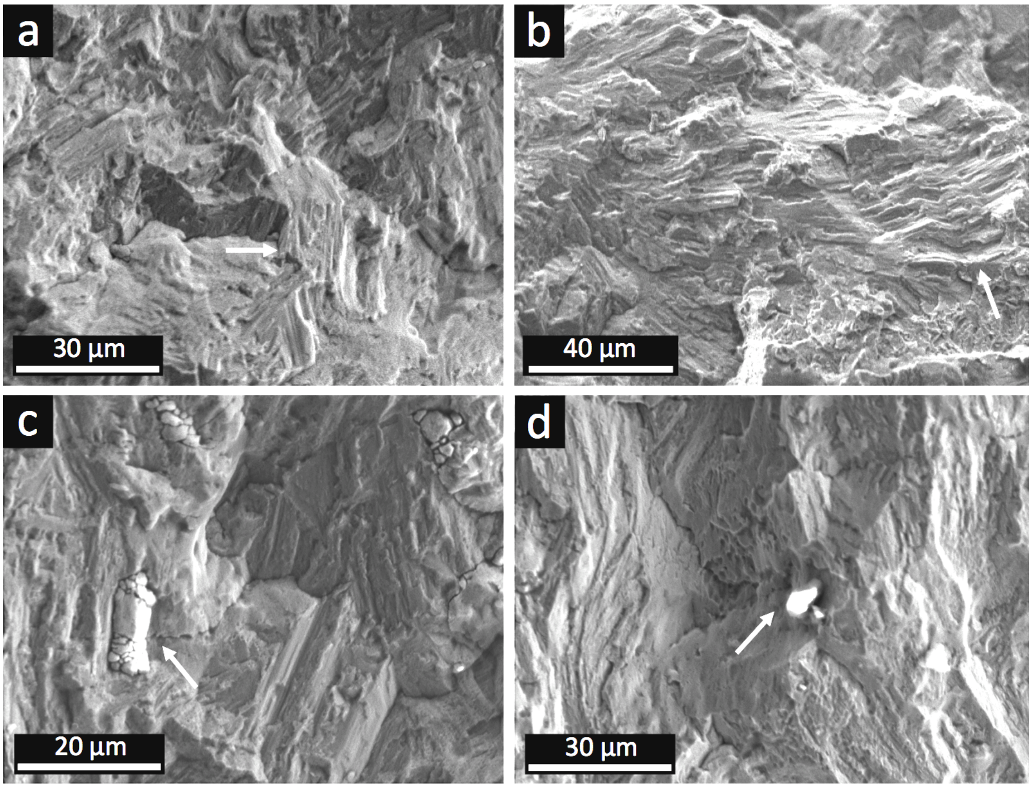

Figure 3.22: (a) Striation features identified within the fatigue zone of M50 spall cracks. (b) Striations indicate incremental propagation of the crack front with cyclic stress. (c) A cracked residual carbide, and (d) a non-metallic inclusion are indicated in the fatigue zone of the spalled M50 ball.

M50 Roller Race

A third fatigue spall failure has been investigated after occurring in an M50 component from a different part of the aircraft gas-turbine engine. Cylindrical roller bearings are used near the mouth of the engine to support fan rotation. Here the roller bearings experience radial loads only, unlike the location bearings which must also support thrust loads [Section 1.1.2]. Due to these different loading conditions the roller bearing raceways are made from through-hardened M50, and a single fatigue spall failure occurred at one of these raceways after 18,000 h service.

Figure 3.23 shows fatigue spalling at the contact surface of an M50 roller raceway. The propagation direction of spalling damage is well-defined, thanks to the fixed rolling direction of the bearing itself, resulting in a V-shaped apex [Figure 3.23 b]. Closer investigation of the spall apex reveals a num-

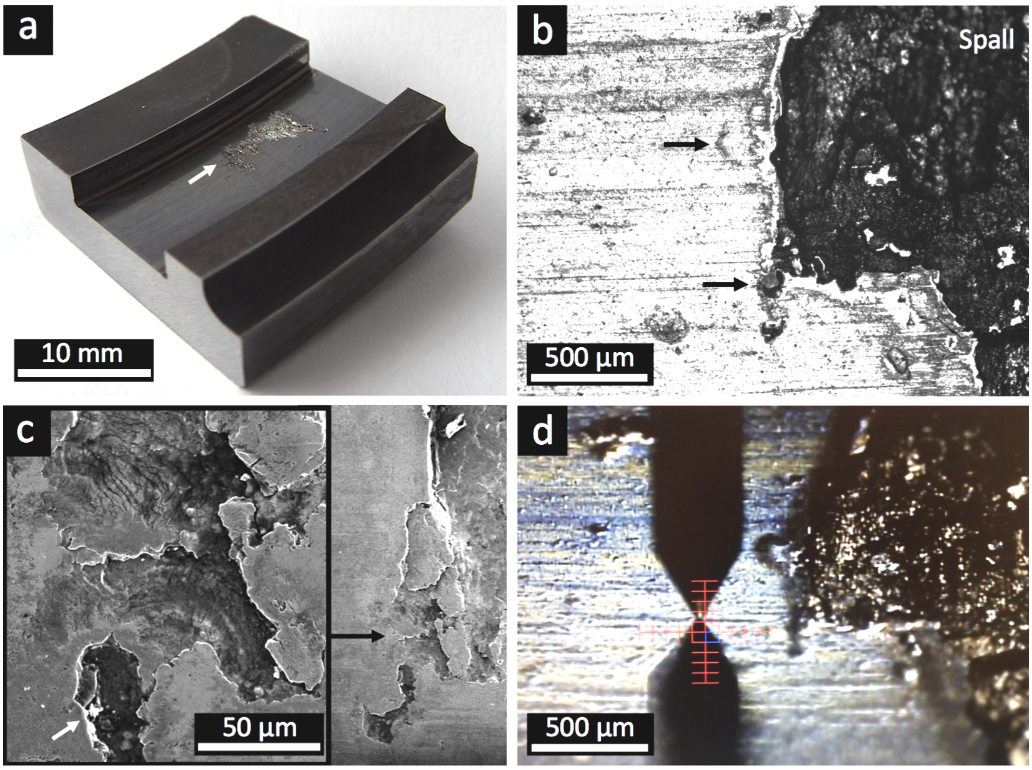

Figure 3.23: (a) M50 roller raceway with a fatigue spall at the contact surface. (b) Surface dents located at the spall apex (rolling direction is left to right). c) SEM backscattered-electron image shows damage radiating from the surface dents and a non-metallic inclusion (indicated). d). The needle of a stylus profilometer approaching the surface dents.

ber of dents at the raceway surface from which spalling may have initiated. SEM examination found beach marks that are seen to radiate from the approximate dent locations and a number of nearby non-metallic inclusions [Figure 3.23 c].

The topography of the raceway surface was characterised using a stylus profilometer, paying particular attention to the dents at the spall apex [Figure 3.23 d]. The needle-like tip of the stylus traces over the raceway spall measuring the height profile of the dents 5 μm in depth. It is suggested that localised stress concentration at the edges of these surface dents acted as a driving force for fatigue crack initiation, encouraged by the presence of non-metallic inclusions in the vicinity of high stress. Figure 3.24 presents a diagrammatic representation of this crack initiation mechanism. Rolling elements impact on the edge of the dent, leading to crack initiation and propagation in the direction of rolling. The behaviour is similar to that which occurs at the edge of a spall, leading to a preferred spall-propagation direction [177].

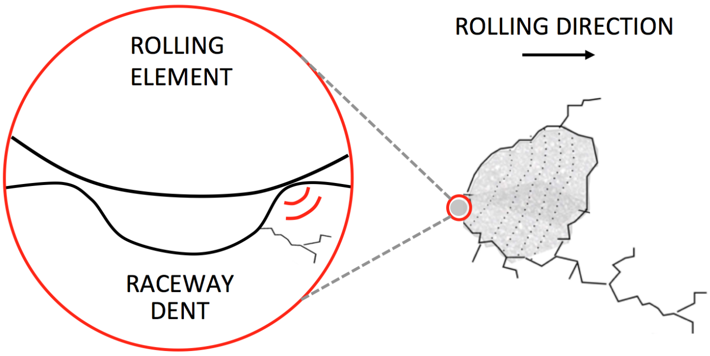

Figure 3.24: Schematic diagram of spalling damage caused by the impact stress concentration at the edge of a surface dent. Non-metallic inclusions in the vicinity would further encourage fatigue cracks. Adapted from [7].

The M50 roller raceway was cross-sectioned through the fatigue spall to examine the material directly beneath the damaged surface. Figure 3.25 shows SEM images of the polished and etched cross-section at the edge of the spall. The material at the contact surface displays localised damage at regions adjacent to residual carbides where separation occurs between the martensitic matrix and the carbide interface [Figure 3.25 a]. The damaged material beneath the spall itself displays cracks which extend outward in the horizontal direction and which follow the prior austenite grain boundaries [Figure 3.25 b]. These crack networks provide further evidence for the intergranular crack propagation favoured in M50 bearing steel, as was previously noted in the fracture surfaces of bearing balls [Figure 3.22].

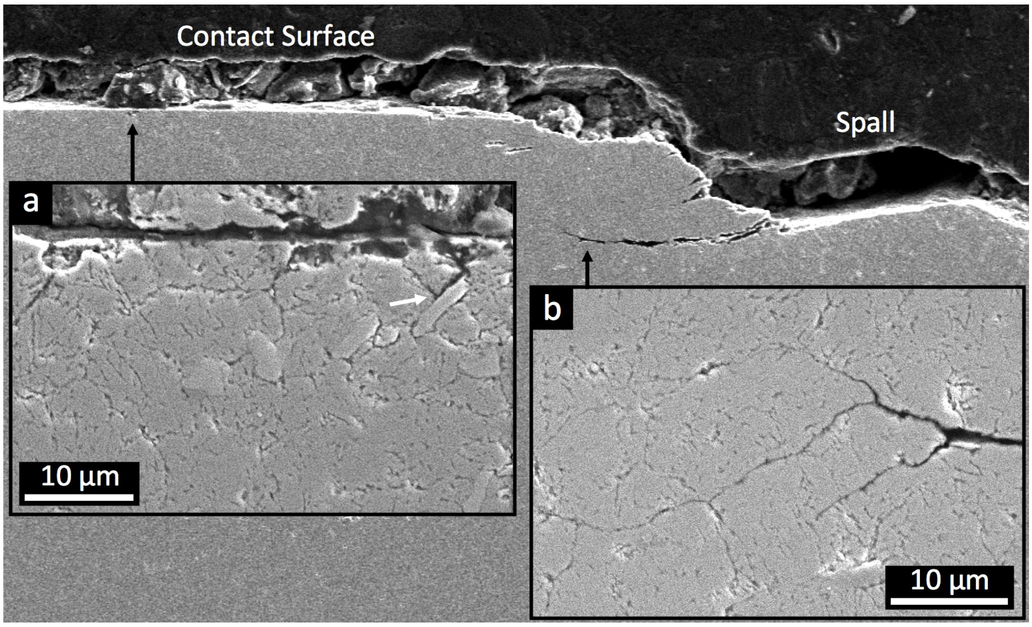

Figure 3.25: M50 roller race cross-section through the fatigue spall. (a) Surface damage is located near residual carbides which separate from the matrix (indicated). (b) Spall damage spreads via subsurface cracks that follow the prior austenite grain boundaries. Note, the rolling direction is into the page.

3.4 Summary and Conclusions

M50 bearing balls exhibit inhomogeneous microstructures with coarse residual carbides resulting from chemical macro-segregation. The residual carbides intersect the contact surface of the bearing balls and after 30,000 h service the number of these surface carbides is reduced by 30%. These are the first observations to show that carbides may break away from the contact surface under the action of shear stress during operation, and supportive evidence has been provided showing separation of M50 carbides from the steel matrix at the surface of M50 roller raceways.

The general M50 microstructure is that of fine martensite containing twins and three carbide morphologies: the M_2C residual carbides; the smaller, spherical MC primary carbides; and plate-like temper carbides that include cementite. XRD evidence and SAD pattern analysis confirms the presence of this iron-rich M_3C phase for the first time in M50. Cementite appears to grow along twin boundaries during tempering and may follow an orientation relationship with twinned martensite. It is likely that the large residual carbides in M50 act as reservoirs for the Mo and V alloying elements, reducing the relative amount of solute available to form secondary carbides during tempering. M_3C will not contribute to the high temperature strength required in aircraft bearings, so these new observations highlight another detrimental effect of the residual carbide segregation in M50 balls.

Spalls on failed M50 bearing balls show internal fatigue cracks which initiate from beneath the contact surface where non-metallic inclusions are observed. Fatigue spalling of an M50 roller raceway was initiated by dents at the raceway surface. An examination of the raceway in cross-section found residual carbides near the contact surface that had separated from the matrix and subsurface cracks beneath the spall that follow prior austenite grain boundaries. These new observations, together with the faceted nature of the ball fracture surfaces prove that intergranular crack propagation is favoured in M50 bearing steel. This indicates a need to strengthen the prior austenite grain boundaries by reducing segregation (a possible cause of grain boundary weakness) and by refining the austenite grain size.

Chapter 4

M50NiL Raceway Characterisation

This chapter focuses on detailed examination of the carburised raceways which support the rolling elements examined in the previous Chapter 3. The surface condition of the M50NiL raceways is damaged by the passing rolling elements and this behaviour has critical implications on the maintained performance of raceway microstructures. Some important general features of the carburised case are examined and a new deformation mechanism is discovered for the first time in bearing steels.

Experimental Methods

Rolls-Royce Trent engine location bearing raceways have been cross-sectioned and examined in the unused condition (0 h) and after various running times approaching 30,000 h [Table 1.2]. M50NiL inner and outer raceways were cross-sectioned radially and tangentially using a diamond cutting wheel. Specimens were ground and polished using progressively finer silicon carbide grinding papers followed by polishing with a 1 μm diamond paste and finally a 0.05 μm colloidal silica suspension. Nital etchant was used to reveal microstructural features; a solution of 3% nitric acid and 97% methanol by volume. In order to preserve the near surface region during grinding, a protective layer of nickel was deposited by sputter coating in some cases. This 1 μm sputter layer was deposited under vacuum at 70 mA for approximately 10 min. Characterisation of the surface at higher magnifications was performed on the JEOL 5800LV SEM with EDX micro-analysis.

Thin M50NiL foils were prepared from specific regions using Ga^+ ion milling on the FEI Helios Nanolab focussed ion beam scanning electron microscope

(FIB-SEM). A protective layer of platinum was introduced by sputter deposition to shield the surface features during ion beam milling. High-resolution imaging was achieved using the JEOL 200CX transmission electron microscope with selected-area diffraction pattern analysis. Grain orientation mapping was attempted using electron backscatter diffraction (EBSD) on the CamScan MX2600 SEM. Sample preparation for EBSD comprised of mechanical polishing followed by ion milling using the FIB or the Gatan Ilion broad beam ion miller.

4.1 Surface Condition

The contact surfaces of ex-service M50NiL raceways show wear tracks of discolouration that indicate the rolling history of the balls during service. Figure 4.1 shows the inner and outer raceways of a number of M50NiL location bearings displaying surface damage of varying severity. The damage is localised at particular contact angles around the grooved raceways, indicating asymmetrical thrust loading conditions [Figure 4.1 c]. Optical microscopy of these rolling tracks reveals internal structure and scoring damage as a function of position. Regular curved indentations are seen and it is thought that these repeating scratches are evidence of ball spinning under thrust loading. Figure 4.2 shows evidence of these kinematic marks at the surface of an M50NiL inner raceway after 120 h aircraft engine service.

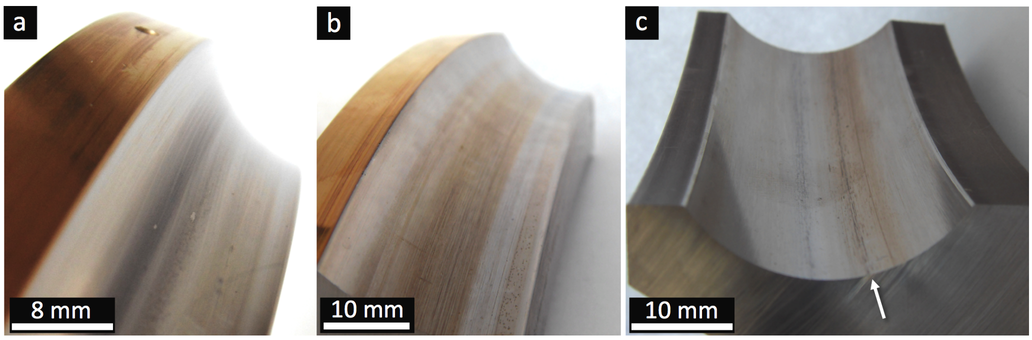

Figure 4.1: (a) M50NiL inner raceway showing tracks of discolouration after 120 h in service. (b) After 29,900 h service the inner raceways display scratches with increased severity. (c) M50NiL outer raceway showing tracks of damage after 29,900 h service. Note the asymmetrical contact angle under thrust loads (indicated).

Kinematic marks describe the dynamic behaviour of the rolling elements during service. The curvature exhibited by the scratches indicates ball spinning under thrust loads and the necessary sliding that this entails. This evidence of plastic shear at the contact surface after only a relatively short period of service (120 h) raises concerns for location bearing tribology. A certain amount of slip is expected within the contact ellipse due to the geometrical considerations [Section 2.2], but under ideal lubrication conditions there should be no reason for metal-on-metal contact and kinematic marks. The consistency of scratch morphologies in Figure 4.2 is unlikely to have been caused by the random occurrence of foreign object debris, so instead it is theorised that the hard residual carbide asperities on the surfaces of M50 balls are responsible. It has been shown in Chapter 3 that surface carbide populations are depleted on ex-service bearing balls, implicating their involvement in surface shear.

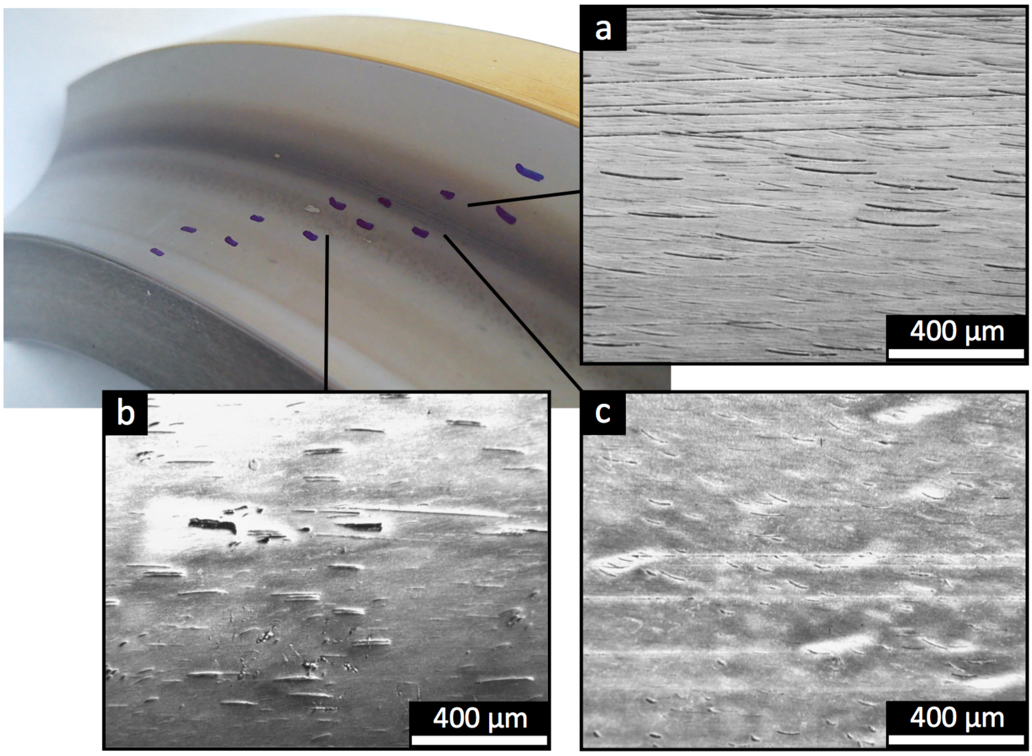

Figure 4.2: M50NiL inner raceway after 120 h aircraft service. (a) Kinematic marks are observed which possess curvature. (b) Deep scratches are seen with repeating morphologies. (c) The curvature of kinematic marks is a function of position.

An investigation of the near surface M50NiL material in cross-section was conducted at positions of raceways showing kinematic marks. The condition of the contact surfaces for three of the ex-service bearing raceways was first compared using low-magnification optical microscopy, followed by higher magnification scanning electron microscopy. Figure 4.3 shows the surface condition of three different location bearing raceways after 120 h, 6,515 h and 29,900 h service. The longest running ex-service bearing shows the most significant plastic deformation at the contact surface [Fig 4.3 c]. Each of these surfaces has been cross-sectioned in the tangential direction which lies parallel to the rolling direction.

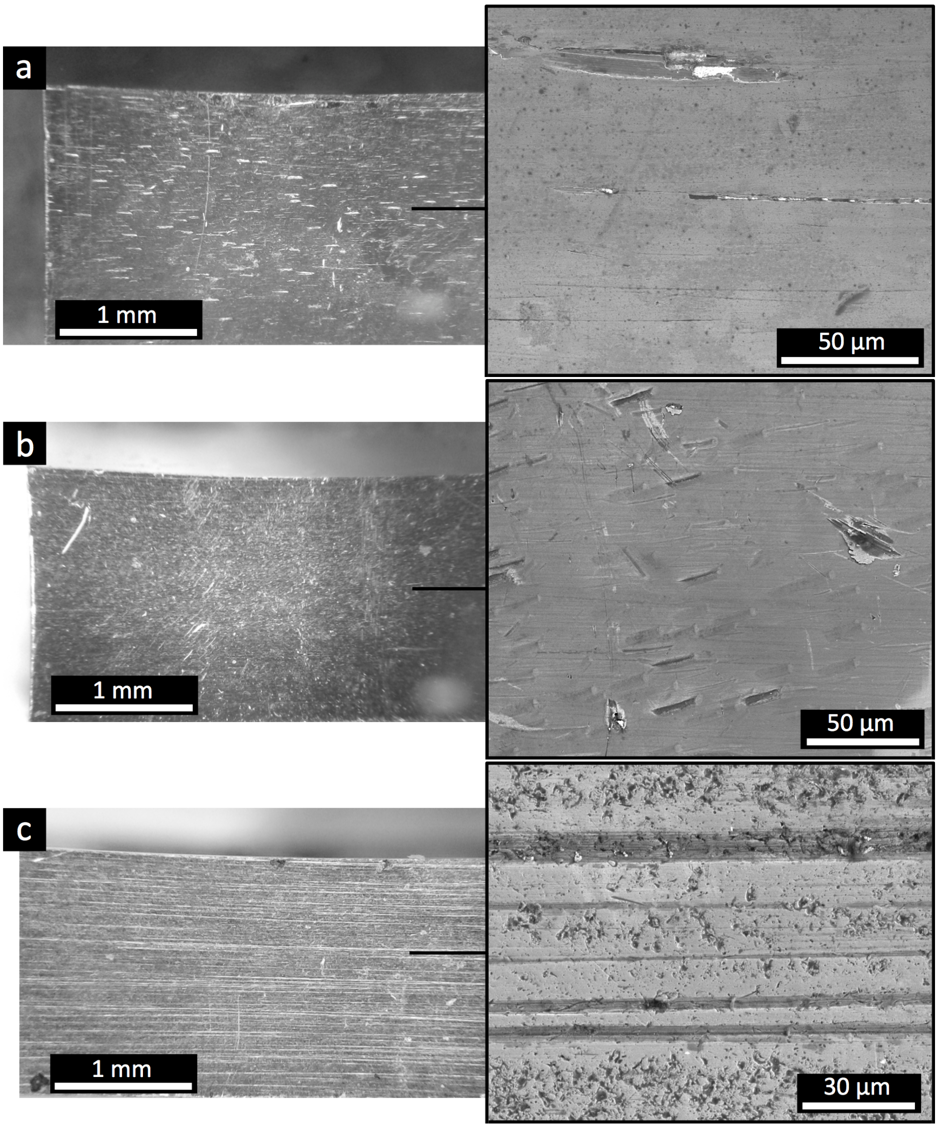

Figure 4.3: The surface condition of M50NiL raceways after operating in aircraft gas-turbine engines for (a) 120 h service, (b) 6,515 h service, and (c) 29,900 h service when pitting damage is visible.

Standard metallographic polishing techniques tended to grind away the M50NiL material at the very near-surface, so a protective layer of nickel was first sputter coated onto the tangential samples prior to polishing. Figure 4.4 shows this sample preparation procedure diagrammatically. It was found that the ex-service material directly beneath the nickel layer displays plastic deformation in the tangential direction of rolling, as indicated by the swept martensite grain [Figure 4.4 b]. This plastic flow is only seen in a very shallow layer of approximately 2 µm in depth, but is present in even the shortest running ex-service bearing (120 h). These observations indicate that significant shear stresses occur at the contact surface, most likely due to component sliding. The deformation direction of the swept grain is not always constant, and in some instances the samples show plastic flow in both the forward and backward tangential directions. Under thrust loads and ball spinning the sliding direction is not always the same as the rolling direction, so this damage reversal is thought to be due to the sliding shear. It appears that the strengthening precipitates in the carburised M50NiL surface are not sufficiently resistant to fracture, as evidenced by the cracked carbide [Fig 4.4 b]. Section 4.2 contains more information on these carbide phases.

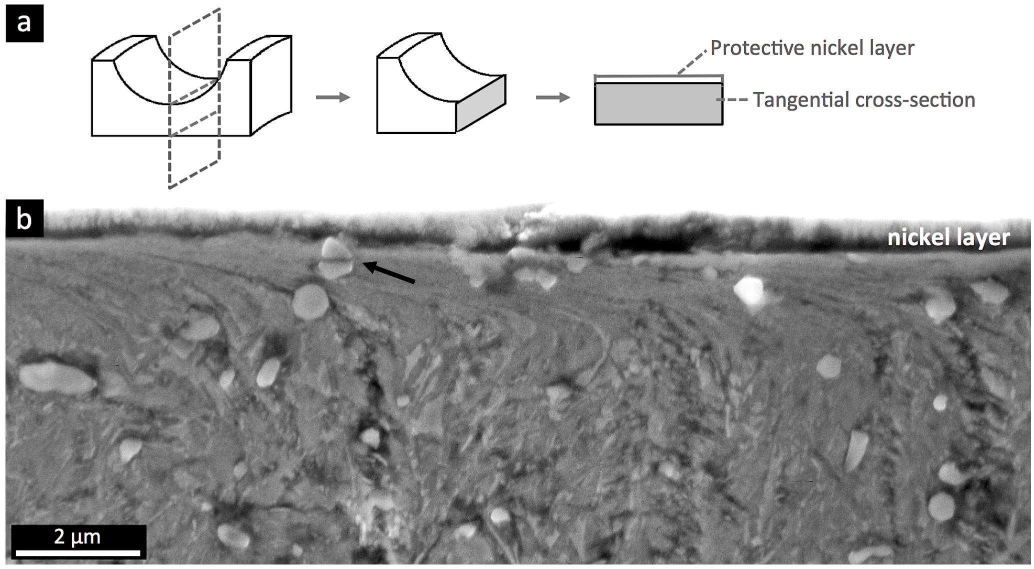

Figure 4.4: (a) Tangential cross-sections of M50NiL raceways along the direction of rolling are protected with a sputtered layer of nickel. (b) After 120 h operation the deformed surface exhibits plastic flow in the direction of rolling. A sheared carbide is seen in this shallow deformation layer (indicated).

The focussed ion beam (FIB) can be used to carefully investigate the shallow region of plastic flow at the surface of M50NiL raceways. Tangential cross-sections were precisely milled from the three ex-service bearing surfaces previously shown in Figure 4.3. The milled surfaces were then imaged at high magnification using charged Ga^+ ions to reveal channeling contrast in individual grains. Figure 4.5 shows FIB-SEM preparation of the sheared surfaces and subsequent images of their deformed microstructures. The plastic flow is always restricted to the shallowest 2 µm, but the character of the deformed zone progresses with time spent in service. The swept grain of martensite plates in the 120 h surface cross-section give way to increasingly fragmented structures after 6,515 h, where there is discontinuity between the sheared surface and the underlying material [Figure 4.5 b]. After almost 30,000 h the directionality is completely lost and the grain-refined surface layer has a well defined boundary [Figure 4.5 c].

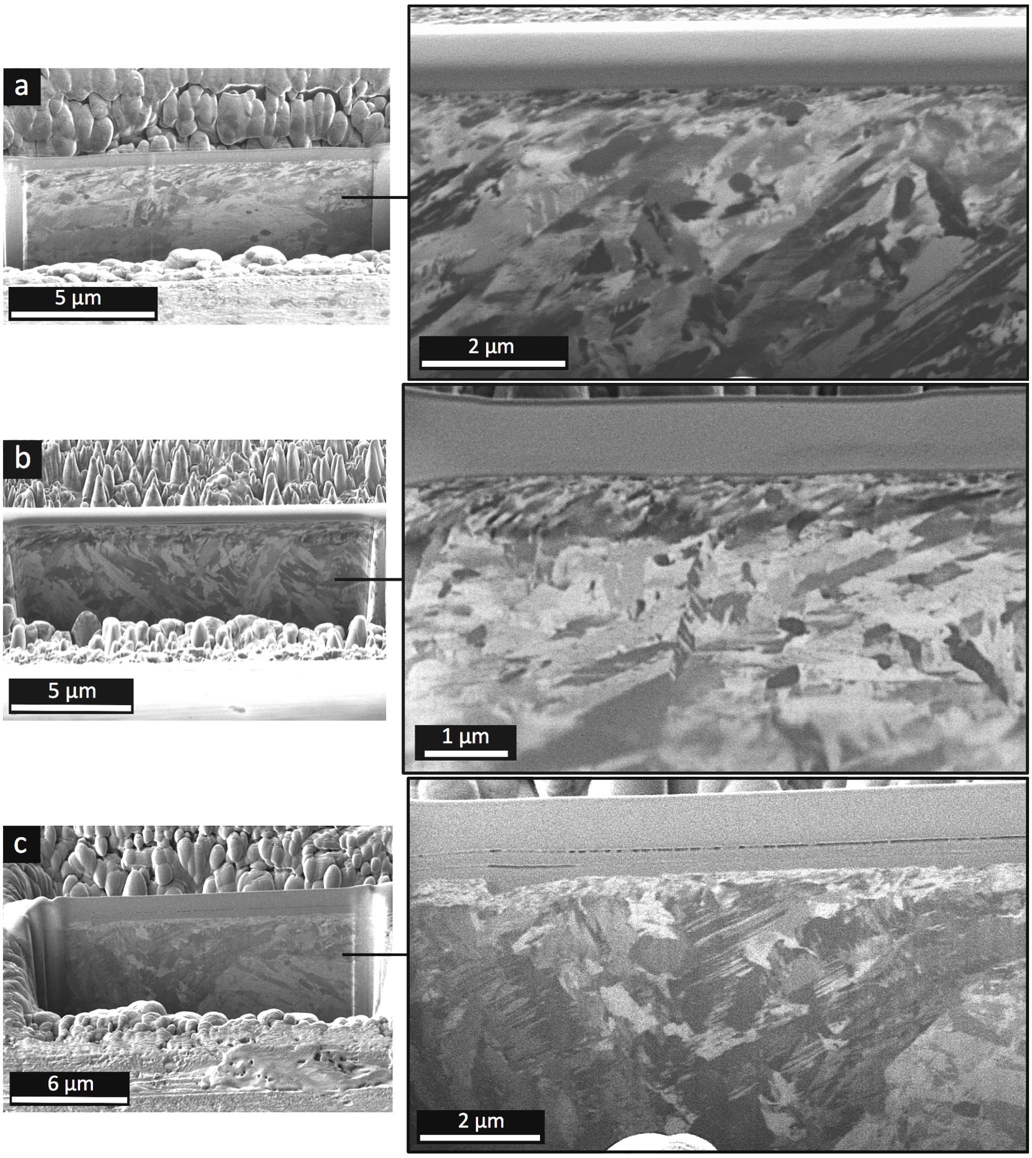

Figure 4.5: FIB-SEM channeling contrast images of the milled contact surfaces of M50NiL raceways. (a) After 120 h service there is directional plastic flow. (b) After 6,515 h service there is discontinuous boundary forming at the deformed surface. (c) After 30,000 h service a distinct deformation layer has been formed.

TEM foils were prepared from each of these ex-service bearing raceway surfaces to examine the tangential shear at the highest resolution. Figure 4.6 shows TEM micrographs of the plastically deformed regions directly beneath the protective platinum layer which only extend to shallow depths of 0.5 μm. The swept grains are quite apparent in the 120 h service bearing [Figure 4.6 a], but this directionality is lost with continued service, leaving an almost com-

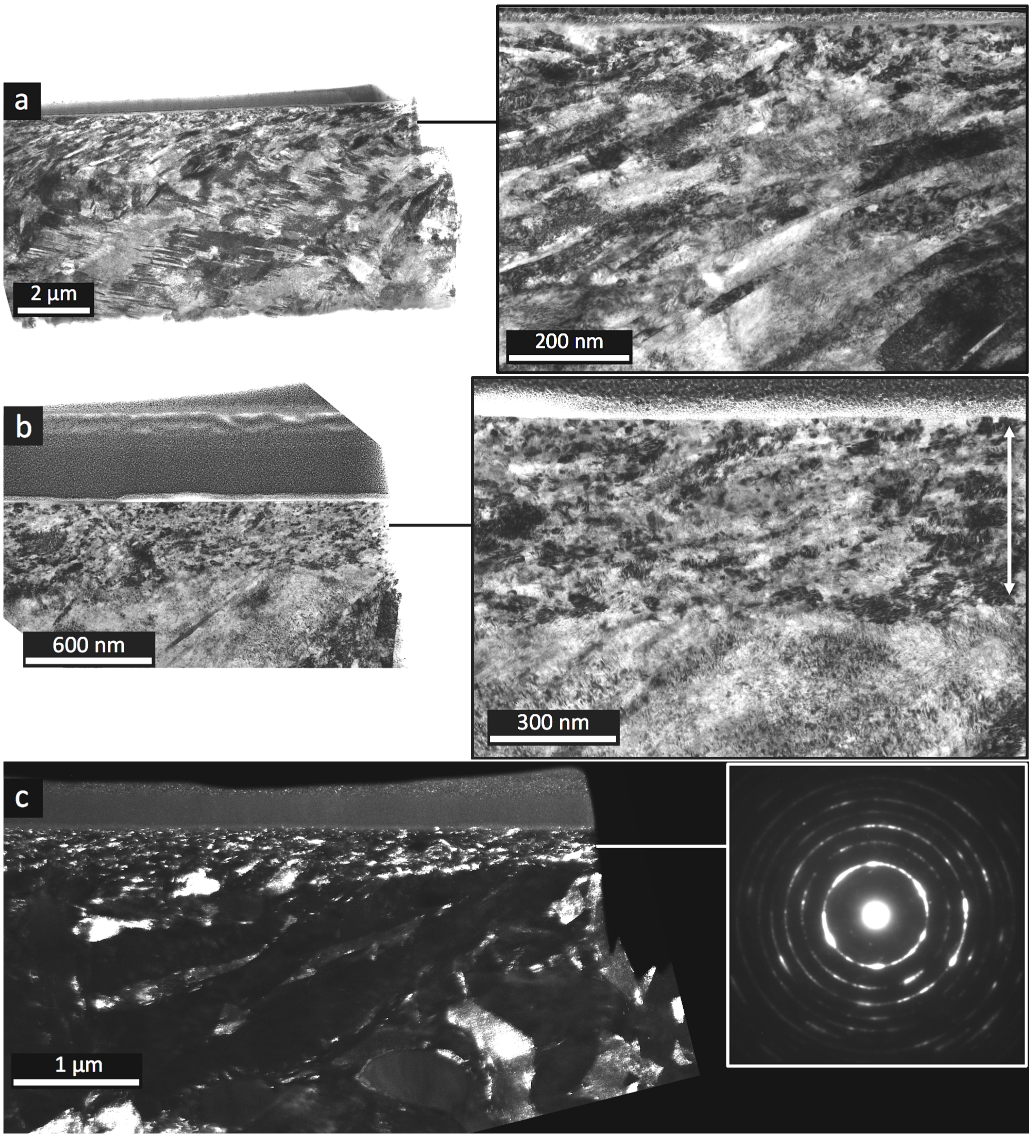

Figure 4.6: (a) Bright field image of a TEM foil from the M50NiL surface after 120 h service shows deformed martensite plates with strong orientation. (b) After 30,000 h service TEM foils show a 0.5 μm wide refined layer containing nanoscale grains. (c) Dark field image of the 30,000 h foil with associated diffraction pattern showing the equiaxed nanoscale ferrite in this grain refined layer.

pletely equiaxed deformation zone after 30,000 h service [Figure 4.6 b]. Dark field imaging with SAD patterns confirm the presence of nanoscale ferrite in this grain refined surface layer [Figure 4.6 c]. The progression of plastic deformation at the surface of M50NiL raceways from swept grain after 120 h service to a nanocrystalline layer after 30,000 h service shows the detrimental effect of sliding shear stresses during aircraft gas-turbine engine bearing operation.

The mechanical properties of the raceway surface will be influenced by the localised damage generated by sliding. The nanoscale ferrite in the grain refined layer should display a correspondingly high hardness, due to the large density of interfaces. Generally, work-hardening of this nature leads to a reduction in subsequent plasticity and therefore reduced toughness. It has been shown that nanocrystalline structures may lose ductility as the grain size is reduced because of the onset of plastic instability [210]. Indeed, the pitting damage seen in Figure 4.3 c seems indicative of a brittle surface layer.

These new observations are presented as evidence for a novel mechanism of surface initiated fatigue failures in aircraft location bearings: a rehardened and embrittled surface layer is generated that will be susceptible to cracking, and delamination may occur along the discontinuous interface with the softer underlying material. Similar delamination theories are well established in the field of wear and tribology [211]. Chapter 5 contains an examination of the work-hardening effect in M50NiL raceways.

4.2 Metallography and Microstructures

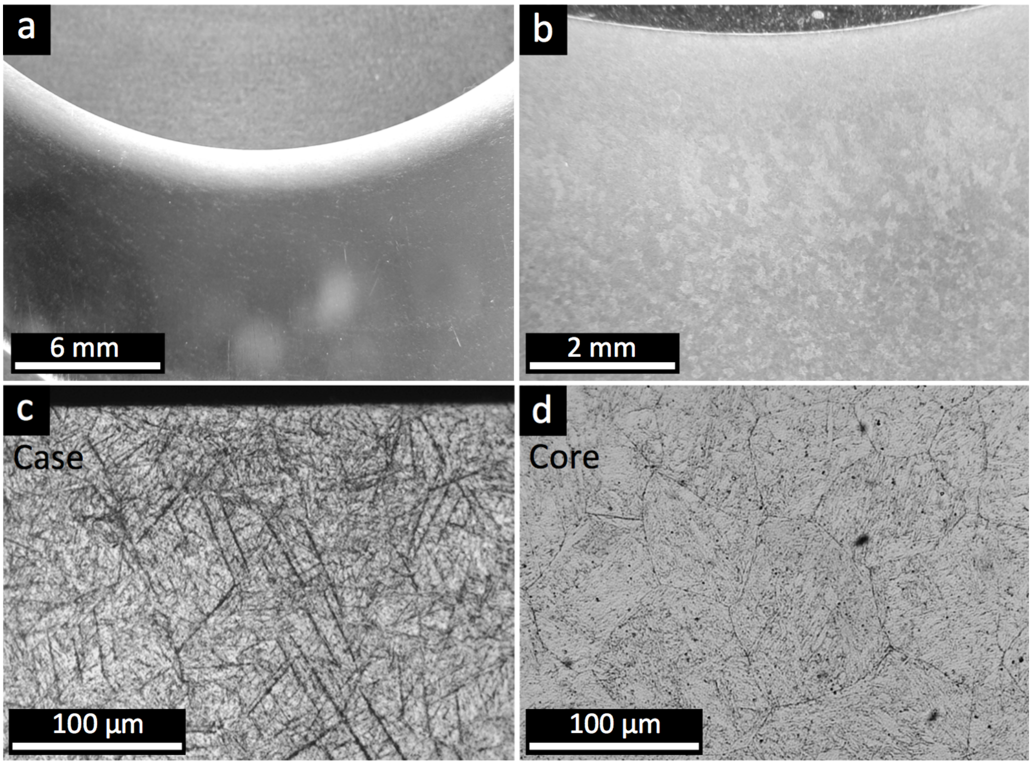

Figure 4.7: (a) M50NiL raceways display a carburised case after polishing. (b) Colloidal silica reveals the prior austenite grains and a case depth around 2 mm deep. (c) Plates of high-carbon martensite in the case are darkened upon etching. (d) Plates of low-carbon martensite and austenite grain boundaries in the M50NiL core material at depths greater than 3 mm.

M50NiL raceways have been cross-sectioned to allow examination of the stressed material beneath the contact surface. Figure 4.7 shows metallographic samples displaying a carburised layer which is visible to the naked eye after polishing. Many fine carbides are present in this carbon-enriched zone, giving it a matte appearance compared to the mirror-like finish of the bulk material where no carbides are seen [Figure 4.7 a]. The carburised zone extends to a case-depth of approximately 2 mm and the transitioning microstructure throughout this region is revealed upon polishing with colloidal silica [Figure 4.7 b]. Chemical etching with 3% nital darkens the high-carbon martensite plates in the case [Figure 4.7 c], but the low-carbon core material is more resistant to etching, instead showing the prior austenite grain boundaries [Figure 4.7 d].

Table 4.1: Average M50NiL grain size determined using the mean lineal intercept method (P_L). The equivalent ASTM number is also given [212].

Raceway	Grain Size	P_L	N_{ASTM}
800 IP	$63 \pm 6\,\mu$m	$15.9 \pm 1.5\,\text{mm}^{-1}$	5.5
900 LP	$40 \pm 4\,\mu$m	$24.8 \pm 2.0\,\text{mm}^{-1}$	6.5

The prior austenite grain size as a function of case depth appears to remain relatively constant in M50NiL [Figure 4.7 c-d]. This might be expected because the austenite grains form well before the carbon diffuses into the material during carburisation. A quantitative comparison of prior austenite grain sizes was conducted across two M50NiL inner raceways from the ex-service location bearings. Table 4.1 presents the average austenite grain size for the two components in terms of the mean lineal intercept[1] and as a standardised grain size number[2] according to the American Society for Testing and Materials (ASTM) [212]. The average grain size was found to vary between 40 - 60 μm for the two components [Table 4.1]. These data indicate that both raceways display quite a coarse grained microstructure [66], that have only just achieved the minimum international standard required for bearing steels at $N_{ASTM} > 5$ [213]. Over fifteen micrographs were taken for each raceway in the investigation of grain size, and from each micrograph the average P_L taken from a grid containing over 10 test lines. The micrographs themselves were taken from regions of the material showing clearly defined austenite grain boundaries, so this typically meant case depths of greater than 2 mm where the low-carbon martensite etches less strongly. It is not possible to say whether these grain sizes are appropriate at all depths, since the prior austenite grain boundaries become more difficult to isolate as you approach the carburised surface. The variation in grain size across the different location bearings is probably due to them coming from different batches of steel which have been separately processed and heat treated. This would highlight a need for more careful control during manufacture, and carburisation treatments in particular, to attain the desired austenite grain size.

[1] A test line of known length, L is overlaid onto an image of the microstructure and the number of times the line intercepts a grain boundary, P_L is counted, then averaged over many images.

[2] $N_{ASTM} = -3.3 + 6.65 \log_{10}(P_L)$

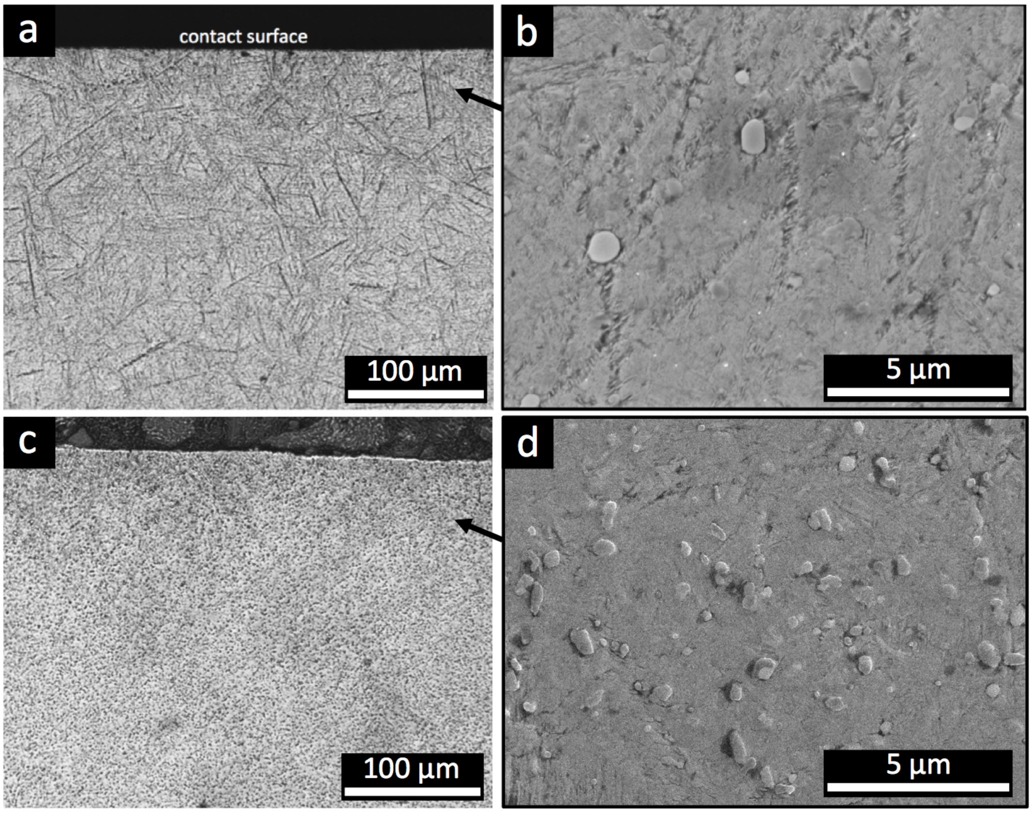

Figure 4.8: (a) Optical micrograph of etched martensite plates in the M50NiL carburised case. (b) Secondary electron images show the plates have internal structure consisting of arrays of parallel bands, and spherical carbides are also seen, (c) The unetched case microstructure shows a high density of spherical carbides. (d) The primary carbides are less than 1 µm in diameter.

Martensite growth is also limited by the parent austenite grain boundary so the average martensite plate length in the M50NiL case is quite large. Figure 4.8 a shows the martensitic plates in the carburised case region that etch darkly because they possess internal structure. SEM imaging reveals arrays of parallel bands running along the centre of the martensite plates [Figure 4.8 b]. These observations are believed to be evidence of twinning of the so-called midrib at the centre of plate martensite that occurs during transformation [214]. The low-carbon core material does not exhibit this twinning behaviour. Spherical carbides are also visible in the carburised microstructure [Figure 4.8 c]. The unetched microstructure shows these precipitates are well distributed and average less than 1 µm in diameter [Figure 4.8 d].

Compositional analysis of the primary carbides in the M50NiL case was attempted using EDX microanalysis. Figure 4.9 shows SEM secondary elec-

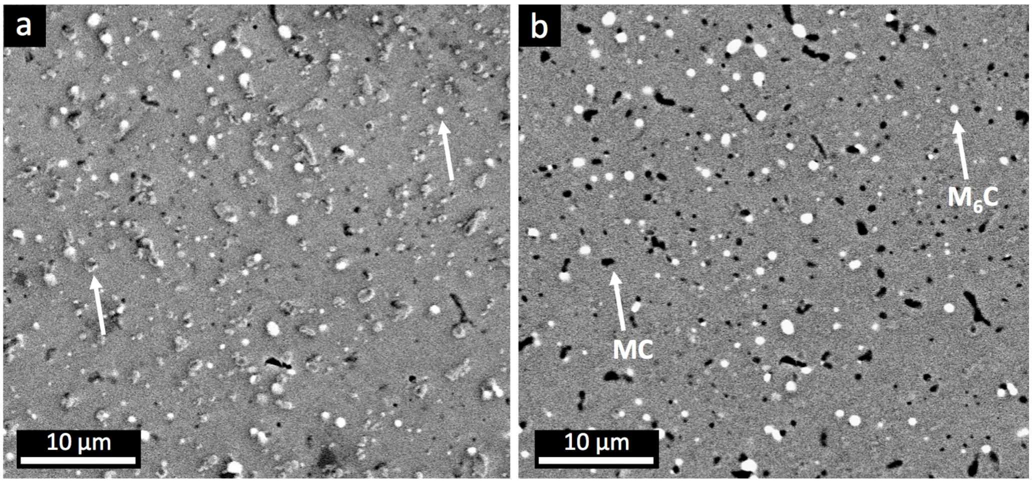

Figure 4.9: (a) SEM secondary electron image of primary carbides in the carburised M50NiL case. (b) Backscattered electron image of the same region reveals different carbide species (indicated). The brightest phases are rich in Mo and the darkest are rich in V.

tron and backscattered electron images comparing the same region in the carburised zone. Variation in greyscale contrast indicates more than one species of primary carbide is present [Figure 4.9 b], contrary to reports in the literature which claim only the MC is found in the carburised M50NiL case [73]. The darkest precipitates are assumed to be these vanadium enriched carbides, and the brightest phases are likely to be molybdenum-rich M_6C carbides [83], although there is some uncertainty. It is not possible to ascertain the exact composition of the carbides using EDX alone due to their small size. A large proportion of the backscattered signal comes from adjacent material surrounding the precipitate, resulting in a disproportionately high iron signal and significant variation. Table 4.2 lists the approximate average composition of these precipitates, consistent with the VC and Mo_6C carbides [83].

Table 4.2: Normalised EDX compositions for M50NiL primary carbides in wt %. (Carbon signal is neglected). The relative proportions of alloying elements are used to estimate the carbide species, with reference to known values in the literature [Table 1.5].

	Fe	Mo	Cr	V	Ni
MC	60.7 ±3.6	13.6 ±1.4	5.0 ±0.3	18.2 ±4.0	2.5 ±0.5
M_6C	64.7 ±11.2	26.2 ±10.9	4.4 ±0.1	1.9 ±1.0	2.9 ±0.5

Transmission electron microscopy (TEM) is required to observe the primary carbides in more detail. Selected-area diffraction (SAD) pattern analysis can be used to confirm the carbide species based upon their crystal structures and unique lattice parameters. TEM foils were prepared from the M50NiL material in the carburised case using the FIB-SEM. Figure 4.10 shows a TEM bright field image from a representative region of the carburised zone displaying two different primary carbides within a martensitic matrix. Smaller precipitates with a plate-like morphology are also seen in amongst twinned regions of the material [Figure 4.10 a]. These are thought to be the temper carbides, and are seen to grow along twin boundaries in the same way as that shown previously for M50 bearing balls [Figure 3.17].

Diffraction pattern analysis of the two primary carbides reveals the presence of the chromium-rich $M_{23}C_6$ phase, together with the vanadium-rich MC carbide [Figure 4.10 b]. The presence of an amorphous ring within the diffraction pattern is thought to be an artefact resulting from FIB damage caused to the carbides during ion milling. These SAD pattern observations together with the EDX data suggest that the $Cr_{23}C_6$ primary carbide species is present in the M50NiL case together with Mo_6C and VC.

Characterisation of the smaller temper carbides using the relatively large SAD aperture proves difficult. The selected area aperture is approximately 500 nm in diameter, so even when positioned correctly over the carbides it will still collect unwanted signal from adjacent phases. There a far fewer of these temper carbides in M50NiL compared with through-hardened M50, and their nanoscale size provides a weak scattering cross-section giving low intensity diffraction patterns. Dark field imaging can help to identify the phases of interest, however: by restricting the transmitted beam to only those electrons scattered by a specific crystal plane the dark field image shows strong intensity in only those regions of the material that contribute. Figure 4.11 shows dark field imaging of the temper carbides from Figure 4.10 with their respective diffraction patterns. Although it has not been possible to accurately identify this temper carbide species, they appear to grow along twin boundaries in the same way as that identified in through-hardened M50 for cementite [Fig 3.16 c].

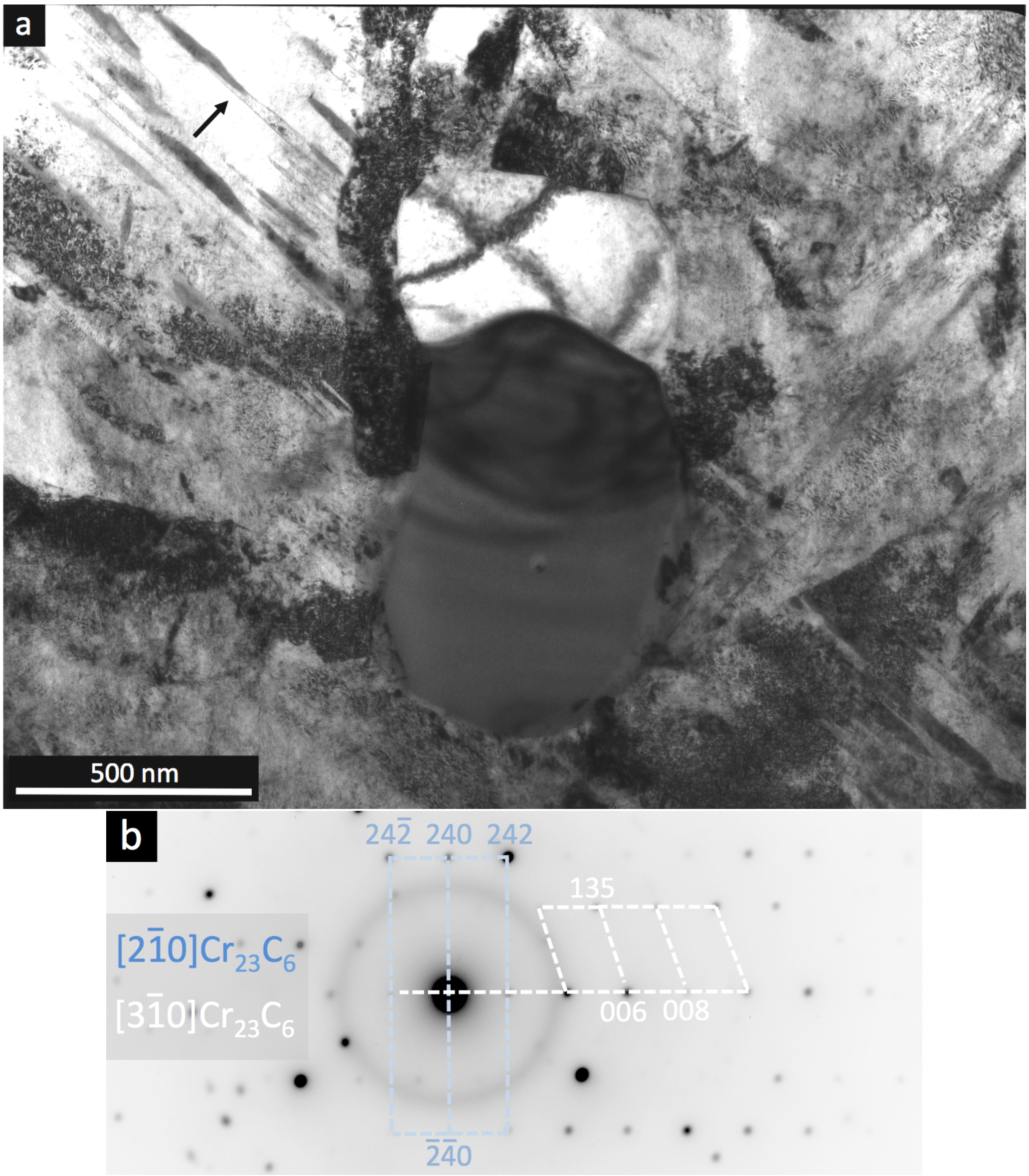

Figure 4.10: (a) Bright field TEM micrograph of two primary carbides in the M50NiL carburised case. Temper carbides are also seen adjacent to twin boundaries (indicated). (b) SAD patterns of the primary carbides central to the image above.

Figure 4.12 contains further evidence for temper carbide nucleation along twin boundaries in M50NiL. The effect is extensive and can even be seen under the SEM with the appropriate channeling contrast imaging techniques [Figure 4.12 a]. The common alignment of these temper carbides indicates a preferred growth direction [Figure 4.12 b]. Song et al. (2002) identified the temper carbides in M50NiL steel as M_2C phase: an orientation relationship was also identified between these molybdenum-rich secondary carbides

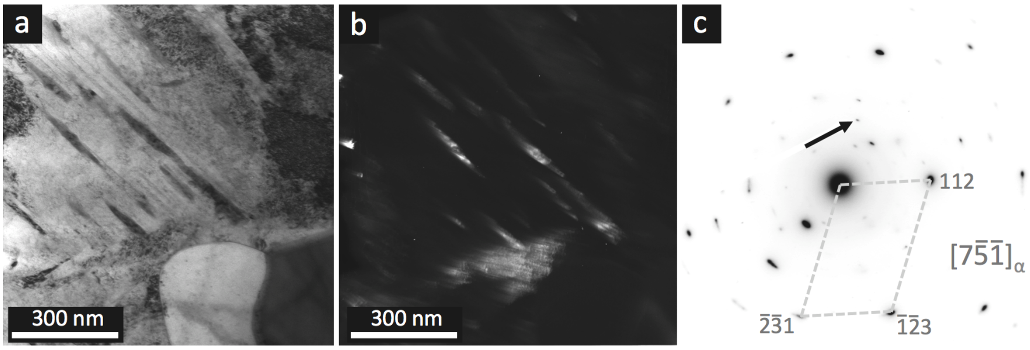

Figure 4.11: (a) Bright field, (b) dark field, and (c) SAD pattern from a region containing temper carbides in the M50NiL case. The dark field image is given by the diffraction spot indicated.

and the ferrite matrix [103]. Confirmation of the carbide phases which form during the tempering of M50NiL raceways could be performed using x-ray diffraction. The non-uniform carbon concentration in the carburised case would influence the stable phases as a function of case depth however, making XRD analysis difficult.

Twinned material is common in the carburised M50NiL microstructure. TEM foils from ex-service bearings and unused material all show widespread twinning in the carburised M50NiL. It is common to see twinning in high-carbon martensite as this shear mechanism can accommodate strain after transformation [215, 216, 217]. Figure 4.13 shows examples of transformation twinned martensite exhibiting uncharacteristic curvature [Figure 4.13 a],

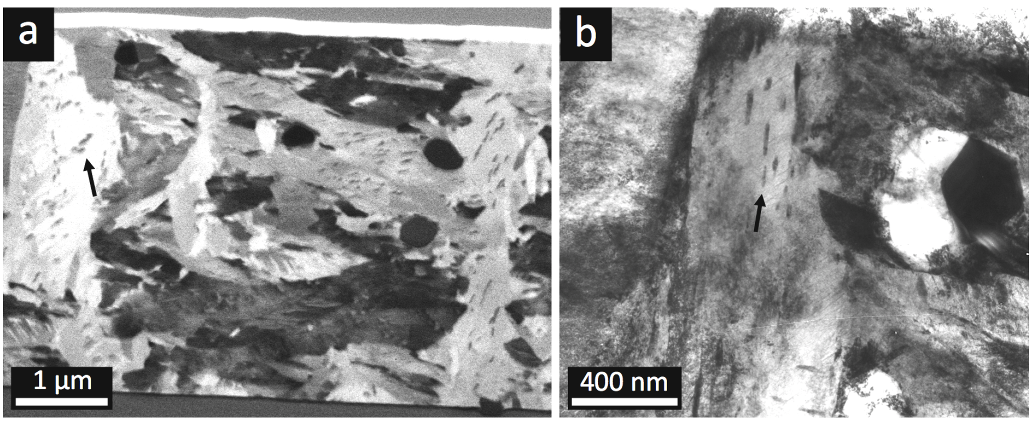

Figure 4.12: (a) Channeling contrast SEM image of secondary carbides at twins in the M50NiL carburised case. (b) TEM micrograph showing secondary carbides aligned in a common direction.

and twins crossing over plate boundaries into neighbouring martensite [Figure 4.13 b]. Since a coordinated crystallographic shear is required, these observations imply subsequent deformation or transformation events after the initial twin nucleation. Liu et al. (2011) observed curved twins in martensitic steels and attributed them to the hot deformation processing of steels [218]. The presence of curved transformation twins in M50NiL would suggest that some similar type of mechanical deformation process is experienced after the hardening heat treatments, either during manufacture or service. Besides these transformation features, an altogether separate twinning morphology has been identified in the carburised M50NiL raceways which also suggests mechanically induced deformation.

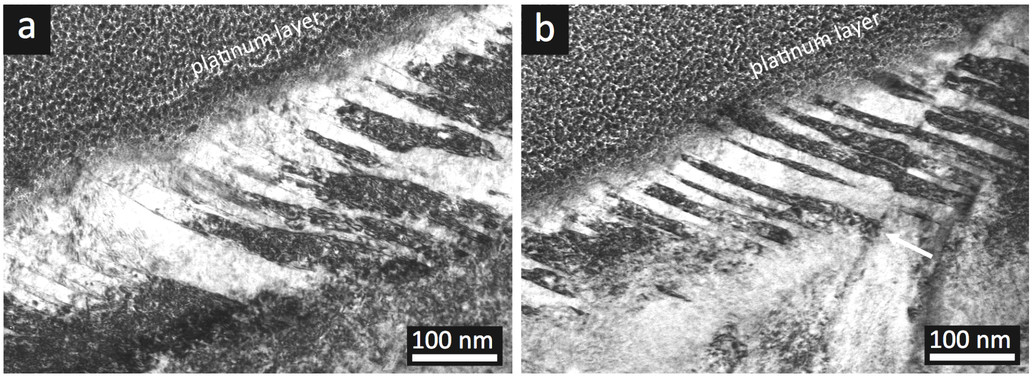

Figure 4.13: (a) Curved transformation twins in the M50NiL carburised case. (b) Twinning is seen either side of a martensite plate boundary.

4.3 Localised Twinning

TEM foils prepared from ex-service bearings exhibit localised twinning in the carbide-rich zone beneath the contact surface of M50NiL raceways. Figure 4.14 shows mechanically twinned martensite adjacent to an M_6C primary carbide. The twins appear to have initiated at the interface, presumably because of strain incompatibility between the carbide and the matrix [Figure 4.14 a]. The twin morphology is inconsistent with transformation twinning, and displays a fine lenticular character with narrow widths on the order of 10 nm. Mechanical twinning can accommodate plastic strain through a co-ordinated crystallographic shear deformation that results in a reversal of the interplanar stacking sequence about the twin plane. In BCC ferrite, this occurs on the $\{112\}$ planes in the $\langle 11\bar{1}\rangle$ directions, and confirmation of the deformation is provided by diffraction pattern analysis [Figure 4.14 b].

Figure 4.15 shows another TEM micrograph from M50NiL raceways after

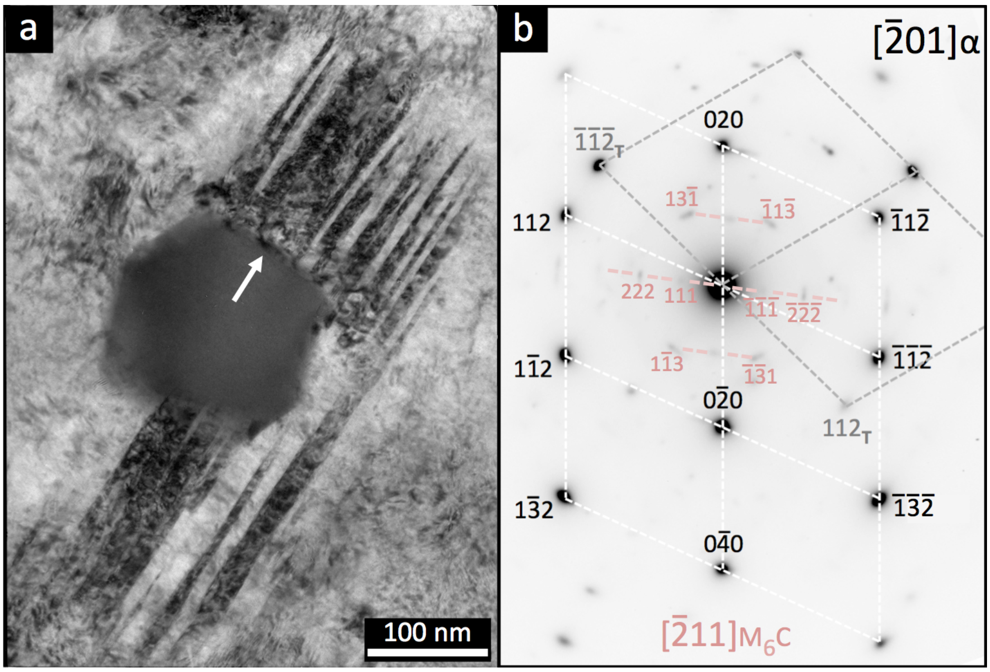

Figure 4.14: (a) Primary carbide with neighbouring mechanical twins in carburised M50NiL. (b) SAD pattern from this region shows twinned ferrite and M_6C.

engine operation. Mechanical twinning is seen again in the matrix adjacent to primary carbides and SAD pattern analysis has been used to confirm the presence of twinned martensite [Figure 4.15 b]. A dark field image was taken by restricting the transmitted beam intensity to only those electrons scattered by the twin reflection [Figure 4.15 c].

It appears that the strain concentration surrounding the primary carbides in

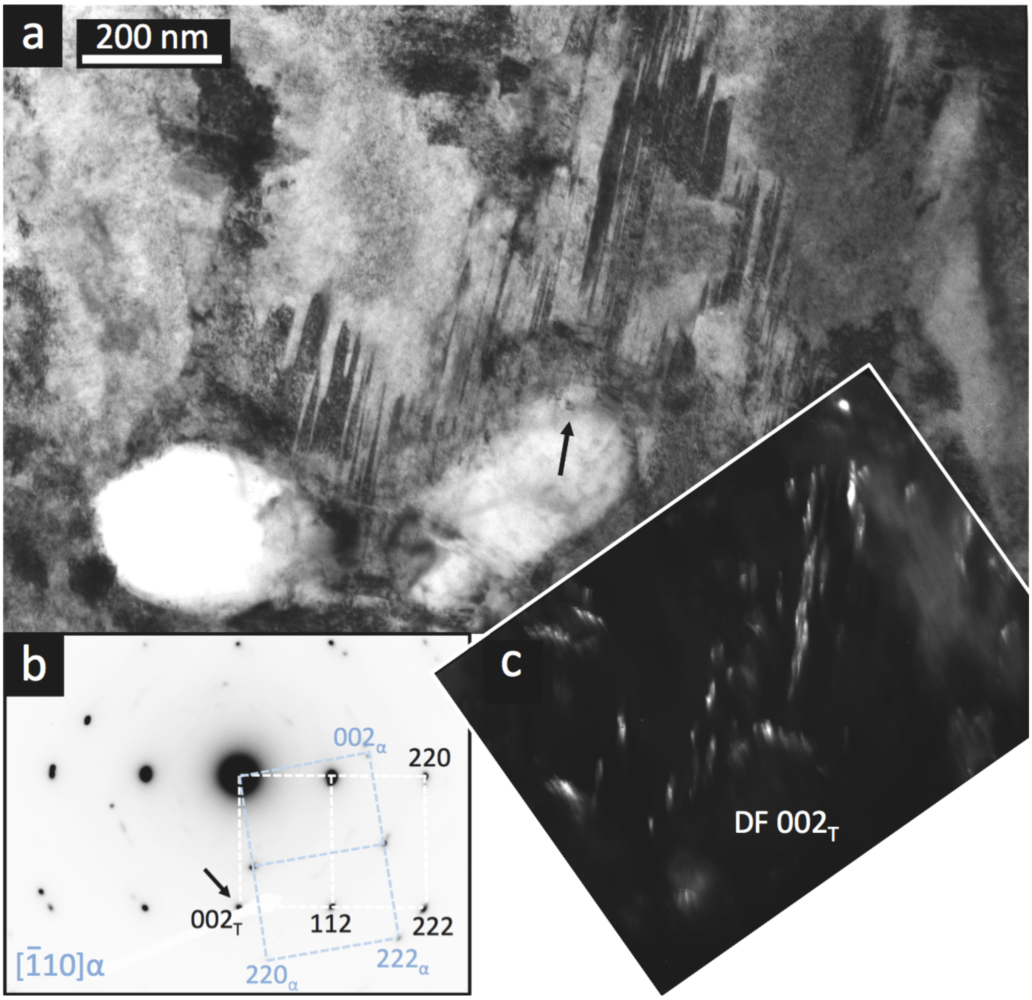

Figure 4.15: (a) Primary carbides in carburised the M50NiL with neighbouring mechanical twins. (b) SAD pattern indexed for twinned ferrite. (c) Dark field image of the same region showing only the $(002)_T$ twinned material.

Figures 4.14 and 4.15 has led to microscopic plasticity in the matrix. In the high-carbon case of M50NiL steel raceways the accommodation mechanism is through a localised twinning shear which acts to accommodate the strain at the carbide interface. The primary carbides themselves are mostly small in size and should not present any immediate risk of fracture, however much larger inhomogeneities have also been observed in the carburised case which may be more significant to the fatigue properties.

Irregular etching features are revealed in the carburised case of M50NiL raceways when polished and etched with a 3% nital solution. Figure 4.16 shows the non-linear morphologies of these localised etching features which are seen in all the M50NiL material examined, including the unused material (0 h). The features are widespread and cover large distances in excess of 200 μm, often intersecting the contact surface itself [Figure 4.16 b]. At higher magnification, SEM imaging reveals the features possess internal arrays of parallel plates [Figure 4.16 c]. The plates show no discernible atomic contrast to the matrix when viewed using backscattered-electron imaging [Figure 4.16 d]. High resolution imaging on the FIB-SEM finds the plates accumulate near interfaces and decorate prior austenite grain boundaries [Figure 4.16 f].

FIB milling was performed along one of the etching features in order to produce a TEM foil containing the plates for further examination. Figure 4.17 describes the H-bar preparation technique for creating thin TEM lamellae using FIB milling. A layer of platinum is sputter deposited onto the etching features to protect the internal plates during the milling process [Figure 4.17 b]. Once the sample has been milled it can be lifted out by platinum welding it to a thin needle-like probe. The sample is transferred to a copper TEM grid and then carefully thinned using a low ion beam current for improved electron transmission in the TEM. The M50NiL foil in transmission shows a bright zone beneath the platinum layer containing diagonal twins and plate-like features [Figure 4.17 d]. Tilting the TEM foil alters the dislocation contrast in the bright zone and causes the diagonal plate features to fade in and out of focus, suggesting they are artificial, but SAD patterns within this zone confirm twinned martensite [Figure 4.17 e].

The etching features in carburised M50NiL have been identified as large networks of twinned material. These features etch darkly due to the high density of twin interfaces within them. This effect is similar to that shown previously for martensite plates with twinned midribs that etch darkly in the carburised case [Figure 4.8 a]. The etching twin networks follow irregular paths however that deviate from the strictly linear midrib of martensite plates, and they also extend far beyond the individual martensite plate length [Figure 4.16 b].

Further examples of locally twinned regions in the carburised microstructure of the M50NiL case are presented in Figure 4.18. TEM foils were pre-

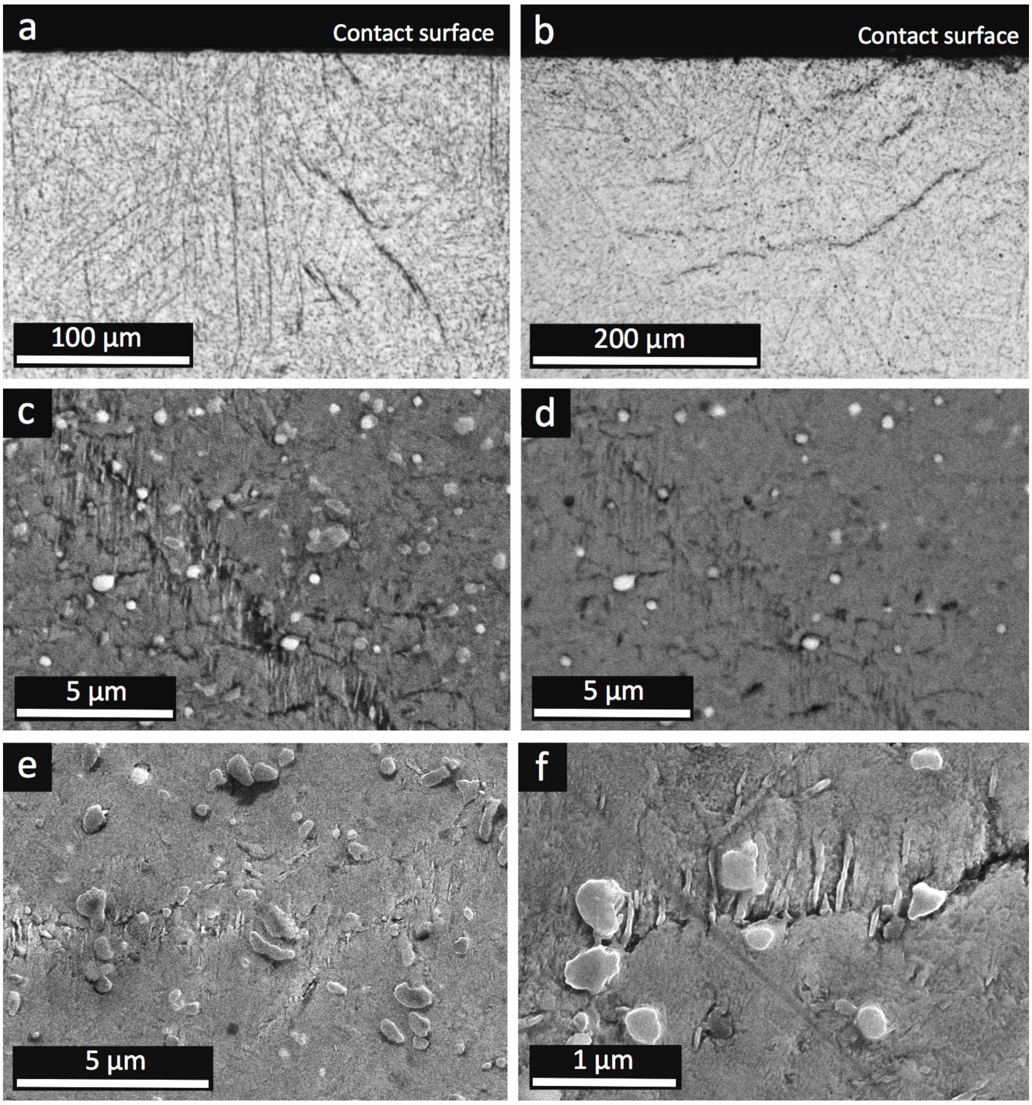

Figure 4.16: (a) Cross-sectioned M50NiL raceways show etching features in the carburised case. (b) Features follow non-linear paths and intersect the contact surface. (c) Secondary electron image of etching features show internal parallel plates. (d) Backscattered-electron image of same region shows no compositional contrast. (e) FIB-SEM imaging finds the plates decorate interfaces. (f) Plates found along a prior austenite grain boundary.

pared using the same FIB milling H-bar technique as before, and were then imaged using the ion beam to show channeling contrast [Figure 4.18 a]. The twinned region directly beneath the platinum interface displays an undulated topography which is responsible for the plate-like internal appearance of the etching features [Figure 4.18 b]. By way of comparison, the twinned midrib of a martensite plate is seen to display a very similar morphology to the localised etching features [Figure 4.18 c]. The similarities seen between the

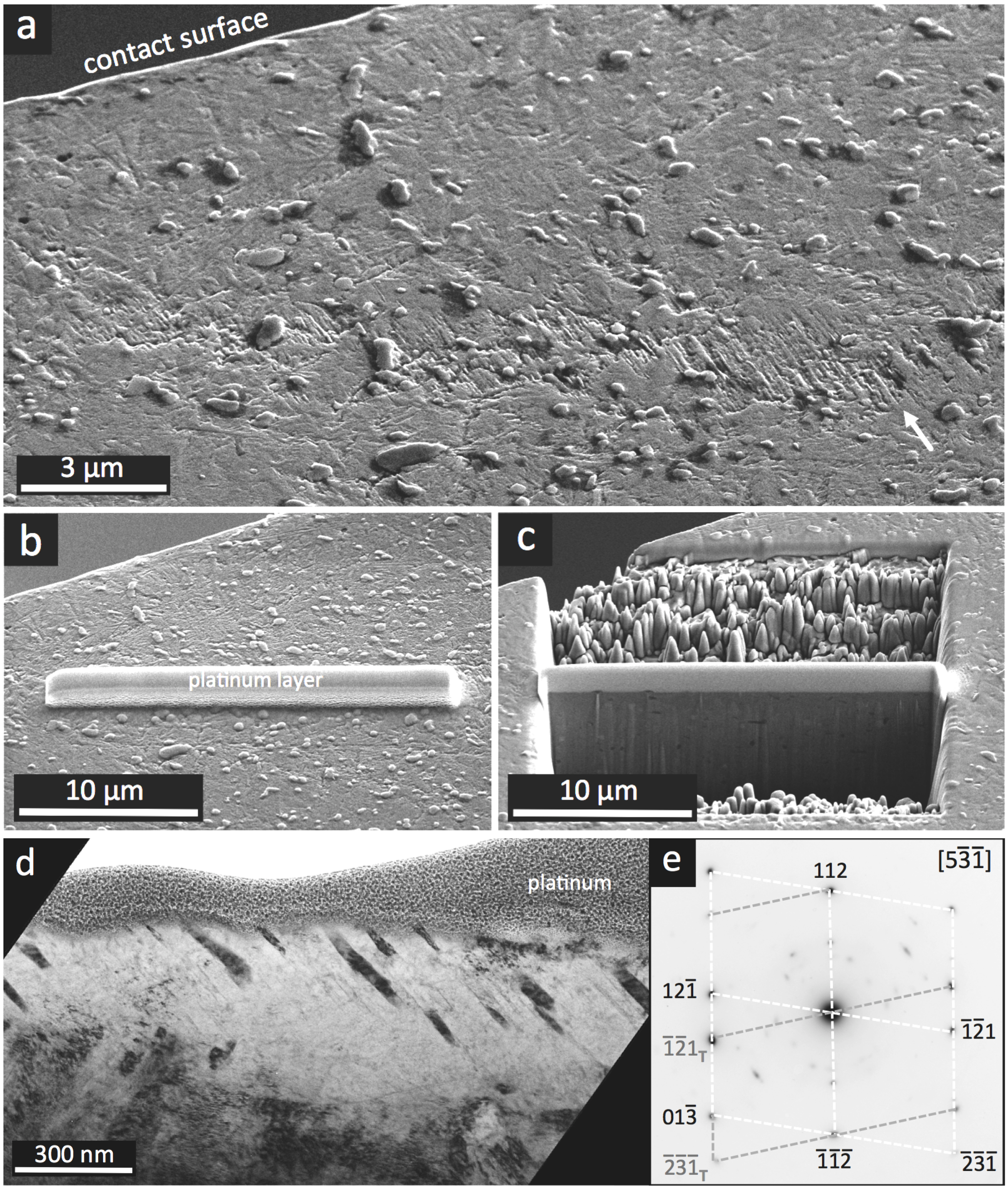

Figure 4.17: (a) An etching feature showing internal plates is selected for further study. (b) Plates in the selected region are protected by a layer of platinum. (c) Surrounding material is milled away in the shape of an H-bar using the FIB. (d) The finished lamella shows diagonal twin boundaries beneath the platinum layer. (e) SAD pattern from this region confirms twins.

etched martensite plates and the larger etched twin networks suggest they are both caused by strain accommodation effects: mechanical twins nucleate at prior austenite grain boundaries in the M50NiL case, analogously to the strain induced twinning seen at primary carbide interfaces [Figure 4.14].

These new observations provide evidence for a previously unreported mi-

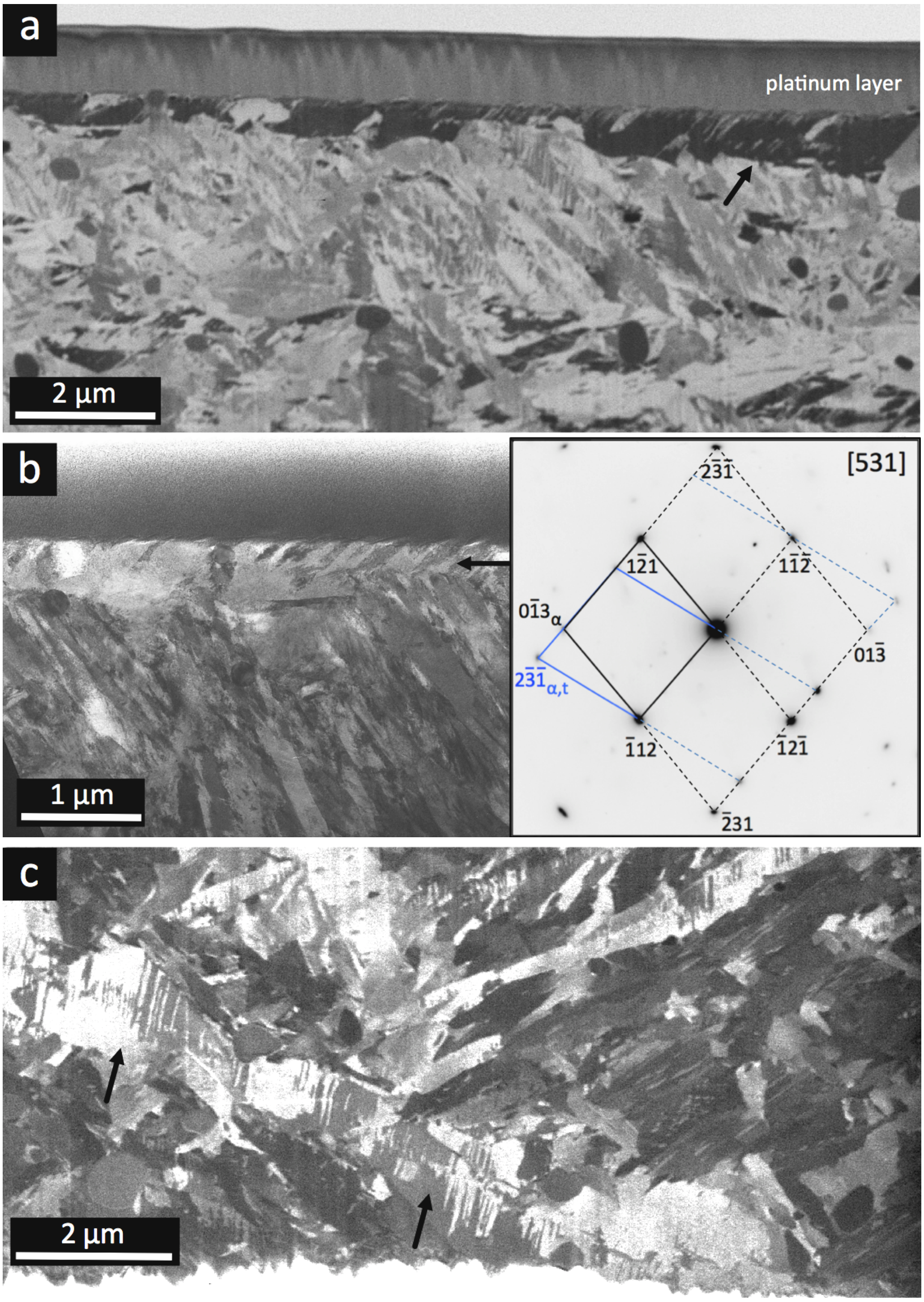

Figure 4.18: (a) Localised twinning in the M50NiL carburised case beneath the platinum layer (indicated). (b) The twins show an undulating topography beneath the platinum layer. (c) Martensite plates show extensive twinning along their central midribs (indicated.

crostructural deformation mechanism in aircraft bearing steels [2]. The concentration of strain at interfaces such as grain boundaries and primary carbides acts as a source for mechanical twin nucleation, given the knowledge that twinning is normally initiated by some defect configuration [216]. In the presence of an external stress field, these regions of increased local strain will be more able to yield, and this plasticity is accommodated through a twinning shear. This behaviour is inherent to the carburised material because the large twin networks were observed in all the M50NiL bearing steel examined, including the virgin microstructure (0 h). Twinning at the interface between carbides and the matrix was only observed in the ex-service bearing material, however.

It is unclear whether these new observations constitute evidence of a damage mechanism that can arise during bearing operation. Yet, it is likely that the presence of such large-scale inhomogeneities in the microstructure is not beneficial to fatigue properties. Evidence has been found that suggests twinned material in M50NiL can itself exhibit a stress raising effect. Figure 4.19 contains examples of surface damage on ex-service M50NiL raceways after 30,000 operation. The damage locations are shown to coincide with the intersection of etched martensite plates impinging on the surface [Figure 4.19]. It was shown previously that the high-carbon martensite etches dark due to internally twinned midribs, therefore it might be expected that the twinned plates would display brittle behaviour. Under RCF, stress concentrations at these features leads to localised damage where the twin networks intersect the contact surface.

Issues of large-scale twin networks along grain boundaries could be minimised by more careful grain refinement during heat treatment and processing. It was shown earlier that grain growth occurs during lengthy carburisation heat treatments resulting in an excessively large prior austenite grain size [Section 4.2]. The parent austenite grain size dictates the martensite plate length where twinning occurs along the central midrib. A more homogeneous microstructure with a reduced martensite plate length may also improve potential issues of damage at twinned material near the contact surface. Finally, the precipitation of temper carbides takes place along twin boundaries in both M50 and M50NiL [Figure 4.11]. The presence of large-scale twin networks will encourage the subsequent growth of temper carbides along these twins, leading to grain boundary carbide precipitation. Fatigue

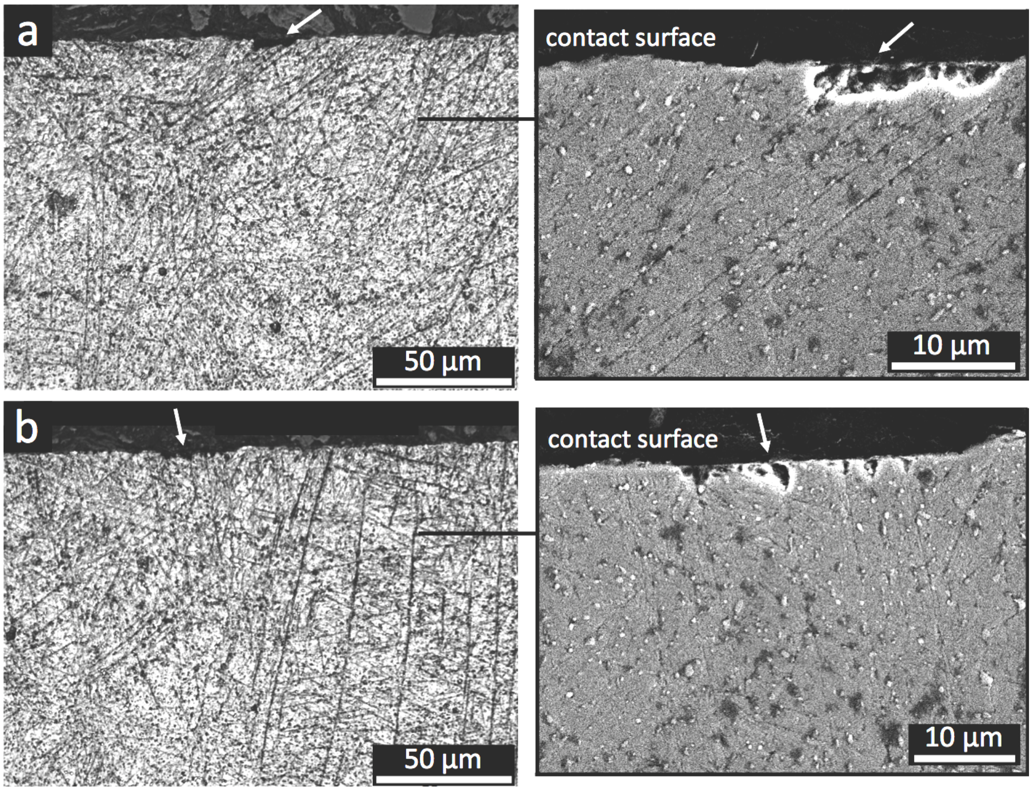

Figure 4.19: (a) Damage at the contact surface of ex-service bearing raceways occurs where twinned martensite plates intersect the surface. (b) Surface breaking twinned material is inhomogeneous and seen to correlate with damage.

cracks have been seen to travel along grain boundaries in M50 but no intergranular cracking has been seen in M50NiL.

4.4 Summary and Conclusions

Microstructural features that develop in M50NiL bearing steel raceways have been identified after periods of operation in the aircraft gas-turbine engine. Curved kinematic marks at the surface describe sliding conditions during service and the spinning of bearing balls [Figure 4.2]. Kinematic marks are caused by the segregated residual carbides on the bearing ball surfaces [Section 3.1].

Directly beneath the kinematic marks is a shallow zone of plastic flow that runs parallel to the tangential shear direction [Figure 4.4 b]. This deformed zone penetrates only to depths of between 1 - 2 µm. The sheared martensite plates in this region become increasingly deformed with continued service until after 30,000 h a nanocrystalline layer of equiaxed ferrite has formed [Figure 4.6]. This rehardened and embrittled surface layer should be less able to resist cracking, so its development provides a novel mechanism for initiating surface fatigue failures in aircraft location bearings that has never before been reported [1]. The observations of severe plastic deformation at the surface result from sliding during bearing operation, poor component tribology and insufficient hardness at the raceway surfaces to resist plastic flow.

The carburised M50NiL microstructure contains large etching features that

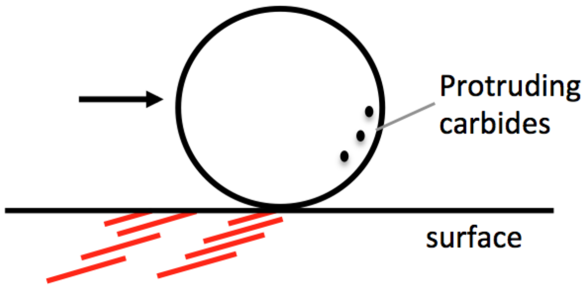

Figure 4.20: Residual carbides on the surfaces of M50 bearing balls cause plastic deformation of M50NiL raceways through sliding and surface shear during operation.

are widespread networks of mechanically twinned martensite [Figure 4.16]. The twin networks decorate interfaces such as prior austenite grain boundaries, and instances were found where mechanical twins had initiated at the interface between primary carbides and the matrix [Figure 4.14]. The stress raising effect of inhomogeneities in bearing steel microstructures is well known, but these new observations reveal a unique damage mechanism never before reported in bearing steels [2]. The diagrams in Figure 4.21 describe this new strain localisation mechanism under rolling contact loading conditions: mechanical twinning will first initiate at stress raising defects in those particular grains at the appropriate orientation to the Hertzian contact stress axis, such that the $\langle 11\bar{1} \rangle$ twin directions lie close to the 45° shear stress.

Large-scale twin networks in M50NiL microstructures are likely to be detri-

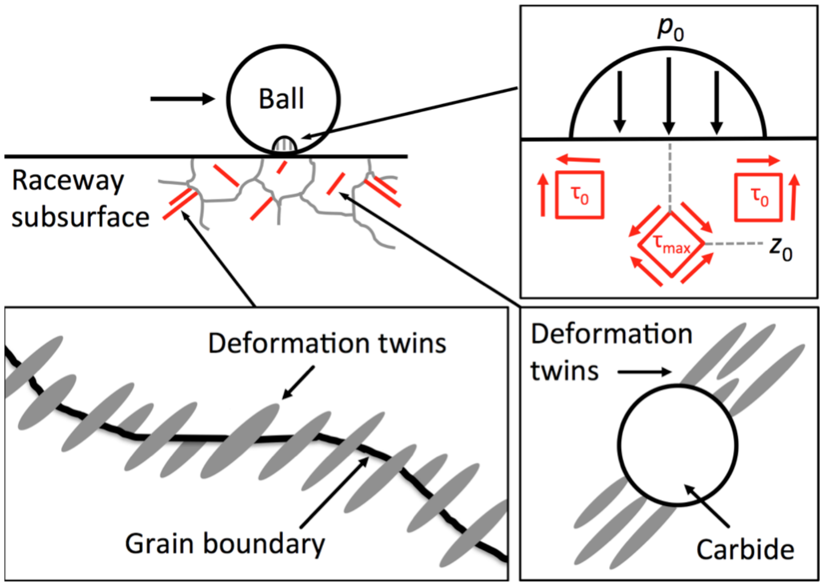

Figure 4.21: M50NiL bearing steels under rolling contact loading exhibit a strain accommodation mechanism through localised mechanical twinning.

mental to the fatigue performance of these aircraft bearing steels. Any inhomogeneity in the stressed volume will act to amplify the applied RCF loads, so the widespread twinned interfaces in carburised raceways represent microstructural defects entering service. Evidence was provided showing instances of localised surface damage which coincided with twinned martensite plates intersecting the contact surface [Figure 4.19]. Whilst rare, these new observations confirm that undesirable properties are exhibited by the twinned material that may reduce aircraft bearing steel performance.

Chapter 5

Material Property Changes

The mechanical properties of a material are intrinsically linked to microstructural features such as grain size, precipitate morphology and phase. Chapters 3 & 4 have focused on characterisation of the ex-service bearing steels for evidence of microstructural change, but an additional approach is to identify changes in the material properties. In this chapter the hardness, residual stress distribution and preferred crystallographic orientation in the ex-service bearing steels are examined using a range of analytical techniques.

Experimental Method

Vickers hardness measurements are taken as a function of carburised case depth in M50NiL raceways and on the surface of M50 bearing balls using the Mitutoyo MVK-H2 micro-hardness indenter with a 200 g load. Residual stress measurements are gathered by X-ray diffraction (XRD) analysis of the ferrite $\{211\}_\alpha$ peak position and full width at half maximum (FWHM). These data are obtained using the Bruker D8 Discover goniometer at the SKF engineering and research centre, Nieuwegein, The Netherlands. Preferred crystallographic orientation in the ex-service raceway microstructures is examined using electron backscatter diffraction (EBSD) on the CamScan MX2600 SEM. Indexing of Kikuchi bands near the deformed contact surface proved unsatisfactory so an alternative approach utilises XRD. Average grain orientation is interpreted from analysis of multiple ferrite pole figures, obtained using peak intensity data gathered on the Bruker D8 Discover goniometer at the University of Manchester's Henry Moseley X-ray Laboratory, U.K.

5.1 Microhardness Testing

Vickers microhardness indentation has been performed on surfaces of through-hardened M50 bearing balls and on cross-sections of carburised M50NiL raceways as a function of depth beneath the surface and contact angle. Indentations were made using a low load of 200 g to produce a smaller indent for a more localised measure of hardness. This also allows closer proximity between neighbouring indents, which as a general rule was greater than three times the diameter of each indent. For example, a series of 20 µm indents would be spaced 60 µm apart. Softer material like that in the M50NiL core produces wider indentations and so require larger spacings between adjacent indents. Placing hardness indentations too close to a free surface will also influence the indent morphology, so care must be taken when approaching the contact surface in cross-sectioned samples.

Figure 5.1 shows images of Vickers microhardness indents made at the contact surface of ex-service bearing balls. The characteristic diamond shaped indents have a width that is inversely proportional to the material hardness, according to:

$$HV = \frac{2\sin(136^\circ/2)F}{d_1 d_2} \tag{5.1}$$

Where d_1 and d_2 are the two diagonal lengths of the indent in mm, and F is the test load in kg. In this investigation the chosen load is 200 g, therefore $F = 0.2$. Care must be taken to choose an appropriate location when placing indents, since local microstructural features such as large residual carbides can influence the hardness measurement [Figure 5.1 a]. A number of indents were purposefully placed in regions showing plastic deformation on the M50 ball surfaces to investigate the properties of this damaged material [Figure 5.1 b].

Figure 5.2 contains microhardness data for a number of M50 bearing balls after different operating lives. In the unused condition (0 h), ball surfaces have an average hardness of 850 ± 20 HV 0.2 (65 HRC). The surface hardness values after 30,000 h service display increased scatter [Figure 5.2]. In some cases the stressed material exceeds the baseline hardness, peaking at 900 HV 0.2 (67 HRC), but in regions displaying noticeable plastic deformation

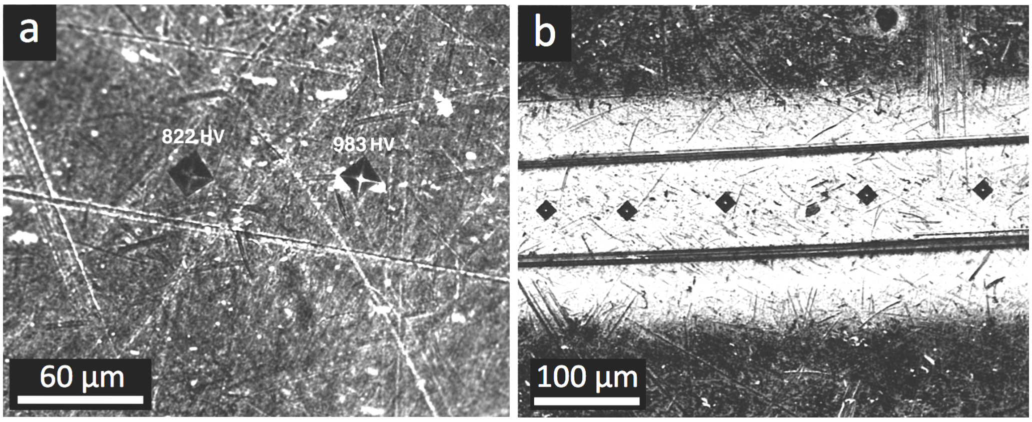

Figure 5.1: Vickers microhardness indents on the damaged surfaces of M50 bearing balls. (a) Large residual carbides can significantly influence the indent measurements. (b) Indents made within plastically deformed material.

the hardness values are reduced to 750 HV 0.2 (58 HRC). The increased scatter of the ex-service ball data will be partly affected by the heavily scratched surface and its influence on indent measurement accuracy. However, these variations may also indicate localised changes in material properties in M50 due to the effects of plastic deformation under surface shear.

Microhardness data for three M50NiL inner raceways with different op-

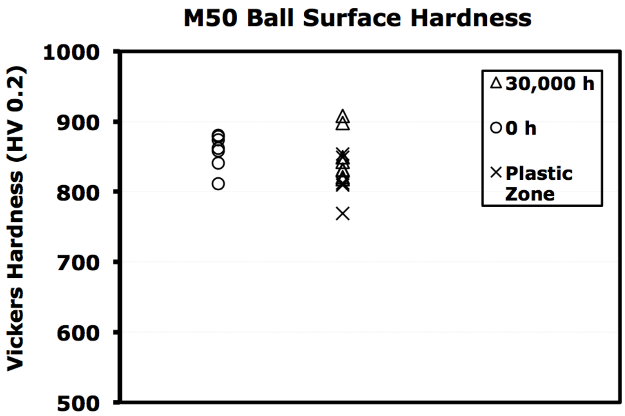

Figure 5.2: Microhardness data taken at the surfaces of M50 bearing balls in the unused condition (0 h) and after 30,000 h. Particular attention was paid to the damaged material on the 30,000 h ball (plastic zone).

erating lives are given in Figure 5.3 as a function of depth beneath the contact surface. All three samples show a characteristic hardness gradient with depth that is consistent with a case-hardened microstructure after carburisation [81]. The unused raceway material (0 h) shows peak hardness values at the surface exceeding 800 HV 0.2 (64 HRC), which gradually fall to 480 HV 0.2 (48 HRC) in the core material beyond 3 mm in depth. The longest running ex-service raceway material (30,000 h) exhibited even higher hardness values at the contact surface, peaking at 900 HV 0.2 (67 HRC). An elevated hardness profile is seen in the first 1 mm case depth before values fall, tending to a similar hardness profile as the virgin material beneath 1 mm. The intermediate service bearing raceway (120 h) displays an overall hardness gradient similar to the 0 h raceway material, with little deviation at the contact surface [Figure 5.3].

The increase in hardness found at the surface of the 30,000 h sample is

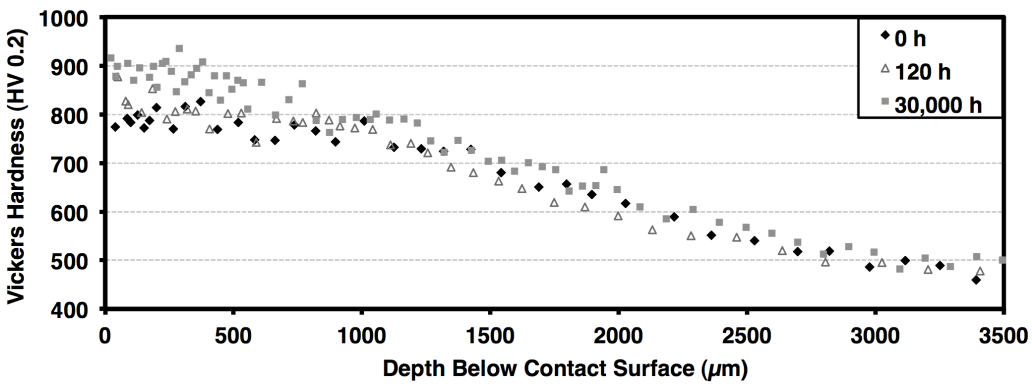

Figure 5.3: Microhardness data for M50NiL raceways of varying service lives. A general hardness gradient is present in all cases due to carburisation but an increase is apparent after 30,000 h.

evidence of work-hardening in M50NiL raceways during aircraft operation. The general hardness profile at depths beyond 1 mm is consistent across all three raceways, so the noticeable increase in surface hardness after 30,000 h is likely caused by the action of rolling contact fatigue stresses, which are a maximum at shallow depths of less than 1 mm [Section 2.1]. The absence of any substantial hardness increase in the 120 h raceway suggests that work-hardening develops slowly in M50NiL, requiring prolonged rolling contact. This mechanism of gradual strain accumulation is different to the reports of work-hardening in the lower-alloyed 52100 bearing steel, which instead take place during stages of rolling contact loading [74].

The degree of scatter in the microhardness data may affect interpretation. Human error can influence the measurement of indent diameters, especially at the low 200 g loads which produce smaller indents. This effect is particularly acute nearest the contact surface, where the hardness of carburised M50NiL is greatest and the indent diameters are at their smallest. To overcome this issue a disproportionate number of additional measurements were made near the contact surface to improve the statistical average. In this way the standard deviation of indent diameters remains relatively constant as a function of depth, at ±25 HV. The choice of indent location as a function of raceway contact angles may also result in statistical variations. It was shown in Section 4.1 that when location bearings operate under thrust loads the contact angle is asymmetrical. In order to study the effects of rolling contact stress during service the hardness measurements should ideally be taken at contact angles which have experienced the majority of rolling history. The exact position of maximum rolling can only be estimated, so a further study was conducted to examine the M50NiL hardness profile over a range of contact angles.

Figure 5.4 describes the cross-sectioning process used to prepare the 120 h ex-service bearing inner raceway for hardness measurement. Tangential slices were taken at a number of displacements between 0° - 20° positions. Each slice is labelled according to its approximate distance from the central position (0 mm), so that the largest values correspond to the highest contact angles (e.g. 13 mm from centre is approximately 20°) [Figure 5.4]. Microhardness measurements of each slice were then taken as a function of depth beneath the carburised case, and these data are presented in Figure 5.5.

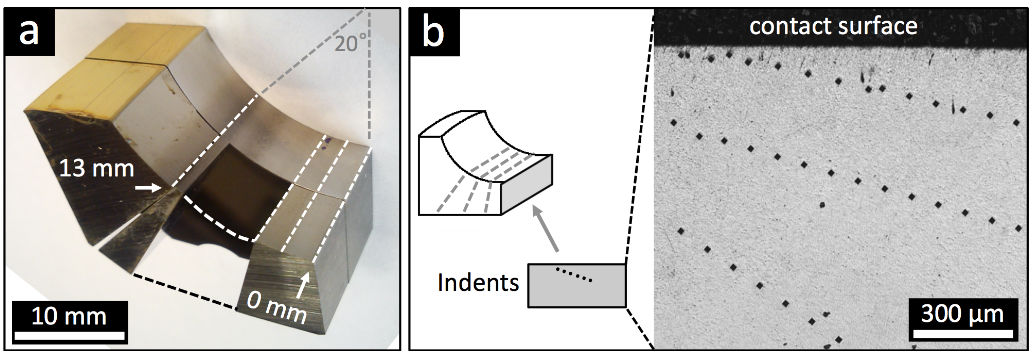

Figure 5.4: (a) M50NiL inner raceways after 120 h service have been tangentially cross-sectioned producing slices at different contact angles defined by their distance up the raceway groove. (b) Microhardness indentation is then performed on each tangential slice as a function of depth.

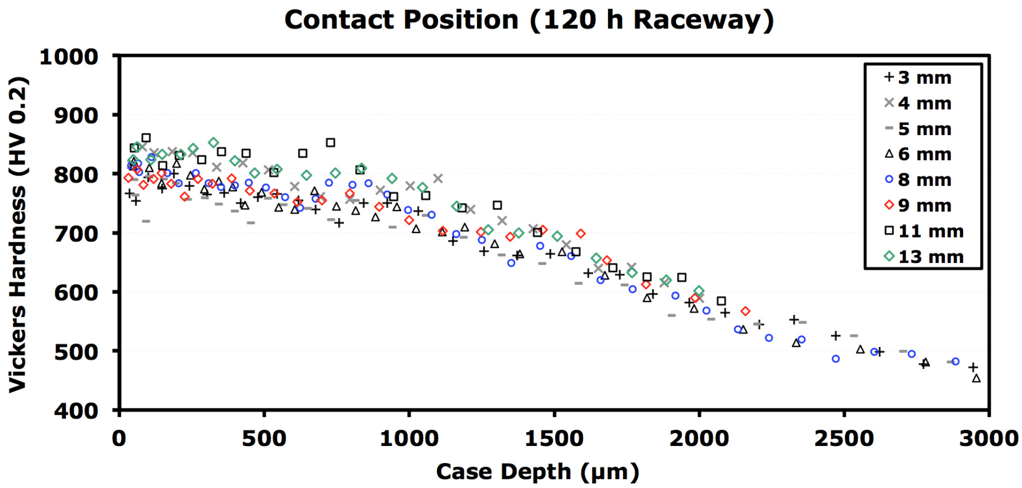

Figure 5.5: Microhardness data as a function of depth and contact angle for an M50NiL raceway after 120 h service. Hardness increases are seen at high angles furthest from the central axis (11 - 13 mm).

There is strong variation in the microhardness data for the 120 h raceway at different contact angles. This is most pronounced nearer the contact surface, where there is scatter of approximately ± 50 HV 0.2. This could be partly due to indent size effects mentioned earlier, but the degree of variation is actually specific to contact angle. The most significant hardness increases are shown at the 11 mm-13 mm positions, furthest from the central axis. This particular M50NiL inner raceway was already shown to exhibit numerous kinematic marks at these high contact angles after 120 h service [Figure 4.2 a]. Given the previous evidence of work-hardening near the surface after 30,000 h service, it is not unexpected to see similar hardness increases near the surface at these high contact angle locations where sliding has occurred. The degree of scatter may also have been influenced by the cross-sectioning procedure. Cutting away slices of material may relieve the compressive residual stress state present in these carburised raceways affecting the hardness behaviour of each slice under indentation.

5.1.1 Discussion

Evidence has been provided that shows work-hardening in the deformed M50NiL surface material after rolling contact loading in aircraft gas-turbine engines. Given the heavy contact loads during operation and the large numbers of fatigue cycles accrued during 30,000 h service, a strain-hardening effect such as this is not surprising. There are many examples in the literature of hardness changes in the low-alloy 52100 bearing steel [15, 74]. Voskamp (1985) reported work-hardening in 52100 soon after contact stress cycling begins, where an initial running-in stage takes place during the earliest fatigue cycles, $N \leq 10^3$ [Section 2.1.2]. This may be different to the behaviour of M50NiL shown in the present work, where the hardness increase appears to be a more gradual phenomenon [Figure 5.3]. Intuitively, the accumulation of strain in the microstructure through dislocation pile-up should increase in proportion to the amount of stress cycling: The longer the time spent in service, the more developed and noticeable the work-hardening effect should be.

Scatter in the microhardness data, such as that evident in Figures 5.2 and 5.5, make the process of reaching strong conclusions more uncertain. There may well be some work-hardening effect in the M50NiL raceways after only 120 h at high angles given the strong correlation with kinematic mark locations [Figure 5.5]. This evidence would suggest that hardness increases at the raceway surface increase in severity as a function of the amount of sliding in the contact ellipse.

Recently, other authors have begun to look at M50NiL bearing steels under rolling contact stress cycling [145, 219]. Bhattarcharya et al. (2014) found evidence of work-hardening in M50NiL test rods at very high contact stresses of 5.5 GPa that required a large number of stress cycles in order to develop. In their work, no hardness increases were seen after fewer than 4,000 stress cycles, requiring up to 10,000 cycles before the changes came about [219]. Arakere and Subhash (2012) also identified work-hardening under accelerated testing: the accumulation of significant plastic strain occurred after 10^7 fatigue cycles, however, which is sooner than the 30,000 h raceway sample in this study (approximately 10^{10}). The data presented in this thesis provide the first evidence for work-hardening of M50NiL material during actual service in aircraft gas-turbine engines where the contact stress is less than 2 GPa.

5.2 Residual Stress Evolution

M50NiL bearing raceways are known to exhibit compressive residual stresses in their case-carburised microstructures after heat-treatment [Section 1.2.3]. The depth over which these compressive stresses extend can be tailored with careful processing, for example by varying the duration and temperature of the carburising treatment. The intention is to produce a beneficial compressive stress at a depth where the maximum shear stresses due to RCF are expected, in order to improve the fatigue performance during service. For this reason it is important to characterise the residual stress profile of the carburised M50NiL raceways before entering service.

The residual stresses in lower-alloyed bearing steels can also be altered by stress cycling, reflecting changes in the microstructure that can occur under rolling contact fatigue [Section 2.1.2]. This section details experiments that have been performed to investigate the residual stress field in the carburised case of ex-service bearing raceways with the intention of comparing the unused M50NiL material with ex-service bearings after aircraft engine operation.

Experimental Method

An appropriate way to calculate the local residual stress at the surface of a component uses X-ray Diffraction (XRD) to measure strains in the polycrystalline lattice. Figure 5.6 shows the experimental setup for the residual stress investigation of M50NiL raceways. Variations in the interplanar spacings, d_{hkl}, are measured as a function of the orientation of the sample axes. With careful measurement of the Bragg angles (θ) for the scattered photons, the subtle shifts in 2θ peak positions can be used to quantify the interplanar elastic strain using the $\sin^2\Psi$ method [220]. Further analysis of the variation in 2θ peak full width at half maximum (FWHM) indicates the level of inelastic strain, after appropriate background corrections, and can even be used as an empirical measure of fatigue damage [126].

XRD measurements were performed using the Bruker AXS D8 Discover goniometer with Cr Kα radiation corresponding to an incident photon energy of 5.4 keV [Figure 5.6 a]. A collimated beam with 0.8 mm diameter aperture was targeted at the contact surface ellipse on the sectioned M50NiL raceways such that the tangential rolling direction lay in the plane of Ψ [Figure 5.6 d]. A fixed position Hi-star 2D detector is placed at the appropriate 2θ angle to measure the d_{211} scattered photons over a range of $2\theta = 149° - 160.2°$.

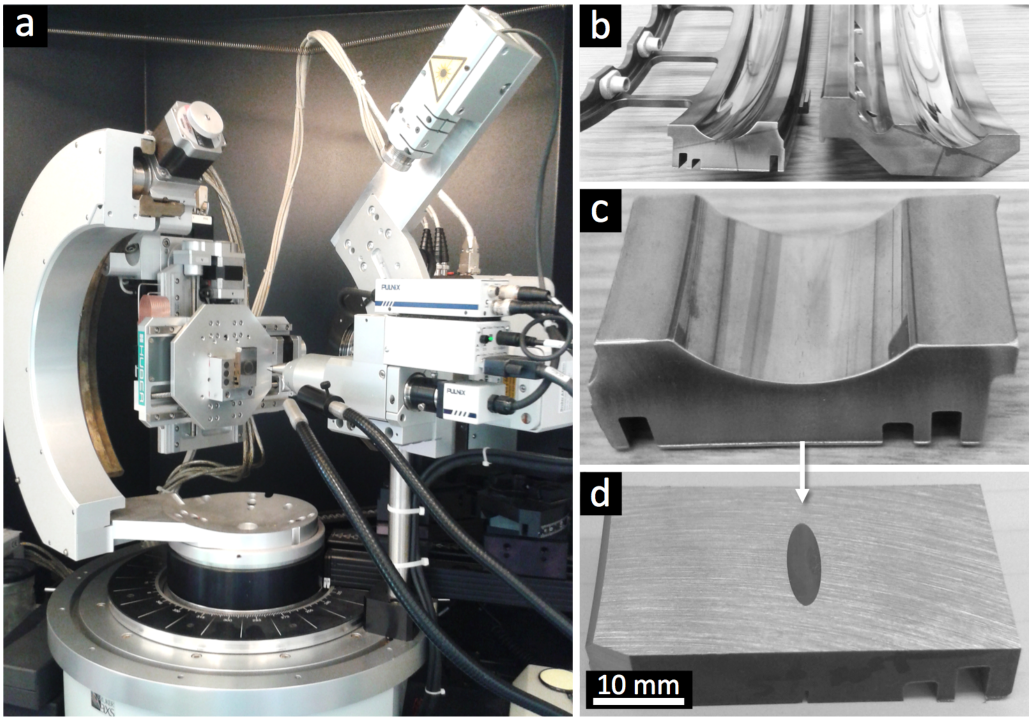

Figure 5.6: (a) Bruker AXS D8 Discover XRD goniometer. (b) Two M50NiL outer raceways from ex-service bearings. (c) The 6,515 h raceway in cross-section. (d) Finished 6,515 h sample after parallel grinding. Note, the tangential rolling direction runs vertically along the semi-major axis of the ellipse.

The sample is rotated through 11 positions in Ψ, ranging between $\pm 45°$, with a dwell time of 60 seconds for each d_{211} measurement. Data analysis is performed using Bruker Leptos software to plot the resulting spectra as a function of $\sin^2\Psi$, producing a graph of the interplanar strain in the tangential direction. Figure 5.7 contains example data to help demonstrate how the $\sin^2\Psi$ method is then employed to obtain the residual stress values. The trend line is evaluated using regression analysis and, assuming plane stress conditions, has a gradient equal to the in-plane stress, according to Equation 5.2:

$$\frac{d_{\Psi}^{\{hkl\}} - d_0}{d_0} = \epsilon_{\Psi}^{\{hkl\}} = \left(\frac{1+\nu}{E}\right)\sigma \sin^2\Psi - \left(\frac{\nu}{E}\right) \tag{5.2}$$

where $\epsilon_{\Psi}^{\{hkl\}}$ is the in-plane strain associated with a given $d_{\Psi}^{\{hkl\}}$ value, d_0 is the value of d_{hkl} at Ψ=0, σ is the residual stress, E is the elastic modulus and ν is Poisson's ratio [157]. The negative gradient displayed in Figure 5.7 indicates a compressive residual stress value of approximately -290 MPa.

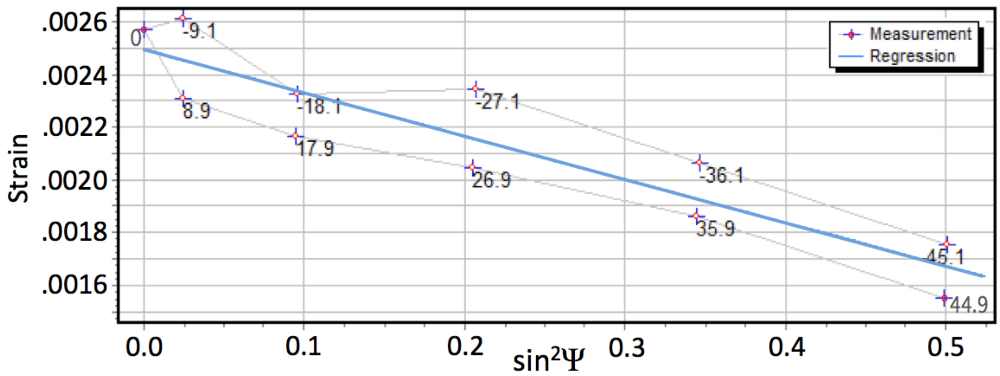

Figure 5.7: The variation in interplanar strain with Ψ angle allows evaluation of the in-plane stress in M50NiL raceways according to the the $\sin^2\Psi$ method of Equation 5.2.

After data collection the sample is taken out of the goniometer and a small amount of material is removed from the contact surface by electropolishing using the Struers A2 electrolyte (5.8% perchloric acid with ethanol). Between 20 - 30 µm of surface material is removed during this process before the sample is carefully loaded back into the goniometer at the same position to repeat the d_{211} measurement process at this new depth. The electropolishing steps are repeated again in regular increments until a total depth of between 800 - 900 µm has been examined. A micrometer is used to accurately measure the amount of material removed however there is still an error associated with the depth values of approximately ± 3%. Relaxation of the residual stresses by the removal of surface material is not thought to be a concern due to the large sample thickness, and historically this procedure has proved effective [20]. Vegter et al. (2015) have shown that this laboratory XRD technique correlates remarkably well with more precise synchrotron measurements of residual stress in 52100 bearing steel [221].

Figure 5.8 shows compressive residual stress profiles as a function of depth beneath the contact surface at three different contact angles in the unused M50NiL raceway (0 h) and in an ex-service raceway after approximately 30,000 h operation. The virgin M50NiL material displays a compressive residual stress profile in the carburised zone averaging between 200 - 400 MPa in magnitude [Figure 5.8 a]. The compressive stress field extends to case depths exceeding 800 μm, and there is no tensile stress component present at these depths. The immediate contact surface is in a state of high compressive stress between 600 - 700 MPa in magnitude, but this is only exhibited at shallow

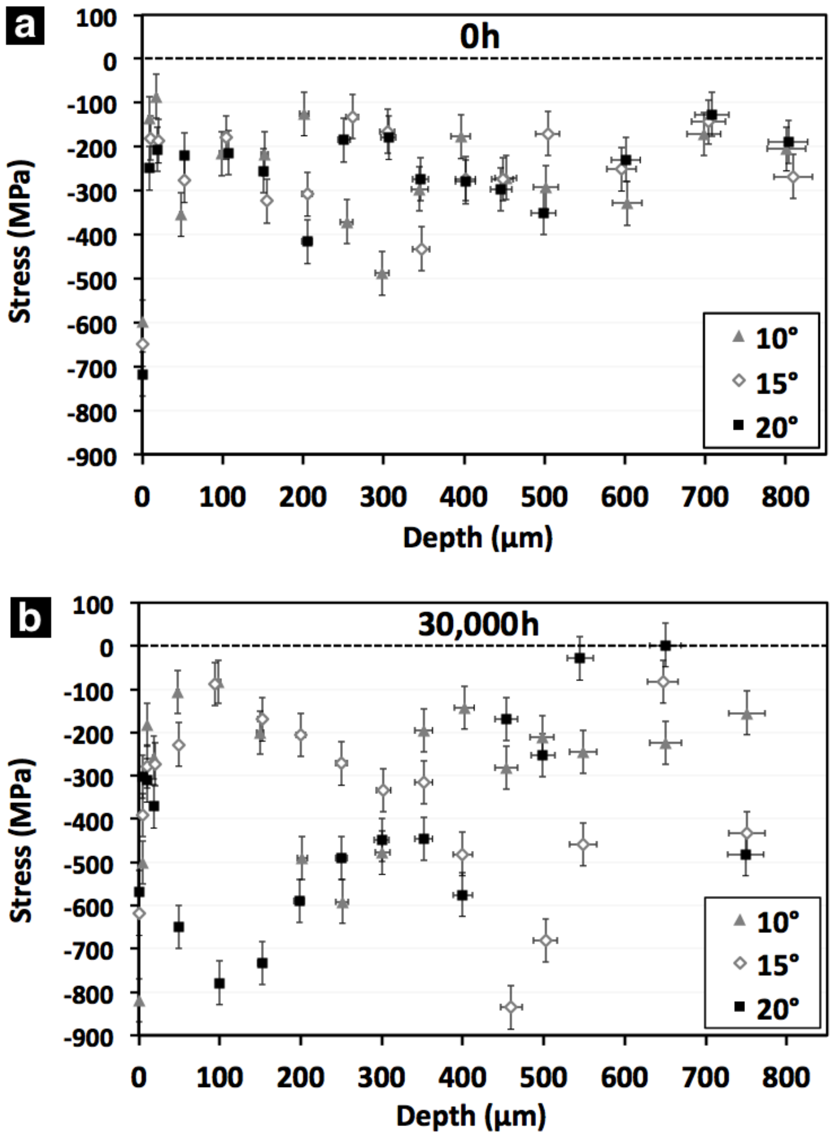

Figure 5.8: Residual stress data as a function of carburised case depth at three different contact angles (10°, 15° and 20°), for (a) a carburised but unused M50NiL raceway (0 h), and (b) after 30,000 h aircraft operation.

depths of less than 25 μm. These data suggest that manufacturing processes create highly localised compressive stresses at the component surface, and carburisation produces a general compressive stress profile quite deep into the M50NiL case. The noticeable degree of scatter between the three different contact angles in this unused raceway is unlikely to be caused by different processing treatments so this level of scatter is inherent to the carburised material itself. There is also an average uncertainty of ± 50 MPa associated with the fitting of each data point as estimated by the Leptos software.

Figure 5.8 b shows enhanced compressive stresses in the ex-service raceway material that are increasingly scattered after 30,000 h operation. The state of compression exhibited in the first 500 μm case depth far exceeds that shown in the unused material (0 h), now peaking at over 800 MPa in magnitude. There are also regions where the stress component appears reduced in magnitude at deeper locations of 600 μm case depth. The immediate contact surface remains in a state of high compressive stress between 600 - 800 MPa in magnitude, and this is still a shallow phenomenon. Although the carburised material is prone to statistical fluctuation, the increase in scatter after 30,000 h aircraft service suggests microstructural changes have occurred. The magnitude of the increased compressive stress varies as a function of contact angle: taking 100 μm case depth as an example, the range in stress is Δ 700 MPa, indicating local sensitivity to ball positioning under asymmetrical thrust loads [Figure 5.8 b].

The two intermediate life ex-service bearings (120 h and 6,515 h) were also examined using XRD, but due to time constraints only one contact angle was measured for each outer raceway. The positions showing the most significant surface damage were chosen for each sample, under the assumption that these regions of material had experienced the most severe stress cycling. For the 120 h raceway this contact angle was approximately 15° and for the 6,515 h raceway it was 5°. Figure 5.9 shows data comparing the residual stress profiles of all four ex-service bearing raceways. The data for the two intermediate raceways show a slight increase in compressive stress magnitude at case depths of around 200 - 300 μm [Figure 5.9]. It is at these depths where the maximum shear stresses are expected [Section 2.1.1]. Although interpretation of these data is difficult given the scatter, the general progression of compressive stress amplitude between 120 h - 6,515 h is consistent with the

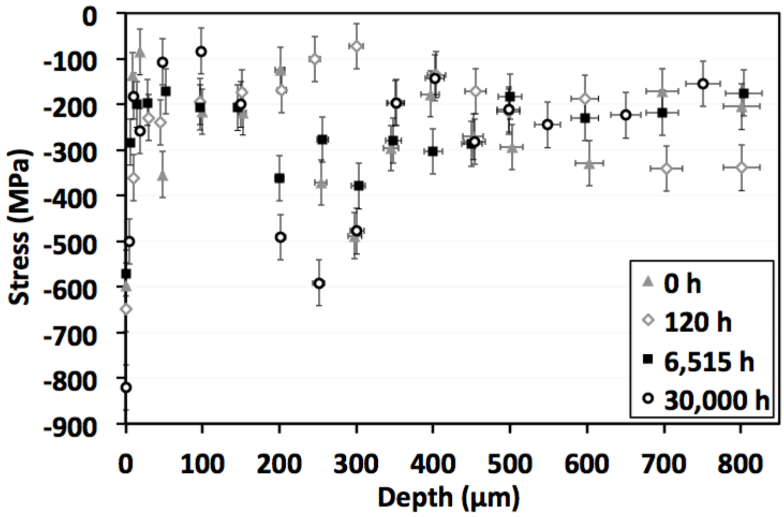

Figure 5.9: Residual stress values as a function of carburised case depth in four different M50NiL raceways with various service lives ranging from unused (0 h) to 30,000 h operation.

data after longer periods of 30,000 h. The near surface stress component of the unused bearing (0 h) at approximately 25 μm depth is lower in magnitude before stress cycling begins.

Topas software was used to calculate the FWHM of the $2\theta_{211}$ peaks after appropriate X-ray background subtraction and corrections for peak asymmetry. Figure 5.10 contains the FWHM values obtained from the XRD data for the longest running (30,000 h service) and the unused M50NiL material presented earlier [Figure 5.8]. The unused M50NiL material displays a peak width averaging $5 \pm 0.5°$, at all three positions about the raceway [Figure 5.10 a]. There appears to be some peak broadening displayed in the 30,000 h material, with FWHM values closer to $6 \pm 1.0°$ on average, and a large amount of scatter between the different contact angles [Figure 5.10 b].

Peak broadening is a phenomenon typically associated with an increase in dislocation density and is possibly linked to microstructural fatigue damage. In traditional, lower-alloyed bearing steels the XRD peak widths have been shown to narrow with an increase in RCF damage, as thermo-mechanical tempering effects lead to dislocation recovery and the dissolution of cementite [126]. This would not be expected in the higher alloyed aircraft bearing steel grades, however, as the thermal stability of the secondary carbides is such that they would not permit softening of the M50NiL microstructure. Instead it appears as though the FWHM values have increased after 30,000 h

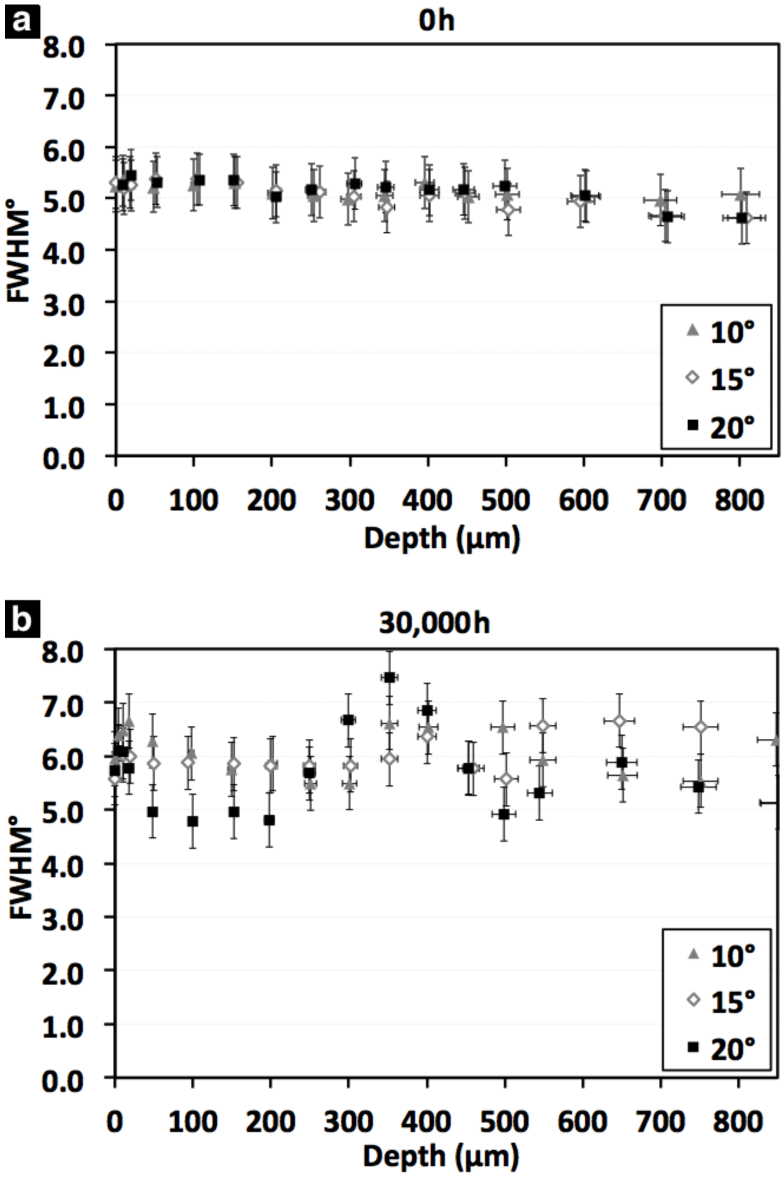

Figure 5.10: Variation in $\{211\}_\alpha$ peak widths (FWHM) as a function of raceway depth before and after 30,000 h aircraft service.

service, indicating the presence of a greater number of lattice defects in the affected material, consistent with the localised deformation of the microstructure.

5.2.1 Discussion

Evidence has been provided for the evolution of residual stresses in M50NiL raceways under the action of rolling contact loading during aircraft engine operation. Carburised raceways display a general compressive residual stress profile beneath the contact surface prior to entry into service, but after 30,000 h operation the magnitude of this compressive stress is increased in magnitude and scatter [Figure 5.8]. The most significant changes are seen at shallower depths of less than 600 μm where the stress amplitude doubles after prolonged bearing operation, from approximately -400 MPa to -800 MPa. This increase in compressive stress magnitude is seen to accumulate over time, and is most pronounced at case depths of between 200 - 300 μm, implicating the action of subsurface shear stresses during RCF [Figure 5.9].

There is strong scatter in the residual stress data as a function of contact angle [Figure 5.8 b]. This observation indicates a heightened sensitivity to ball positioning under asymmetrical thrust loads. The degree of sliding at the surface is related directly to the contact angle, so these variations in residual stress as a function of position may point towards sliding damage. Such observations also coincide with the microhardness data presented earlier which showed noticeable scatter as a function of contact angle [Figure 5.5]. Finally, the XRD peak broadening phenomenon identified in the FWHM data provides strong evidence for localised damage and microstructural evolution in M50NiL bearing steel [Figure 5.10].

5.3 Crystallographic Texture Development

Heavy plastic deformation during steel manufacturing processes lead to crystallographic texture in the end product, with deformed grains that become aligned and elongated in a preferred direction. Such anisotropy in steel is an important consideration when designing structural components that must support heavy loads and resist fatigue crack propagation. M50NiL raceways are ring-rolled in the austenite phase field during manufacture. If this process introduces a preferential crystallographic texture in the components they would need to be assessed before entering service to maintain adequate quality control. There are a number of techniques for investigating crystallographic orientation in components. Electron backscatter diffraction (EBSD) is a microscopy technique useful for mapping the local grain orientations in a sample. XRD offers a more macroscopic examination of preferred orientation in bulk samples but cannot directly identify the local microstructural features that may be involved.

During bearing operation, heavy RCF loads can themselves induce preferred texture in the stressed volume of material [20]. The directional nature of rolling contact stresses may favour local plasticity in grains at particular crystallographic variants, producing anisotropic deformation and a textured microstructure. Experiments have been performed on ex-service bearing raceways from aircraft engines to examine the M50NiL steel for evidence of crystallographic texture. Comparison made between the unused material (0 h) and the stressed samples after various service lives aims to identify changes in the microstructure that have occurred under rolling contact loading during operation.

5.3.1 Electron Backscatter Diffraction

Tangential cross-sections of M50NiL raceways were prepared for EBSD analysis using a number of different surface preparation techniques, ranging from standard metallographic polishing with colloidal silica, to ion beam milling using both broad ion beam (BIB) and FIB. The area of interest was the stressed material just below the contact surface of ex-service bearing raceways. Directional deformation of the microstructure is observed in these areas beneath the surface caused by the shear stresses of bearing operation [Section 4.1]. Examination of the near surface material using EBSD aimed to identify the grain orientations in the carburised M50NiL raceways.

Figure 5.11 shows the sample cross-sectioning and preparation procedures. Surface condition is extremely important in EBSD because the technique relies upon elastic scattering of electrons from a very shallow region of the sample surface. Standard metallographic polishing can introduce strain at the surface and in carburised M50NiL, polishing leaves the hard primary carbides exposed in relief against the softer steel matrix, reducing the smooth uniformity of the surface needed for EBSD. An improved surface condition can be obtained using ion beam milling techniques which sputter away material from the carburised case with high accuracy and uniformity. The BIB technique produces a smooth but undulating surface topography with limited results [Figure 5.11 c]. FIB-SEM milling is the most precise technique and produces surfaces of fine uniformity without introducing additional strain like that caused by mechanical polishing [Figure 5.11 f].

EBSD analysis was performed using the CamScan MX2600 SEM with a field-emission electron source. The polished samples are angled at 70° to the incident beam and the scattered electrons are detected by an array of four CCD cameras. The projected Kikuchi diffraction patterns can be indexed automatically using HKL Flamenco acquisition software, given the appropriate calibration for BCC α-iron. Figure 5.12 contains a partial EBSD map and pole figure for the BIB milled M50NiL raceway sample shown in Figure 5.11 d. The initial results for these well-polished samples were poor, with an indexing rate of less than 10% [Figure 5.12 a]. In failing to correctly identify a statistically reasonable number of grains within the selected area, the output pole figures are inaccurate and susceptible to bias [Figure 5.12 c]. It is clear from the EBSD maps that certain grain orientations are more successfully indexed, skewing the data and leading to artificially strong signal for this variant.

The greatly improved surface condition of samples prepared using FIB milling still failed to improve upon the low indexing rate for the carburised M50NiL raceways. This suggests that the difficulty in indexing was not due to poor surface finish but instead was inherent to the carburised material. Any effect which reduces the order and symmetry of the crystal lattice makes Kikuchi band indexing more difficult. The high dislocation density in the high-carbon

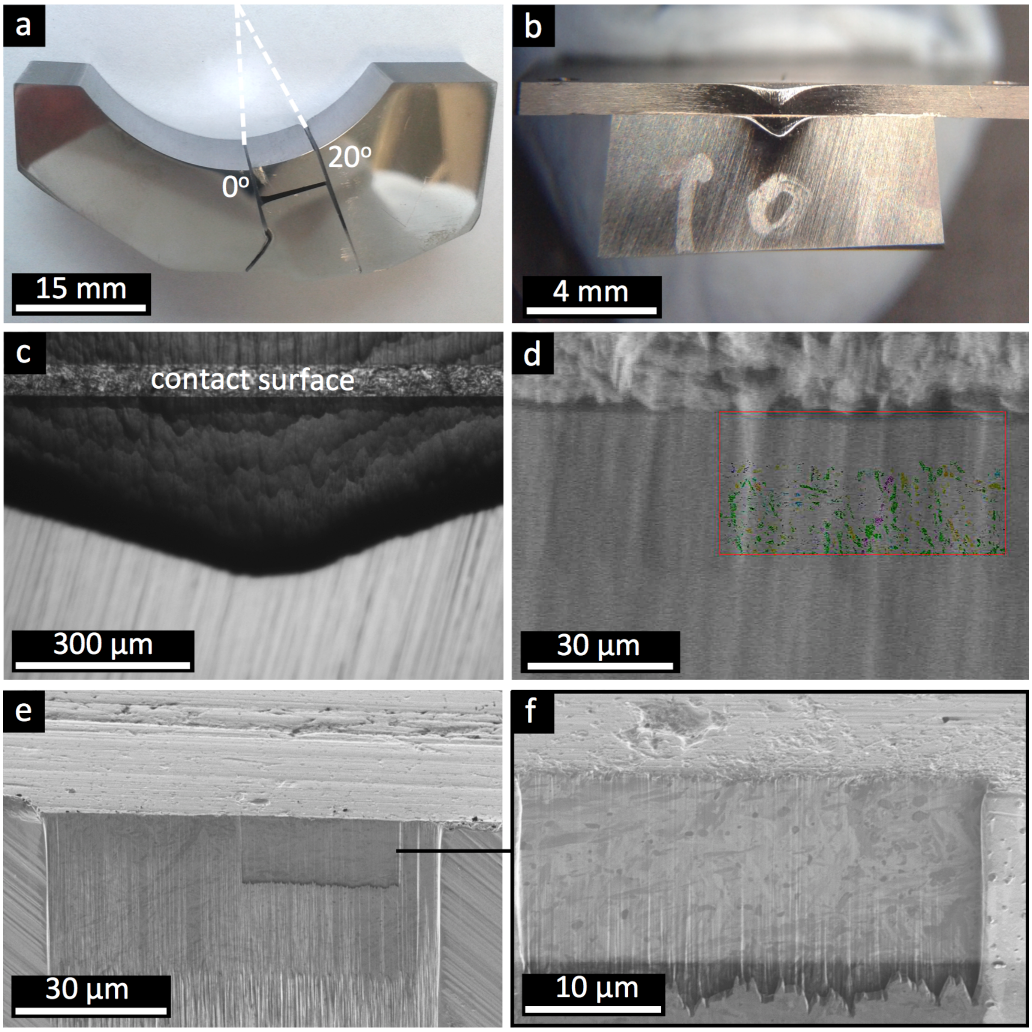

Figure 5.11: (a) M50NiL outer raceway tangential sectioning. (b) BIB milling of the 0° tangential surface. (c) The milled region is smooth but not perfectly uniform. (d) An EBSD map detecting grains within the BIB sample (inset). (e) FIB milling of a tangential section at the contact surface. (f) The higher quality surface with grains visible under channeling contrast.

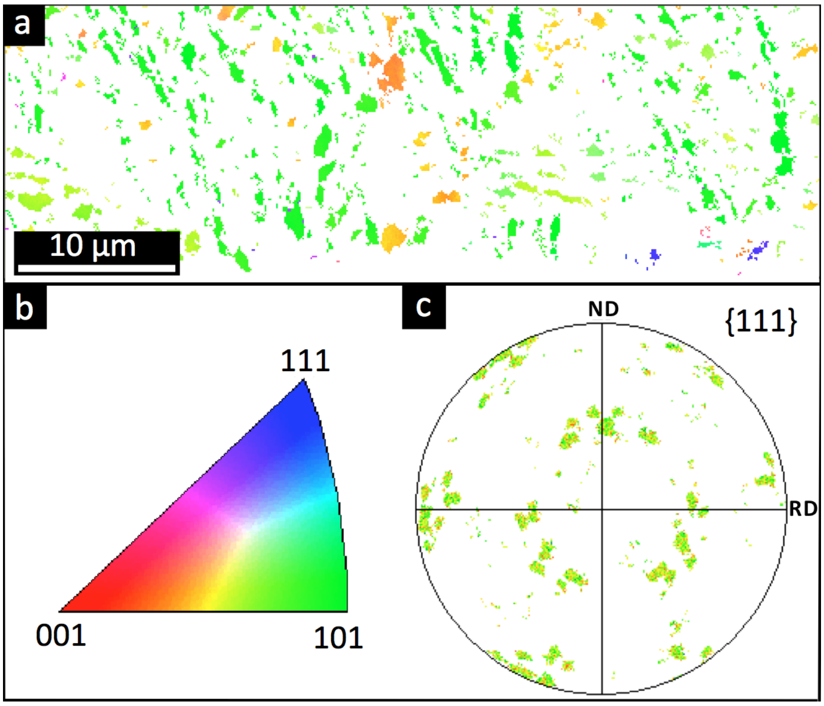

Figure 5.12: (a) EBSD map for the M50NiL carburised surface with a 9% index rate, the white areas correspond to non-indexed material and the green have [101] orientations according to (b). (c) The {111} pole figure for this map shows a strong texture bias.

martensitic case of M50NiL increases disorder and stacking defects. The fine martensite plate size and the high density of other carbide phases complicate the process further. There is known to be a compressive residual stress field in the carburised case [Section 5.2]. This will manifest as strain, altering the lattice parameters and interplanar spacings making indexing more error prone. Finally, the plastically deformed surface region of interest is known to exhibit sheared microstructures after operation in aircraft engines [Section 4.1]. The EBSD technique therefore proved inappropriate for examination of deformation textures in high-carbon martensite, so an alternative method was sought using XRD.

5.3.2 X-ray Diffraction

Experiments have been performed to investigate the average crystallographic orientation of the M50NiL microstructure in the carburised case of ex-service bearing raceways. By investigating the X-ray diffracted peak intensities as a function of macroscopic sample orientation, pole figures can be constructed to show the preferential grain orientations in the material. A textured sample will produce figures where poles cluster whereas a perfectly random distribution of crystals results in pole figures with a uniform distribution of poles. Collecting a number of pole figures allows construction of the orientation distribution function (ODF) which uses an angular coordinate system to fully describe the preferred crystallographic texture in 3D [222]. Interpretation of the ODF can be difficult, but often the pole figures alone can provide a satisfactory description.

Figure 5.13 shows the experimental setup for the crystallographic texture investigation of M50NiL raceways. X-ray diffraction measurements were performed using the Bruker AXS D8 Discover goniometer with Co Kα radiation

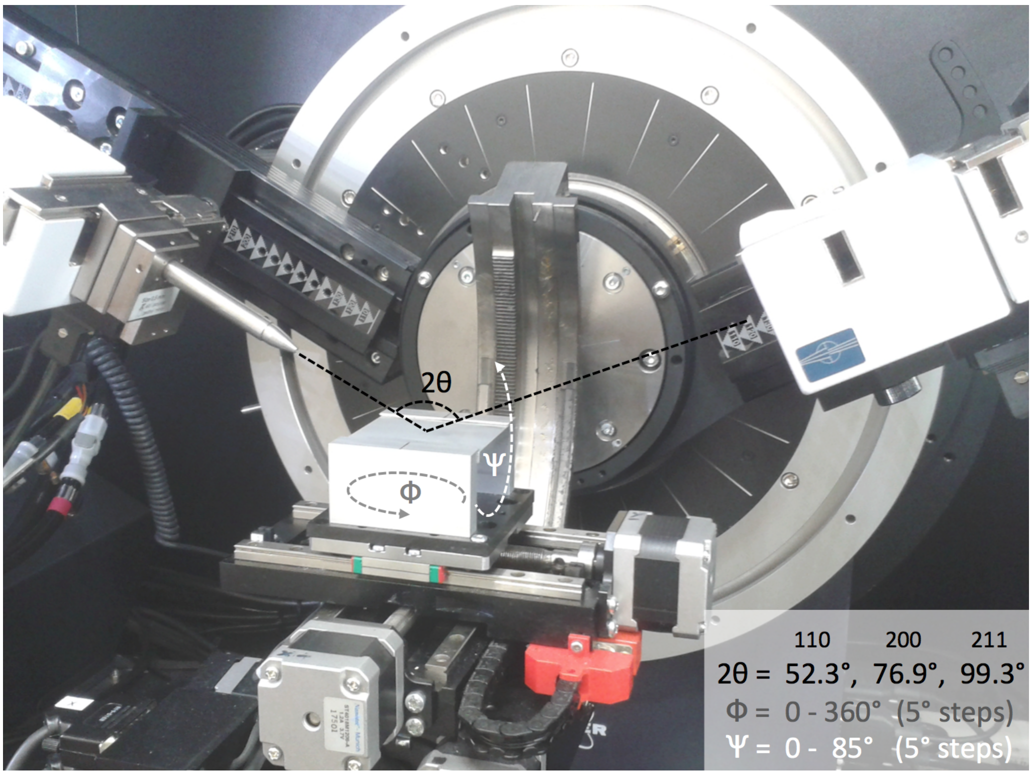

Figure 5.13: Bruker AXS D8 Discover goniometer with 3D eulerian cradle that rotates in Θ, Φ and Ψ (indicated).

corresponding to an incident photon energy of 6.9 keV. The collimated beam with 0.5 mm diameter spot was targeted at the contact surface of the sectioned M50NiL raceways whilst they were simultaneously rotated 360° in Φ and through 0 - 85° in Ψ [Figure 5.13]. At each position the {110}, {200} and {211} ferrite peaks were examined near their related 2θ angles of 52.3°, 76.9° and 99.3° respectively, producing three pole figures for each sample. A Lynx-Eye position sensitive detector permitted short dwell times of only 1 s at each angular position, so with 5° increments the overall collection time was approximately 1 h per pole figure. Four raceway samples were examined (0 h, 120 h, 6,515 h and 30,000 h) at two case depths each (0 μm and 200 μm), creating 24 pole figures in total. A corundum sample was used to calibrate the detection intensity and two corrections were applied to the real data to account for background subtraction and defocussing at high Ψ and Φ angles.

The raceway samples were cross-sectioned in a similar way to those in the residual stress investigation [Figure 5.6]. Due to time constraints, no electropolishing stages were possible in this investigation, so only two depths could be measured per sample. Figure 5.14 shows the sample geometries after grinding to produce parallel sided sections with only a small ellipse remaining of the contact surface. Taking measurements at positions away from the ellipse is equivalent to being at a shallow depth beneath contact surface. In this way, multiple depth measurements can be approximated us-

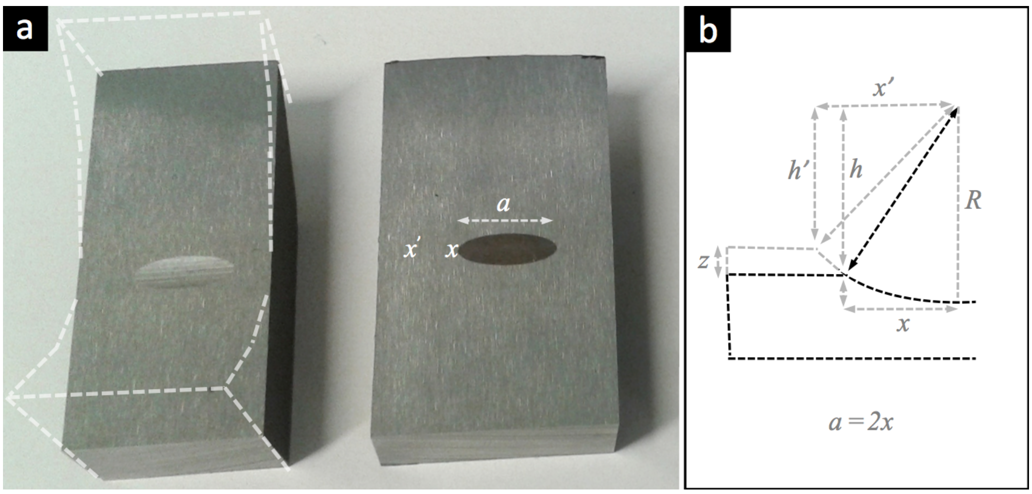

Figure 5.14: (a) M50NiL outer raceways after sectioning. Two measurements x and x' correspond to surface and subsurface measurements, respectively. (b) Schematic diagram describing the sample geometry used to calculate the approximate depth z given the displacement x' from the semi-major ellipse.

ing a single sample without needing to remove material. With reference to the sample geometry, the approximate depth z can be calculated given the displacement x' from the ellipse [Figure 5.14 b]. Two measurements were taken per sample in this investigation; one adjacent to the surface ellipse at approximately 0 μm depth (x), and another at approximately -200 ±50 μm beneath the contact surface (x').

If crystallographic texture is present in a material, figures will display poles with anisotropic intensities that cluster as a function of position. Figure 5.15 shows examples of textured pole figures from the literature for demonstration. Contours highlight regions of strong intensity near the centre of these {110} pole figures for the 52100 bearing steel, with respect to the macroscopic rolling direction (RD) [Figure 5.15]. It was expected that similar strong contour variations would be shown in the experimental data for M50NiL aircraft bearing steel raceways.

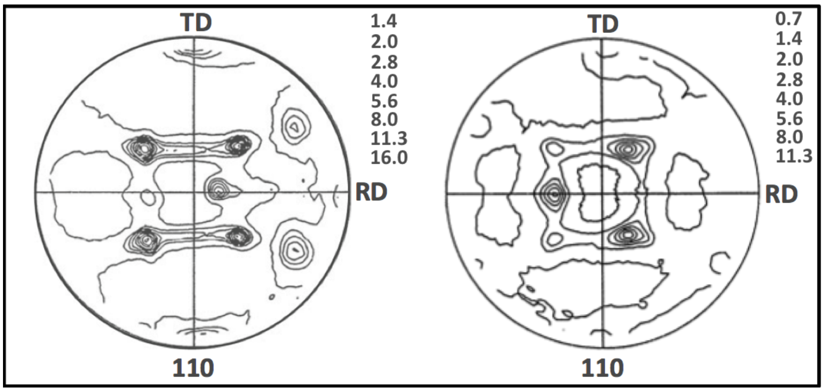

Figure 5.15: Examples of preferred crystallographic texture in the {110} pole figures of 52100 bearing steels. After [223, 224].

Figures 5.16 - 5.19 present the experimental XRD data as sets of three pole figures, {110}, {200} and {211}, for each of the four ex-service raceway samples at the two different depths. These data generally show weak contour intensities with randomised orientations and no obvious signs of texture, except in one particular case. The {110} pole figures tend to show clustering of intensities at low angles, around the centre of the figures. This is most significant in the 30,000 h ex-service bearing raceway. Figure 5.19 contains the best example of a subtle texture development in the M50NiL material at 200 μm beneath the surface. Here, the {110} pole figure shows increased intensity around the central position with three discrete poles in a triangular

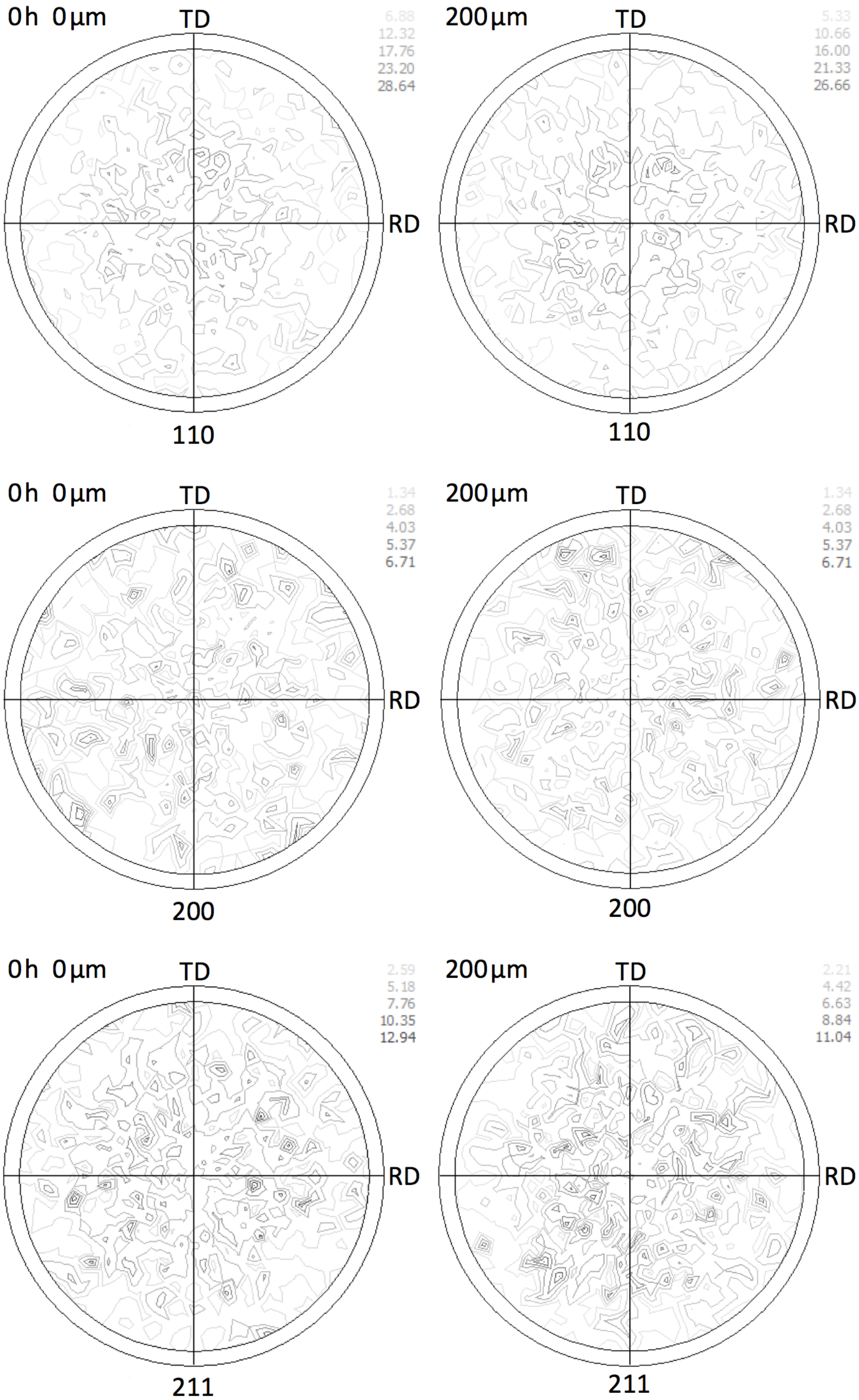

Figure 5.16: {110}, {200} and {211} pole figures for the unused M50NiL raceway. Measurements are taken at the contact surface (0 µm) and approximately 200 µm beneath the surface.

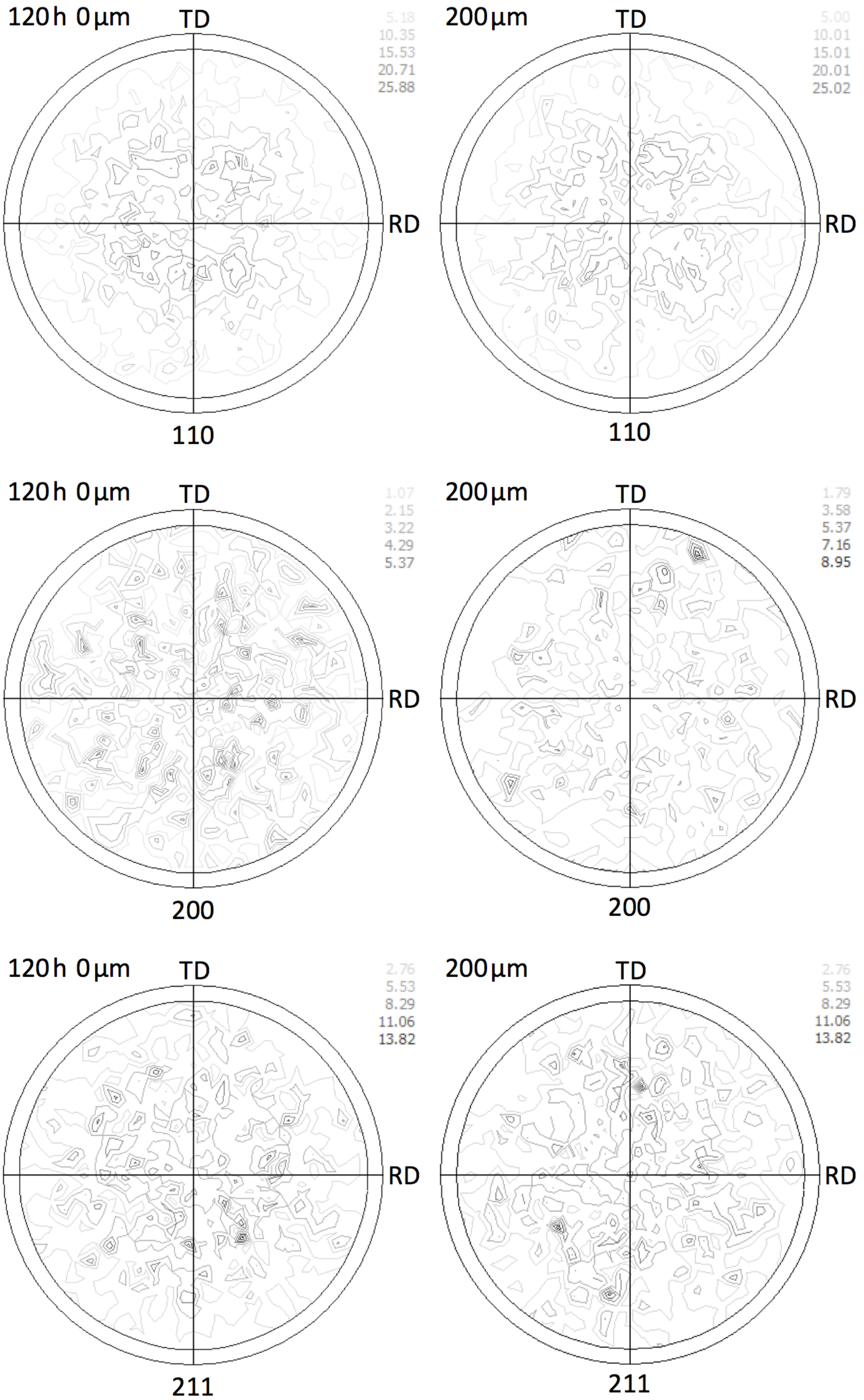

Figure 5.17: {110}, {200} and {211} pole figures for the M50NiL raceway after 120 h service. Measurements are taken at the contact surface (0 µm) and approximately 200 µm beneath the surface.

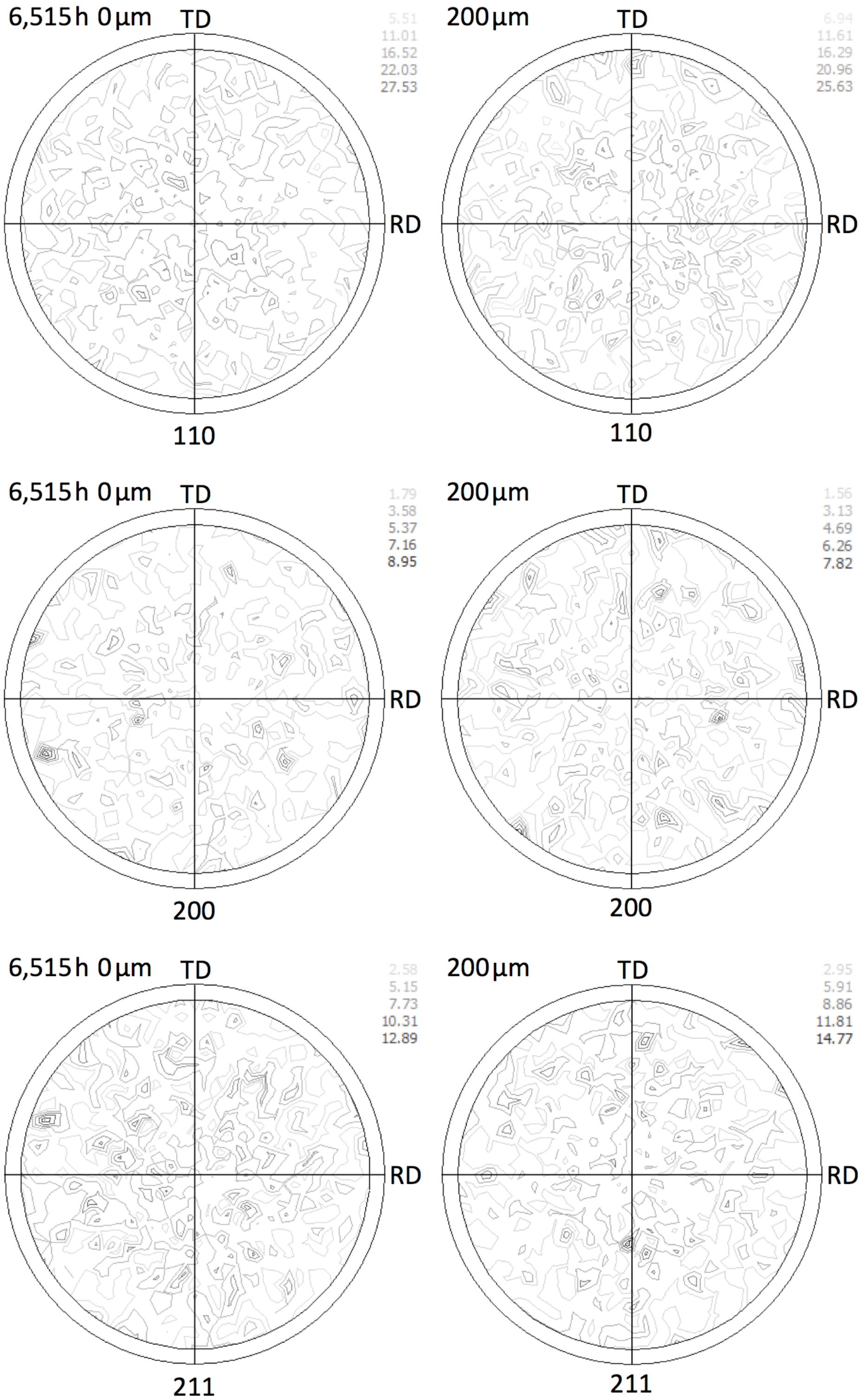

Figure 5.18: {110}, {200} and {211} pole figures for the M50NiL raceway after 6,515 h service. Measurements are taken at the contact surface (0 µm) and approximately 200 µm beneath the surface.

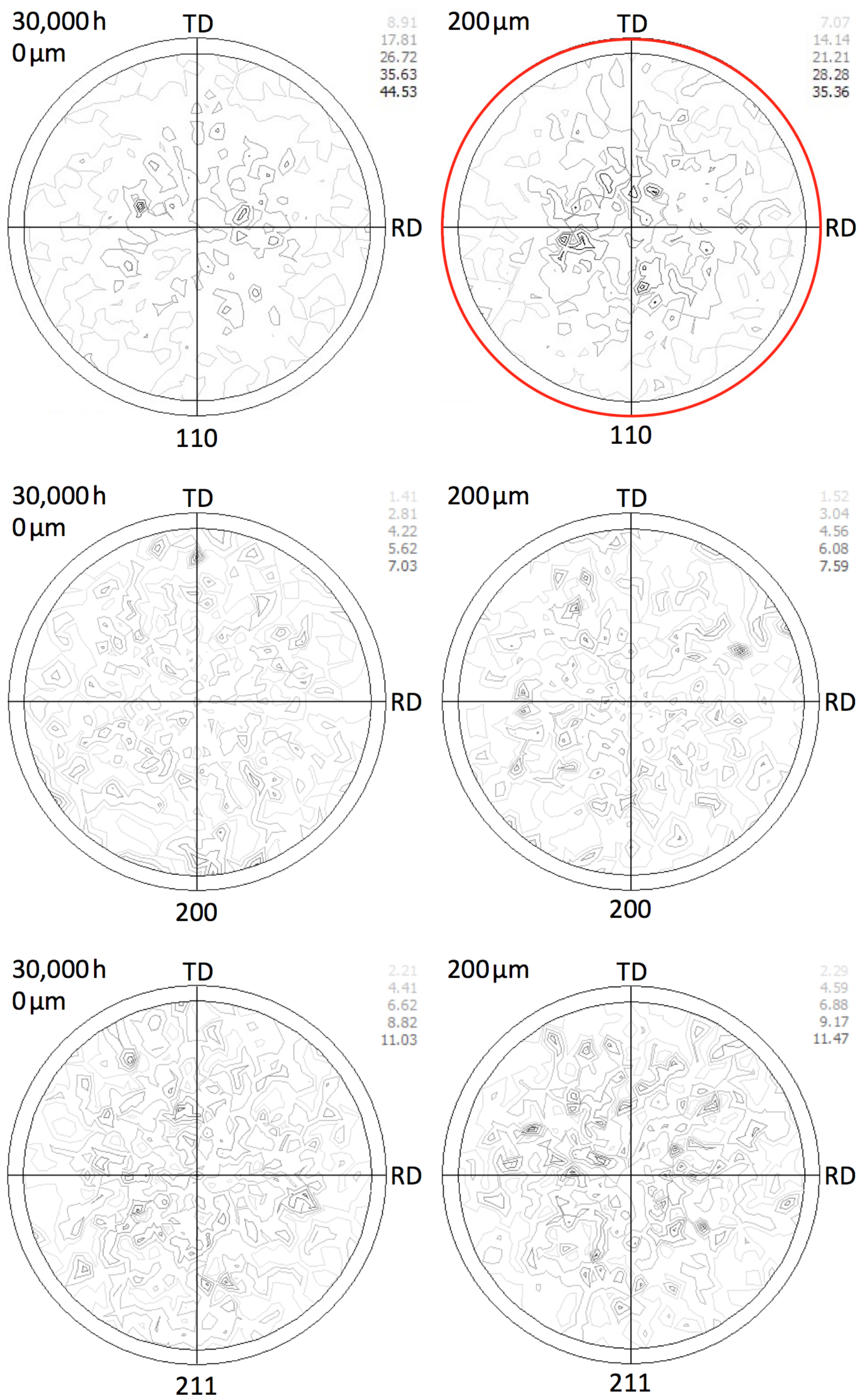

Figure 5.19: {110}, {200} and {211} pole figures for the M50NiL raceway after 30,000 h service. Measurements are taken at the contact surface (0 µm) and approximately 200 µm beneath the surface.

formation [Figure 5.19]. The three-fold symmetry of this pole figure gives an indication as to which crystallographic planes may be involved (the {111} planes) but comparisons with textured pole figures in the literature can provide further clarification.

Figure 5.20 compares the {110} pole figure of M50NiL material at 200 µm beneath the raceway surface with another pole figure from the literature: this same exact texture has been reported by Voskamp and Mittermeijer (1996), who performed accelerated RCF testing on the lower alloyed 52100 bearing steel at high contact stresses [224]. The {111} [211] texture found in their work is identical to that identified at 200 µm beneath the M50NiL raceway surface after 30,000 h operation and strongly supports this new evidence for texture development in aircraft bearing steels. Figure 5.20 also includes a diagram depicting the crystallographic nature of this preferred texture in

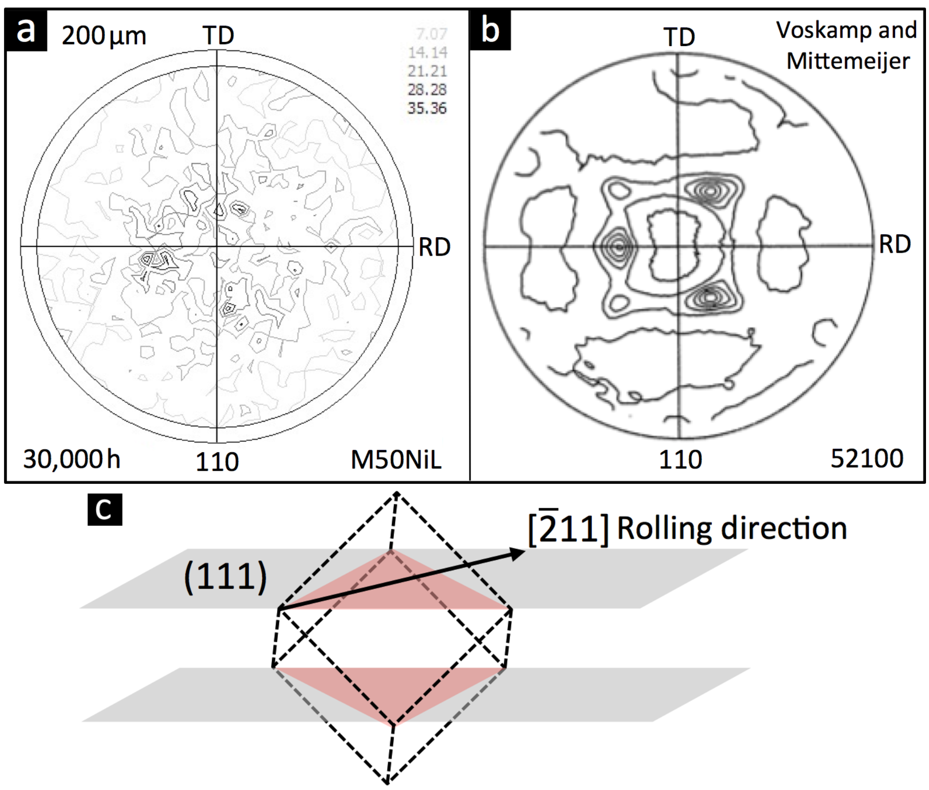

Figure 5.20: (a) The {110} pole figure for M50NiL raceways after 30,000 h service. (b) The identical {110} pole figure for 52100 bearing steel taken from Voskamp and Mittemeijer (1996) for comparison [224]. (c) Unit cell representation of the preferred {111} [211] texture developed in M50NiL raceways during aircraft engine operation.

relation to the unit cell. These observations are presented as further evidence for the microstructural changes that take place under rolling contact loading in aircraft engine bearings.

5.3.3 Discussion

The EBSD technique proved to be ineffective in dealing with the highly strained M50NiL material below the contact surface of aircraft bearing raceways, despite employing multiple surface preparation techniques. The microstructure is inherently difficult to index due to the presence of many primary carbide phases; the fine martensite plate size; the high dislocation density in the transformed case where compressive residual stresses are present; and finally, the severe plastic deformation in the near surface region [Section 4.1].

An alternative examination using XRD found a subtle development of texture after 30,000 h operation. Of the 24 pole figures collected and analysed, only one showed signs of texture development after the longest period of stress cycling (30,000 h). Identical texture development in lower alloyed bearing steels from the literature were produced under accelerated testing conditions at high stresses exceeding the 2 GPa upper limit of in the aircraft engine operation. Therefore these new observations of a subtle texture in aircraft bearing steels after a very high number of cycles are new evidence of a rolling contact fatigue response that occurs during engine service.

A relatively short XRD dwell time of only 1 s was used at each angular position. Since this interpretation of texture relies upon variations in signal intensity as a function of sample orientation, maximising the signal with a longer dwell time may lead to stronger texture observations. The choice of raceway contact angle and the depth of material investigated may have also been limited in scope. For instance, it is unclear whether the technique sampled material from the appropriate contact angles where microstructural changes may have taken place, although every effort was made to focus on regions showing the most significant damage at the contact surface.

5.4 Summary and Conclusions

Material property changes have been identified in bearing steels after operation in aircraft gas-turbine engines. The M50NiL raceways show a multitude of evidence to suggest gradual alterations occur in the carburised microstructure under rolling contact loading:

Work-hardening is observed in the first 1 mm case depth after 30,000 h service. The gradual accumulation of plastic strain will affect the yield strength in the carburised case, since hardness and strength are intrinsically linked material properties. Hardness changes are also seen after 120 h bearing operation with a greater degree of scatter in these data. The highly localised variations in hardness as a function of contact angle are thought to show the influence of ball sliding severity within the contact ellipse.

Changes in the residual stress profiles of M50NiL raceways mirror the hardness increases seen after 30,000 h service. The compressive residual stress is doubled after long periods of operation in aircraft gas turbine engines, and the data show an increase in scatter which highlights the microstructural disorder produced under rolling contact loading. Variations in the residual stress distribution as a function of contact angle are also seen. This is new evidence to support the theory that different fatigue behaviours occur in M50NiL raceways as a function of the amount of sliding experienced at different contact angles.

A subtle texture is developed in ex-service bearing raceways after 30,000 h operation. The preferred {111} [211] orientation is identical to that reported in the literature for lower-alloyed bearing steels under accelerated RCF testing. This is the first time that ex-service components from aircraft engines have been examined with such detail and these texture observations, together with the residual stress and hardness changes, provide new evidence for the gradual microstructural evolution of M50NiL bearing steels under rolling contact loading.

Chapter 6

Fatigue Behaviour Under Laboratory Testing

Access to ex-service components from aircraft gas-turbine engines is not always possible, so instead engineers utilise special laboratory test-rigs to investigate the behaviour of bearing steel samples under rolling contact loads. Laboratory testing offers a number of benefits; providing increased control over test variables such as speed, load and lubrication conditions. The ability to accelerate failures in components by using very high contact stresses can reduce the testing time necessary and provide large volumes of test data for statistical analysis of fatigue. Yet, there may be downsides to using artificially high contact stresses as these non-representative operating conditions provide a tenuous basis for describing fatigue behaviours at the lower contact stresses of real-life operation.

Chapters 3 - 5 contained extensive characterisation of ex-service bearing material. This chapter describes RCF experiments performed on a particular laboratory test-rig using different contact stress levels and test samples with different surface roughness values [Section 6.2]. Both M50 and carburised M50NiL steel samples were tested and their microstructures characterised after test completion. Damage at the surface is the dominating feature and the inverse correlation between surface roughness and RCF life is shown.

6.1 Three Ball-on-rod Test Rig

A rolling contact test rig has been made available for laboratory testing after donation by SKF, who assisted in this work. Figure 6.1 describes the specific geometry of this particular RCF test rig designed with a three ball-on-rod configuration [196]. The test material is a 9.5 mm diameter cylinder centrally enclosed by three ball elements each of 12.7 mm diameter. The sample rod is gripped from one end by an electric motor and rotated up to speeds of 3,600 rpm. This is significantly less than the 12,500 rpm speeds encountered in aircraft gas-turbine engines. The three surrounding balls are compressed against the rod by the outer raceway cups which are loaded using three coiled springs. A load cell is used to calibrate the force provided by spring compression and these loading conditions are adjusted before each experiment.

The contact force, P, between each ball and the sample rod is based upon

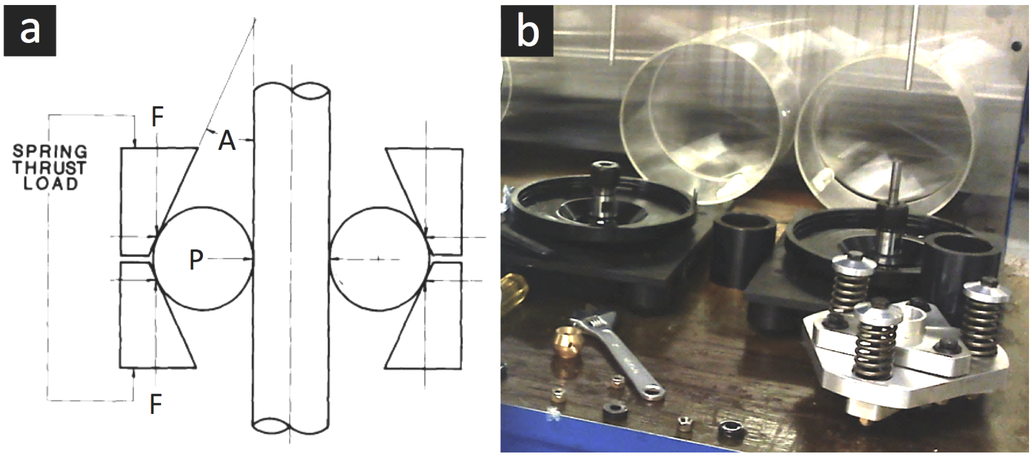

Figure 6.1: (a) Schematic diagram of the three ball-on-rod RCF test rig, viewed from the side. The load F on the balls acts at an angle A to the rod. After [196]. (b) The test rig showing the three coiled spring setup.

the test rig geometry, according to:

$$P = \frac{2Fg}{3\tan(A)} \tag{6.1}$$

Where F is the applied load according to the load cell (in kg), g is the acceleration due to gravity and A is the 25° contact angle of the raceway cups [Figure 6.1 a]. The contact stress between the balls and the sample rod is then found using P from Equation 6.1, according to:

$$p_0 = \left(\frac{6PE'^2}{\pi^3 R'^2} \right)^{1/3} \tag{6.2}$$

Where E' is the reduced elastic moduli of the ball and rod, and R' is the combined radius of curvature [Section 2.1.1]. Using these equations, a 4 kg applied load equates to approximately 2 GPa contact stress, and a 30 kg applied load equates to approximately 4 GPa contact stress.

The lubricant used is BP Turbo oil 2380 which is supplied from above, dripping into the system at a controlled rate. The electric motor is controlled via a computer interface and once the speed has been selected the machine is then left to run. A piezoelectric accelerometer is attached to the RCF rig to log the vibration levels during testing. If the severity of vibration reaches a certain pre-defined threshold, the test is automatically stopped and the time of stoppage recorded. The intention is to detect spalling failures through the increased vibration caused by this damage, however the upper limit of the machine's vibration threshold is quite low so instances of premature stoppage were encountered [Section 6.1.3].

The duration of each test before stoppage occurs is used to calculate the number of fatigue cycles, based upon the speed of revolution and the diameter of the rod. For example, at the maximum speed of 3,600 rpm the number of rolling contact cycles accrued during one hour is N = 516,024. Tests typically ran for periods of between 10^2-10^3 h (between 4 - 40 days) before the vibration threshold was met, corresponding to fatigue lives of $N_f = 10^8$. However, the termination of the tests did not always correspond to sample failure. Bearing ball failures were encountered during RCF rig testing, and these sometimes came before damage to the sample rods. Figure 6.2 shows evidence of the ball spalling failures which raised the vibration level and prematurely ended the testing.

Examination of the failed ball reveals two clear rolling tracks on the ball surface, located either side of the damaged contact zone and spaced approximately 6 mm apart [Figure 6.2 a]. These features describe the fixed rolling behaviour of the balls due to the outer raceway cups press against the bearing ball from above and below [Figure 6.1 a]. The test rig design prevents random ball precession during rolling, enforcing a preferred rolling direction

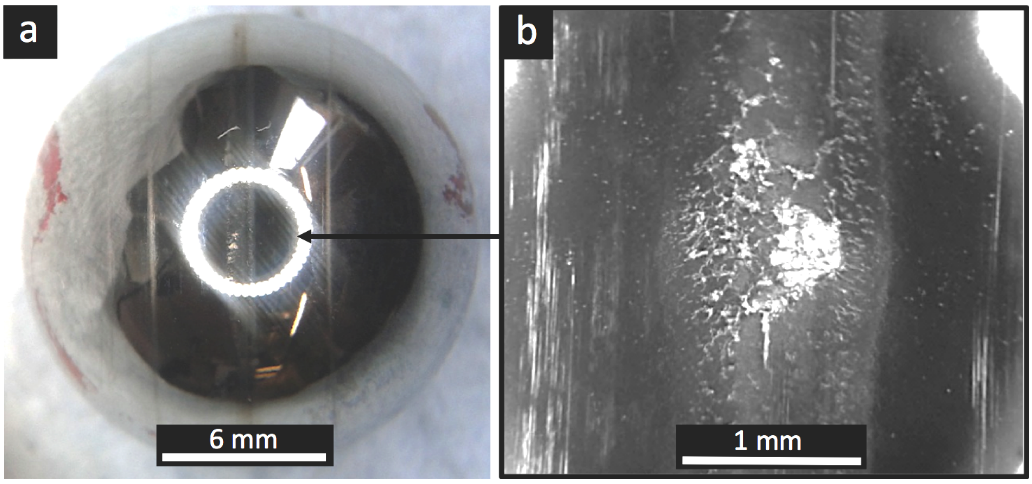

Figure 6.2: (a) Bearing ball from the RCF test rig displaying surface damage (b) Spalling has occurred within the contact zone on the ball surface.

and restricting the contact stresses to a small area of repeated loading. The balls are made from 52100 bearing steel, and evidently they exhibit poorer fatigue properties than the sample rod materials (M50 and M50NiL). Premature ball failures will trigger the automatic vibration sensors and discontinue the testing before a reasonable number of fatigue cycles have been accrued in the sample material. Since the rolling direction of the bearing balls is fixed, there will be no spinning and therefore less sliding within the contact ellipse. Sliding behaviour is a key observation in the ex-service location bearings and leads to the unique damage mechanisms revealed for the first time in Chapters 3 - 5. Therefore, the three ball-on-rod RCF test rig may fail to accurately reproduce the sliding conditions necessary to study the particular type of surface dominated fatigue behaviour that occurs in aircraft bearings.

6.1.1 Surface Roughness Investigation

M50 and carburised M50NiL sample rods for testing in the RCF rig have been heat treated and prepared with varying degrees of surface finish. Figure 6.3 shows the preparation of sample rods produced with three different finishing procedures; grit-blasting, ball-milling and turning. Grit-blasting was performed using 500 μm alumina particles as an abrasive media to manually roughen some of the M50 steel sample rods after heat-treatment. Samples for ball-milling were tumbled in a vessel containing a finer 200 μm alumina grit for periods of 24 - 48 h. The smoothest sample rods were turned on a machine lathe using cubic boron-nitride tool bits.

Two analytical techniques were used to measure the surface roughness

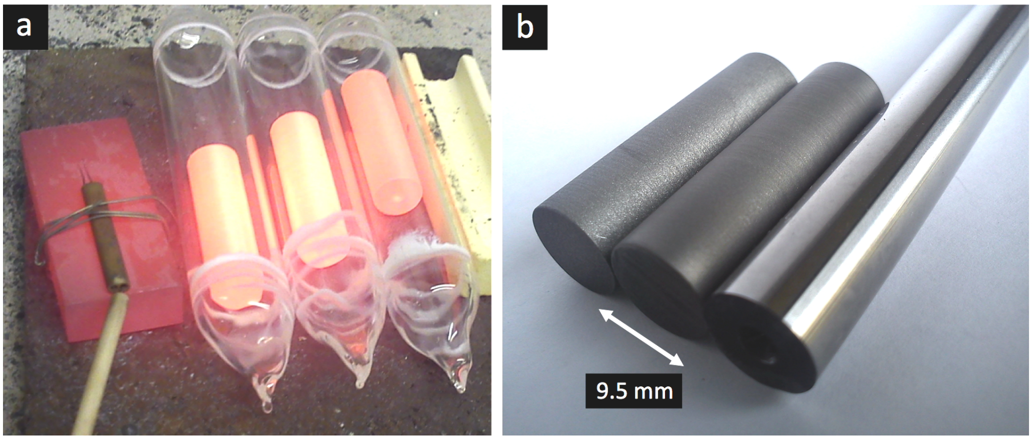

Figure 6.3: (a) M50 sample rods heat-treated to the specified treatment outlined in Figure 1.10. (b) Sample surfaces finished using grit-blasting, ball-milling and turning (from left to right).

values of each of the finished sample rods according to the mean centreline average R_a [Equation 2.7]. Each technique was utilised over a range of resolutions in order to examine the reproducibility of these roughness values across different length scales. A contact technique using the Veeco Dektak stylus profilometer, traces a 3 mm test line across the sample surface at a chosen scan speed, affecting the number of discrete height measurements made along the fixed line of length x. A 10 s scan will see 3000 measurements made, but a 20 s scan will record 6000 measurements along the same test line, hence the resolution of this contact technique is the proximity of neighbouring height measurements in the x direction, and is fixed by varying the scan speed. A non-contact technique using the Wyko RST optical interferometer utilises the scattering of white-light from the sample surface to measure roughness at three different magnifications, $\times 5, \times 10, \times 20$. The area sampled is then discretised into an array of 238×368 data points and the R_a roughness value taken as the average deviation of the heights within this area. Hence, the resolution of the optical technique is fixed by the pixel width within the field of view for a given magnification.

Tables 6.1 and 6.2 contain the R_a roughness data gathered using the contact and non-contact techniques respectively, for each of the samples prepared using the three different finishing procedures. Figures 6.4 and 6.5 show graphically the data from Tables 6.1 and 6.2 respectively. As expected, the grit-blasting gave the poorest roughness average, followed by the ball-milling, and the turned samples possess the best surface finish.

The R_a roughness data found using the contact technique are relatively consistent, however major discrepancies arise using the optical method as a function of the resolution. This behaviour can be understood due to the smaller sampling area used to calculate the R_a values at higher optical magnifications. Small scan areas are more likely to miss the larger imperfections of a rough surface, so the macroscopic scratches are ignored at higher resolutions. This disparity was deemed too great to warrant further use of the

Table 6.1: Surface roughness R_a of sample rods found using stylus profilometry. The resolution in x refers to the proximity of neighbouring height measurements.

Grit-blasted R_a (µm)	Ball milled R_a (µm)	Turned R_a (µm)	Resolution in x (µm)
2.62	1.79	0.08	1.00
-	1.81	0.09	0.77
2.65	1.84	0.09	0.50
2.65	1.85	0.09	0.33
2.65	1.86	0.10	0.25
2.69	1.86	0.10	0.20

Table 6.2: Surface roughness R_a of sample rods found using optical interferometry. The resolution is given in terms of the pixel width for each height measurement.

Grit-blasted R_a (µm)	Ball milled R_a (µm)	Turned R_a (µm)	Resolution in pixel (µm)
5.70	3.40	-	3.23
3.69	1.86	0.18	1.68
2.31	1.62	0.15	0.84

optical technique, but also highlights the inherent importance of resolution and sampling effects on the measurement of surface roughness.

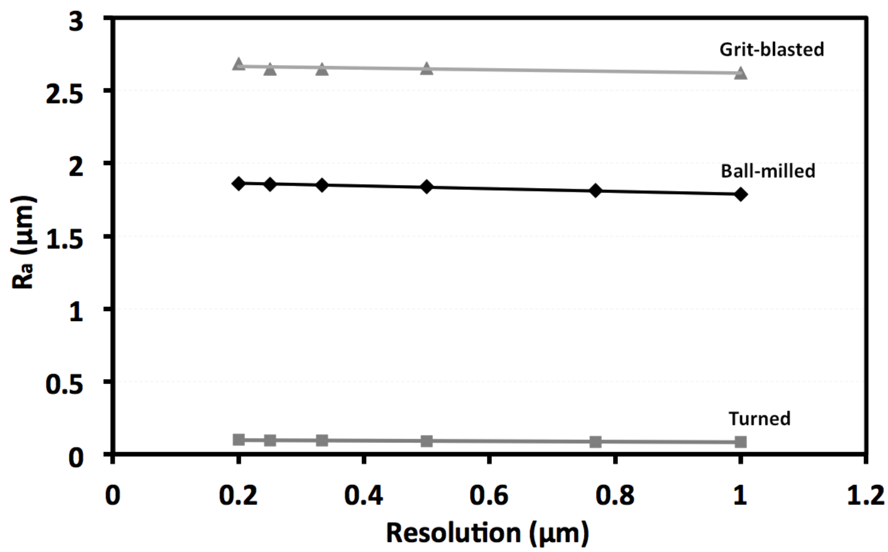

Figure 6.4: Surface roughness R_a using contact profilometry.

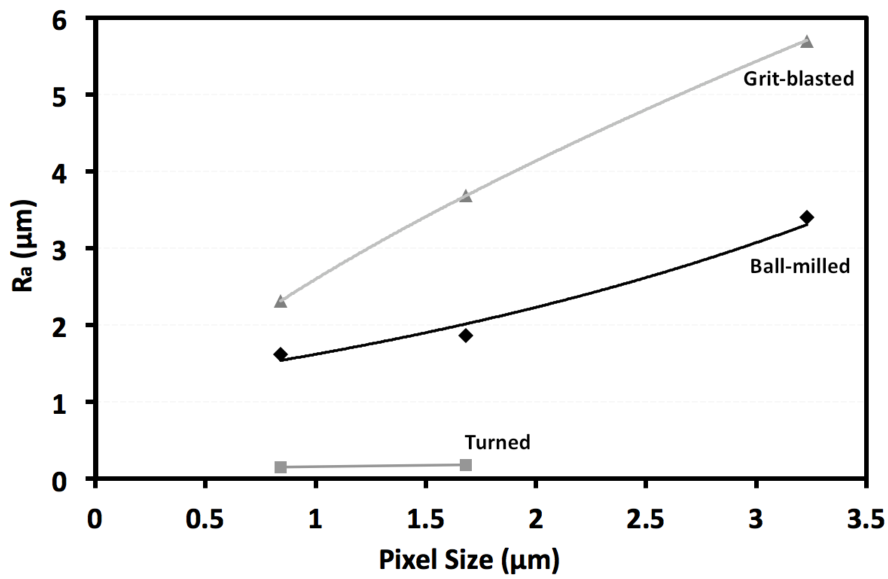

Figure 6.5: Surface roughness R_a using optical interferometry.

The sample rods measured in this roughness investigation were not all destined for RCF rig testing. For instance, the grit-blasted samples show a high degree of surface roughness ($R_a = 2.7$ µm), which would be excessive under the precise loading conditions of the test rig. Since the vibration sensor would immediately trip automatic shutdown for these excessively rough samples an upper limit was set at approximately $R_a = 1\,\mu m$. Those ball-milled and turned samples that did become endurance test pieces all possess surface roughness values of less than $R_a = 1\,\mu m$, as will be presented later [Section 6.1.3].

6.1.2 M50 Bearing Ball Topography

The surface roughness of a newly machined M50 bearing ball (0 h) has been characterised prior to aircraft engine operation. Atomic Force Microscopy (AFM) is used to examine the height profiles of two types of surface feature; the typical machining scratches, and the protrusion of residual carbides. The AFM technique measures the topography of the component surface by scanning across it with a nanoscale cantilever tip attached to a piezo-electric transducer. The oscillating needle-point is extremely sensitive to changes in height at the surface, relaying this information to a computer for analysis. A 2D line scan can then be obtained in the form of a single line plot of heights, or a collection of line scans can be used to produce a 2D surface map of the topography. Figure 6.6 shows how the M50 ball surfaces prior to service have a mirror-like finish, but also exhibit occasional grinding scratches. In order to investigate the severity of these scratches a new ball (0 h) was sectioned

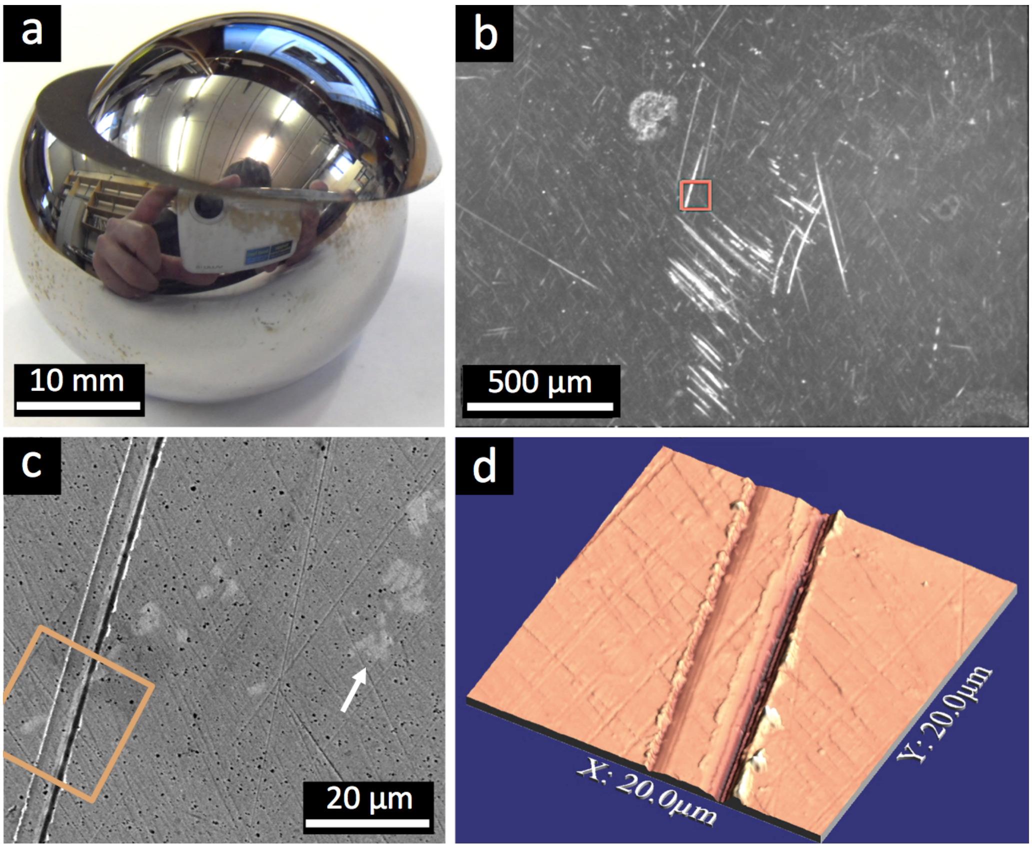

Figure 6.6: (a) An unused M50 bearing ball sectioned using EDM. (b) Optical microscopy shows manufacturing defects on the ball surface. (c) SEM image of the same scratched region also showing residual carbides (indicated). (d) AFM topography map of the surface profile from the same scratched region.

using EDM to produce a flat bottomed hemisphere allowing height data to be collected at the central apex which is approximately horizontal [Figure 6.6 a]. A representative set of scratches at the ball surface were chosen for characterisation using the AFM [Figure 6.6 b]. SEM analysis reveals a pair of parallel grinding scratches together smaller imperfections and residual carbides are also visible [Figure 6.6 c]. The resulting 2D surface map of this 20 μm^2 area on the new ball surface intersects the grinding scratches [Figure 6.6 d]. The physical height data are converted into colour contrast scale, with the brightest regions matching the highest peaks and the darkest regions representing the deepest valleys. A flattening procedure was also performed on these data to account for the spherical curvature of the ball using a parabolic correction [225].

Table 6.3 contains height data for the 2D map in Figure 6.6 d. The grinding scratch averages at -200 nm in depth with plastically deformed edges that are raised by a similar amount in height. The resulting peak-to-trough displacement of this asperity approaches 500 nm or 0.5 µm. The average roughness of the entire area containing the scratch is only $R_a = 0.02$ µm however. The asperities are at the higher end of roughness values accepted by Rolls-Royce for new components, but the area examined is small and contains a large defect, so is statistically biased. Note, the R_a value is less than half that of the R_q value, highlighting the relative sensitivity of these two parameters to surface defects [Table 6.3].

Another region of the new ball displaying surface breaking residual carbides

Table 6.3: AFM height data for the M50 ball surface in Fig 6.6 d.

R_a	R_q	R_t	Peak Asperity
20 ± 4 nm	45 ± 9 nm	314 nm	497 nm

was investigated using AFM. The intention was to investigate the possibility of protruding carbide asperities at the surfaces of M50 balls which cause large shear stresses and plastic deformation during bearing operation [Chapter 3]. Figure 6.7 shows an SEM image of the surface area characterised, containing various imperfections and residual carbides visible with brighter contrast to centre of the image [Figure 6.7 a]. The resulting 2D surface map of this 50 μm^2 area on the new ball surface intersects surface carbides [Figure 6.7 b]. The surface topography is slightly elevated in the region containing the carbides, but the overall profile remains relatively flat. The AFM height data

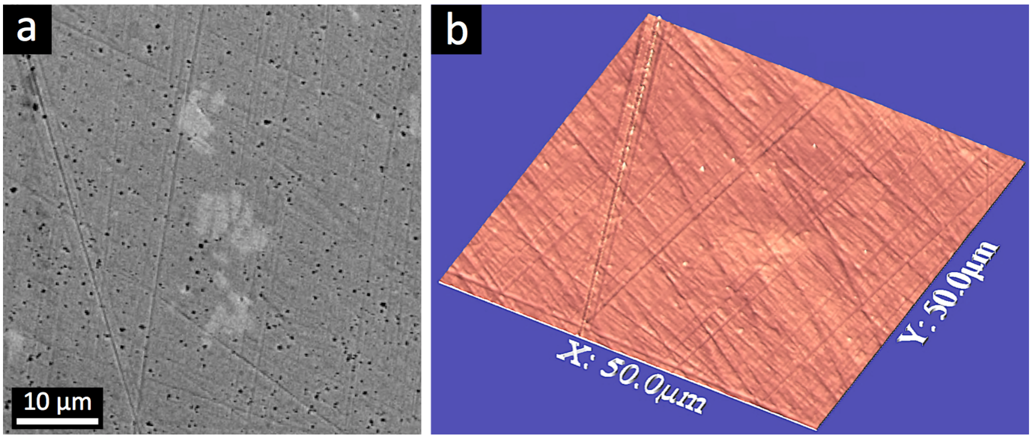

Figure 6.7: (a) The new bearing ball surface shows grinding scratches and residual carbides in the centre of the SEM image. (b) AFM topography map of the surface profile from the same region shows only minor carbide protrusion.

shows they protrude only a little from the surrounding matrix, by an average height of 0.1 µm, and are therefore apparently less pronounced than some of the machining scratches. The stiffness and hardness values of these primary carbides are known to be higher than the surrounding softer matrix however, so during rolling contact the relative protrusion height may increase, exposing more of the carbide cross-section. Under low lubrication conditions the apparently minor carbide protrusions may still cause significant damage.

6.1.3 Endurance Testing

M50 and M50NiL steel sample rods have been prepared with a range of different surface finishes [Section 6.1.1]. Each sample rod was loaded into the three ball-on-rod RCF test rig and ran until failure. These endurance tests were performed at contact stresses of 2 GPa and 4 GPa. Figure 6.8 contains the endurance test data for all of the sample rods tested, and these data and their testing parameters are also presented in Table 6.4. The failure data reveal a clear trend between the increase in surface roughness and the reduction in fatigue life N_f of aircraft engine bearing steels [Figure 6.8].

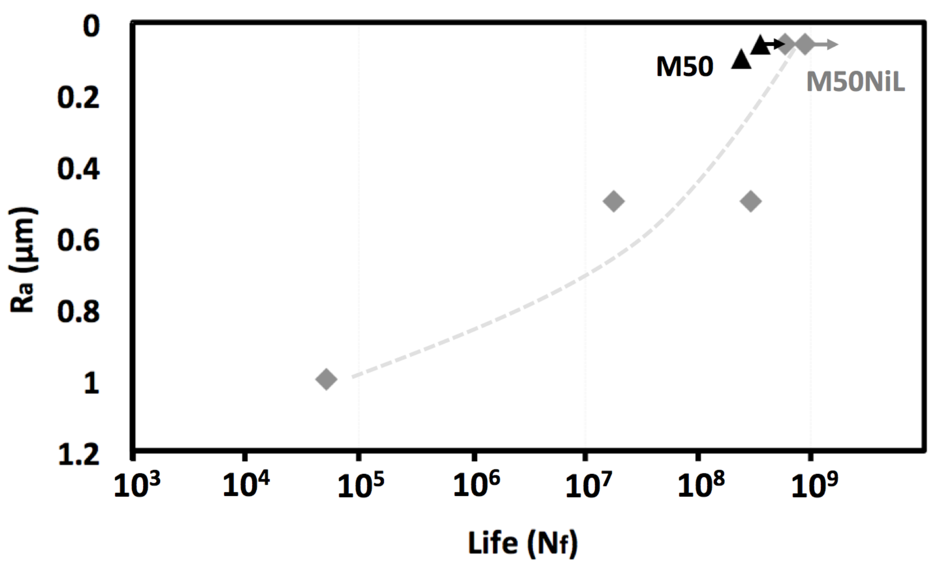

Figure 6.8: Fatigue lives of M50 and M50NiL steels as a function of surface roughness during RCF rig testing under the conditions specified in Table 6.4. The arrows indicate discontinuation without failure.

Table 6.4: RCF life data for M50 and M50NiL test samples with various surface finishes.

R_a (µm)	Duration (h)	Life (N_f)	Stress (GPa)	Sample
0.06	1,696	8.8×10^8	2	M50NiL
0.06	1,149	5.9×10^8	**4**	M50NiL
0.06	688	3.5×10^8	2	M50
0.1	463	2.4×10^8	2	M50
0.5	568	2.9×10^8	2	M50NiL
0.5	35	1.8×10^7	**4**	M50NiL
1.0	0.1	5.2×10^4	2	M50NiL

When roughness is kept to a minimum of $R_a = 0.06\,\mu m$ the bearing steels experience long fatigue lives approaching 10^9 stress cycles. Over these prolonged fatigue testing durations the M50NiL test rods outperform through-hardened M50 [Figure 6.8].

The increase in contact stress from 2 GPa to 4 GPa is responsible for a reduction in the M50NiL fatigue life [Table 6.4]. Figure 6.9 presents the fatigue life data in the form of standard S-N curves. The effect of increased contact stress is to reduce the fatigue life of these aircraft bearing steels. Increased surface roughness is also seen to move the S-N curves to the left, reducing the fatigue lives as indicated by the arrows in Figure 6.9.
An examination of the failed test rods after test completion indicates that

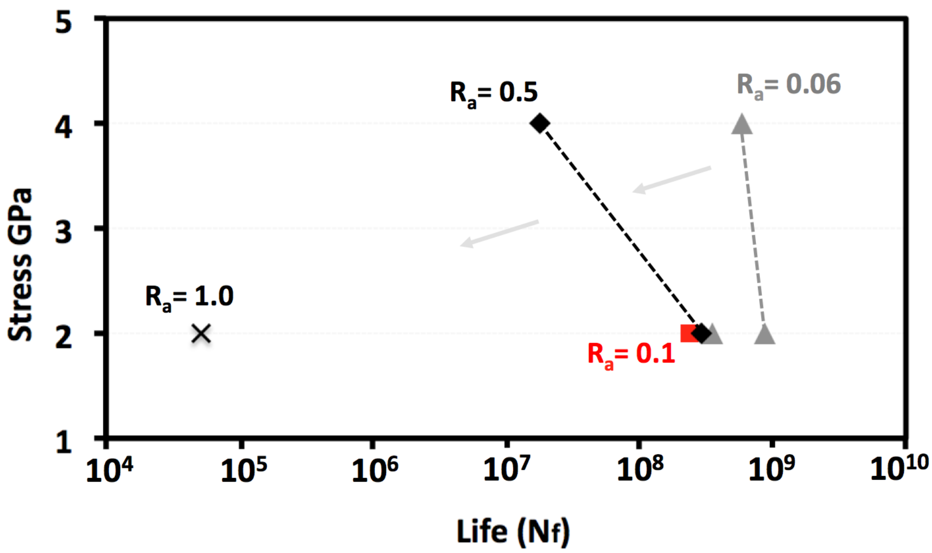

Figure 6.9: Failure curves for M50 and M50NiL steels as a function of contact stress during RCF rig testing under the conditions specified in Table 6.4.

spalling has not occurred on any of these RCF samples. Instead the level of surface damage was severe enough to reach the vibration sensor threshold and trigger an automatic shutdown. Characterisation of the rolling tracks and contact zones on a number of sample rods was carried out. Figure 6.10 shows the sample rod surfaces after RCF endurance testing. Plastic deformation is visible within the rolling tracks that seems to be influenced by the surface roughness of the samples prior to RCF stress cycling [Figure 6.10 d]. The widths of the rolling contact zone correlates with the applied contact stress, growing wider as the loads are elevated to 4 GPa [Figure 6.10 e]. In some cases more localised damage is observed within the contact zone. De-

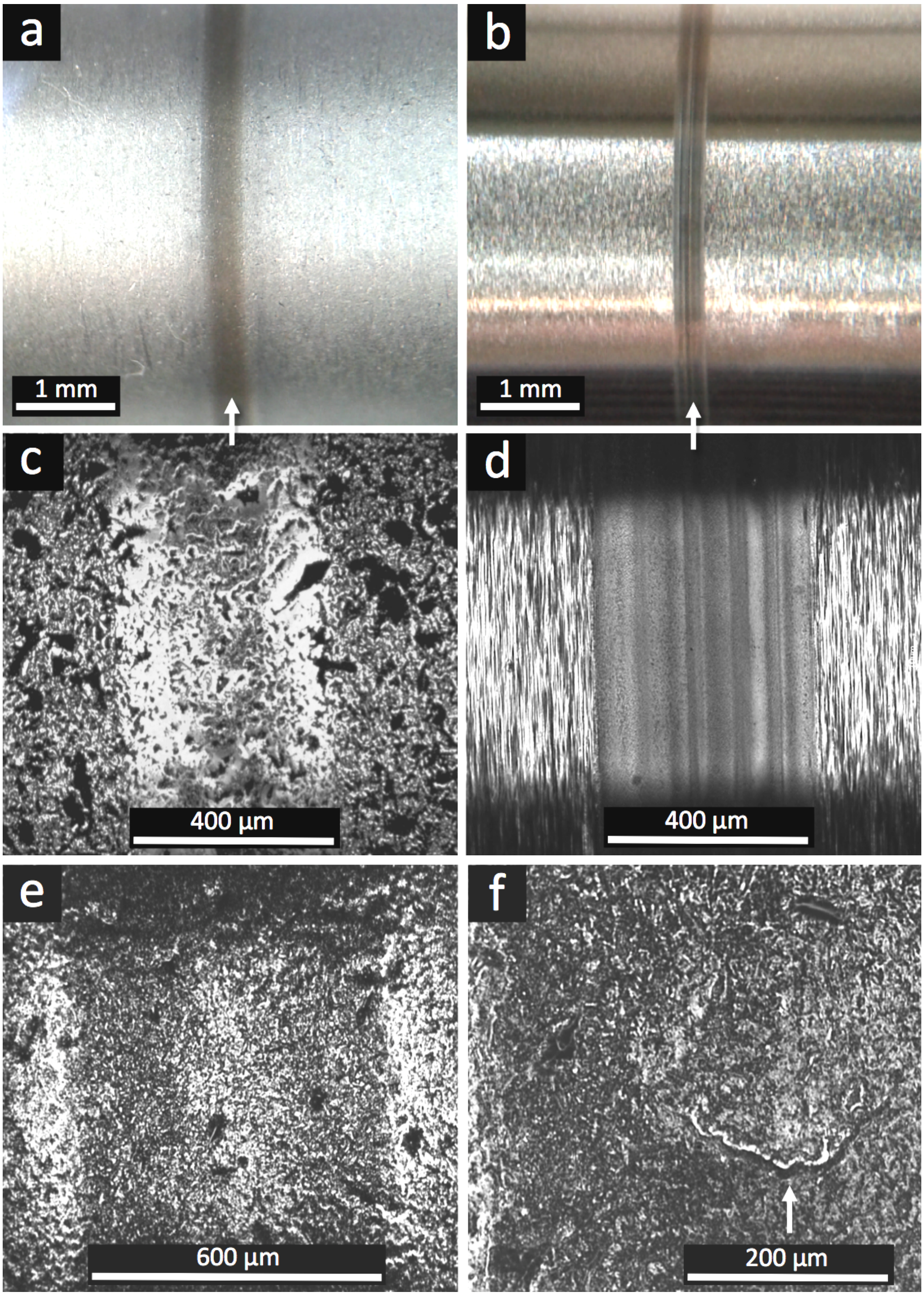

Figure 6.10: (a) M50NiL test rod with rolling track (Ball-milled). (b) M50NiL test rod with rolling track (Turned). (c) The contact zone is plastically deformation. (d) The contact zone is smoothly deformed. (e) At 4 GPa the ball-milled M50NiL rod shows a wider rolling track. (f) Fatigue crack in the M50NiL sample after 1.8×10^7 cycles at 4 GPa (Ball-milled).

bris indentation is evident in many of the samples and a singular crack was also discovered, displaying the characteristic V-shaped apex indicative of the fixed rolling direction [Figure 6.10 f]. This surface crack was found on the $R_a = 0.5\,\mu m$ M50NiL sample rod after running at GPa for 1.8×10^7 cycles. Ball spalling was also encountered during this particular test and may have contributed to the damage [Figure 6.2].

The endurance tested RCF rods were cross-sectioned in order to investigate the fatigued microstructures beneath the contact surface. Sectioning was performed in both the longitudinal direction, along the length of the test rods, and in the circumferential direction, through the rolling contact zone. Figure 6.11 describes the cross-sectioning process of the RCF test rig samples. The longitudinal cross-sections of M50NiL display a carburised case beneath the surface [Figure 6.11 c]. The microstructures of all the test rods examined were in remarkably good condition. No evidence of material decay was observed and only the contact surfaces showed any obvious signs of damage [Figure 6.11 d-e].

It is thought that the duration of the endurance testing was not sufficient to precipitate microstructural changes in the aircraft bearing steel sample rods, despite even the high contact stresses of 4 GPa used in some cases. It was not possible to run the tests for longer periods due to the automatic shutdown procedure of the vibration sensor on the RCF test rig. Therefore, the endurance test data do not strictly represent the fatigue lives of these steels, since the tests did not culminate in fatigue failure. Instead the excessive surface damage on the rods or unforeseen ball damage led to their discontinuation and the endurance test data [Table 6.4].

The use of RCF test rig data to produce L_{10} fatigue life curves will not be possible in situations where failures are not caused. There is also an insufficient number of samples available to gain a statistically reliable probability distribution using the Weibull analysis [Section 2.3.2].

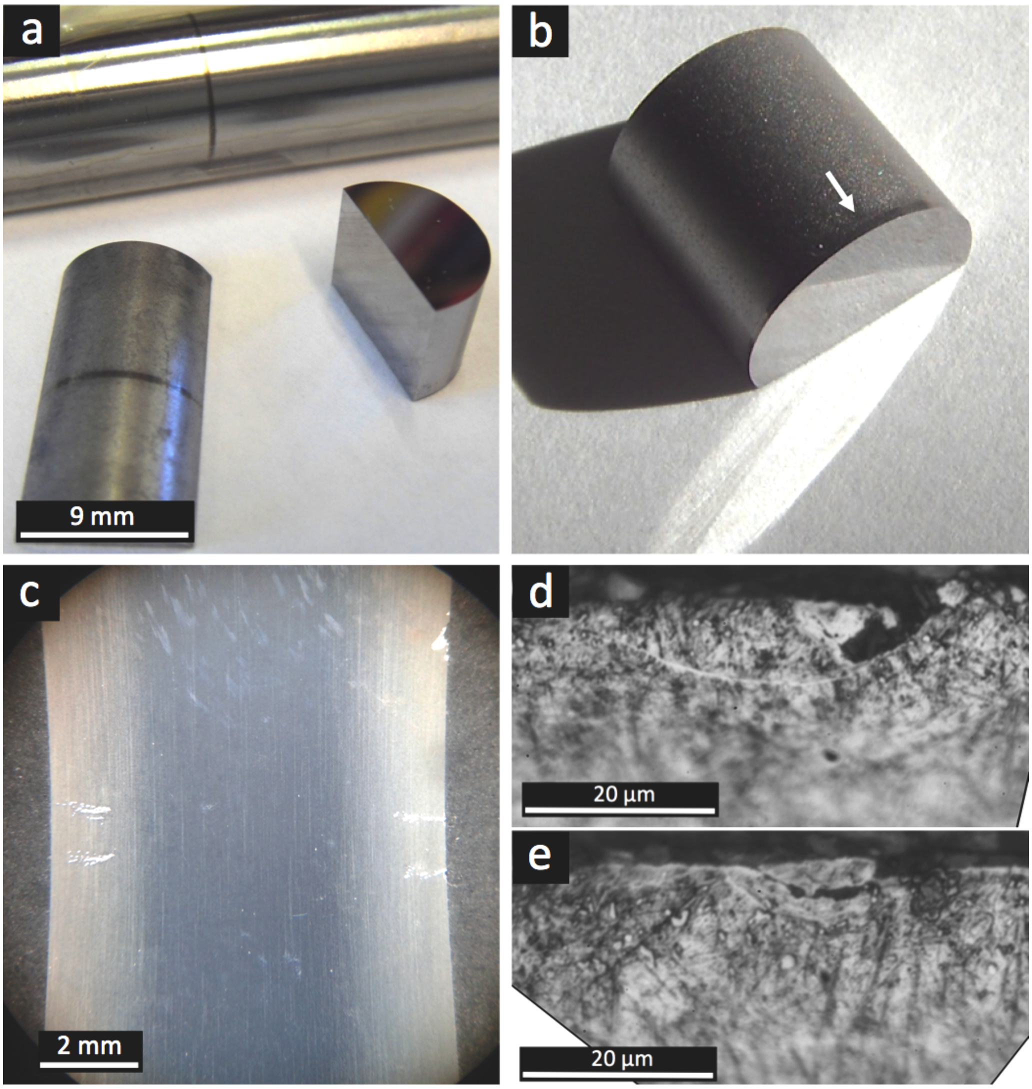

Figure 6.11: (a) RCF test rods in cross-section. (b) The circumferential cross-section is made through the rolling contact zone (indicated). (c) M50NiL test rod shows carburised case in longitudinal cross-sections. (d-e) Surface damage on the $R_a = 0.5\,\mu m$ M50NiL rod after 2.9×10^8 cycles at 2 GPa.

6.2 Summary and Conclusions

Rolling contact test rigs have been used to investigate the behaviour of aircraft engine bearing steels under laboratory conditions. Endurance test data prove that surface roughness has a significant impact on bearing steel performance, reducing the operational life of M50 and M50NiL. Contact stress is also a key contributor to fatigue performance, with increases in applied load causing reductions in rolling contact life under testing. The carburised M50NiL samples outperform through-hardened M50 when tested under equal conditions with identical roughness and contact stress values. The fatigued material remains in remarkably good condition aside from plastic deformation at the contact surface itself. Excessive distress at the sample surfaces is likely to have triggered the piezoelectric vibration sensors, prematurely ending the endurance tests before more significant microstructural damage could occur. An insufficient number of fatigue failures were produced to gain a statistically reliable probability distribution using the Weibull analysis and therefore the use of RCF test rig data to produce L_{10} fatigue life curves has not been possible.

Chapter 7

Conclusions and Further Work

Experimental evidence has been gathered which describes the behaviour of aircraft bearing steels under rolling contact loading. Characterisation of ex-service material after operation in aircraft gas-turbine engines provides a clearer understanding of the surface dominated failure mechanisms. Plastic flow at the contact surfaces is encouraged by the sliding conditions of operation, and the rolling contact loads have less harmful effects on the microstructures. A gradual evolution of the material properties during service has been identified, affecting hardness, stress distribution and preferred crystallographic orientation in bearing steel raceways. These behaviours are more significant after prolonged periods of rolling contact, but the varying degree of sliding-to-rolling experienced at the different contact angles is also influential. The supplementary investigation of sample material in the rolling contact test-rig highlights the importance of maintaining adequate surface finish on bearing components.

A number of topics for future work are suggested which derive directly from the observed material behaviours of current aircraft bearings. It is hoped that the conclusions drawn from this thesis can help to inform future progress in bearing steel metallurgy. Improvements in steel processing to reduce inhomogeneity and new surface treatments are suggested. A number of further experiments are also proposed which would build upon the findings in this work.

7.1 Sliding and Surface Fatigue

Residual carbide segregation is seen throughout M50 bearing balls [Figure 3.6]. These coarse carbides intersect the contact surface and cause damage to M50NiL bearing raceways under the high-sliding conditions of aircraft engine operation. The tangential shear stresses resulting from sliding cause fragmentation and loss of the M50 ball carbides [Figure 3.4], together with heavy plastic deformation in a shallow region of the carburised M50NiL raceways [Figure 4.4]. This damage progresses with continued service from the plastic flow of deformed martensite plates towards a grain-refined nanoscale structure of equiaxed ferrite [Figure 4.6]. The rehardening and embrittlement of this discontinuous layer will encourage cracking at the surface and possible delamination. Evidence of work hardening at M50NiL raceway surfaces has been observed and appears to be directly related to the amount of sliding present in the contact zone [Figure 5.5]. These new observations provide unique evidence for a surface fatigue damage mechanism that occurs during the normal operation of aircraft bearing steels [Figure 7.1].

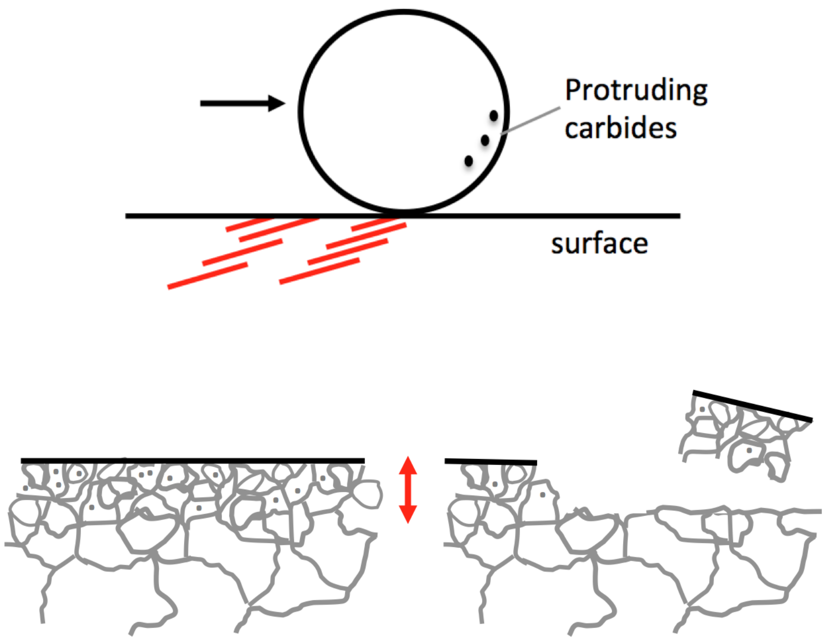

Figure 7.1: Plastic deformation of the M50NiL raceway surfaces due to component sliding and residual carbides on M50 bearing balls. The damage progresses towards an embrittled layer of nanocrystalline ferrite where cracking and delamination may occur.

7.2 Microstructural Evolution

Gradual changes in the material properties of M50NiL raceways take place with prolonged rolling contact loading during aircraft bearing operation. The residual stress distribution in the carburised case intensifies with service [Figure 5.8], and a preferred crystallographic texture develops after 30,000 h [Figure 5.20]. These new observations, and the concomitant work-hardening of the surface microstructure [Figure 5.3], describe the gradual accumulation of plastic strain in the stressed volume of ex-service bearing material. A novel strain accommodation mechanism through a mechanical twinning shear has been identified for the first time in bearing steels [2]. Localised plasticity takes place at inhomogeneities in the carburised material, such as at interfaces between primary carbides and the matrix [Figure 4.14]. Widespread twin networks decorate prior austenite grain boundaries, representing defects entering service [Figure 4.16], and macroscopic damage has been observed where twinned material intersects the contact surface [Figure 4.19].

The diagrams in Figure 7.2 put forth this new strain localisation mechanism under rolling contact loading conditions: mechanical twinning will first initiate at stress raising defects in those particular grains at the appro-

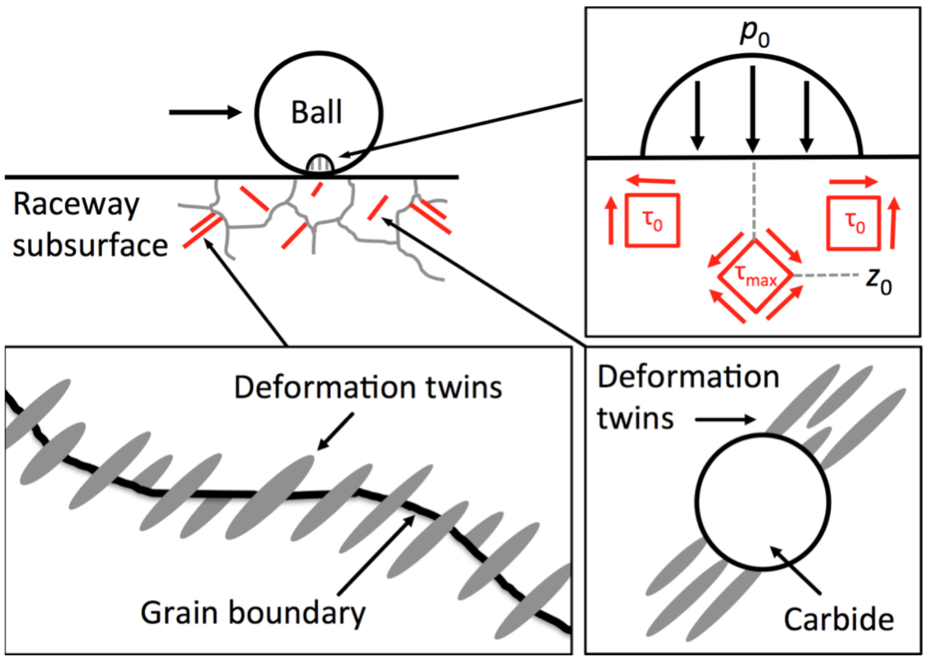

Figure 7.2: M50NiL bearing steels under rolling contact loading exhibit a strain accommodation mechanism through localised mechanical twinning.

priate orientation to the Hertzian contact stress axis, such that the $\langle 11\bar{1} \rangle$ twin directions lie close to the 45° shear stress. Figure 7.3 describes the twinning shear for body-centred cubic (BCC) materials in more detail. In BCC materials, twinning is more likely to occur at high strain rates and at low temperatures [216]. The high-speed and high-cycle fatigue conditions of rolling contact in the aircraft engine will result in very high strain rates, approaching $1.5 \times 10^7\,\mathrm{s}^{-1}$.

The twin shear carries with it a large strain of $1/\sqrt{2}$ and a number of

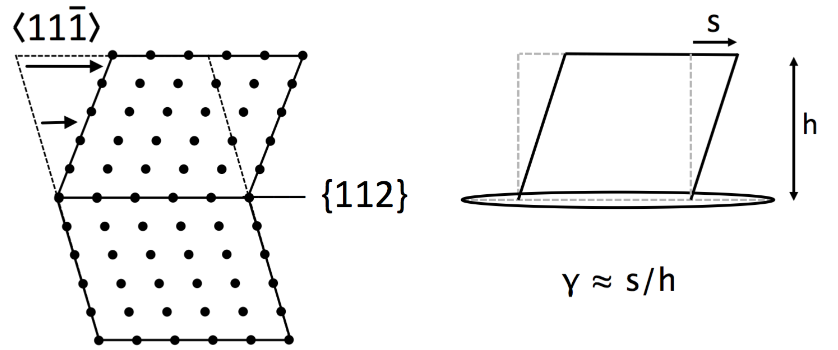

Figure 7.3: Twinning in a BCC crystal lattice. The shear displacement s is proportional to the height h above the twin plane, so the morphology adopted is a thin plate with sharp edges in order to minimise strain energy.

authors have considered the brittle characteristics associated with these deformation features [226]. Gilbert et al. (1964) examined the phenomenon of twin-induced grain boundary cracking BCC metals [227]. Fatigue crack initiation at intersecting twins in BCC structures has been reported [228], and the detrimental role that twins can play in the fatigue behaviour of ferritic steels has provided some concern [229, 230]. Taniguchi et al. (2007) found the fatigue life of a ferritic stainless steel was significantly reduced when containing deformation twins [231]. Therefore the new evidence proposed in this thesis is an important contribution to the literature on the behaviour of aircraft bearing steels under rolling contact and reveals many of their unique damage mechanisms that have never been previously reported.

7.3 Further Work

The topics covered in the following section are suggestions for future work which derive directly from the observed material behaviours of current aircraft bearings reported in this thesis. As a consequence, the evidence of damage mechanisms seen to occur during operation can help to inform future progress in bearing steel metallurgy:

1. Residual carbide segregation in M50 bearing balls could be effectively reduced by implementing a new process route utilising powder metallurgy (PM). The hot isostatic pressing (HIP) of M50 powders to create bearing components will bypass the slow solidification effects of cooling from liquid steel, leading to a reduction in inhomogeneity and residual carbide size [101]. It is likely that a reduction in residual carbides at the surface of PM M50 would improve the tribology conditions and limit the plastic flow witnessed on M50NiL raceways. Future investigations into PM could focus, not only on the reduction of residual carbides in terms of size and volume fraction, but also on the resulting RCF performance of these HIPed components compared with the through-hardened ingot-cast bearing balls studied in this thesis.

2. Another way to prevent damage caused by carbide asperities on rolling elements is to seek an alternative material to M50: military aircraft utilise hybrid bearings which combine M50NiL raceways with ceramic bearing balls. The future adoption of silicon-nitride (Si_3N_4) ceramic balls in hybrid bearings for civil aircraft engine could provide fatigue performance benefits and also save weight, due to the lower density ceramics [232]. The elastic modulus and hardness of Si_3N_4 balls exceed those of through-hardened M50 [187], and superior thermal stability is also shown [181]. However, the desirable mechanical properties of these ceramic components will actually lead to higher contact stress in the raceways. Under Hertzian contact loads, the elevated modulus of Si_3N_4 balls would result in less elastic deformation than for steel balls, producing a more concentrated stress at the raceways. Mosleh et al. (2012) found that the hybrid bearing combination of Si_3N_4 balls rolling upon M50 test rods actually under-performed in RCF tests compared

with the all-steel M50 components. If hybrid bearings are to eventually replace the fully-steel aircraft bearing components an improvement in the current raceway properties will also be required.

3. Nitriding is a surface treatment which exposes the working surfaces of a component to a nitrogen rich atmosphere, such as ammonia gas, to allow the inward diffusion of nitrogen into the steel surface. The precipitation of nitrides in the surface layer act to strengthen the steel, providing elevated hardness and an increased compressive residual stress compared with carburising [43]. The process is similar to carburising, only that the carbide precipitates are replaced by nitrides which surpass the hardness of standard carburising [233]. One downside to the nitriding process is that the treatment initially forms a brittle 'white layer' at the surface that must first be removed with grinding before the components can be used [174]. Any improvements offered by the nitrided surface are also restricted to quite shallow depths, so a combination of both carburising and subsequent nitriding may offer a compromise between deep compressive stress and elevated hardness nearer contact surface [234]. It is suggested that future implementation of carbo-nitriding for aircraft bearing raceways would reduce the surface damage seen in M50NiL by providing elevated resistance to plastic flow.

4. Wear testing is designed to investigate the surface tribology of materials under enforced sliding and rubbing conditions. The dominant damage mechanism during aircraft bearing engine operation is caused by the sliding behaviour at the surfaces, so future investigations of these steels utilising wear tests could prove revealing. A number of authors have looked at the wear properties of M50 [136, 181, 182], but subsequent microstructural characterisation is also needed to relate these wear tests to the plastic flow seen in raceway surfaces after service. Wang et al. (2012) reported the development of a grain-refined layer and delamination at the surface of M50 under wear testing [168], and these very same damage mechanisms have been demonstrated in the aircraft bearings after operation. Mukhopadhyay et al. (2014) found sheared features beneath the surface of M50 steel after abrasive wear testing [167]. The morphologies of those features appeared remarkably

similar to the localised twinned material reported for the first time in this thesis, so it is possible that wear tests could also provide a method for investigating the twinning damage mechanism.

5. The stacking fault energy (SFE) of a material affects the dislocation mobility and general deformation behaviour. Mechanical twins in iron can be described as a stacking fault in the {112} plane [235], and therefore consideration of the SFE may help to understand the localised twinning seen in M50NiL raceways. The SFE is influenced by bearing steel chemistry, so future work could examine the effects of making small changes to the steel composition, and the impact this has on the twinning damage mechanism. Maki and Wayman (1976) found an increase in twin populations as a function of increased nickel content in Fe-Ni-C martensites [217]. It is suggested, therefore, that reducing the nickel content in M50NiL could have a noticeable effect on the SFE and widespread twin networks in aircraft bearing raceways.

6. Synchrotron radiation sources provide high energy photons which can be used to examine the residual stress and texture developments in M50NiL raceways with superior accuracy when compared with laboratory X-ray diffraction (XRD) [221]. It is likely that the increased resolution offered by high energy synchrotron radiation would provide stronger evidence for two of the material property changes discussed in this thesis: residual stress evolution and crystallographic texture development. The photon beam is also far more intense than the weaker surface reflection method of laboratory XRD, providing stronger signal contrast for identification of the smaller temper carbide phases. Attempts were made during this work to arrange beam-time at a national synchrotron facility but these applications were initially unsuccessful. Given the new evidence of residual stress and texture changes found in aircraft bearing steels using laboratory XRD, future efforts to seek synchrotron beam-time would likely prove successful.

Bibliography

[1] J. R. Nygaard, M. Rawson, P. Danson, and H. K. D. H. Bhadeshia. Bearing steel microstructures after aircraft gas turbine engine service. *Materials Science and Technology*, 30:1911–1918, 2014.

[2] J. R. Nygaard, R. H. Vegter, M. Rawson, P. Danson, and H. K. D. H. Bhadeshia. Mechanical twinning in aircraft engine bearing steel. *ASTM STP 1580*, pages 525–537, 2015.

[3] A. Kitchen. Cr-Mo-V Bearing Steel. Material Specification MSRR6083, Rolls-Royce Plc., 2011.

[4] A. Kitchen. Low Carbon 4Cr-4Mo-3.4Ni Carburising Steel. Material Specification MSRR6113, Rolls-Royce Plc., 2010.

[5] H. J. Bohmer, T. Hirsch, and E. Streit. Rolling contact fatigue behaviour of heat resistant bearing steels at high operational temperatures. *ASTM STP 1327*, pages 131–151, 1998.

[6] R. W. K. Honeycombe and H. K. D. H. Bhadeshia. *Steels: Microstructure and properties.* Butterworth-Heinemann, Oxford, 3rd edition, 2006.

[7] H. K. D. H. Bhadeshia. Steels for bearings. *Progress in Materials Science*, 57:268–435, 2012.

[8] R. Schlatter and J. P. Stroup. Improved M50 aircraft bearing steel through advanced vacuum melting processes. *Journal of Vacuum Science and Technology*, 9:1326–1333, 1972.

[9] J. F. Braza, P. K. Pearson, and C. J. Hannigan. The performance of 52100, M-50, and M-50 NiL steels in radial bearings. *SAE Technical Paper Series*, 932470:1–13, 1993.

[10] L. Rosado, N. H. Forster, K. L. Thompson, and J. W. Cooke. Rolling contact fatigue life and spall propagation of AISI M50, M50NiL, and AISI 52100, Part I: Experimental Results. *Tribology Transactions*, 53:29–41, 2010.

[11] Y. Murakami. *Metal Fatigue: Effects of Small Defects and Nonmetallic Inclusions*. Elsevier, 2002.

[12] G. Lundberg and A. Palmgren. Dynamic capacity of rolling bearings. *Acta Polytechnica*, 1:1–56, 1947.

[13] H. Swahn, P.C. Becker, and O. Vingsbo. Martensite decay during rolling contact fatigue in ball bearings. *Metallurgical Transactions A*, 7A:1099–1110, August 1976.

[14] D. Zhu, F. Wang, Q. Cai, M. Zheng, and Y. Cheng. Effect of retained austenite on rolling element fatigue and its mechanism. *Wear*, 105:223–234, 1985.

[15] H. Muro and N. Tsushima. Microstructural, microhardness and residual stress changes due to rolling contact. *Wear*, 15:309–330, 1970.

[16] H. Schicht, E. Schreiber, and O. Zwirlein. Effects of material properties on bearing steel fatigue strength. *ASTM STP 987*, pages 81–101, 1988.

[17] K. Sugino, K. Miyamoto, M. Nagumo, and K. Aoki. Structural alterations of bearing steels under rolling contact fatigue. *Transactions ISIJ*, 10:98–111, 1970.

[18] J. A. Martin, S. F. Borgese, and A. D. Eberhardt. Microstructural alterations of rolling-bearing steel undergoing cyclic stressing. *Journal of Basic Engineering*, pages 555–567, 1966.

[19] D. Scott, B. Loy, and G. H. Mills. Metallurgical aspects of rolling contact fatigue. *Proc. Instn. Mech. Engrs.*, 181(3):94–103, 1966.

[20] A. P. Voskamp. *Microstructural changes during rolling contact fatigue*. PhD thesis, Technische Universiteit Delft, Netherlands, 1997.

[21] T. B. Lund. Sub-surface initiated rolling contact fatigue - influence of non-metallic inclusions, processing history and operating conditions. *ASTM STP 1524*, 7:81–96, 2010.

[22] J. A. Martin and A. D. Eberhardt. Identification of potential failure nuclei in rolling contact fatigue. *Transactions of the ASME*, 67:1–11, 1967.

[23] L. Vincent, B. Coquillet, and P. Guiraldenq. Fatigue damage of ball bearing steel: Influence of phases dispersed in the martensitic matrix. *Metallurgical Transactions A*, 11A:1001–1006, 1980.

[24] P. K. Pearson and T. W. Dickinson. The role of carbides in performance of high-alloy bearing steels. *ASTM STP 987*, pages 113–131, 1988.

[25] F. Sadeghi, B. Jalalahmadi, T. S. Slack, N. Raje, and N. K. Arakere. A review of rolling contact fatigue. *Journal of Tribology*, 131:1–15, 2009.

[26] Q. Chen, G. T. Hahn, C. A. Rubin, and V. Bhargava. The influence of residual stresses on rolling contact mode II driving force in bearing raceways. *Wear*, 126:17–30, 1988.

[27] Y. P. Chiu. The mechanism of bearing surface fatigue - experiments and theories. *Tribology Transactions*, 40:658–666, 1997.

[28] H. A. Spikes, A. L. Olver, and P. B. Macpherson. Wear in rolling contacts. *Wear*, 112:122–144, 1986.

[29] A. Warhadpande and F. Sadeghi. Effects of surface defects on rolling contact fatigue of heavily loaded lubricated contacts. *Journal of Engineering Tribology*, 224:1061–1077, 2010.

[30] G. Xu and F. Sadeghi. Spall initiation and propagation due to debris denting. *Wear*, 201:106–116, 1996.

[31] E. N. Bamberger. Status of understanding for bearing materials. Technical report, NASA, Lewis Research Centre, Ohio, 1983.

[32] B. L. Averbach and E. N. Bamberger. Analysis of bearing incidents in aircraft gas turbine mainshaft bearings. *Tribology Transactions*, 34:241–247, 1991.

[33] F. J. Ebert and P. Poulin. The effect of cleanliness on the attainable bearing life in aerospace applications. *Tribology Transactions*, 38:851–856, 1995.

[34] W. A. Glaeser and S. J. Shaffer. *Contact Fatigue*, volume 19, 331-336. ASM International, 1996.

[35] A. V. Olver. The mechanism of rolling contact fatigue - an update. *Journal of Engineering Tribology*, 219:313–330, 2005.

[36] A. Oila, B. A. Shaw, C. J. Aylott, and S. J. Bull. Martensite decay in micropitted gears. *Journal of Engineering Tribology*, 219:77–83, 2005.

[37] J. A. Wright, J. T. Sebastian, C. P. Kern, and R. J. Kooy. Design, development and application of new, high-performance gear steels. *Gear Technology*, pages 46–53, 2010.

[38] M. H. Evans. White structure flaking in wind turbine gearbox bearings. *Materials Science and Technology*, 28:3–21, 2012.

[39] E. N. Bamberger. Materials for rolling element bearings. *ASME Bearing Design*, pages 1–46, 1980.

[40] A. S. Gohardini, G. Doulgeris, and R. Singh. Challenges of future aircraft propulsion: A review of distributed propulsion technology and its potential application for the all electric commercial aircraft. *Progress in Aerospace Sciences*, 47:369–391, 2011.

[41] E. F. Josef. An overview of performance characteristics, experiences and trends of aerospace engine bearings technologies. *Chinese Journal of Aeronautics*, 20:378–384, 2007.

[42] S. Lacey and H. Kawamura. Bearings for aircraft gas turbine engines (part 1). *NSK Motion and Control*, 5:1–5, 1998.

[43] A. Dodd, N. Mitamura, H. Kawamura, and Y. Ohura. Bearings for aircraft gas turbine engines (part 2). *NSK Motion and Control*, No. 6:1–8, 1999.

[44] D. McCormick. Roller bearings pick up the pace. *Design Engineering*, pages 29–32, 1981.

[45] Rolls-Royce Ltd. *The Jet Engine*. Key Publishing, Derby, 5th edition, 1973.

[46] T. A. Harris, M. A. Ragen, and R. F. Spitzer. The effect of hoop and material residual stresses on the fatigue life of high speed, rolling bearings. *Tribology Transactions*, 35:194–198, 1992.

[47] C. Bathias. Gigacycle fatigue properties of bearing steels. *ASTM STP 1524*, pages 160–178, 2010.

[48] New Hampshire Ball Bearings Inc. Roller and ball bearings design guide. Minebea Co., Peterborough, NH, 2010.

[49] J. H. Mohn, H. M. Hodgens, H. E. Munson, and W. E. Poole. Improvement of the corrosion resistance of turbine engine bearings. *Pratt and Whitney Aircraft Report*, AD-A147 430:1–146, 1984.

[50] X. Xu, Z. Yu, and Y. Chen. Fracture and wear failure of a locomotive turbocharger-bearing sleeve. *Journal of Failure Analysis and Prevention*, 2011.

[51] W. R. Hinton. An investigation into the causes of ball bearing failures in types P2 and P3 engine-driven generators. *Wear*, 16:3–42, 1970.

[52] T. A. Harris and M. N. Kotzalas. *Rolling Bearing Analysis: Essential concepts of bearing technology*. CRC Press, Boca Raton, Fl, 5th edition, 2007.

[53] F. B. Pickering. *Physical Metallurgy and the Design of Steels*. Applied Science Publishers Ltd., London, 1978.

[54] H. K. D. H. Bhadeshia. MP10 process modelling. Mphil lecture notes, University of Cambridge, 2012.

[55] H. K. D. H. Bhadeshia. *Bainite in steels*. Institute of Materials, 1 Carlton House Terrace, London, 3rd edition, 2001.

[56] H. S. Yang and H. K. D. H. Bhadeshia. Austenite grain size and martensite start temperature. *Scripta Materialia*, 60:493–499, 2009.

[57] W. Solano-Alverez and H. K. D. H. Bhadeshia. White-etching matter in bearing steel. part 1: Controlled-cracking of bearing steel. *Metallurgical and Materials Transactions A*, 45:4907–4915, 2014.

[58] S. Carey and D. Herring. Low-pressure carburizing process development of M50 NiL. *Heat Treating Progress*, pages 43–46, 2007.

[59] P. K. Pearson. The history and future of aircraft turbine engine bearing steels. *ASTM STP 1327*, pages 335–353, 1998.

[60] B. C. D. Cooman, J. G. Speer, I. Y. Pyshmintsev, and N. Yoshinaga. *Materials design: the key to modern steel products*. Grips media GmbH, 2007.

[61] E. V. Zaretsky. Bearing and gear steels for aerospace applications. Technical memorandum, NASA, Lewis Research Centre, Ohio, 1990.

[62] T. A. Harris, J. Skiller, and R. F. Spitzer. On the fatigue life of M50 NiL rolling bearings. *Tribology Transactions*, 35(4):731–737, 1992.

[63] B. L. Averbach, B. Lou, P. K. Pearson, R. E. Fairchild, and E. N. Bamberger. Fatigue crack propagation in carburized high alloy bearing steels. *Metallurgical Transactions A*, 16:1253–1265, 1985.

[64] H. J. Bohmer. Residual stresses and material behaviour of M50NiL and RBD. *ASTM STP 1195*, pages 34–48, 1993.

[65] A. Iqbal and J. E. King. The role of primary carbides in fatigue crack propagation in aeroengine bearing steels. *International Journal of Fatigue*, 12:234–244, 1990.

[66] E. V. Zaretsky. Rolling bearing steels - A technical and historical perspective. *Materials Science and Technology*, 28:58–69, 2012.

[67] J. A. Rescalvo and B. L. Averbach. Fracture and fatigue in M-50 and 18-4-1 high speed steels. *Metallurgical Transactions A*, 10:1265–1271, 1979.

[68] A. Iqbal. Heat treatment response of triple and quintuple tempered M50 high speed steel. *European Journal of Scientific Research*, 17(2):150–159, 2007.

[69] H. J. Bohmer, T. Losche, F. J. Ebert, and E. Streit. The influence of heat generation in the contact zone on bearing fatigue behaviour. *Transactions of the ASME*, 121:462–467, 1999.

[70] H. Chu, C. Chen, and J. Yang. Rolling contact bearing steel for operation at 120 to 250c. *ASTM STP 1195*, pages 185–196, 1993.

[71] Tribology Handbook ed. M. J. Neale, editor. *Rolling Bearing Materials*. Butterworths, London, 1973.

[72] M. Flourous. Correlations for heat generation and outer ring temperature of high speed and highly loaded ball bearings in an aero-engine. *Aerospace Science and Technology*, 10:611–617, 2006.

[73] D. W. Hetzner and W. V. Geertruyden. Crystallography and metallography of carbides in high alloy steels. *Materials Characterization*, 59:825–841, 2007.

[74] A. P. Voskamp. Material response to rolling contact loading. *Journal of Tribology*, 107:359–366, 1985.

[75] SKF Plc. AISI-M50 VIM-VAR AMS 6491. *SKF Heat Treatment - Data card*, 2000.

[76] C. Ooki, K. Maeda, and H. Nakashima. Improving rolling contact fatigue life of bearing steels through grain refinement. *NTN Technical Review*, 71:2–7, 2004.

[77] H. E. Chandler. What users should know about clean steel technology. *Metal Progress*, pages 52–59, 1981.

[78] B. V. Molotilov and P. I. Yugov. Metallurgy of bearing steel. *Steel in Translation*, 38:565–568, 2008.

[79] H. Nakashima. Trends in materials and heat treatments for rolling bearings. *NTN Technical Review*, 76:10–17, 2008.

[80] D. Scott and J. Blackwell. The effect of some manufacturing variables on the performance of high-speed tool-steel ball bearings. *Wear*, 18:19–28, 1971.

[81] M. A. Klecka, G. Subhash, and N. K. Arakere. Microstructure-property relationships in M50-NiL and P675 case-hardened bearing steels. *Tribology Transactions*, 56(6):1046–1059, 2013.

[82] Shingo Yamasaki. *Modelling Precipitation of Carbides in Martensitic Steels*. PhD thesis, University of Cambridge, Darwin College, 2004.

[83] B. Decaudin, C. D. Mariadassou, and G. Cizeron. Structural study of M50 steel carbides. *Journal of Alloys and Compounds*, 226:208–212, 1995.

[84] J. E. Bridge, G. N. Maniar, and T. V. Philip. Carbides in M-50 high speed steel. *Metallurgical Transactions*, 2:2209–2213, 1971.

[85] A. D. B. Gingell, D. G. Jones, K. J. A. Mawella, and H. K. D. H. Bhadeshia. Carbide precipitation in some secondary hardened steels.

[86] F. A. Butterfield and T. R. McNelley. Porosity associated with insoluble carbides in VIM-VAR AISI M-50 steel and its probable effects on rolling contact fatigue. *Journal of Tribology*, 108(3):352–357, 1986.

[87] K. Kim, K. Oh, J. Lee, and D. Lee. Quantitative relationship between degree of center segregation and large carbide size in continuously cast bloom of high carbon chromium bearing steel. *ASTM STP 1524*, pages 3–16, 2010.

[88] ASTM International. Standard practice for assessing the degree of banding or orientation of microstructures. *ASTM International*, E 1268 - 01:1–29, 2002.

[89] E. J. Pickering and H. K. D. H. Bhadeshia. Macrosegregation and microstructural evolution in a pressure-vessel steel. *Metallurgical and Materials Transactions A*, 45:2983–2997, 2014.

[90] R. J. Parker and E. N. Bamberger. Effect of carbide distribution on rolling-element fatigue life of AMS 5749. *NASA Technical Report*, 2189:1–15, 1983.

[91] P. K. Adishesha. Effect of steel making and processing parameters on carbide banding in commercially produced ASTM A-295 52100 bearing steel. *ASTM STP 1419*, pages 27–46, 2002.

[92] F. Stahl, T. Hirsch, and P. Mayr. Application of continuous casting steel 100Cr6 (SAE 52100) for bearing balls. *ASTM STP 1327*, pages 216–230, 1998.

[93] F. Hengerer, J. Beswick, and A. Kerrigan. Evaluation of the continuous casting method for bearing steel production - SKF experience. *ASTM STP 1195*, pages 237–251, 1993.

[94] G. Akaishi, K. Doi, Y. Matsushima, I. Takagi, and Y. Fukuzaki. Production of high-carbon ball and roller bearing steel in BOF-FL-CC process. *Wire Journal International*, pages 92–98, 1999.

[95] Doherty and Melford. Solidification and microsegregation in killed steel ingots with particular reference to 1C-1.5Cr steel. *Journal of the iron and steel institute*, pages 1131–1143, 1966.

[96] T. L. Carter. A study of some factors affecting rolling-contact fatigue life. *NASA Technical Report*, R-60:1–48, 1960.

[97] W. J. Anderson. Effect of fiber orientation, temperature and dry powder lubricants on rolling contact fatigue. *Tribology Transactions*, 2:108–120, 1959.

[98] K. Okamoto, S. Shiko, and T. Ota. Dissolution of massive carbide in high carbon, chromium steel by soaking. *Transactions ISIJ*, 7:197–204, 1967.

[99] K. Kumagai, Y. Takata, T. Yamada, and K. Mori. Fatigue life of high-carbon chromium ball bearing steel produced by electric furnace. *ASTM STP 987*, pages 348–359, 1988.

[100] E. V. Zaretsky. Rolling element fatigue life of ausformed M50 balls. Technical note, NASA, Washington, D.C., 1968.

[101] L. Fontaine. *Elaboration par metallugie des poudres et caracterisation d'aciers rapides pour roulements de turbines aeronautiques.* PhD thesis, Ecole Nationale superieure des Mines de Paris, 1991.

[102] I. Hucklenbroich, G. Stein, H. Chin, W. Trojahn, and E. Streit. High nitrogen martensitic steels for critical components in aviation. *Materials Science Forum*, 318-320:161–166, 1999.

[103] S. G. Song, H. Du, and E. Y. Sun. Lattice orientation relationship between the M_2C carbide and the ferrite matrix in the M50NiL bearing steel. *Metallurgical and Materials Transactions A*, 33:1963–1969, 2002.

[104] T. Reti. *Residual stresses in carburized, carbonitrided, and case-hardened components.* ASM International, Materials Park, OH, 2002.

[105] P. J. Withers and H. K. D. H. Bhadeshia. Residual stress Part 2 - Nature and origins. *Materials Science and Technology*, 17:366–375, 2001.

[106] E. N. Bamberger and D. J. Kroeger. Rolling element fatigue life of a carburized modified M50 bearing steel. Final technical report, NASA, Lewis Research Centre, Ohio, 1984.

[107] B. L. Averbach and B. Lou. *Fatigue Crack Propagation Through Residual Stress Fields*, volume ICF 6. India, 1984.

[108] J. C. Clark, editor. *Fracture Tough Bearings for High Stress Applications*, number 1138, California, July 1985. American Institute of Aeronautics and Astronautics.

[109] S. Cretu and N. G. Popinceanu. The influence of residual stresses induced by plastic deformation on rolling contact fatigue. *Wear*, 105:153–170, 1985.

[110] N. H. Forster, L. Rosado, W. P. Ogden, and H. K. Trivedi. Rolling contact fatigue life and spall propagation of AISI M50, M50NiL, and AISI 52100, Part III: Metallurgical Examination. *Tribology Transactions*, 53:52–59, 2010.

[111] N. Binot, A. Viville, and H. Carrerot. Duplex treatment, carburizing and nitriding of a secondary hardening steel - application to aeronautical ball bearings. *Treatments and Tribology*, 334:1–7, 2001.

[112] P. J. Withers and H. K. D. H. Bhadeshia. Residual stress part 1 - measurement techniques. *Materials Science and Technology*, 17:355–365, 2001.

[113] Y. B. Guo and M. E. Barkey. Modelling of rolling contact fatigue for hard machined components with process-induced residual stress. *International Journal of Fatigue*, 26(6):605–613, 2004.

[114] C. Xiaomin. *Experimental and numerical approaches for improving rolling contact fatigue of bearing steel through enhanced compressive residual stress.* Doctoral thesis, Ohio State University, 2007.

[115] M. Jacobson. Surface integrity of hard-turned M50 steel. *Proceedings of the Institution of Mechanical Engineers*, 216:47–54, 2002.

[116] J. J. Bush, W. L. Grube, and G. H. Robinson. Microstructural and residual stress changes in hardened steel due to rolling contact. *Transactions of the ASME*, 54:390–413, 1961.

[117] D. Novovic, R. C. Dewes, D. K. Aspinwall, W. Voice, and P. Bowen. The effect of machined topography and integrity on fatigue life. *International Journal of Machine Tools and Manufacture*, 44:125–134, 2004.

[118] M. Jacobson and F. Gunnberg. Effects of hard turning on the fatigue life of ball bearings. *Proc. Instn. Mech. Engrs.*, 218:1855–1859, 2004.

[119] S. McKelvey and A. Fatemi. Influence of surface finish on fatigue behaviour of forged steel including heating method, hardness, and shot cleaning effects. Final report, AISI American Iron and Steel Institute, 2011.

[120] Y. K. Chou and C. J. Evans. Tool wear mechanism in continuous cutting of hardened tool steels. *Wear*, 212:59–65, 1997.

[121] E. V. Zaretsky, R. J. Parker, W. J. Anderson, and S. T. Miller. Effect of component differential hardnesses on residual stress and rolling contact fatigue. Technical note, NASA, Washington, D.C., 1965.

[122] K. Hirakawa, N. Ikeda, S. Okita, and A. Kiuchi. Inner ring fracture characteristics under rolling contact. *NSK Motion and Control*, 7:15–23, 1999.

[123] N. Tsushima. Various types of failures in rolling bearings. *SAE Technical Paper Series*, 870797:11–15, 1987.

[124] E. N. Bamberger, E. V. Zaretsky, and H. Signer. Endurance and failure characteristic of main-shaft jet engine bearing at 3x10^6 DN. *Journal of Tribology*, 98:580–585, 1976.

[125] N. Tsushima, H. Yamada, and K. Maeda. Changes in X-ray parameters with loading cycles in rolling contact in through-hardened bearing steels. *Tribology Transactions*, 30(4):465–471, 1986.

[126] R. H. Vegter, H. A. Verschoor, and A. Girones. X-ray microdiffraction for the analysis of bearing operation conditions. *Journal of ASTM International*, 3:227–233, 2007.

[127] S. Hillman, H. Heuer, H. U. Baron, J. Bamberg, A. Yashan, and N. Meyendorf. Near-surface residual stress-profiling with high frequency eddy current conductivity measurement. In *AIP Conference proceedings*, volume 1096, pages 1349–1355, 2009.

[128] S. Desvaux, M. Duquennoy, J. Gualandri, and M. Ourak. The evaluation of surface residual stress in aeronautic bearings using the barkhausen noise effect. *NDT&E International*, 37:9–17, 2004.

[129] H. Hertz. On the contact of elastic solids. *J. reine und angewandte Mathematik*, 92:156–171, 1882.

[130] A. B. Jones. Metallographic observations of ball bearing fatigue phenomena. *Steel*, 119:68–70, 97–100, 1947.

[131] A. Grabulov, R. Petrov, and H. W. Zandbergen. EBSD investigation of the crack initiation and TEM/FIB analyses of the microstructural changes around the cracks formed under rolling contact fatigue (RCF). *International Journal of Fatigue*, 32:576–583, 2010.

[132] A. Vincent, G. Lormand, P. Lamagnere, L. Gosset, D. Girodin, G. Dudragne, and R. Fougeres. From white etching areas formed around inclusions to crack nucleation in bearing steels under rolling contact fatigue. *ASTM STP 1327*, pages 109–123, 1998.

[133] C. Qing, S. Eryu, Z. Dongmei, G. Juwen, and F. Zhonghe. Measurement of the critical size of inclusions initiating contact fatigue cracks and its application in bearing steel. *Wear*, 147:285–294, 1991.

[134] W. E. Littman. The mechanism of contact fatigue. *NASA SP*, 237:309–377, 1970.

[135] W. J. Greenert. The toroid contact roller test as applied to the study of bearing materials. *ASME Journal of Basic Engineering*, 84:181, 1962.

[136] M. J. Martin, M. P. Alanou, H. P. Evans, R. W. Snidle, H. Kawamura, and A. Dodd. Scuffing performance of m50 bearing steel lubricated was a gas turbine engine oil at high sliding speeds. *Tribology Transactions*, 44:465–471, 2001.

[137] S. Das Bakshi, A. Leiro, B. Prakash, and H. K. D. H. Bhadeshia. Dry rolling/sliding wear of nanostructured bainite. *Wear*, 316:70–78, 2014.

[138] S. Das Bakshi, P. H. Shipway, and H. K. D. H. Bhadeshia. Three-body abrasive wear of fine pearlite, nanostructured bainite and martensite. *Wear*, 308:46–53, 2013.

[139] T. A. Harris and M. N. Kotzalas. *Rolling Bearing Analysis: Advanced concepts of bearing technology*. CRC Press, Boca Raton, Fl, 5th edition, 2006.

[140] G. Popescu, A. Gaeblli, G. M. Espejel, and B. Wemekamp. Microplastic material model and residual stress fields in rolling contacts. *ASTM International*, 14603, 2007.

[141] G. F. Dambaugh. Fatigue considerations of high strength rolling bearing steels. White paper, Simulia, 2006.

[142] A. P. Voskamp. Fatigue and material response in rolling contact. *ASTM STP 1327*, pages 152–166, 1998.

[143] K. L. Johnson. *Contact Mechanics*. Cambridge University Press, 1985.

[144] B. Jalalahmadi and F. Sadeghi. A voronoi FE fatigue damage model for life scatter in rolling contacts. *ASME Journal of Tribology*, 132:1–14, 2010.

[145] N. K. Arakere and G. Subhash. Work hardening response of M50-NiL case hardened bearing steel during shakedown in rolling contact fatigue. *Materials Science and Technology*, 28:34–38, 2012.

[146] F. T. Barwell. The effect of lubrication and nature of superficial layer after prolonged periods of running. *Properties of Metallic Surfaces*, 18:101–123, 1953.

[147] J. F. Braza and P. K. Pearson. Tribological and metallurgical evaluation of ferritic nitrocarburized M-50 and M-50NiL steels. *ASTM STP 1195*, pages 49–60, 1993.

[148] R. Osterlund and O. Vingsbo. Phase changes in fatigued ball bearings. *Metallurgical Transactions A*, 11A:701–707, 1980.

[149] W. Solano-Alverez and H. K. D. H. Bhadeshia. White-etching matter in bearing steel. part 2: Distinguishing cause and effect in bearing steel failure. *Metallurgical and Materials Transactions A*, 45:4916–4931, 2014.

[150] R. Osterlund, O. Vingsbo, L. Vincent, and P. Guiraldenq. Butterflies in fatigued ball bearings - formation mechanisms and structure. *Scandinavian Journal of Metallurgy*, 11:23–32, 1982.

[151] N. Tsunekage, K. Hashimoto, T. Fujimatsu, and K. Hiraoka. Initiation behaviour of crack originated from non-metallic inclusion in rolling contact fatigue. *Journal of ASTM International*, 7(2), 2010.

[152] F. Kyozaburo, M. Yasuo, and A. Tstutomu. Development of long life bearing steel for full film lubrication and for poor and contaminated lubrication. *NSK Motion and Control*, 1:30–36, 1996.

[153] A. P. Voskamp and G. E. Hollox. Failsafe rating of ball bearing components. *ASTM STP 987*, pages 102–112, 1988.

[154] D. Nelias, M. L. Dumont, F. Couhier, G. Dudragne, and L. Flamand. Experimental and Theoretical Investigation on Rolling Contact Fatigue of 52100 and M50 Steels Under EHL or Micro-EHL Conditions. *Transactions of the ASME*, 120:184–190, 1998.

[155] P. Sahoo. *Engineering tribology.* PHI Learning Pvt. Ltd., 2005.

[156] A. H. Nahm. Effect of grain flow orientation on rolling contact fatigue life of AISI M-50. *Transactions of the ASME*, 104:330–334, 1982.

[157] Jurgen Gegner. *Tribological Aspects of Rolling Bearing Failures.* Tribology - Lubricants and Lubrication. InTech, 2011.

[158] O. Zwirlein and H. Schicht. Rolling contact fatigue mechanisms - accelerated testing versus field performance. *ASTM STP 771*, pages 358–379, 1982.

[159] P. Gloeckner and F. J. Ebert. Micro-sliding in high-speed aircraft engine ball bearings. *Tribology Transactions*, 53:369–375, 2010.

[160] C. H. Hager, G. L. Doll, R. D. Evans, and P. J. Shiller. Minimum quantity lubrication of M50/M50 and M50/Si3N4 tribological interfaces. *Wear*, 271:1761–1771, 2011.

[161] L. Wang and R. J. K. Wood. The influence of contact conditions on surface reaction layers formed between steel surfaces lubricated by an aviation oil. *Tribology International*, 40:1655–1666, 2007.

[162] A. Warhadpande, B. Leonard, and F. Sadeghi. Effects of fretting wear on rolling contact fatigue life of M50 bearing steel. *Proc. Instn. Mech. Engrs.*, 222:69–80, 2008.

[163] ISO International Standard. Rolling bearings - damage and failures - terms, characteristics and causes.

[164] D. Popgoshev and R. Valori. Rolling contact fatigue evaluation of advanced bearing steels. *ASTM STP 771*, pages 342–357, 1982.

[165] B. R. Nielson, B. Torp, C. M. Rangel, M. H. Simplicio, A. C. Consiglieri, M. F. DaSilva, F. Paszti, J. C. Soares, A. Dodd, J. Kinder, M. Pitaval, P Thevenard, and R. G. Wing. Improvement of the corrosion resistance of M50 bearing steel by implantation with metal ions. *Nuclear instruments and methods in physics research*, B59:772–777, 1991.

[166] A. Dodd, J. Kinder, B. Torp, B. R. Nielson, C. M. Rangel, and M. F. DaSilva. The effect of ion implantation on the fatigue life and corrosion resistance of M50 steel bearings. *Surface and Coatings Technology*, 74:754–759, 1995.

[167] P. Mukhopadhyay, P. S. Kannaki, M. Srinivas, and M. Roy. Microstructural developments during abrasion of M50 bearing steel. *Wear*, 315:31–37, 2014.

[168] L. Wang, B. Peng, L. Gu, and J. Wang. Tribological performance of m50 steel tribo-parts. *Tribology Transactions*, 55:191–198, 2012.

[169] R. A. Baughman. Effect of hardness, surface finish, and grain size on rolling-contact fatigue life of M-50 bearing steel. *Journal of Basic Engineering*, 82:287–294, 1960.

[170] M. Hasegawa, J. Liu, K. Okuda, and M. Nunobiki. Calculation of the fractal dimensions of machined surface profiles. *Wear*, 192:40–45, 1996.

[171] W. Grzesik and S. Brol. Hybrid approach to surface roughness evaluation in multistage machining processes. *Journal of Materials Processing Technology*, 134:265–272, 2003.

[172] J. Schmit, S. Han, and E. Novak. Ball bearing measurement with white light interferometry. *Proc. of SPIE*, 7389, 2009.

[173] A. Jackson and A. Cameron. An interferometric study of the EHL of rough surfaces. *ASLE Transactions*, 19:50–60, 1976.

[174] M. P. Alanou, H. P. Evans, and R. W. Snidle. Effect of different surface treatments and coatings on the scuffing performance of hardened steel discs at very high sliding speeds. *Tribology International*, 37:93–102, 2004.

[175] W. Cheng, H. S. Cheng, and L. M. Keer. Longitudinal crack initiation under pure rolling contact fatigue. *Tribology Transactions*, 37:51–58, 1994.

[176] V. M. M. B. da Mota, P. M. G. P. Moreira, and L. A. A Ferreira. A study of the effects of dented surfaces on rolling contact fatigue. *International Journal of Fatigue*, 30:1997–2008, 2008.

[177] N.K. Arakere, N. Branch, G. Levesque, V. Svendsen, and N. H. Forster. Rolling contact fatigue life and spall propagation of AISI M50, M50NiL, and AISI 52100, Part II: Stress Modelling. *Tribology Transactions*, 53:42–51, 2010.

[178] W. Cheng, H. S. Cheng, and L. M. Keer. Experimental investigation on rolling/sliding contact fatigue crack initiation with artificial defects. *Tribology Transactions*, 37:1–12, 1994.

[179] R. P. Shevchenko. Lubricant requirements for high temperature bearings. *SAE Technical Paper Series*, 660072:309–322, 1966.

[180] H. K. Trivedi, D. T. Gerardi, and L. Rosado. Evaluation of fatigue and wear characteristics of M50 steel using synthetic ester turbine engine lubricants - part 1. *Wear*, 185:111–117, 1995.

[181] T. H. C. Childs and A. Mimaroglu. Sliding friction and wear up to 600c of high speed steels and silicon nitrides for gas turbine bearings. *Wear*, 162:890–896, 1993.

[182] L. Rosado, H. K. Trivedi, and D. T. Gerardi. Evaluation of fatigue and wear characteristics of M50 steel using synthetic ester turbine engine lubricants - part ii. *Wear*, 196:133–140, 1996.

[183] L. D. Wedeven, D. Evans, and A. Cameron. Optical analysis of ball bearing starvation. Technical Memorandum 52869, NASA, Lewis Research Centre, Ohio, 1970.

[184] B. J. Hamrock and D. Dowson. Isothermal elastohydrodynamic lubrication of point contacts. Technical Note 8317, NASA, Lewis Research Centre, Ohio, 1976.

[185] R. J. Chittenden, D. Dowson, J. F. Dunn, and C. M. Taylor. A theoretical analysis of the isothermal elastohydrodynamic lubrication of concentrated contacts I. direction of lubricant entrainment coincident with the major axis of the hertzian contact ellipse. *Proceedings of the Royal Society A*, 397:245–269, 1985.

[186] M. Woydt and R. Wasche. The history of the Stribeck curve and ball bearing steels: The role of Adolf Martens. *Wear*, 268:1542–1546, 2010.

[187] M. Mosleh, K. Bradshaw, J. H. Belk, and J. C. Waldrop. Fatigue failure of all-steel and steel-silicon nitride rolling ball combinations. *Wear*, 271:2471–2476, 2011.

[188] I. Krupka, M. Vrbka, and M. Hartl. Effect of surface texturing on mixed lubricated non-conformal contacts. *Tribology International*, 41:1063–1073, 2008.

[189] R. W. K. Honeycombe. *The Plastic Deformation of Metals*. Edward Arnold (Publishers) Ltd, London, 1968.

[190] A. A. Griffith. The phenomena of rupture and flow in solids. *Philosophical Transactions of the Royal Society of London*, 221:163–198, 1921.

[191] P. Paris and F. Erdogan. A critical analysis of crack propagation laws. *Journal of Fluids Engineering*, 85:528–533, 1963.

[192] E. N. Bamberger, B. L. Averbach, P. K. Pearson, S. Vanpeit, and M. J. Price. Improved fatigue life bearing development. Final Report AD-B137 279, Air Force Wright Aeronautical Laboratories, 1989.

[193] S. Eryu, H. Xingyuan, W. Chansheng, Z. Yaomin, and C. Qing. A method of detecting rolling contact crack initiation and the establishment of crack propagation curves. *Tribology Transactions*, 31:6–11, 1988.

[194] S. Ito, N. Tsushima, and H. Muro. Accelerated rolling contact fatigue test by a cylinder-to-ball rig. *ASTM STP 771*, pages 125–135, 1982.

[195] P. J. Blau. Rolling contact wear. *Wear*, 18:257–262, 1992.

[196] D. Glover. A ball-rod rolling contact fatigue tester. *ASTM STP 771*, pages 107–124, 1982.

[197] E. V. Zaretsky. in search of a fatigue limit: A critique of ISO standard 281:2007. *Tribology & Lubrication Technology*, pages 30–40, 2010.

[198] E. V. Zaretsky, J. V. Poplawski, and C. R. Miller. Rolling bearing life prediction - past, present and future. *NASA Technical Memorandum*, 210529, 2000.

[199] European Aviation Safety Agency. Certification specifications for engines. *EASA CS-E*, 018, 2009.

[200] ISO International Standard. Tool steels and bearing steels - micrographic method for assessing the distribution of carbides using reference photomicrographs.

[201] A. Garg, T. R. McNelley, and J. L. Perry. Analysis of microporosity associated with insoluble carbides in VIM-VAR AISI M-50 steel. *Metallography*, 20:89–98, 1987.

[202] T. L. Carter. Effect of fiber orientation in races and balls under rolling-contact fatigue conditions. *National Advisory Commitee for Aeronautics*, Technical Note 4216:1–37, 1958.

[203] K. Kanaya and S. Okayama. Penetration and energy-loss theory of electrons in solid targets. *J. Phys. D: Appl. Phys.*, 5, 1972.

[204] K. Nakamura and M. Yashima. Crystal structure of NaCl-type transition metal monocarbides MC (M=V,Ti,Nb,Ta,Hf,Zr), a neutron powder diffraction study. *Materials Science and Engineering B*, 148:69–72, 2008.

[205] K. Madhav Reddy, T. N. Rao, J. Revathi, and J. Joarder. Structural stability of Mo2C during thermochemical processing. *Journal of Alloys and Compounds*, 494:386–391, 2010.

[206] D. Fruchart, P. Chaudouet, R. Fruchart, A. Rouault, and J. P. Senateur. Etudes structurales de composes de type cementite. *Journal of Solid State Chemistry*, 51:246–252, 1984.

[207] D. C. Azubike, A. Chrysanthou, and U. O. Igiehon. A crystallographic re-examination of the (Fe,W)6C phase field in the Fe-W-C system. *Powder Diffraction*, 7:162–163, 1992.

[208] A. A. Kelley and K. M. Knowles. *Crystallography and Crystal Defects*. Wiley, 2nd. ed. edition, 2012.

[209] L. Xiaogang, Q. Chen, and S. Eryu. Initiation and propagation of case crushing cracks in rolling contact fatigue. *Wear*, 122:33–43, 1988.

[210] N. Tsuji, Y. Ito, Y. Saito, and Y. Minamino. Strength and ductility of ultrafine grained aluminum and iron produced by ARB and annealing. *Scripta Materialia*, 47:893–899, 2002.

[211] N. P. Suh. An overview of the delamination theory of wear. *Wear*, 44:1–16, 1977.

[212] American Society for Testing and Materials. Standard test methods for determining average grain size. *ASTM International*, E112-10, 2004.

[213] International Organization for Standardization. Heat-treated steels, alloy steels and free-cutting steels. *ISO International Standard*, 683-17, 1999.

[214] T. Maki and C. M. Wayman. Transmission electron microscopy studies of thin foil martensite in Fe-Ni and Fe-Ni-C alloys. *Acta Metallurgica*, 25:681–693, 1977.

[215] F. H. Samuel and D. S. Sarma. Deformation of plate martensite in Fe-Ni and Fe-Ni-C alloys. *Metal Science*, 16:171–173, 1982.

[216] J. W. Christian and S. Mahajan. Deformation twinning. *Progress in Materials Science*, 39:1–157, 1995.

[217] T. Maki and C. M. Wayman. Transformation twin width variation in Fe-Ni and Fe-Ni-C martensites. *Japan Institute of Metals*, pages 69–74, 1976.

[218] H. Liu, X. Jin, H. Dong, and J. Shi. Martensitic microstructural transformations from the hot stamping, quenching and partitioning process. *Materials Characterization*, 62:223–227, 2011.

[219] A. Bhattarcharya, G. Subhash, and N. Arakere. Evolution of subsurface plastic zone due to rolling contact of M-50 NIL case hardened bearing steel. *International Journal of Fatigue*, 59:102–113, 2014.

[220] *Standard Test Method for Residual Stress Measurement by X-ray diffraction for bearing steels*, volume E2860-12. ASTM International, 100 Barr Harbor Drive, West Conshohocken, PA, 2012.

[221] R. H. Vegter, T. Buslaps, Y. Kadin, and H. A. Verschoor. Measurement of residual stresses in ball bearings by synchrotron radiation. *ASTM STP 1580*, pages 590–601, 2015.

[222] H. R. Wenk and P. Van Houtte. Texture and anisotropy. *Reports on Progress in Physics*, 67:1367–1428, 2004.

[223] E. J. Mittemeijer. *Fundamentals of Materials Science*. Springer, 2011.

[224] A. P. Voskamp and E. J. Mittemeijer. *Metallurgical and Materials Transactions A*, 27, 1996.

[225] L. Horcas, R. Fernandez, J. M. Gomez-Rodriguez, J. Colchero, J. Gomez-Herrero, and A. M. Baro. WSXM: A software for scanning probe microscopy and a tool for nanotechnology. *Rev. Sci. Instrum.*, 78, 2007.

[226] C. N. Reid. The association of twinning and fracture in BCC metals. *Metallurgical Transactions A*, 12:371–377, 1981.

[227] A. Gilbert, G. T. Hahn, C. N. Reid, and B. A. Wilcox. Twin-induced grain boundary cracking in BCC metals. *Acta Metallurgica*, 12:754–755, 1963.

[228] M. Anglada. A mechanism for fatigue crack nucleation at the twin-matrix interface of BCC metals. *Journal of Materials Science Letters*, 8:885–886, 1989.

[229] J. Bolansky and T. Smida. Deformation twins - probable inherent nuclei of cleavage fracture in ferritic steels. *Materials Science and Engineering A*, 323:198–205, 2002.

[230] F. Sorbello, P. E. J. Flewitt, G. Smith, and A. G. Crocker. The role of deformation twins in brittle crack propagation in iron-silicon steel. *Acta Metallurgica*, 57:2646–2656, 2009.

[231] T. Taniguchi, Y. Kaneko, and S. Hashimoto. Fatigue lives of a ferritic stainless steel containing deformation twins. *Key Engineering Materials*, 353-358:283–286, 2007.

[232] L. Wang, R. J. K. Wood, T. J. Harvey, S. Morris, H. E. G. Powrie, and I. Care. Wear performance of oil lubricated silicon nitride sliding against various bearing steels. *Wear*, 255:657–668, 2003.

[233] X. A. Wang, M. F. Yan, C. S. Zhang, and Y. X. Zhang. Microstructure and mechanical properties of surface layer of M50NiL steel plasma nitrided. *Surface Engineering*, 30:218–223, 2014.

[234] S. Ooi and H. K. D. H. Bhadeshia. Duplex hardening of steels for aeroengine bearings. *ISIJ International*, 52:1927–1934, 2012.

[235] A. W. Sleeswyk. Emissary dislocations: Theory and experiments on the propagation of deformation twins in α-iron. *Acta Metallurgica*, 10:705–725, 1962.